

**Development of low bandgap donor-acceptor polymers for
use in optoelectronics**

By

Saif Mia

A thesis submitted to

the Faculty of Graduate and Postdoctoral Affairs

in partial fulfillment of the requirements for the degree of

Doctor of Philosophy

in

Chemistry

Carleton University

Ottawa, Ontario, Canada

April 2016

© Copyright, Saif Mia, Ottawa, ON, Canada, 2016

Abstract

Development of organic optoelectronic devices have gained great deal of attention in recent years due to unique advantages over their inorganic counterpart such as easy processability and flexibility. The focus of development has gone into conjugated organic polymers and tuning band gap. Adopting donor-acceptor (D-A) methodology have been the most effective strategy in conceptualizing these developments. This thesis consists of four parts. The first part consists of design, syntheses and characterization of diketopyrrolopyrrole (**DPP**)- based polymers bearing thermal cleavable moiety used for multilayer device structure. These polymers show spectral response from 300-800 nm and display reasonable solubility prior to cleavage. Multilayer films were easily processed with good retention of PCBM and are excellent candidate for tandem devices. In the second part, introduction of a stronger acceptor, diazapentalene (**DAP**), in polymer to achieve coverage of longer wavelength and study of multilayer device for photodetection. Furthermore, conversion of the **DPP**-based polymers to their thiolactam analogue were demonstrated. The converted polymers show bathochromic shift in absorption and large spectral response tailing at 1400 nm. The multilayer device consisting of polymer **DAPb-DTP** exhibit superior detectivity, responsivity and EQE in the NIR region from 750 to 1000 nm. In the third section, development of cross-linkable polymer for use as p-type interface layer was demonstrated. The cross-linked films were rendered insoluble using palladium catalyst. In the last section, modified benzothiadiazole (**BT**)- based polymers were synthesized to study electrochromic activity in the near-infrared region and also demonstrate intramolecular hydrogen-bonding to increase the strength of the **BT** unit.

Acknowledgements

I would like to express my deepest appreciation towards the following people who have helped me throughout my PhD.

Firstly, I would like to show my gratitude to my supervisor, Dr. Wayne Wang, for his mentorship, guidance, patience, encouragement, and motivation.

I would also like to thank Dr. Jane Gao for her assistance and suggestion. She helped me keep the lab to regulatory code. I would also like to thank all my colleagues in the laboratory whom not only helped me come up with alternative ideas when I was stuck but also made my experience at Carleton University more enjoyable: Gang Qain, Duo Li, Wendy Hao, Khama Rani Ghosh, Sukanta Kumar Saha, Songqiu Zhou and Di Zhang.

To Jim Logan, Tony O'Neil, Keith Bourque, Elena Munteanu, Peter Mosher and Chantelle Gravelle: I would like to say thank you all for support of the instrumental techniques and guidance.

Finally, I wish to dedicate this thesis to my parents, who raised me and helped me get to where I am today. To my family and friends, for their love, endless support and encouragement.

To Parveen, my beloved wife, I would like to thank you for the endless support and encouragement.

Table of Contents

Abstract.....	I
Acknowledgements.....	II
Table of Contents.....	III
List of Figures.....	VIII
List of Schemes.....	XIV
List of Tables.....	XV
List of Symbols and Abbreviations.....	XVI
Chapter 1 Introduction in Visible-Near Infrared Organic Materials	1
1.1 Conjugated polymers.....	1
1.2 Band-gap tuning.....	3
1.2.1 Bond length alteration.....	4
1.2.2 Mean deviation from planarity.....	5
1.2.3 Aromatic resonance energy.....	5
1.2.4 Effect of substitution.....	6
1.2.5 Interchain coupling in the solid state.....	7
1.2.6 Effect of conjugation length.....	7
1.2.7 Effect of donor-acceptor charge transfer.....	8
1.3 Donor-acceptor polymers.....	9
1.3.1 Polythiophenes and derivatives.....	9
1.3.2 Ladder molecules.....	11
1.3.3 Donor-acceptor systems.....	12
1.3.3.1 Effect of spacer units.....	15
1.3.3.2 Effect of electron acceptors.....	16
1.3.3.3 Effect of electron donors.....	18
1.4 Photovoltaics.....	18
1.4.1 Working principles of photovoltaics.....	19
1.4.1.1 Single layer junction.....	19

1.4.1.2 Bilayer junction.....	20
1.4.1.3 Bulk heterojunction and tandem heterojunction.....	21
1.4.2 Organic photoelectric process.....	23
1.4.2.1 Light absorption and exciton formation.....	24
1.4.2.2 Exciton migration.....	24
1.4.2.3 Exciton dissociation.....	25
1.4.2.4 Charge migration and charge collection.....	26
1.4.3 Photodetectors parameters.....	26
1.4.4 Polymers used in photovoltaic devices.....	28
1.4.4.1 Polymers for solar cell devices.....	29
1.4.4.2 Polymers for photodetectors.....	35
1.5 Rationale and Objectives.....	39
References.....	41

Chapter 2 Design, Synthesis, Characterization of Soluble-to-Insoluble Diketopyrrolopyrrole based Polymers and Their Use in Multilayer Devices

2.1 Introduction	52
2.2 Results and discussions	55
2.2.1 Synthesis of acceptor monomer	55
2.2.2 Synthesis of donor monomers	57
2.2.3 Synthesis of D-A polymers	58
2.2.4 Characterization	61
2.2.4.1 Cleavage of the BOC group	61
2.2.4.2 Thermal stability	64
2.2.4.3 Absorption of BDPP and DPP polymers	66
2.2.4.4 Solvatochromism and Halochromism.....	68
2.2.4.5 Electrochemical property	69
2.2.5 Preparation and characterization of multilayer films	71
2.2.5.1 Organic field effect measurements	73
2.2.5.2 X-ray diffraction analysis	77

2.2.5.3 EQE and dark current measurements.....	78
2.3 Conclusion	80
2.4 Experimental	80
2.4.1 Materials	80
2.4.2 Measurements	81
2.4.3 Solubility test	82
2.4.4 Film preparation	83
2.4.3.1 Multilayer preparation	83
2.4.3.2 EQE device fabrication.....	83
2.4.4 Synthesis	84
References	101

Chapter 3 Transformation of Diketopyrrolopyrrole Polymers into Dithioketopyrrolopyrrole (DTPP) and Diazapentalene (DAP) Polymers and their Use in Visible-near Infrared Photodetectors

3.1 Introduction	105
3.2 Results and discussions	108
3.2.1 Synthesis of DTPP and DAP monomer	108
3.2.2 Synthesis of DAP polymers	109
3.2.3 PDTPP polymer reaction	111
3.2.4 IR characterization	112
3.2.5 NMR characteristics of PDTPP and DTPP-polymers	116
3.2.6 Absorption characterization	119
3.2.6.1 Optical properties of DAPP polymers	119
3.2.6.2 Optical properties of DTPP polymers	122
3.2.6.3 Photodegradation of PDTPP and DTPP polymers	124
3.2.7 Thermal characterization	127
3.2.8 Electrochemical characterization and band gap calculation	129
3.2.8.1 DAP polymers.....	129
3.2.8.2 DTPP polymers.....	131
3.2.9 Photodetector performances.....	132

3.2.9.1 Single-layer photodetector based on DAP polymers	132
3.2.9.2 Multilayer photodetector performances of DPP-DAP polymers	137
3.2.9.3 Photodetector based on DTPP polymers	141
3.3 Conclusion.....	142
3.4 Experimental.....	143
3.4.1 Materials.....	143
3.4.2 Instruments.....	143
3.4.3 Photodegradation measurement of PDTPP and DTPP polymers	144
3.4.4 Multilayer device fabrication and characterization.....	144
3.4.4 Synthesis.....	146
References.....	152

Chapter 4 Synthesis and Characterization of Cross-linkable Functionalized Isoindigo-carbazole Polymers for Use in Photovoltaic Devices as Hole Blocking Layer

4.1 Introduction	156
4.2 Results and discussions.....	161
4.2.1 Syntheses of polymers.....	161
4.2.1.1 Crosslinking of polymers.....	163
4.2.2 IR characterization.....	164
4.2.3 NMR characterization.....	165
4.2.4 Thermal analysis	167
4.2.5 Absorption	168
4.2.6 Electrochemical property and band gaps.....	169
4.3 Conclusion.....	172
4.4 Experimental.....	172
4.4.1 Materials	172
4.4.2 Instruments	173
4.4.3 Cross-linking procedure	173
4.4.4 Synthesis	173

References.....	178
Chapter 5 Electrochromic Study of Benzothiadiazole Based Polymers	
5.1 Introduction.....	184
5.2 Results and discussions.....	190
5.2.1 Synthesis of benzothiadiazolo-based donor-acceptor polymers bearing thermally cleavable group	190
5.2.2 IR characteristic	192
5.2.3 Thermal properties	193
5.2.4 Absorption properties	194
5.2.5 Electrochemical properties and band gaps	198
5.2.6 Electrochromic properties of the chromophores	200
5.2.7 OTFT measurements	204
5.3 Conclusion.....	205
5.4 Experimental.....	206
5.4.1 Materials	206
5.4.2 Instruments	206
5.4.3 OTFT fabrication	206
5.4.4 Synthesis	207
References	210
Conclusion and Outlook	214
Contribution to Knowledge	216
Appendices.....	217
Appendix A: ^1H and ^{13}C NMR spectra of compounds and polymers.....	217
Appendix B: IR, Mass spectra and GPC data	265
Appendix C: Thermal and electrochemical data	287
Appendix D: Film properties	292

List of Figures

Figure 1.1. Factors affecting the band gap of polymer	3
Figure 1.2. Conjugated polymers in the aromatic (ground-state) and quinoid forms	4
Figure 1.3. Regioregularity of polychalcogens	5
Figure 1.4. Transformation of small π -conjugated unit to linear or 2D enlargement	7
Figure 1.5. Absorption of fused porphyrins	8
Figure 1.6. Hybridization of the energy levels of a donor (D) and acceptor (A)	9
Figure 1.7. Structure of polythiophene derivatives and resonance structures.	10
Figure 1.8. PITN derivatives	10
Figure 1.9. Ladder polymers	11
Figure 1.10. Rylene systems	12
Figure 1.11. Preparation of polysquaraines.....	13
Figure 1.12. General structure of acceptors, donors and bridging unit used in D- π -A- π -D repeating segment.....	15
Figure 1.13. The - π -A- π - moiety having thiophene and pyrrole spacer.....	16
Figure 1.14. Strong acceptors of benzochalcogenodiazole and thienothiadiazole and corresponding D-A polymers.....	17
Figure 1.15. D-A polymers containing cyano, nitro and fluorinated BT acceptors	17
Figure 1.16. Electron donor effect on the band gap	18
Figure 1.17. Single junction cell	20
Figure 1.18. Bilayer junction	21
Figure 1.19. Bulk and tandem heterojunction	23
Figure 1.20. (a) Photoelectric process (1) light absorption and exciton formation (2) exciton migration (3) exciton dissociation (4) charge migration and charge collection (b) Sun irradiance (red) and number of photons (black) as a function of wavelength.....	24

Figure 1.21. Structures of fullerene-based electron acceptors used in photovoltaic devices: [60]PCBM, [70]PCBM and ICBA	29
Figure 1.22. Structure of PPV and P3HT	30
Figure 1.23. Donor-acceptor polymers PCPDTBT, PSBTBT, PCDTBT, TTBDT, PTB7-Th	31
Figure 1.24. DPP-based polymers	32
Figure 1.25. Polymer PFO-DBT and APFO-15	33
Figure 1.26. Polymers BDT-BT-DT and BDT-FBT-2T	34
Figure 1.27. Polymer PDTP-DFBT and tandem cell configuration	35
Figure 1.28. Polymers F8TBT, PT-TT and PTZBTTT-BDT used in photodetectors	37
Figure 1.29. (a) Polymers PTT, PDDTT, PDAPBDT (b) Detectivities of Si, InGaAs and PDDTT-based photodetectors (c) EQE vs. wavelength and calculated detectivities at 500 nm and 800 nm of PDDTT	38
Figure 1.30. DAP, DPP and BT structure	39
Figure 2.1. Tandem cell configuration	52
Figure 2.2. Functionalization of DPP	54
Figure 2.3. Hydrogen bonds between the DPP units in the solid state	53
Figure 2.4. Infrared spectroscopy of (a) BDPP and (b) DPP units	62
Figure 2.5. ¹ H NMR (300 MHz) of BDPP-TBTT (top) and DPP-TBTT (bottom) in tetrachloroethane-D ₂	63
Figure 2.6. TGA of BDPP-BT , BDPP-TPT and BDPP-TBT	65
Figure 2.7. Absorption spectra of polymers in 1,2,4-trichlorobenzene (a) at room temperature, (b) after heating at 180 °C, (c) film at room temperature (d) film after heating at 180 °C	67
Figure 2.8. Absorption spectra of (a) DPP-TPTB and (b) DPP-BI in different solvents and reagents. TCB: 1,2,4-trichlorobenzene, PC: propylene carbonate, CSA: camphorsulfonic acid, TEA: trimethylamine	69
Figure 2.9. CV of polymers on ITO in 0.1 M Bu ₄ NPF ₆ in acetonitrile at scan rate of 100 mV/s (a) with BOC (b) without BOC	70
Figure 2.10. Multilayer film fabrication (a) AFM of DPP-BI (roughness ~0.5	

nm) (b) AFM of PDPP-F spin coated on top of partially covered DPP-BI layer. Left shows droplet like PDFF-F (roughness ~ 15 nm) and right showing bottom layer of DPP-BI	72
Figure 2.11. Absorption of the films of DPP-BI (~60 nm), PDPP-F (~75 nm) and bilayer DPP-BI (bottom layer) with PDPP-F (top layer)	72
Figure 2.12. Typical configuration of organic field-effect transistor	73
Figure 2.13. Organic semiconducting materials used for OFET	75
Figure 2.14. Transfer (a) and output (b) characteristics of OFET based on polymer DPP-TPTa	76
Figure 2.15. Out-of-plane X-ray diffraction of BDPP-TBT (black) and DPP-TBT (red)	78
Figure 2.16. Device architecture	79
Figure 3.1. Energy level of DPP, PPO and DAP	106
Figure 3.2. Photodetectors properties of P4 (a) EQE (b) Detectivity	107
Figure 3.3. Possible Pd complex with PDTPP	111
Figure 3.4. IR spectra of DAP polymers in KBr pellet	113
Figure 3.5. IR spectra of (a) PDPP and PDTPP monomers on NaCl (b) DTPP polymers KBr pellet	114
Figure 3.6. IR spectra of DTPP photodegradation	115
Figure 3.7. ¹ H NMR (a) and ¹³ C spectra (b) of PDPP and PDTPP in CDCl ₃	117
Figure 3.8. ¹ H NMR of (a) DPP- and DTPP-DTPa (b) DPP- and DTPP-BT in CDCl ₃	118
Figure 3.9. ¹ H NMR of PTDPP before and after decomposition (b) ¹³ C NMR of PTDPP before and after decomposition in CDCl ₃	119
Figure 3.10. Absorption spectra of DAP polymers (a) in solution CHCl ₃ (b) spin-coated on glass film	120
Figure 3.11. (a) Absorption of DAP polymers in CHCl ₃ with CSA (b) Film absorption of DAPb-DTPa at room temperature and submerged in 0.1 M CSA in MeOH	121
Figure 3.12. Optical properties of converted PDPP to PDTPP (10 ⁻⁵ M in CHCl ₃)	122

Figure 3.13. Optical properties of converted DPP to DTPP polymers in TCB..	123
Figure 3.14. Photodegradation of PDTPP (10^{-5} M) (a) in CHCl_3 (b) THF (c) Plot of $\ln(A_t/A_0)$ vs. time for determination of rate constants k (d) Photographic images of the solution vs. time	125
Figure 3.15. Photodegradation of DTPP-DTPa (10^{-5} M) (a) in THF (b) Plot of $\ln(A_t/A_0)$ vs. time for determination of rate constants k (c) Photostability of DTPP-BT (10^{-5} M)	127
Figure 3.16. (a) TGA and (b) DSC of DAP polymers	128
Figure 3.17. TGA of DTPP polymers	129
Figure 3.18. Cyclic voltammetry of DAP polymers on ITO in 0.1 M Bu_4NPF_6 in acetonitrile at scan rate of 100 mV/s	130
Figure 3.19. Cyclic voltammetry of (a) DPP/DTPP-DTPa (b) DPP/DTPP-BT on ITO in 0.1 M Bu_4NPF_6 in acetonitrile at scan rate of 100 mV/s	131
Figure 3.20. Photodetector properties of DAP polymers (a) EQE at -2 V bias (b) responsivity at -2 V bias (c) detectivity at -0.1 V bias	133
Figure 3.21. Difference between tandem cells and ternary blend	134
Figure 3.22. Mechanism of ternary blend (a) cascade charge transfer (b) parallel-like charge transfer	135
Figure 3.23. Photodetector properties of ternary blend Device A: BDPP-TPTB:DAPb-TPT and Device B: BDPP-TPT:DAPb-TPT (a) current-density voltage (J-V) characteristics (b) EQE at -2 V bias (c) responsivity at -2 V bias (d) detectivity at -0.1 V bias	137
Figure 3.24. Multilayer device configuration	137
Figure 3.25. Photodetector properties of multilayer devices (a) Spectral responsivity of devices a-f under -2 V bias (b) Specific detectivity of devices a-f under voltage of - 0.1 V. (c) Responsivity (bar) at 750 nm for devices a-c, e, f and at 900 nm for device d . Dark current density (squared line) under -0.1 V bias	139
Figure 3.26. Photodetector response for Device C and D (a) Detectivity/responsivity at -0.1 V bias for device C. (b) Detectivity/responsivity at -0.1 V bias for device D. (c) External quantum	

efficiency profile for device C and D at -2 V	141
Figure 3.27. Photodetector performance of DTPP polymers (a) J-V curve of DTPP-DTPa (b) EQE of DTPP-DTPa (c) J-V curve of DTPP-BT (d) EQE of DTPP-BT	142
Figure 4.1. Device architecture of (a) conventional (b) inverted	158
Figure 4.2. Bathocuproine (BCP) and Polyethylenimine (PEI)	159
Figure 4.3. Structure of (a) isoindigo (b) indigo (c) indole	161
Figure 4.4. Proposed catalytic pathway for 3,3'-biindole	163
Figure 4.5. Cross-linked polymer iI-Cbz-1 submerged in CHCl ₃ (a) drop-cast (b) spin-cast film	164
Figure 4.6. IR spectra of polymers iI-Cbz-1 , iI-Cbz-2 and iI-Cbz-3 (a) before crosslinking on NaCl plate (b) after crosslinking by ATR-IR	165
Figure 4.7. ¹ H NMR spectra of polymer PCbz , PiI , iI-Cbz-1 , iI-Cbz-2 and iI-Cbz-3 in CDCl ₃	166
Figure 4.8. Thermal properties of polymers (a) TGA (b) DSC	167
Figure 4.9. Absorption spectra of polymers (a) in CHCl ₃ (b) as film (c) as film after cross-linking	169
Figure 4.10. CV of polymers (a) PCbz and PiI (b) iI-Cbz-1 , iI-Cbz-2 and iI-Cbz-3 (c) crosslinked PiI , iI-Cbz-1 , iI-Cbz-2 , iI-Cbz-3	172
Figure 4.11. Energy levels of cross-linked polymers	172
Figure 5.1. Structure of PEDOT and spectroelectrochemical properties	187
Figure 5.2. Structures of P1-P5	189
Figure 5.3. IR spectra of polymers (a) BI-BTP and BI-DPTQ (b) BIH-BTP and BIH-DPTQ in KBr pellet	193
Figure 5.4. Thermal stability of BI-BTP and BI-DPTQ (a) TGA (b) DSC... ..	194
Figure 5.5. (a) Normalized absorption (b) fluorescence emission spectra of five polymers P1-P5 in chlorobenzene (c) normalized absorption (d) fluorescence emission on film of P1-P5 (e) leaf-color of P3	196
Figure 5.6. Normalized UV of BI(H)-BTP and BI(H)-DPTQ (a) in TCB (b) thin glass film	197

Figure 5.7. The neutral, radical cation and dication states during redox process of polymer P3	199
Figure 5.8. Normalized square-wave voltammetry of BI(H)-BTP and BI(H)-DPTQ	200
Figure 5.9. UV/Vis/NIR absorption spectra of polymer P1 and P3-P5 thin films on ITO-coated glass substrate (in CH ₃ CN with 0.1 M Et ₄ NClO ₄ as the supporting electrolyte) at neutral (dashed) and oxidized (solid)	201
Figure 5.10. p-Doping (a) absorption a P3 film on ITO-coated glass slide from 0 V to 1 V (b) reflectance of a P3 film on ITO-coated glass slide in front of reference mirror from 0 V to 1 V	202
Figure 5.11. Changes in optical transmission of film of P3 at (a) 1310 nm (b) 1550 nm over time with stepping potentials between +1.0 V and 0 V	204
Figure 6.1. BDPP-based polymers	214
Figure 6.2. DAP polymers	215

List of Schemes

Scheme 2.1. Synthesis of BDPP	55
Scheme 2.2. Mechanisms of reactions involved in the synthesis of BDPP	56
Scheme 2.3. Synthesis of donor monomers BT , TBT , TBTT , TPTa , TPTB , BI , DTPa-b	58
Scheme 2.4. Synthesis of soluble BDPP-based polymers and conversion to insoluble DPP-based polymers	59
Scheme 2.5. General catalytic cycle of palladium-catalyzed cross-coupling ...	60
Scheme 3.1. Synthesis of DAPa and DAPb	108
Scheme 3.2. Mechanism of Lawesson's reagent reaction with DPP	109
Scheme 3.3. Synthesis of DAP polymers	110
Scheme 3.4. DTPP polymerization	111
Scheme 3.5. Synthesis of DTPP polymers	112
Scheme 4.1. Syntheses of polymers PiI , PCbz , ii-Cbz-1 , ii-Cbz-2 and ii- Cbz-3	162
Scheme 5.1. Synthetic routes to polymers P1-P5 . Reagents and conditions: (i) Bu ₄ NBr ₃ , CH ₂ Cl ₂ , 25 °C, 3h (ii) Pd(PPh ₃) ₄ , K ₂ CO ₃ (aq, 2 M), toluene, Aliquat 336, 95 °C, 24h (iii) 1,4-dioxane-2,3-diol, AcOH, 60 °C, overnight (iv) 1,4- dioxane-2,3-diol, AcOH, 60 °C, overnight (v) PhNSO, TMSCl, pyridine, 80 °C, overnight (vi) SeO ₂ , THF, reflux, 4h	189
Scheme 5.2. Synthesis of polymers BI-BTP and BI-DPTQ	192

List of Tables

Table 1.1. Resonance Energy (RE) and Resonance Energy per Electron (REPE)	6
Table 2.1. Yields, molecular weights and PDI of BDPP polymers	61
Table 2.2. Solubility in chloroform (mg/mL) of BDPP- and DPP-based polymers at ambient temperature	64
Table 2.3. Thermal stability of BDPP-based polymers	65
Table 2.4. Absorption of BDPP and DPP polymers	67
Table 2.5. Electrochemical properties of BDPP and DPP polymers	70
Table 2.6. Hole motilities of BDPP-TPT	76
Table 2.7. Average and best hole mobility of BDPP-TPT	76
Table 2.8. Summary of EQE and Dark current for the devices A-D	80
Table 3.1. Molecular weights and PDI of polymers	110
Table 3.2. UV-vis absorptions of polymers	120
Table 3.3. Optical summary of converted PDPP and DPP-based polymers in TCB	124
Table 3.4. Electrochemical properties and band gaps of polymers	130
Table 3.5. Performance of OPDs based on single-layer DAP polymers	133
Table 3.6. Photodetector properties of multilayer devices	138
Table 4.1. The ratio of Cbz and il in polymers il-Cbz-1 , il-Cbz-2 and il-Cbz-3	167
Table 4.2. Thermal properties of polymers	168
Table 4.3. Electrochemical properties and band gaps of polymers	171
Table 5.1. Characterizations of Polymers P1-P5	195
Table 5.2. Absorption characteristic of BI(H)-BTP and BI(H)-DPTQ	198
Table 5.3. Summary of OTFT measurements	205

List of Symbols and Abbreviations

AFM	Atomic force microscopy
BDPP	di- <i>tert</i> -butyl 3,6-bis(5-bromothiophen-2-yl)-1,4-dioxopyrrolo[3,4- <i>c</i>]pyrrole-2,5(1 <i>H</i> ,4 <i>H</i>)-dicarboxylate
BHJ	Bulk heterojunction
BI	Biindole
BOC	<i>Tert</i> -butyloxycarbonyl
BTD	Benzothiadiazole
BBTD	Benzo[1,2- <i>c</i> :4,5- <i>c'</i>]bis([1,2,5]thiadiazole
BTP	Dibenzo[<i>a,c</i>][1,2,5]thiadiazolo[3,4- <i>i</i>]phenazine
CHCl ₃	Chloroform
CV	Cyclic voltammograms
D*	Detectivity
D-A	Donor-Acceptor
DAP	3,6-Di(thiophen-2-yl)pyrrolo[3,4- <i>c</i>]pyrrole-1,4-dithiol
DPP	3,6-Di(thiophen-2-yl)-2,5-dihydropyrrolo[3,4- <i>c</i>]pyrrole-1,4-dione
DSC	Differential scanning calorimetry
DTPP	3,6-Di(thiophen-2-yl)-2,5-dihydropyrrolo[3,4- <i>c</i>]pyrrole-1,4-dithione
DMF	<i>N,N</i> -dimethylformamide
DMSO	Dimethyl sulfoxide
DPTQ	6,7-Diphenyl-[1,2,5]thiadiazolo[3,4- <i>g</i>]quinoxaline
EQE	External quantum efficiency
ETL	Electron transfer layer
GPC	Gel permeation chromatography
HOMO	Highest occupied molecular orbital
HTL	Hole transfer layer
ICT	Intramolecular charge transfer
ITO	Indium tin oxide
LUMO	Lowest unoccupied molecular orbital

LR	Lawesson's reagent
NIR	Near-Infrared
OFET	Organic field effect transistor
OPD	Organic photodetector
OPV	Organic photovoltaic
OSC	Organic solar cells
OTFT	Organic thin film transistors
P3HT	Poly(3-hexylthiophenes)
[60]PCBM	[6,6]-Phenyl-C ₆₁ -butyric acid methyl ester
[70]PCBM	[6,6]-Phenyl-C ₇₁ -butyric acid methyl ester
PCE	Power conversion efficiency
PEDOT	Poly(3,4-ethylenedioxythiophene)
PL	Photoluminescence
PSS	Poly(styrenesulfonate)
R	Responsivity
TGA	Thermogravimetric analysis
TCB	Trichlorobenzene
THF	Tetrahydrofuran
E_g	Band gap
E_{ox}	Onset oxidation potential
E_{red}	Onset reduction potential
τ_{exc}	Exponential life time of an exciton
λ_{max}	Maximum absorption wavelength
T_d	Decomposition Temperature
T_g	Glass Transition Temperature
XRD	X-ray diffraction

Chapter 1 Introduction in Visible-Near Infrared Organic Materials

Optoelectronics is the study and application of electronic devices which serves to detect or control light in the UV-visible and infrared. It is based on quantum mechanical effects of light on semiconducting material and are essential components for commercial and military electronics such as photodiodes, phototransistors, photoresistors and photodetectors. The use of inorganic materials with such applications have a long history. As the field of microelectronics progresses, the demand for new affordable and fast processing materials increases. Substantial focus has gone into organic semiconducting material as a substitute to the more expensive and toxic inorganic conducting/semiconducting elements. In contrast, organic materials are lighter, cost less to manufacture, requires minimal material and solution processable on flexible substrate. However, due to fundamental difference in the photoelectric process, the efficiencies of organic semiconductors are generally lower to their inorganic counterpart. Therefore, a great deal of research has gone into improving their development.

1.1 Conjugated polymers

With their initial discovery in early 1970s, there have been increasing interest in π -conjugated polymers for use in photovoltaic applications. In 2000, Alan Heeger, Alan MacDiarmid and Hideki Shirakawa were rewarded the Nobel Prize in Chemistry for their work with conjugated polymer. They are carbon-based macromolecule which are connected by alternating double and single bond. Due to the alternating double bond, which can resonate through the backbone, conjugated polymers can exhibit electrically

semiconducting properties and behave like inorganic semiconductors. Polymer semiconductor requires two essential features. Firstly, an extended orbital overlapping along the polymer backbone should result in delocalization of the π -electrons, thus enabling proper charge transport. Secondly, the energy levels, namely the lowest unoccupied molecular orbital (LUMO) and the highest occupied molecular orbital (HOMO), of the polymer should be adequate to allow for the formation of the relatively small band gap, thus enabling proper electronic state. The typical band gaps of semiconducting polymers are in 1.0 – 3.0 eV, whereas the insulating polymers have the large band gaps over 3.0 eV [1, 2]. The unique electronic and optical properties of conjugated polymers, concurrent with their inexpensive solution-based processing are ideal for their use in the electronics industry. To date, conjugated polymers have found many commercial and potential applications, such as light-emitting devices, nonlinear optical devices, photovoltaic devices, field-effect transistors, electro-magnetic shielding, biosensors, battery [3-8].

The key factor that governs the productivity of conjugated polymers is the band gap. The energy separation between π -bonding and π^* -antibonding is relatively small and the lateral bond contributes to limited orbital overlap. This leads to bandgap between 1 to 3 eV, which is ideal to cover the optimal spectral domain. Common conjugated polymers, such as poly(*p*-phenylene), have relatively high band gap, roughly around 3 eV [9]. In some cases, high band gap materials are not ideal and particular band gap is required for certain application. For example, polymer solar cell devices require materials to have band gap between 1.1- 1.5 eV to absorb the most solar irradiation to maximize efficiency [10].

1.2 Band-gap tuning

The optical and electronic properties of a conjugated compound or polymer is governed by their energy gap, which is the energy separation between the HOMO and LUMO. The band gap between the valence and conduction band corresponds to the energy gap between the HOMO-LUMO level, which is relevant for optical absorption, photoluminescence, and other photophysical properties [11-13]. Therefore, it is key to engineer the band-gap to fit the profile of the application and modifying the band gap involves at the molecular level. The band gap of polyaromatic π -conjugated systems is determined by five factors: bond length alteration ($E^{\delta r}$), the mean deviation from planarity (E^{θ}), aromatic resonance energy (E^{Res}), the inductive or mesomeric electronic effects of eventual substitution (E^{sub}) and the intermolecular or interchain coupling in the solid state (E^{int}) [14]. The sum of these factors equates to the band gap (E_g)

$$E_g = E^{\delta r} + E^{\theta} + E^{Res} + E^{sub} + E^{int}$$

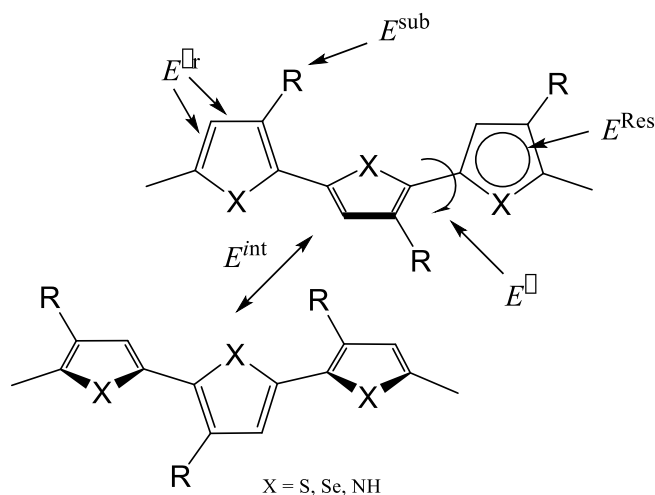


Figure 1.1: Factors affecting the band gap of polymer

Other factors that contribute to the band gap are the effect of conjugation length and donor-acceptor charge transfer.

1.2.1 Bond length alteration

In a π -conjugated system, the effect of bond length alternation originates from Peierls gap, which predicts that the smaller the bond length alteration the lower the energy gap of the conjugated system [15]. Bond length alternation is the difference between single and double bond characteristic in the backbone of a conjugated system. One example of the Peierls prediction is polyacetylene, in which the polymer would have metallic characteristics if the distance between all the carbon atoms were theoretically identical. Thus, minimizing the bond length alteration, which in turn would reduce the band gap of the conjugated system [16,17]. In a conjugated system, two forms exist, the aromatic form and the quinoid form (Fig 1.2). In such a system, like polypyrrole and polythiophene, a non-degenerate ground state corresponds to a single geometric structure which is the aromatic state. In a quinoid-like system the ionization potential is much lower and also contains a larger electron affinity than that of aromatic state. Therefore, an increase of quinoid character would effectively reduce the band gap; furthermore, quinoid structure increase double-bond characteristics between carbon atoms in the repeating unit, leading to reduction of bond length alternation [18,19].

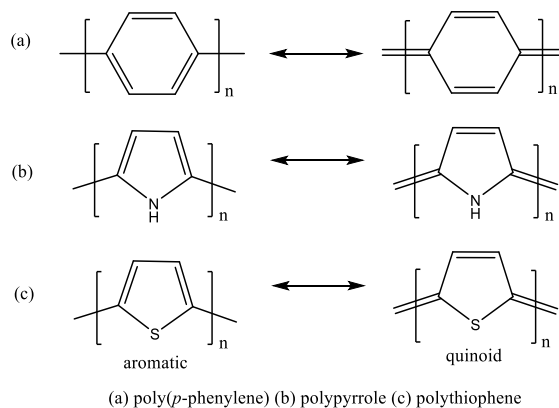


Figure 1.2: Conjugated polymers in the aromatic (ground-state) and quinoid forms

1.2.2 Mean deviation from planarity

The second factor is the deviation from planarity (E^{θ}). In most conjugated polymers, a nondegenerate state exists and the repeating unit is connected by a single bond. This allows for free interannular rotation. Regioregularity can affect the torsion angle of the system and thus affect the orbital overlap and in turn affecting the band gap (Fig. 1.3) [20, 21]. One prime example of nonplanarity that has been studied extensively is poly(3-hexylthiophene) (**P3HT**). Studies demonstrated that in a head-to-head arrangement, the absorption and emission occurs at a lower wavelength (higher energy); furthermore, there is an increase of the Stokes shift. This is attributed to the conformational strain in the first excited state [22, 23].

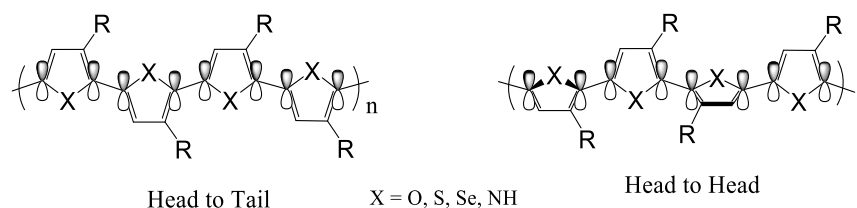


Figure 1.3: Regioregularity of polychalcogens

1.2.3 Aromatic resonance energy

Another factor that contributes to the band gap is aromatic resonance energy (E^{Res}). The resonance energy is the measure of extra stability of a conjugated system with respect to isolated double bonds. Circulation of π -electrons in the confined cyclic structure and along the conjugated backbone gives rise to aromaticity. This was first introduced by August Kekule, where he postulated that electrons are free to cycle around the benzene structure alternating single- and double-bonded to one another [24-26]. To provide a more reliable source prediction in aromaticity, Hess and coworkers

calculated resonance energy per electron (REPE) of different types of aromatic compounds and their corresponding polymers, and what was found is that the more positive REPE is, the more aromatic it is (Table 1.1). To compare REPE with the bandgap, decreasing bandgap correlates to a decreasing REPE, which means the less aromatic the polymer is [27, 28].

Table 1.1: Resonance Energy (RE) and Resonance Energy per Electron (REPE)

Compound	Re (β)	REPE (β)	Eg (eV)
Benzene	0.390	0.065	3.4
Pyrrrole	0.233	0.039	3.1
Thiophene	0.193	0.032	2.1
Furan	0.044	0.007	2.3
Isothianaphthene	0.247	0.025	1.1

1.2.4 Effects of substitution

Adding substituents, E^{sub} , not only influences the band gap but also electronic parameters such as ionization potential and electron affinity [29]. Electronic effects originate from the inductive and mesomeric effects. Introducing electron donating or electron withdrawing group can influence the HOMO or LUMO level of the chromophore, which in turn will affect the band gap of the polymer. Adding substituents is a good tool to synthesize polymers with tunable band gaps [30]. Moreover, changing from alkyl side chain to alkoxy group have shown to decrease in the HOMO energy level. In addition to band gap tuning, alkyl substitution can influence processability and physical properties such as phase behavior, structural order and

charge transport [31, 32]. Branched alkyl chains are more effective for inducing solubility compared to their linear chain counterpart. However, a balance needs to be taken since bulky side chain can affect π - π interaction by lengthening π - π stacking distance, and thus reducing charge carrier mobility [32, 33].

1.2.5 Interchain coupling in the solid state

Another important factor is interchain coupling (E^{int}) or interchain interaction. Molecular packing affects π - π interaction or intermolecular charge transfer and plays an important role not only in the band gap tuning but also in charge motility [34]. Generally, polymers in solution have blue shift in absorption relative to the solid state. This is due to π -stacked aggregation and interchain interaction in the solid state, which can contribute to a decrease in the band gap [35]. Thus, regioregular polymers have a higher packing order than random analogs. The bulky groups in polymers can hinder solid-state packing and intermolecular interaction and thus increase the band gap [36].

1.2.6 Effect of conjugation length

Extension of conjugation length can lead to a decrease in the HOMO-LUMO gap. By covalently linking or fusing a π -conjugated monomer either in a linear fashion or by two-dimensionally, the conjugation length can be increased (Fig. 1.4).

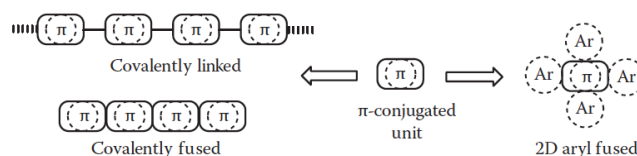


Figure 1.4: Transformation of small π -conjugated unit to linear or 2D enlargement

Calculations show that energy levels can differ with different repeating unit of thiophene for oligothiophenes, with every extra thiophene, there's a gradual decrease in band gap [37]. In comparison to covalently linking, covalent fusion of π -conjugated units can further lower the band gap and absorb in the near-infrared region. One prime example of fused aryl is the large Zn(II)-porphyrin tape reported by Osuka et al. They have successfully synthesized meso-meso-linked porphyrin arrays which were fused by using a facile synthetic method. Fused porphyrins displayed a drastic redshift in absorption, showing three distinct bands showing panchromatic characteristics. Band III correlates to number of fused porphyrins, with the increasing of repeating unit band III progressively deepens into the infrared (Fig. 1.5) [38-40].

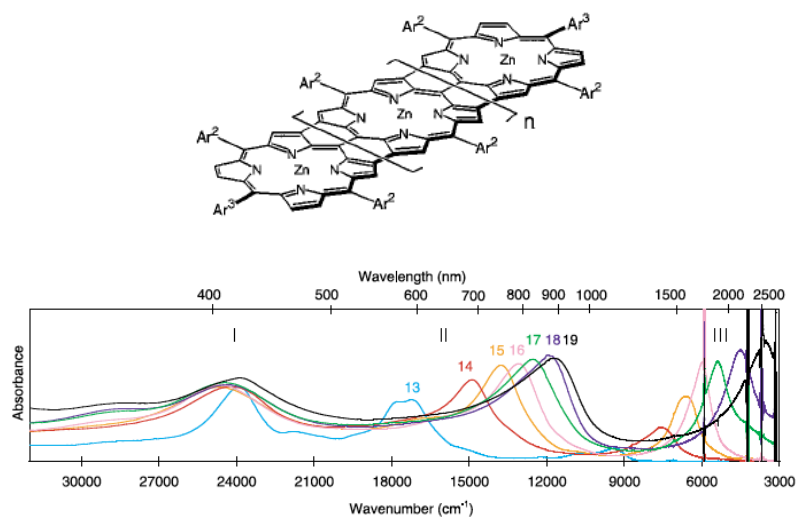


Figure 1.5: Absorption of fused porphyrins (Adapted with permission from Ref. 38)

1.2.7 Effect of donor-acceptor charge transfer

One of the most useful strategy in lowering band gap is introducing electron donor (D) coupled with electron acceptor (A) [41]. D-A compounds can exhibit two forms of resonance, one with increased double-bond characteristics ($D-A \leftrightarrow D^+=A^-$),

reducing bond length alteration, similarly, decreasing the Peierls gap. Secondly, hybridization of the energy levels of the donor and acceptor can raise the HOMO level than that of the donor material and lower the LUMO level than that of the acceptor molecule. This leads to smaller HOMO-LUMO separation (Fig. 1.6) [42, 43].

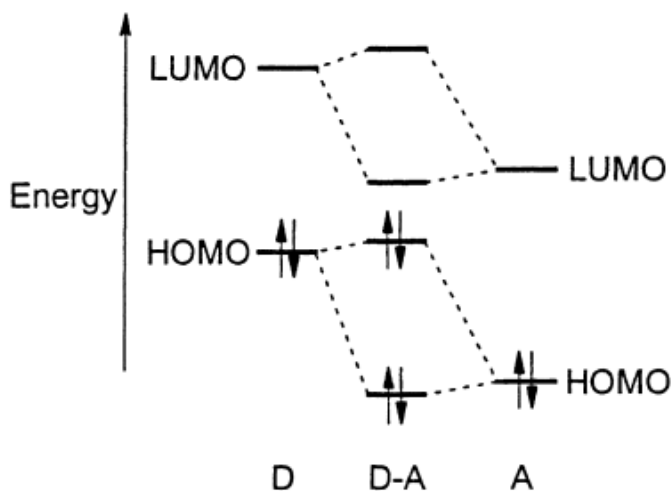


Figure 1.6: Hybridization of the energy levels of a donor (D) and acceptor (A)

1.3 Low band gap polymers

1.3.1 Polythiophenes and derivatives

Polythiophene is one of the most important representative class of conjugated polymers that have been extensively studied for use in nonlinear optical device, polymer LEDs, electrochromics, sensors, solar cells, nano-switches and many more [44, 45]. The band gap of polythiophene is 2 eV; furthermore, introducing alkyl chain in the 3-position lowers π - π^* transition, giving poly(3-hexylthiophene) (P3HT) with a band gap of 1.9 eV [37, 46]. Also, it was found that increasing molecular weight causes a red shift of the λ_{\max} and thus chain length plays an important role in the solid state packing [47]. Since there is a limited contribution from the quinoid state due to a large torsion

angle in P3HT, various polythiophene analogues have been synthesized for particular studies and applications.

Polyisothianaphthene (PITN) contains the repeating unit of a thiophene fused with benzene ring at the 3 and 4 position (Fig 1.7). The quinoid form of PITN has a quite different HOMO-LUMO level than that of the aromatic form. The band gap of PITN was determined to be 1 eV, which is much lower than P3HT, due to the many resonance forms including the quinoid structure. PITN in its doped form is highly transparent and conducting, reaching up to $50 \Omega^{-1}\text{cm}^{-1}$ [48].

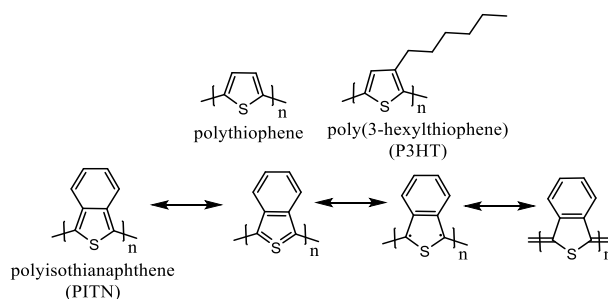


Figure 1.7: Structure of polythiophene derivatives and resonance structures

Since the discovery of PITN, many papers have been reported on different synthesis and structural variation such as dialkoxyisothianaphthene (**1**) and fused thienothiophenes (**5**) (Fig. 1.8) [49-53]. Pomerantz and Gu have synthesized a new low band polymer (**4**) prepared by oxidization polymerization, giving a band gap of 1.2 eV [52]. Their study has off sprung different derivatives of (**4**) widely used in organic solar cells [54].

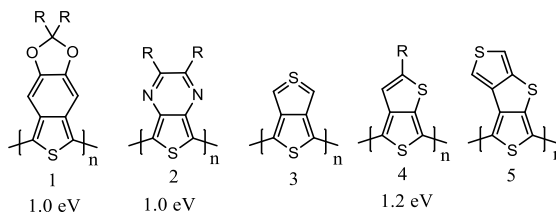


Figure 1.8: PITN derivatives

1.3.2 Ladder molecules

Ladder or ribbon polymer development is a unique approach by reducing bond-length alternation and increasing π -conjugation length. Ladder polymer consist of cyclic subunit that are connected to each other by two links. One of the earliest ladder polymer synthesized was the poly(benzimidazobenzophenanthroline) (BBL) by Air Force Wright Aeronautical Laboratories in 1970s [55]. Since its initial fruition, a great of deal of research have gone to improve processability of BBL material due to good photoconductivity, large optical nonlinearity and high electron affinity. Recently, Wang et al., have designed a facile method on synthesizing BBL-like derivative which show good solubility in common organic solvents [56-59]. Another well-known example of ladder polymer is polyacene that is considered to contain the fused *trans*-polyacetylene chains (Fig. 1.9). Calculation shows that polyacene would show metallic conductor properties and could theoretically reach zero band gap [60]. However, due to difficulty of the synthesis, no well-developed methods have been postulated. Higher acene are very reactive and only been isolated in a matrix [61]. Pentacene is a popular choice for research in organic thin-film transistor (OFETs) and has high hole mobility up to $5.5 \text{ cm}^2\text{V}^{-1}\text{s}^{-1}$, exceeding that of amorphous silicon [62].

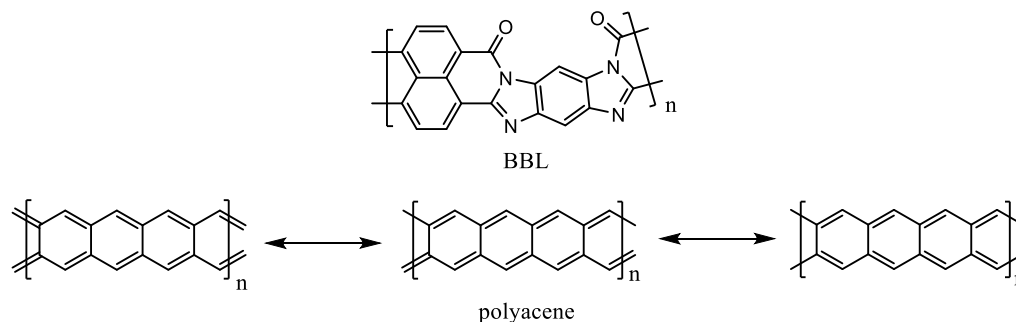


Figure 1.9: Ladder polymers

Rylenes are another example of extended ladder systems (Fig 1.10). Rylene diimides are robust, versatile class of polycyclic that exhibit excellent thermal and oxidative stability, along with high electron affinity and electron mobility. They are good candidates for variety of electronic applications such as laser dyes and photovoltaic materials [63, 64]. Mullen et al. have synthesized up to six fused naphthalene units (**6**) with absorption maximum reaching 953 nm [65]. Furthermore, incorporating donor-acceptor charge transfer, the absorption compound **7** reaches over 1000 nm [66].

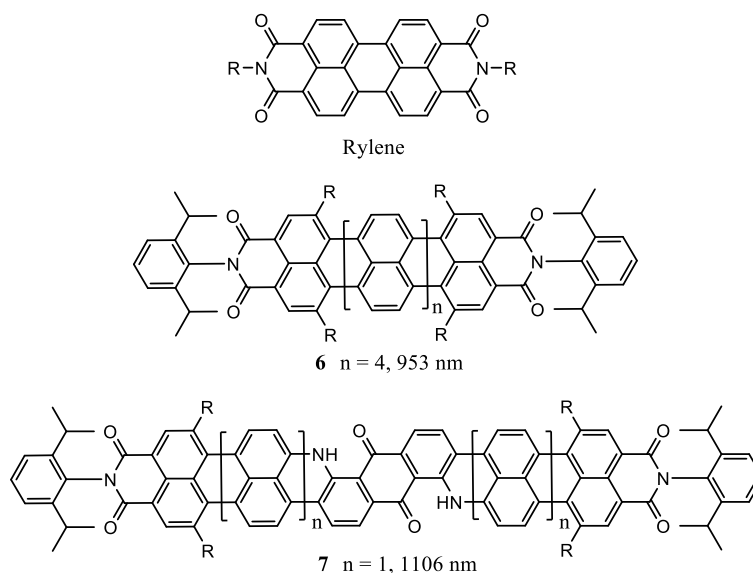


Figure 1.10: Rylene systems

1.3.3 Donor-acceptor systems

The concept of donor-acceptor small molecules and polymers was first introduced by Havinga et al. in 1992. Using condensation polymerization, various donor molecules were coupled with acceptor units' squaric acid and croconic acid (Fig. 1.11). These polymers show a variety of band gaps, ranging from 1.2 to 0.45 eV for

polymer **10** [41, 67].

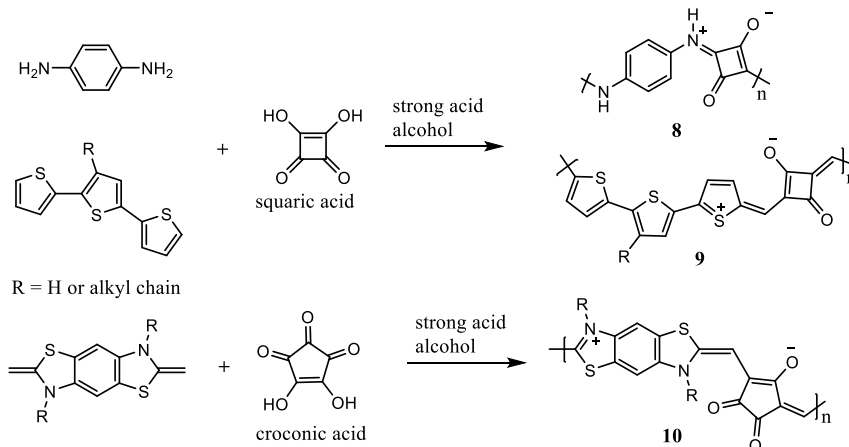
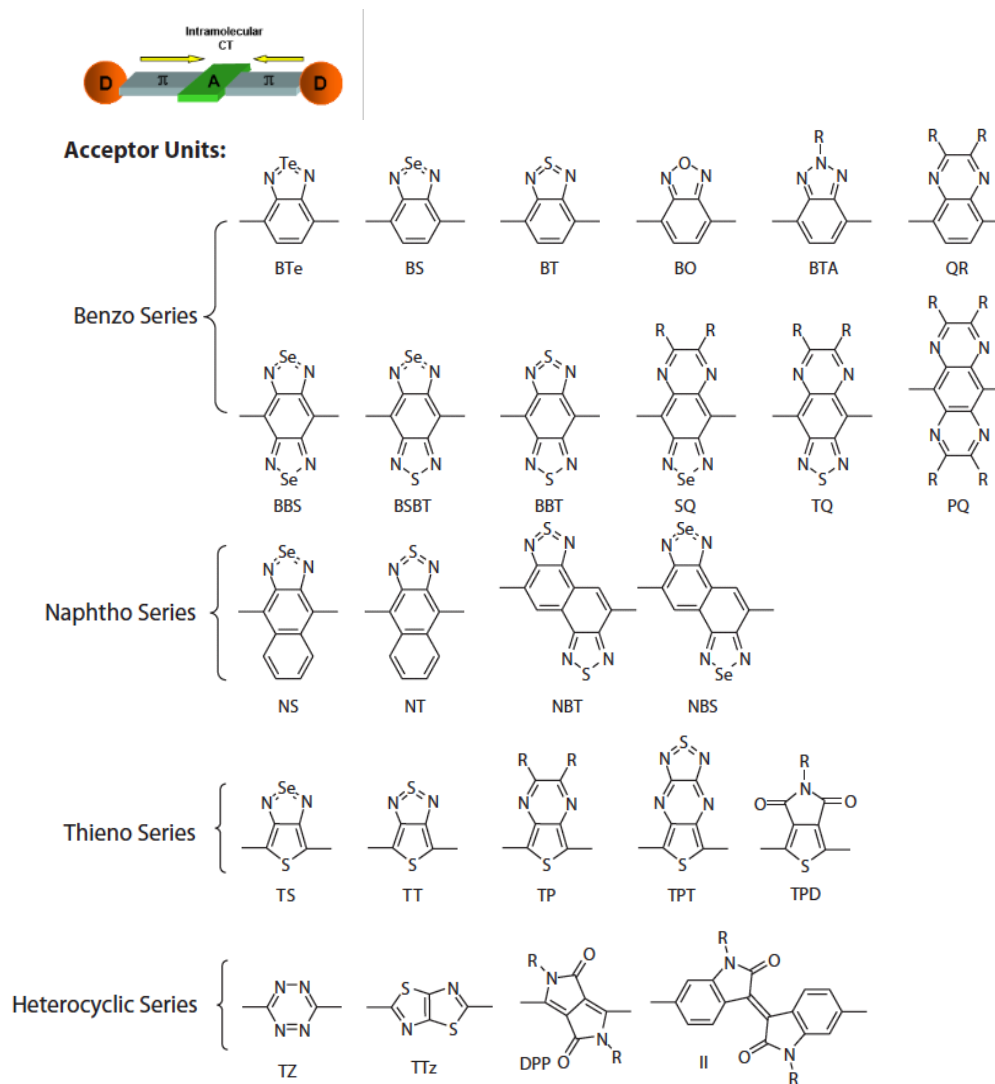


Figure 1.11: Preparation of polysquaraines

Since its first introduction, using D-A system has been the main tool for band gap engineering. It is a critical challenge in developing polymers with good film-forming properties along with good electronic properties. Combination of different donors and acceptors can lead to polymers that can concurrently exhibit low ionization potential and high electron affinities, which in turn can lead to facile mobility of both hole and electron charges. Reduction of E_g can be done by using the alternating donor and acceptors in the repeating unit. Using different strength of D/A units, the polymers can be tuned to absorb at different spectral wavelengths. Furthermore, having the proper D-A units can achieve cancellation of bond length alteration, efficient push-pull interaction between the D-A molecule and planarization of the polymer backbone. To ensure effective conjugation length and efficient intermolecular charge transfer between the D and A molecules, introducing a π -spacer to form the D- π -A- π -D segment is essential (Fig. 1.12). Proper selection of suitable donors, acceptors and spacers have been subjected to intensive studies, especially for research on organic solar cells [68, 69]. The acceptor molecules usually contain aryl or heterioaryl unit with one or more

electronegative atoms. The most common acceptor units are the benzo and heterocyclic series. The designs of the donor molecules are usually based on thiophene and benzene containing electron donating substituent, such as alkoxy or alkyl groups.



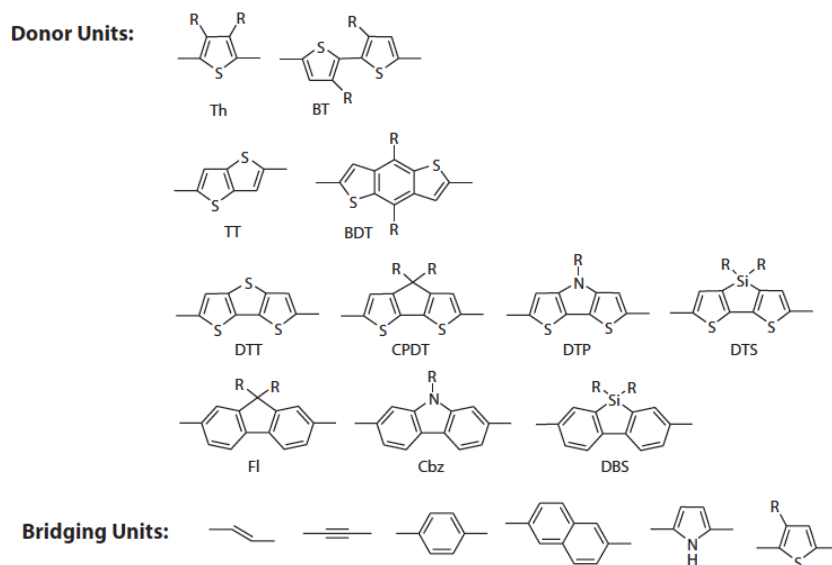


Figure 1.12: General structure of acceptors, donors and bridging unit used in D- π -A- π -D repeating segment

1.3.3.1 Effect of spacer units

The π -spacer unit is typically linked to the acceptor unit as part of the monomer. Most commonly used spacers are vinylene, ethylene, phenylene, naphthylene, thiophene and pyrrole (Fig. 1.12). The main goal of the spacer unit is to reduce the dihedral or torsion angle between the two donors and acceptor unit. From experimental observation, ethylene-linkage polymer has a larger torsional angle compared to vinylene-linkage, concurrently, showing a lower band gap. This suggests that there is stronger backbone planarity [70-72]. Thiophene spacer is the most commonly unit used in D-A polymers due to several advantages. Thiophene is flat, small size, good thermal, photochemical stability and has reactive sites for further functionalization, such as adding halogens, alkyl groups to impact the solubility of the polymer [73, 74]. Incorporating pyrrole spacer further affects the charge transfer from donor to acceptor

and lowers the band gap due to the hydrogen bonding between the N-H proton and the neighboring acceptor such as BT or BBT (Fig 1.13). Furthermore, it is suggested that intramolecular hydrogen bonding can contribute the changing the energy level of the quinoid form by sharing or removing electrons from the nitrogen atom on the acceptor unit [75, 76].

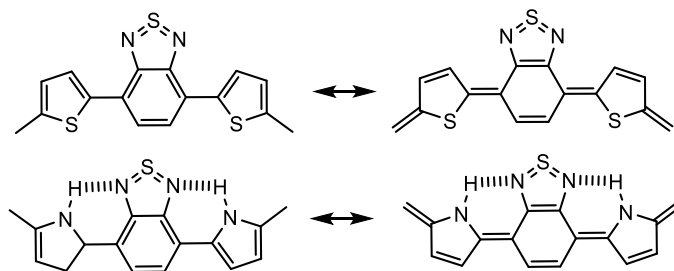


Figure 1.13: The $-\pi$ -A- π - moiety having thiophene and pyrrole spacer

1.3.3.2 Effect of electron acceptors

With the large number of acceptors available, it is important to determine which acceptor units will provide the desirable properties. The challenge is to determine the relationship between the structure and band gap property in D-A polymers. Study done by Seferos et al. showed that by changing the atom on the benzochalcogenodiazole unit from S to Se to Te, the band gap can be tuned (**11a-c**, Fig 1.14). It was found that substituting to heavier atom leads to redshift due to low ionization potential and increase of bond length, ultimately, lowering the aromaticity of the acceptor. The band gap of the polymers was found to be 1.59, 1.46 and 1.06 eV for the S-, Se- and Te- containing polymers, respectively [77]. Changing the acceptor unit to benzobisthiadiazole (BBT) coupled with thienothiophene afforded polymer **12** with the absorption onset around 2200 nm and the optical band gap of 0.56 eV [78]. Further studies indicate that only

certain types of acceptors can affect the band gaps of D-A polymers more than the donor does. Among all, the strong acceptors are BBS, BSBT, BBT, NBT, NBS, TS, TT and TPT (Fig 1.12).

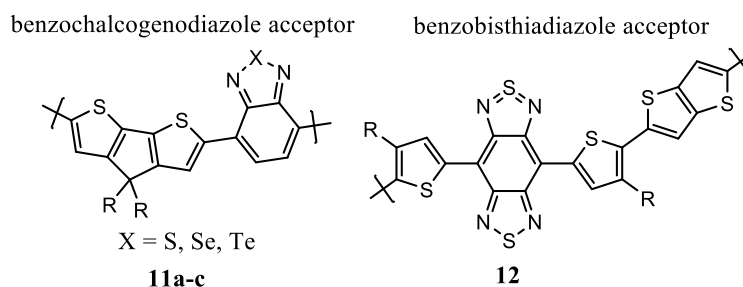


Figure 1.14: Strong acceptors of benzochalcogenodiazole and thienothiadiazole and corresponding D-A polymers

Furthermore, adding electron-withdrawing substituents would improve the strength of the acceptor unit and the most common and widely used are cyano-, nitro-group and fluorine atom. Using the Knoevenagel condensation and subsequent electrochemical polymerization, polymers **13-14** with band gap reaching as low as 0.6 eV were obtained [79, 80]. The film of polymer **15** has the λ_{max} of 768 nm and the optical band gap of 1.1 eV [81]. Introducing fluorine atom (**16**) has shown to reduce both HOMO and LUMO levels simultaneously while retaining the band gap, which is important for solar cell application [82-84].

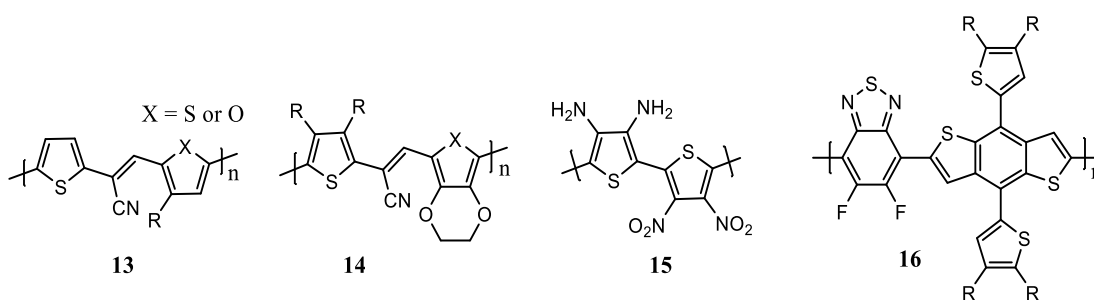


Figure 1.15: D-A polymers containing cyano, nitro and fluorinated BT acceptors

1.3.3.3 Effect of electron donors

The effect of donor molecule on the band gap mainly relates to the structural feature of the donor molecule. Donor molecules with fused ring structure and extended conjugation system show a high-lying HOMO level and favor narrow band gap for their corresponding D-A polymers. Among the listed donors in Fig. 1.12, thiophene based donors are more favorable, even though benzene based donor are more aromatic, because they cause less steric hindrance and enable better electron delocalization due to better orbital overlap. One prime example is polymers **17-19**, changing the donor from fluorene to carbazole to dithienopyrrole led to a gradual bathochromic shift (Fig. 1.16). The difference in band gap is due to orbital mixing between the donor and acceptor units through the adjacent thiophene spacer [85-87].

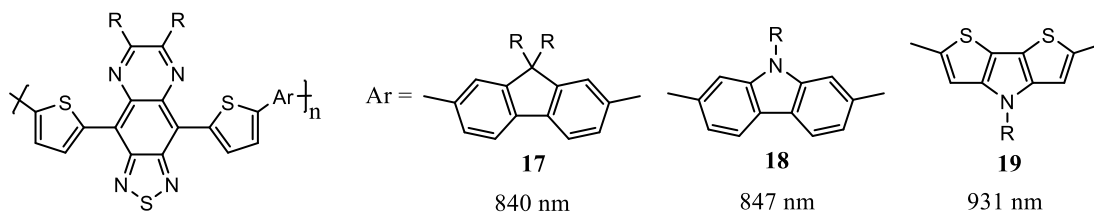


Figure 1.16: Electron donor effect on the band gap

1.4 Photovoltaics

Photovoltaic is the process of converting solar energy into direct current electricity by using semiconducting materials that exhibit photovoltaic effect. A photovoltaic effect is the process where electrons present in the valence band is excited to conduction band when sunlight hits the surface of the material. Organic photovoltaics (OPVs) have gained great deal of attention due to flexibility, cost-effective and easy tunability of organic materials [88]. OPVs, like their inorganic

counterpart, converts light into current, however the difference between them is the charge generation. However, due to the fundamental difference in the conduction mechanism, the efficiencies of organic semiconductors are generally lower compared to their inorganic counterpart. In OPV devices, there are two principle working modes. First is the photovoltaic mode, where under a zero bias, the flow of the photocurrent of the device is restricted and voltage builds up. This process exploits voltage buildup and electrical power is released, which is the basis for solar cells. The second mode, which is often under reverse bias (voltage at the cathode higher than at the anode), consumes power to detect a signal and the devices are conventionally called photodetectors [89]. In most cases, device architecture for both modes are the same, except the figure of merits are different. Solar cells depend on power conversion efficiency, solar intensity and large surface area, whereas, photodetectors require small surface area, low noise and low power consumption [90, 91].

1.4.1 Working principles of photovoltaic devices

1.4.1.1 Single layer junction

The simplest form of a photovoltaic device is the single layer junction. Usually these devices are the made by sandwiching a photoactive layer between two electrodes. The organic active layer, either small molecule or polymer, is placed on top of high work function material, such as indium tin oxide on glass. Then a low work function metal is used as the second electrode, such as aluminum, magnesium or calcium (Fig. 1.17). The difference in the work function in the electrodes sets an electric field in the organic layer and potential created allows the cell to create a circuit. The earliest single

layer device was made by Kearns and Calvin which was based on magnesium phthalocyanine (MgPc) using an Aluminum/MgPc/Silver cell, which gave a low power conversion efficiency (PCE), below 0.1% [92]. The inefficiency is due to the fact the electric field is not strong enough to separate the photogenerated charges and often recombine rather than reach the electrodes. No recorded single layer junction was demonstrated for use for photodetector devices.

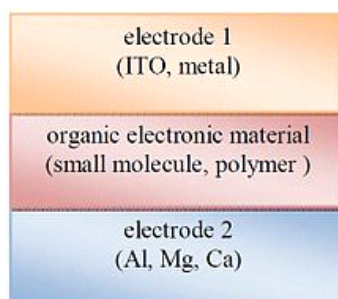


Figure 1.17: Single junction cell

1.4.1.2 Bilayer junction

The bilayer junction was first introduced by Tang in 1986 [93]. This cell uses two different layers between the electrodes. The layers would differ by electron affinity and ionization energy and electrostatic forces are generated in the interface of the layers, which is used to separate the charges (Fig. 1.18). The materials are chosen such that one layer has high electron affinity and ionization, thus acting as electron acceptor and the second layer is the electron donor. Tang used perylene derivatives as the acceptor layer and copper phthalocyanine (CuPc) as the donor and achieved PCE of 1% [93]. Concurrently with single layer junction, bilayer also has issue of charge separation. In organic materials, when photons are absorbed, Frenkel excitons are created, however the binding energy of such excitons are in the magnitude of 0.1-1 eV, therefore, the

diffusion length of the exciton is approximately 10 nm [88]. Thus, the thickness of the active layer should be at the same range as the diffusion length. Due to this restriction, bilayer junction has been outdated for use in solar cell. However, recently, Shafian et al. have demonstrated organic photodetector (OPDs) using a bilayer with sequential deposition of P3HT and fullerene showing a superior result compared to their bulk heterojunction counterpart, with detectivity 3.4 times higher and lower dark current [94].

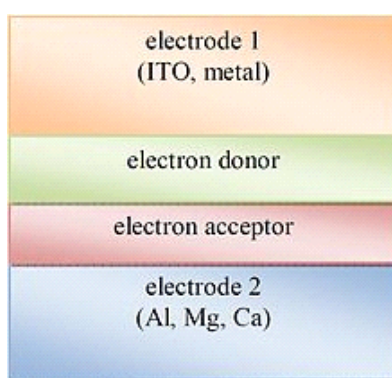


Figure 1.18: Bilayer junction

1.4.1.3 Bulk heterojunction and tandem heterojunction

To solve the thickness issue, the concept bulk heterojunction (BHJ) was first introduced by Yu et al [95]. In this junction donor- and acceptor- type materials are mixed together to make a polymer blend. Due to the larger interfacial area made by the donor-acceptor material, excitons are more likely to reach the interface and dissociate. BHJ layer has advantage over the bilayer because the thickness can be larger enough for efficient photon absorption and comply the diffusion length of excitations [96]. The polymer blend solution is usually spin-coated or casted on top of a conducting layer, most commonly used is poly(3,4-ethylenedioxythiophene):poly(styrenesulfonate)

(PEDOT:PSS), and the two components will self-assemble into interpenetrating network connecting the two electrode (Fig. 1.18) [97]. PEDOT:PSS forms an Ohmic contact with the photoactive layer for efficient charge collection and covers pinholes on the ITO/glass surface [88]. Using C_{60} and its derivative as the electron acceptor blended with polymer donor (MEH-PV) and ITO as the anode and Ca as the cathode a PCE of 2.9% was achieved [95]. Since its introduction, adopting bulk heterojunction has been the norm for developing new efficient OPVs. The first development of BHJ OPDs was demonstrated in 1993 by Sariciftci et al. using poly(phenylene-vinylene) and fullerene as the active layer and showed dark current below 100 pAcm^{-2} under reverse bias [98].

Due to the inherent design of BHJ, the thickness of the material cannot exceed more than 100 nm because exciton lifetime is in the order of nanoseconds, which will lead to charge recombination [88]. With the limitations of single junction devices, employing tandem devices have become the norm. Using tandem cells or multiple BHJ can simultaneously absorb lower and higher energy photons thus minimizing the thermalization losses, whereas in single BHJ the material is restricted to bandgap of the donor material. The conventional design works the same way that of single BHJ, however an intermediate layer is placed on top of the bottom cell. The intermediate layer, which consists of an electron and hole-transporting layer (ETL and HTL) helps recombine the charge carrier. On top of the intermediate layer the second active layer is applied along with the electrode (Fig. 1.19) [99]. Typically, one cell absorbs high band gap and the other cell absorbs the lower band gap, overall covering a larger spectral region. Adopting tandem cell have reached record PCE up to 11.5% [100].

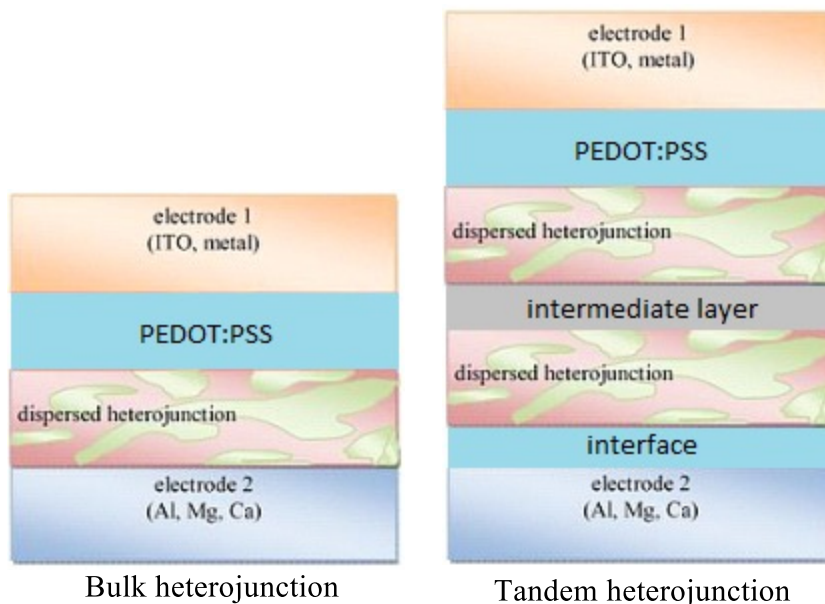


Figure 1.19: Bulk and tandem heterojunction

1.4.2 Organic Photoelectric Process

The sun is a stable source of renewable energy and approximately 5 million tons of energy is released every second. As that energy travels through space and to earth atmosphere it is re-emitted to lower energy to about 1000 Wm^{-2} which is abbreviated as air mass 1 (AM1) in ideal condition at the equator. However, in North America and Europe the absorption loss is higher resulting in AM 1.5 (Fig. 1.19b) [101]. As the irradiance hits an OPV device (both solar cell and photodetector) there are four important processes involved in the mechanism (1) light absorption and exciton formation (2) exciton migration (3) exciton dissociation (4) charge migration and charge collection (Fig 1.20a).

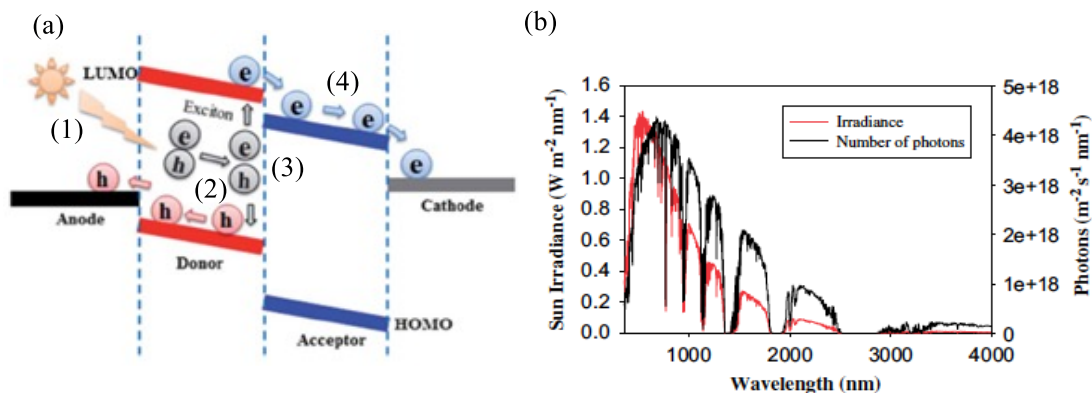
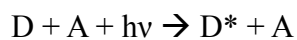


Figure 1.20: (a) Photoelectric process (1) light absorption and exciton formation (2) exciton migration (3) exciton dissociation (4) charge migration and charge collection (b) Sun irradiance (red) and number of photons (black) as a function of wavelength

1.4.2.1 Light absorption and exciton formation

When a photon hits the donor material matching the frequency, it is excited from the ground state $D(S_0)$ to exciton state $D^*(S_1)$. Since the binding energy of the exciton is fairly large, proper energetic photon is required.



For efficient collection of photons, the absorption of the active layer should match the solar emission spectrum. According to Shockley-Queisser limit, the optimal band gap for single light absorbing medium with the maximum efficiency is approximately around 1.1 eV. Lowering the band gap of the organic material it is possible to harvest more sunlight and increase the photocurrent.

1.4.2.2 Exciton migration

Once the exciton is formed it needs to migrate to the donor-acceptor interface and form free charge carrier. However, with the limited diffusion length and lifetime,

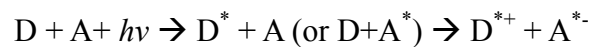
the exciton migration is in competition with other decay process, such as luminescence or radiative recombination to ground state. The lifetime of the exciton (τ_{exe}) can be measured by following equation

$$\tau_{exe} = \frac{(L_{exe})^2}{D_{exe}}$$

Where L_{exe} is the distance of the exciton is able to cross and D_{exe} is the diffusion coefficient of the excitons. Since the lifetime of exciton is the magnitude of several nanoseconds, the L_{exe} can be calculated to be around 10 nm. The implication of this is that the excitons that are formed within the distance of L_{exe} from the interface will contribute to charge dissociation. Therefore, a great deal of study has gone into increasing the diffusion coefficient or making the interfacial larger.

1.4.2.3 Exciton dissociation

Creating free charge carrier is one of the key step in converting solar energy into electrical energy. In this process an electron is transferred from the donor (D) material to an electron acceptor (A) material with the aid of additional energy $h\nu$. The donor material has low electron affinity and the acceptor material has high electron affinity, the difference in the affinity is the driving force for exciton dissociation. The exciton at the interface decays via charge-separated state which forms radical cation of the donor (D^{*+}) and radical anion of the acceptor (A^{*-}).



For efficient charge generation, it is essential for the charge-separated state to be in a thermodynamically and kinetically most favorable pathway for the exciton. Therefore, it is important for the energy absorbed be directed to complete decay such as

fluorescence or non-radiative decay.

1.4.2.4 Charge migration and charge collection

In this process the free charge carriers are migrated from their respective donor and acceptor into the electrodes. The electron migrates into the acceptor and then into the cathode, while the hole migrates through the donor backbone and into the anode, creating a circuit. The mobility of charge carrier for organic material is relatively small, usually less than $1 \text{ cm}^2/\text{Vs}$, compared to inorganic semiconductors ($100\text{-}10000 \text{ cm}^2/\text{Vs}$) [102]. Therefore, it is imperative to design organic material to have large charge mobility. The collection of the free charge carriers are usually accomplished by transparent conductive oxide, such ITO, on one side and a metal contact on the other side. Furthermore, these electrodes have different work function creating potential difference and driving the electric current.

1.4.3 Photodetectors Parameters

An organic photodetector (OPD) is a device that converts optical signal, i.e. solar spectrum, into different kind of signal, such as electrical signal in the form of current or voltage. Currently, OPDs are in development stage and have the potential for wide variety of applications both commercial and military uses such as charge-coupled devices (CCD), which is used for biological imaging, radiation detection, missile flame detection, medical instrumentation and optical communication [103-105].

OPD devices are constructed the same way as photovoltaic devices and the working mechanism is based on photoelectric effect, i.e. absorption of photon to

generate hole-electron pair. However, the parameters for OPDs are different from OPVs, which are spectral response, external quantum efficiency (EQE), dark current, responsivity (R), detectivity and noise equivalent power.

For any given application, an OPD can only respond to specific wavelength range. When designing a device, it is imperative to choose a proper material that can respond to photo signal. Many organic materials have been synthesized to detect light in the ultraviolet-visible region, however materials responding in the near-infrared region are limited.

EQE is defined as the ratio of the number of charge carrier collected by the electrodes compared to number of photons absorbed from the incident light. EQE is integrated over solar spectrum and it evaluates the amount of current the cell will produce when exposed to light. The ideal spectral shape for quantum efficiency would be square-shaped, where the EQE is constant across the spectrum, however, due to recombination it is not always so.

Dark current is the constant current in absence of radiation. It is referred as the reverse bias leakage current, where the electrical flow is not allowed to occur. Dark current measures the random generation of electrons and holes in a device and determines how much of the device response is actually due to the radiation. It plays a key role in device performances and it should be minimized to improve power consumption and effectiveness of photocurrent readout process [105].

Responsivity is characterized as the ratio of photocurrent to incident light intensity and it indicates how effective the device responds to optical signal.

$$R = EQE \frac{\lambda q}{hc} = \frac{I_{ph}}{P_{opt}} = \frac{I_{d,ph} - I_{d,dark}}{P_{opt}}$$

Where I_{ph} is the photocurrent and P_{opt} is the incident light intensity. $I_{d,ph}$ and $I_{d,dark}$ are the drain current under illumination and in dark, respectively. Responsivity is proportional to quantum yield, so it very important for material to have high EQE [106].

Detectivity characterizes the ability of OPD device to detect a small photo signal. Detectivity is given by the following equation:

$$D^* = \frac{R \cdot \sqrt{A}}{\sqrt{2qI_{dark}}} = \frac{R}{\sqrt{2qJ_{dark}}}$$

where A is the detector active area, I_{dark} is dark current density, $2qJ_{dark}$ is the shot noise power spectral density, and R is responsivity. The common merit on quantifying the limit of detection with the presence of noise is the noise equivalent power (NEP), which is the reciprocal of detectivity. Thus, D^* is also defined as

$$D^* = \frac{\sqrt{\Delta f \cdot A}}{NEP}$$

where Δf is the electrical bandwidth.

1.4.4 Polymers Used in Photovoltaic Devices

Device architecture have been optimized to work for both photovoltaic mode and photoconductive mode, thus similarly, organic semiconductors can also be exploited for use in solar cell and photodetector devices. Until recently, organic polymers have only been developed for solar cell and since the charge generation is identical for both modes it is imperative for such materials also be developed for OPDs. Herein in this section several examples of polymers used in solar cell application are shown, which can also be established for OPD application.

1.4.4.1 Polymers for Solar Cell devices

The most commonly used n-type (acceptor) material used in photovoltaic is fullerene (C_{60}) and its derivatives. Since its initial discovery in 1985, they have been subject to intense research for use in electronics due to many intrinsic advantages. Fullerenes have a low lying LUMO level ranging from, -3.67 to -3.75 eV and have high electron affinity, therefore, they are thermodynamically favorable to accept electrons from excited p-type (donor) material. Furthermore, fullerenes have a triply degenerate LUMO level with the HOMO-LUMO separation relatively small. The small gap suggest that reduction should occur at mild potential leading to fulleride anions and is able accept up to six electrons [107]. Photo-induced electron transfer from donor material to fullerene is much faster than decay of luminescence or radiative recombination [108]. However, C_{60} or C_{70} suffers from poor solubility in common organic solvents, so scientists have designed derivatives by implementing alkyl chains to improve solubility, [6,6]-phenyl- C_{61} -butyric acid methyl ester ([60]PCBM), [6,6]-phenyl- C_{70} -butyric acid methyl ester ([70]PCBM) and indene- C_{60} bisadduct (Fig. 1.21).

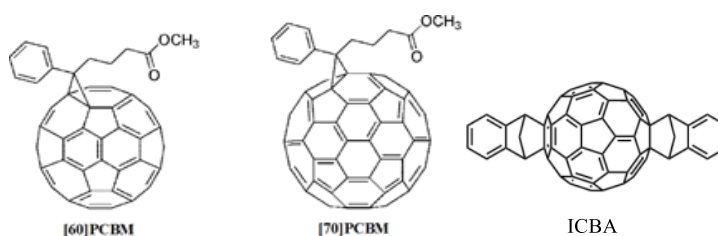


Figure 1.21: Structures of fullerene-based electron acceptors used in photovoltaic devices: [60]PCBM, [70]PCBM and ICBA

One of the earliest material used for polymer solar cells (PSCs) is the polymer poly[2-methoxy-5-(2'-ethylhexyloxy)-p-phenylene vvinylene] (MEH-PPV). Yu et al.

blended MEH-PPV with C_{60} and its derivatives to give the first PSC with a high PCE [95]. This work led to a new era of polymer blend research for use in solar energy conversion. With significant optimization, research has led to PCE more than 3% for PPV-based devices [109, 110]. However, due to low hole mobility and small spectral range, new materials were being investigated. The soluble poly-thiophenes, especially P3HT, became the standard material for PSC development due to higher hole mobility and broader spectrum coverage. With optimizing the device and morphology, PCEs of 4-5% were reached (Fig. 1.21) [111, 112].

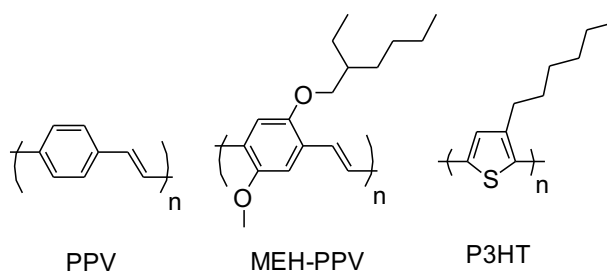


Figure 1.22: Structure of PPV and P3HT

In recent years, many polymers have been developed for high performance for PSC. One of them is poly[2,6-(4,4-bis-(2-ethylhexyl)4H-cyclopenta[2,1-b;3,4-b']dithiophene)-alt-4,7-(2,1,3-benzothiadiazole)] (PCPDTBT), a low-bandgap polymer whose absorption tailing up to 900 nm (Fig. 1.23). Solar cells made from this polymer initially showed efficiency of 3%, but after device optimization, such as adding solvent additive, researchers were able to reach PCE up to 5.5% [113, 114]. Another polymer that was developed poly[N-9'-hepta-decanyl-2,7-carbazole-alt-5,5-(4',7'-di-2-thienyl-2',1',3'-benzothiadiazole)] (PCDTBT), initially gave PCE of 3.6% [115]. But after incorporating a titanium oxide (TiO_x) layer as an optical spacer, PCE was increased to 6.1% [116]. One of the most impressive polymer designed composed

of alternating thieno[3,4-b]-thiophene (TT) and benzodithiophene (BDT) units. This donor-acceptor polymer is capable of reaching PCEs of 7-8% (Fig 1.23) [117-119]. Following this polymer, PCEs of more than 7% were frequently reported, such as using the polymer PTB7-Th, PCE of approximately 10% in a single bulk heterojunction was reached [120, 121].

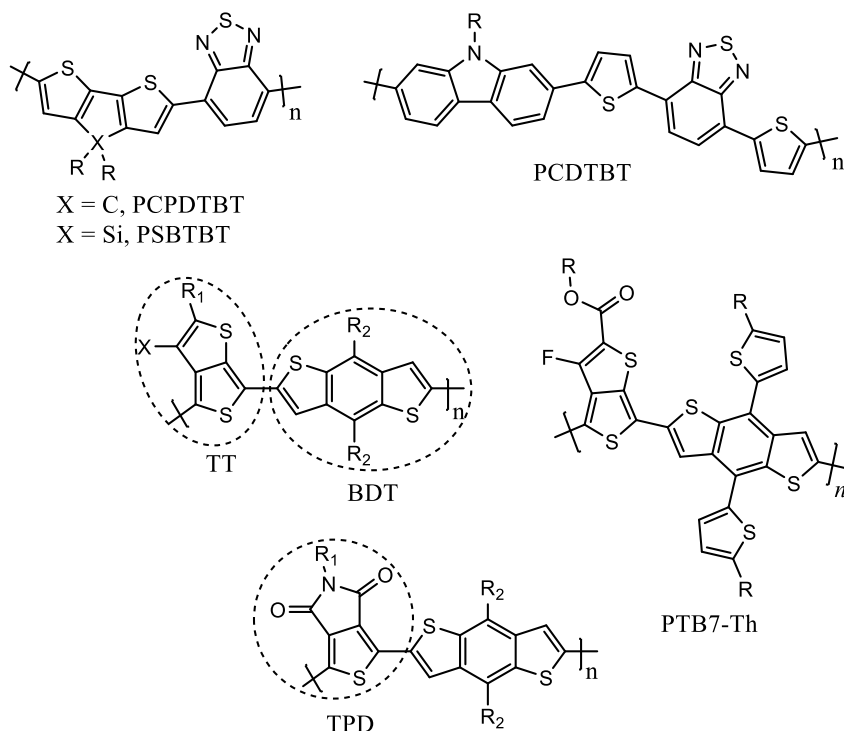


Figure 1.23: Donor-acceptor polymers PCPDTBT, PSBTBT, PCDTBT, TTBDT, PTB7-Th

Diketopyrrolopyrrole (DPP) was first introduced in the early 1970s and was widely used as a pigment in inks, paints and plastics (Fig. 1.24). Recently, because of strong fluorescent performance and exceptional chemical and thermal stability, they have been investigated for optical-electronic applications [122]. DPP is two fused five-membered heterocyclic γ -lactam with a substituted aromatic bridging unit in the 3,6-position. DPP is a highly electron deficient unit with strong π - π interaction, which

results in efficient charge transport and typically used for making donor-acceptor polymers. Due to having relatively low lying HOMO and LUMO level, they have been used in organic light-emitting diodes (OLED), organic- thin film transistors (OTFT) and PSCs [123, 124]. Ong et al. have reported a solution processed DPP-based polymer (DPP-TT) that have achieved record high hole mobility for p-type material of $10.5 \text{ cm}^2\text{V}^{-1}\text{s}^{-1}$ (Fig 1.24) [125]. Furthermore, DPP-based polymers (PBDTT-SeDPP) have been used in BHJ solar cell and have reached PCE up to 7.2% in a single cell junction and a 9.5% in a tandem cell junction with a band gap of 1.38 eV [126].

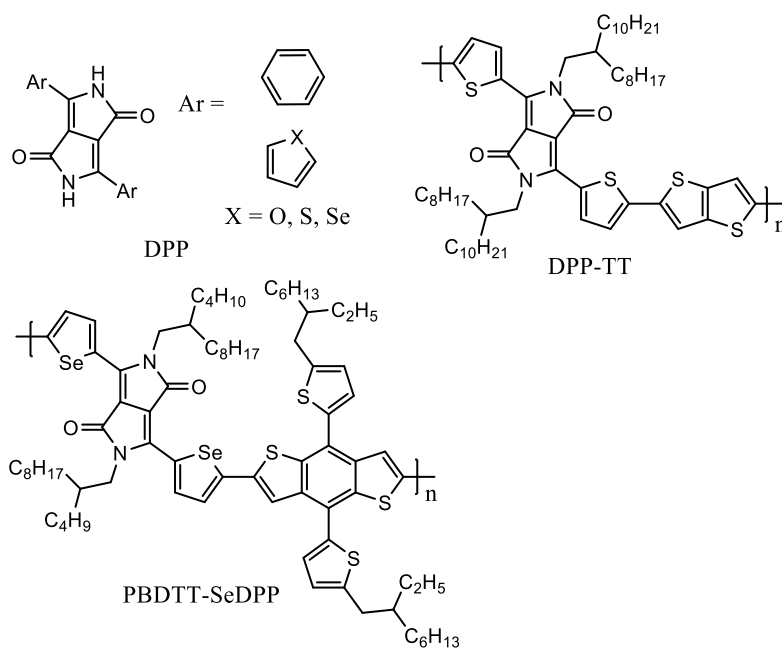


Figure 1.24: DPP-based polymers

Material innovation is one of the key driving force of improving performances in PSCs. The key issues for polymer design include engineering the band gap, achieving high short circuit (J_{sc}) current, high open current voltage (V_{oc}) (solar cell parameters), attain high carrier mobility, material processability and stability. In most cases these issues are interconnected and in ideal cases, these factors should be

optimized in a single polymer. P3HT has been the one of the most popular donor with a HOMO level at 4.9 eV and a V_{OC} of 0.6 V and serves as a reference for polymer design. Several polymers have been synthesized with V_{OC} approximately 1.0 V by incorporating electron rich donor such as fluorene and carbazole, with PCE of 1.95% for PFO-DBT and 3.5% for APFO-15 (Fig. 1.25) [127, 128].

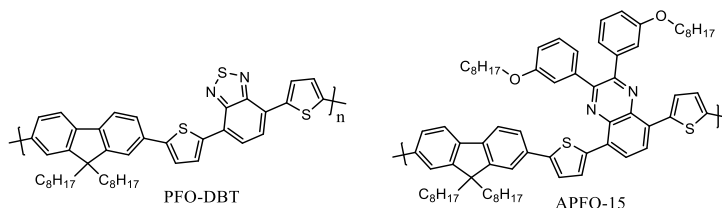


Figure 1.25: Polymer PFO-DBT and APFO-15

Just improving V_{OC} isn't enough to improve the solar cell efficiency. J_{SC} is another important parameter and to improve it is vital to have broader solar spectrum. However, narrowing the band gap alone might not be enough to increase J_{SC} , carrier mobility, intermolecular interaction and molecular chain packing impacts J_{SC} . An example of this is replacing the bridging carbon atom in PCPDTBT with silicon atom (PSBTBT) (Fig. 1.23) showed higher crystallinity, improving hole mobility and enhancing molecular packing, ultimately leading to higher value of J_{SC} and achieving PCE up to 5.5% [114, 129, 130].

Improving both V_{OC} and J_{SC} simultaneously remains a great challenge. Narrowing the band gap may improve J_{SC} , but V_{OC} may decrease due to higher HOMO level. Recently, researchers have demonstrated introducing fluorine atom into TT unit in PTB7-Th (Fig. 1.23) reduces both HOMO and LUMO levels simultaneously, while improving V_{OC} and retaining small band gap [117-119]. Another example of this is shown by Janssen et al. where incorporating fluorine atom in the BT unit (Fig. 1.26)

improved V_{OC} , J_{SC} and FF simultaneously from 11.2 mAcm^{-2} to 13.3 mAcm^{-2} for J_{SC} , 0.75 V to 0.85 V for V_{OC} and 0.64 to 0.68 for the FF. The efficiency also improved from 5.4% to 7.7% [131].

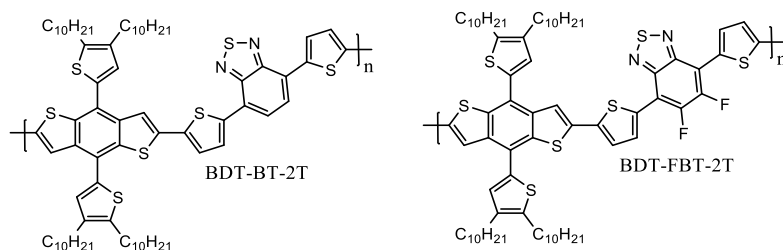


Figure 1.26: Polymers BDT-BT-DT and BDT-FBT-2T

Improving fill factor has been a great mystery to researchers. From material design point of view, molecular planarity, intermolecular interaction, crystallinity and side-chain tuning have been seen to affect the FF. A prime example of this is the use of the acceptor unit TPD (Fig. 1.23), side-chain optimization has improved π -stacking, crystallinity and miscibility and thus increasing the FF from 55% to 68% and achieved efficiency of 7% [132].

Other ways to improve the PCE of devices is the development of novel acceptor material. For example, replacing C₆₀ to C₇₀ derivatives often improved J_{SC} by 10% and the V_{OC} can be improved since the LUMO level effect the charge migration. Achieving an upshifted LUMO leads to higher V_{OC} . In a recent development, C₆₀ with indene bisadduct (ICBA) (Fig. 1.21) has an upshifted LUMO level of 0.17 eV compared to [60]PCBM and using this acceptor resulted in a 40% improvement in V_{OC} in P3HT-based PSC [133, 134].

To have a commercially viable use for OPV the efficiency must rise above 15% [135]. For a single junction cell with a donor material at 1.5 eV, a practical efficiency can only be reached to 11%. Therefore, adopting multilayer BHJ or tandem solar cell

have become the norm. Theoretical calculation show that tandem cell can reach maximum efficiency of up to 15% by combining a bottom donor having a band gap of 1.6 eV with a top donor having a band gap of 1.3 eV [136]. Yang et al. have shown tandem cell with identical sub-cells based on PDTP-DFBT:[70]PCBM BHJ (Fig. 1.27) with light absorption in the visible region with EQE percentage of above 70% and improved PCE from 8.1% in a single junction to 10.2% in tandem cell [137]. Furthermore, they have developed a triple-junction cell which reached efficiency up to 11.55% [138].

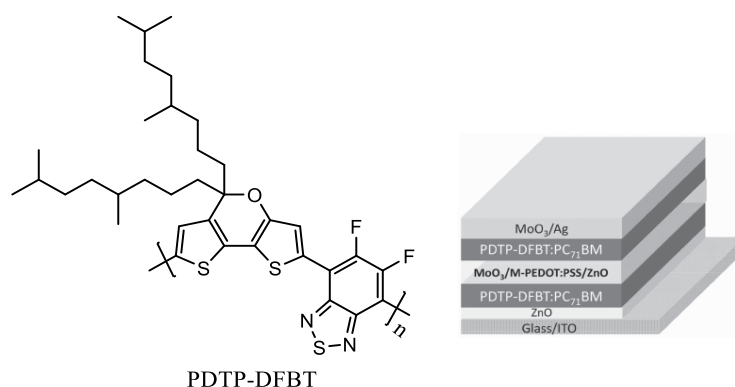


Figure 1.27: Polymer PDTP-DFBT and tandem cell configuration (Adapted with permission from Ref. 137)

1.4.4.2 Polymers for Photodetectors

Development of optoelectronic devices for sensing application have variety of application such as image sensing, optical communication, environmental monitoring, chemical/biological sensing and etc. The current inorganic photodetectors, GaN, Si and InGaAs, are used for three sub-bands, 250 to 400 (UV), 450 to 800 (visible) and 900 to 1700 (NIR), respectively. Typically, silicon photodetectors have detectivity in 4×10^{12} Jones region, whereas InGaAs detectors are greater than 10^{12} Jones when cooled at 4

K [139]. Therefore, it is imperative to design panchromatic material that can operate in broad spectral range with high detectivity and sensitivity at room temperature operation.

Thoroughly studied solution processed P3HT-[60]PCBM have relatively high carrier mobility with good spectral range from 400 to 600 nm and peak EQE about 70% have been used for photoluminescence based bio-chemical sensors [140]. Furthermore, new class of polyfluorene derivatives (F8TBT) (Fig. 1.28) and copolymers blended with P3HT have reached EQE of 26% and dark current density as low as 40 pA/mm² which have been used for blue-green light detection [141].

Compared to blue-green light detection, fewer examples of red-light sensitive OPDs have been reported. Initially small molecule phthalocyanines, squaraines and porphyrin dye represents the most classical choice for red photon harvesting with absorption peaked from 600-800 nm. Adopting phthalocyanines, response have reached near infrared detection up 800 nm, however due to solubility issues, thermal evaporation is used to make PD devices [142]. Solution processed thienothiadiazole co-polymers (PT-TT) have reached EQE of 15% in 700-800 nm with detectivity at 1.4×10^{12} Jones and low dark current [143]. In a recent publication, researchers have used thiadiazolobenzotriazol based polymer (PTZBTTT-BDT) (Fig. 1.28) to give spectral response from 400 to 1100 nm with dark current reaching as low as 1.25×10^{-10} Acm⁻², detectivity up to 1.75×10^{13} Jones and EQE of 16% at 800 nm. These results demonstrated polymer PDs comparable to Si-based PDs [144].

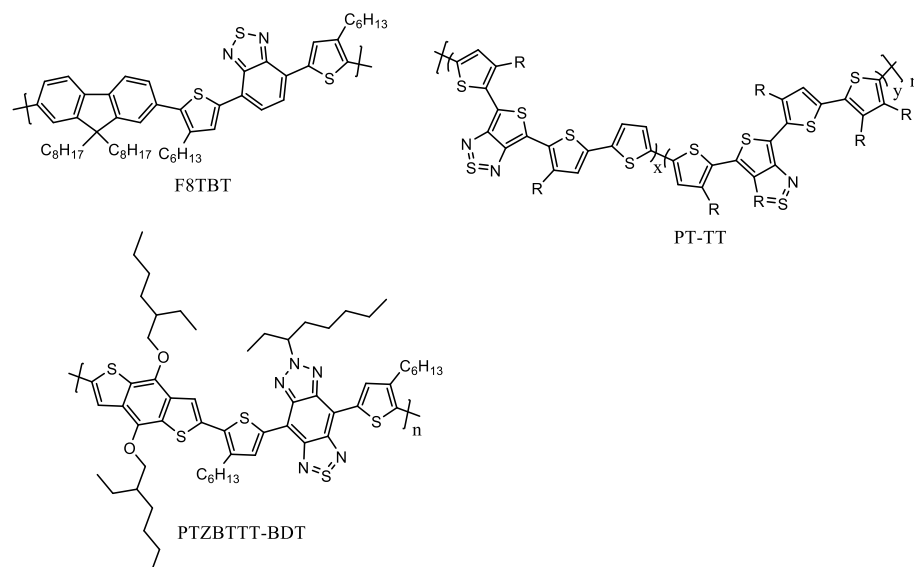


Figure 1.28: Polymers F8TBT, PT-TT and PTZBTTT-BDT used in photodetectors

Development of near infrared polymers with high detectivity, responsivity and extension further into NIR region, i.e. 1500 nm have become a challenge. Exploiting donor-acceptor method, Yang et al. have demonstrated a photodetector with responsivity up to 900 nm with EQE of $\sim 40\%$ at bias of -5 V using BHJ design with the polymer PTT with a band gap of 1.3 eV (Fig 1.29a). The device NEP, where the minimum impinging optical power that a detector can distinguish from the noise, was calculated to be $3.85 \times 10^{-12} \text{ W}/\text{H}^{1/2}$ at 850 nm at 4 kHz, however it was still inferior to commercially available NIR detectors [145]. A similar approach was adopted by Gong et al. to develop panchromatic material (PDDTT) (Fig. 1.29a). The polymer exhibited spectral response from 300 to 1450 nm, with detectivity greater than 10^{13} Jones from 300 to 1150 nm and 10^{12} Jones from 1150 to 1450. When compared to Si and InGaAs detector, the polymer shows performance similar or even better in terms of photodetectivity and photoresponse (Fig.1.29b-c) [139]. Qian et al. reported a new analogue of DPP, 2,5-diazapentalene (DAP) coupled with BDT donor to give the

polymer PDAPBDT with a narrow band gap of 1.19 eV. BHJ solar cell based on this polymer performed poorly with low PCE, although, has promising use for NIR photodetector. The device configuration was ITO/PEDOT:PSS/active layer/Al and the active layer is a blend of PDAPTBT and [60]PCBM in a weight ratio 1:3. The dark current density was measured to be 3.27 nAcm^{-2} at bias of -0.1 V which is lower than that of reported high-detectivity based on narrow band-gap polymer. The low dark current can be attributed to the low lying HOMO level. However, it showed low EQE value at 800 nm of 4% and detectivity of 1.6×10^{11} Jones. This is likely due to large domain size in the active layer and close LUMO levels of the polymer and [60]PCBM, leading to insufficient exciton dissociation [146].

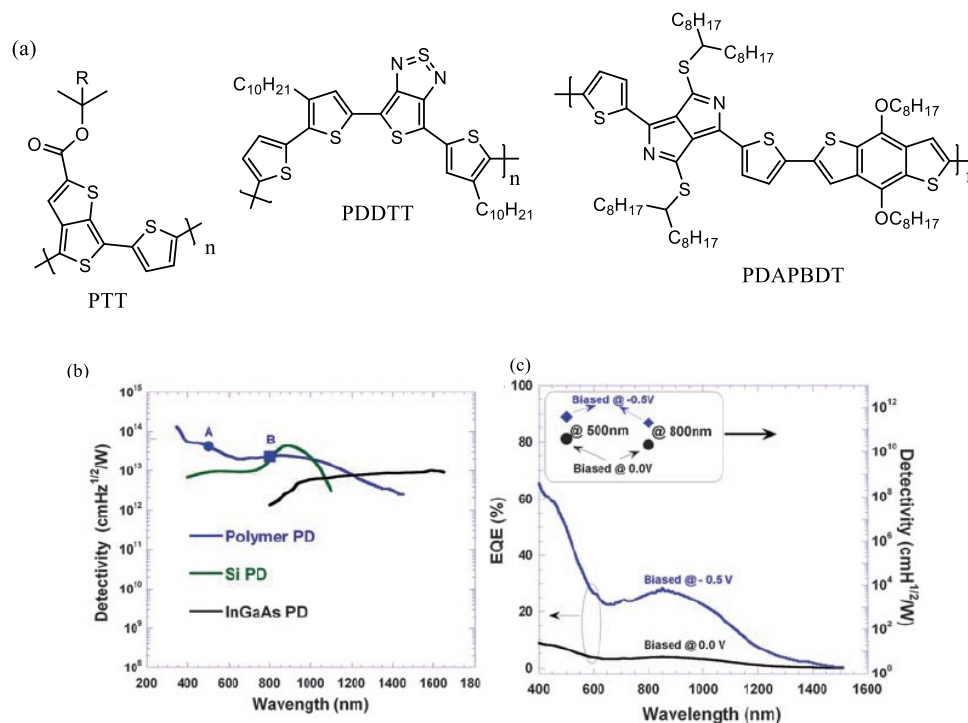


Figure 1.29: (a) Polymers PTT, PDDTT, PDAPBDT (b) Detectivities of Si, InGaAs and PDDTT-based photodetectors (c) EQE vs. wavelength and calculated detectivities at 500 nm and 800 nm of PDDTT) (Adapted with permission from Ref. 139)

1.5 Rationale and Objectives

Performance and commercialization of OPVs are now at standstill and a great deal of effort are needed to develop new conjugated polymers. Furthermore, OPDs are currently in the palmary stages in development and have a great potential for a wide variety of commercial and military uses such as night vision surveillance, remote control and imaging. Compared to their inorganic counterpart, which require vacuum deposition at high temperature, OPDs can be processed at ambient temperature and large area with minimal material. However, it has long been a challenge to develop organic polymers with high EQE, low noise-to-signal and high detectivity in the NIR region.

DPP has shown to be an excellent electron acceptor and have been used to make many conjugated D-A polymers with the absorption from 500 to 800 nm. Analogue to DPP is the stronger acceptor of DAP and the DAP based D-A polymers have low band gaps and absorptions up to 1400 nm. Both DPP and DAP based polymers can cover the entire UV-Vis-NIR spectral region and thus are highly desirable for use in broad-spectrum OPV and OPDs.

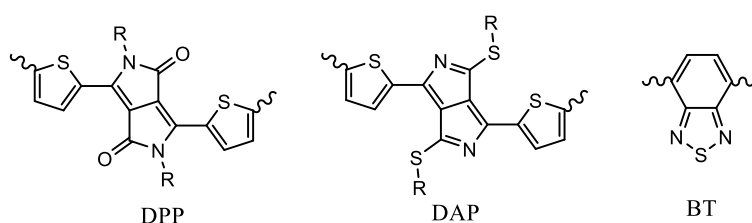


Figure 1.30: DAP, DPP and BT structure

Designing a polymer to absorb a large spectral region has become a technical challenge, therefore researcher have developed multilayer device, where one polymer layer is used to absorbs at a higher wavelength and the second polymer layer absorbs lower

wavelength. However, these devices require an interlayer, typically vacuum deposited, to separate the bottom and the top layers.

The objective of this thesis is to design and synthesize DPP-based polymers with cleavable bearing precursor to change the solubility of the polymers. With that in mind, the soluble polymer can be solution processed and the cleavable group can be removed to render the polymer insoluble. With this process, a second layer, DAP polymer, can be incorporated without the use of an intermediate layer to produce solution-processable multilayer devices for use in optoelectronics. Furthermore, optimizing device architecture has also been a focal point on innovation to maximize performance. PEDOT:PSS is the most widely used hole transfer layer due to high conductivity and high work function. However, the acidic and hygroscopic nature of PEDOT:PSS causes degradation and reduces device stability. Therefore, we developed solution processed polymer which can be chemically cross-linked rendering it insoluble and can potentially serve as a HTL to replace the commonly used PEDOT:PSS.

Emerging electrochromic materials have found wide commercial use such as car rear-view mirrors, smart windows and display [147, 148]. Although with the commercial application, variable transmission is somewhat limited by their lack of attenuation in the NIR portion of the spectrum. 2,1,3-Benzothiadiazole (BT) (Fig. 1.29) and its derivatives are one of the most commonly used acceptors due to its strong electron-withdrawing ability and high electron mobility [149]. Using modified BT unit, D-A polymers were designed and electrochromic properties in the telecommunication wavelength were explored.

References

- [1] T. Xu, L. Yu, *Mater. Today*, **2014**, *17*, 11.
- [2] A. Virkar. "Introduction to Organic Semiconductors Transistors and Conductors." Investigating the Nucleation, Growth, and Energy Levels of Organic Semiconductors for High Performance Plastic Electronics. N.p.: Springer Science & Business Media, 2011. 3-4. Print.
- [3] J. Soloducho, A. Swist, *Protein sensor for glucose detection*, P 394553, **2011**.
- [4] J.-Z. Wang, S.-L. Chou, H. Liu, G. X. Wang, C. Zhong, *Materials Letters*, **2009**, *63*, 2352.
- [5] J. H. Burroughes et al. *Nature*, **1990**, *347*, 539.
- [6] M. T. Bernius, E. P. Woo, *Semiconducting polymer field effect transistor*, US Patent 6204515, **2001**.
- [7] A. Hagfeldt, M. Gratzel, *Acc. Chem. Res.*, **2000**, *33*, 269.
- [8] S. R. Marder, *Chem. Commun.*, **2006**, 131.
- [9] M. Satoh, M. Tabata, F. Uesugi, F. Kaneto, K. Yoshino, *Synt. Met.*, **1987**, *17*, 595.
- [10] P. W. M. Blom, V. D. Mihailechi, L. J. A. Koster, D. E. Markov, *Adv. Mater.*, **2007**, *19*, 1551.
- [11] H. A. M. van Mullekom, J. A. J. M. Vekemans, E. E. Havinga, E. W. Meijer, *Mater. Sci. Eng. R*. **2001**, *32*, 1.
- [12] Z. Li, H. Meng, *Organic Light-Emitting Materials and Devices*, CRC Press: New York, 2007.
- [13] C. Winder, N. S. Sariciftci, *J. Mater. Chem.* **2004**, *14*, 1077.

- [14] Roncali, J. *Chem. Rev.* **1997**, *97*, 173.
- [15] R. E. Peierls, *Quantum Theory of Solids*, Oxford University Press: London, 1956.
- [16] L. M. Tolbert, *Acc. Chem. Res.* **1992**, *25*, 561.
- [17] T. A. Albright, J. K. Burdett, M.-H. Whangbo, in *Orbital Interactions in Chemistry*, Wiley: New York, 1985, p. 229.
- [18] J. L. Brédas, B. Thémans, J. G. Fripiat, J. M. André, R. R. Chance, *Phys. Rev. B: Condens. Matter*, **1984**, *29*, 676.
- [19] J. L. Brédas, *J. Chem. Phys.* **1985**, *82*, 3808.
- [20] R. S. Mulliken, C. A. Rieke, W. G. Brown, *J. Am. Chem. Soc.* **1941**, *63*, 41.
- [21] J. L. Brédas, G. B. Street, B. Themans, J. M. André, *J. Chem. Phys.* **1985**, *83*, 1323.
- [22] B. Xu, S. Holdcroft, *Macromolecules*, **1993**, *26*, 4457.
- [23] R. D. McCullough, R. D. Lowe, M. Jayaraman, D. L. Anderson, *J. Org. Chem.* **1993**, *58*, 904.
- [24] P. v. R. Schleyer, *Chem. Rev.* **2001**, *101*, 1115.
- [25] A. T. Balaban, P. v. R. Schleyer, H. S. Rzepa, *Chem. Rev.* **2005**, *105*, 3436.
- [26] P. v. R. Schleyer, *Chem. Rev.* **2005**, *105*, 3433.
- [27] B. Jr. Andes Hess, L. J. J. Schaad, *Am. Chem. Soc.* **1971**, *93*, 305.
- [28] B. Jr. Andes Hess, L. J. Schaad, *J. Am. Chem. Soc.* **1973**, *95*, 3907.
- [29] A. S. Kafafi, *Chem. Phys. Lett.* **1990**, *169*, 561.
- [30] J. P. Lowe, S. A. Kafafi, *J. Am. Chem. Soc.* **1984**, *106*, 5837.
- [31] Y. Liang, D. Feng, Y. Wu, S.-T. Tsai, G. Li, C. Ray, L. Yu, *J. Am. Chem. Soc.*,

- 2009**, *131*, 7792.
- [32] J. M. Szarko, L. Guo, Y. Liang, B. Lee, B. S. Rolczynski, J. Strzalka, T. Zu, S. Loser, T. J. Marks, L. Yu, L. X. Chen, *Adv. Mater.*, **2010**, *22*, 5468.
- [33] F. He, W. Wang, W. Chen, T. Xu, S. B. Darling, J. Strzalka, Y. Liu, L. Yu, *J. Am. Chem. Soc.*, **2011**, *133*, 3284.
- [34] N. Kim, B. H. Lee, D. Choi, G. Kim, H. Kim, J.-R. Kim, J. Lee, Y. H. Kahng, K. Lee, *Chem. Phys. Lett.* **2012**, *109*, 106405.
- [35] Y.-W. Su, S.-C. Lan, K.-H. Wei, *Mater. Today*. **2012**, *15*, 554.
- [36] C. H. Woo, B. C. Thompson, B. J. Kim, M. F. Toney, J. M. J. Fréchet, *J. Am. Chem. Soc.* **2008**, *130*, 16324.
- [37] U. Salzner, J. B. Lagowski, P. G. Pickup, R. A. Poirier, *Synth. Met.* **1998**, *96*, 177.
- [38] A. Tsuda, A. Osuka, *Science*, **2001**, *293*, 79.
- [39] H. S. Cho, D. H. Jeong, S. Cho, D. Kim, Y. Matsuzaki, K. Tanaka, A. Tsuda, A. Osuka, *J. Am. Chem. Soc.* **2002**, *124*, 14642.
- [40] D. Kim, A. Osuka, *Acc. Chem. Res.* **2004**, *37*, 735.
- [41] E. E. Havinga, W. Hoeve, H. Wynberg, *Polym. Bull.* **1992**, *29*, 119.
- [42] G. Brocks, A. Tol, *J. Phys. Chem.* **1996**, *100*, 1838.
- [43] G. Brocks, A. Tol, *Synth. Met.* **1996**, *76*, 213.
- [44] *Handbook of Conducting Polymers*, 2nd ed. (Eds: T. Skotheim, J. Reynolds, R. Elsenbamer), Marcel Dekker, New York **1998**, in press.
- [45] *Handbook of Conducting Polymers* (Ed: T. Skotheim), Marcel Dekker, New York **1986**.

- [46] L.J.A. Koster, V.D. Mihailetschi, P.W.M. Blom, *Appl. Phys. Lett.* **2006**, *88*, 093511.
- [47] P. Schilinsky, U. Asawapirom, U. Scherf, M. Biele, C.J. Brabec, *Chem. Mater.* **2005**, *17*, 2175.
- [48] M. Kobayashi, N. Colaneri, M. Boysel, F. Wudl, A.J. Heeger, *J. Chem. Phys.* **1985**, *82*, 5717.
- [49] Y. Ikenoue, F. Wudl, A.J. Heeger, *Synth. Met.* **40** (1991) 1.
- [50] M. Pomerantz, B. Chaloner-Gill, L.O. Harding, J.J. Tseng, W.J. Pomerantz, *Synth. Met.* **1993**, *55-57*, 960.
- [51] C. Arbizzani, M. Catellani, M. Grazia Cerroni, M. Mastragostoni, *Synth. Met.* **1997**, *84*, 249.
- [52] M. Pomerantz, G. Xiaormin, *Synth. Met.* **1997**, *84*, 243.
- [53] S. Inaoka, D.M. Collard, *Synth. Met.* **1997**, *84*, 193.
- [54] M. E. Cinar, T. Ozturk, *Chem. Rev.*, **2015**, *115*, 3036.
- [55] F. E. Arnold, R. L. Van Deusen, *J. Appl. Polym. Sci.* **1971**, *15*, 2035.
- [56] S. A. Jenekhe, L. R. de Paor, X. L. Chen, R. M. Tarkka, *Chem. Mater.*, **1996**, *8*, 2401.
- [57] J. A. Osaheni, S. A. Jenekhe, J. Perlstein, *J. Phys. Chem.*, **1994**, *98*, 12727.
- [58] J. R. Lindle, F. J. Bartoli, O.-K. Kim, Y. S. Lee, J. S. Shirk, Z. H. Kafafi, *Appl. Phys. Lett.*, **1990**, *56*, 712.
- [59] Q. Wang, W. Qiao, Z. Y. Wang, *RSC Adv.*, **2014**, *4*, 9967.
- [60] M. Kertesz, *Macromolecules.* **1995**, *28*, 1475.
- [61] J. E. Anthony, *Angew. Chem. Int. Ed.* **2008**, *47*, 452.

- [62] Y. Yamashita, *Sci. Technol. Adv. Mater.* **2009**, *10*, 024313.
- [63] M. Sadrai, L. Hadel, R. R. Sauers, S. Husain, K. Krogh-Jespersen, J. D. Westbrook, G. R. Bird, *J. Phys. Chem.* **1992**, *96*, 7988.
- [64] P. Panayotatos, D. Parikh, R. Sauers, G. Bird, A. Piechowski, S. Husain, *Solar Cells*, **1986**, *18*, 71.
- [65] N. G. Pschirer, C. Kohl, F. Nolde, J. Qu, K. Müllen, *Angew. Chem. Int. Ed.* **2006**, *45*, 1401.
- [66] C. Kohl, S. Becker, K. Müllen, *Chem. Commun.* **2002**, 2778.
- [67] E.E. Havinga, W. ten Hoeve, H. Wynberg, *Synth. Met.* **1993**, *55-57*, 299.
- [68] Y. Li, *Acc. Chem. Res.* **2012**, *45*, 723.
- [69] Z.-G. Zhang, *J. Mater. Chem.* **2012**, *22*, 4178.
- [70] M. Levitus, K. Schmieder, H. Ricks, K. D. Shimizu, U. H. F. Bunz, M. A. Garcia-Garibay, *J. Am. Chem. Soc.* **2001**, *123*, 4259.
- [71] R. Pizzoferrato, M. Berliocchi, A. Di Carlo, P. Lugli, M. Venanzi, A. Micozzi, A. Ricci, C. Lo Sterzo, *Macromolecules*, **2003**, *36*, 2215.
- [72] D. L. Zeng, J. W. Chen, Z. Chen, W. H. Zhu, J. He, F. Yu, H. Huang, H. R. Wu, C. Liu, S. J. Ren, J. P. Du, J. Sun, E. J. Xu, A. Cao, Q. Fang, *Macromol. Rapid Commun.* **2007**, *28*, 772.
- [73] S.-C. Lan, P.-A. Yang, M.-J. Zhu, C.-M. Yu, J.-M. Jiang, K.-H. Wei, *Polym. Chem.*, **2013**, *4*, 1132.
- [74] H. Zhou, L. Yang, S. Xiao, S. Liu, W. You, *Macromolecules*, **2009**, *43*, 811.
- [75] H. A. M. van Mullekom, J. A. J. M. Vekemans, E. W. Meijer, *Chem. Eur. J.* **1998**, 1235.

- [76] G. Qian, Z. Y. Wang, *Can. J. Chem.* **2010**, *88*, 192.
- [77] G. L. Gibson, T. M. McCormick, D. S. Seferos, *J. Am. Chem. Soc.* **2012**, *134*, 539.
- [78] J. Fan, J. D. Yuen, M. Wang, J. Seifert, J.-H. Seo, A. R. Mohebbi, D. Zakhidov, A. Heeger, F. Wudl, *Adv. Mater.* **2012**, *24*, 2186.
- [79] H.A. Ho, H. Brisset, P. FreÁre, J. Roncali, *J. Chem. Soc., Chem. Commun.* **1995**, 2309.
- [80] G.A. Sotzing, C.A. Thomas, J.R. Reynolds, *Macromolecules.* **1998**, *31*, 3750.
- [81] Q.T. Zhang, J.M. Tour, *J. Am. Chem. Soc.* *120* (1998) 5355.
- [82] S. C. Price, A. C. Stuart, L. Q. Yang, H. X. Zhou, W. You, *J. Am. Chem. Soc.* **2011**, *133*, 4625.
- [83] Y. Liang, D. Feng, Y. Wu, S.-T. Tsai, G. Li, C. Ray, L. Yu, *J. Am. Chem. Soc.* **2009**, *131*, 7792.
- [84] L. Yuan, Y. Zhao, J. Zhang, et al. *Adv. Mater.* **2015**, *27*, 4229.
- [85] X. Zhang, T. T. Steckler, R. R. Dasari, S. Ohira, W. J. Potscavage, S. P. Tiwari, S. Coppee, S. Ellinger, S. Barlow, J.-L. Bredas, B. Kippelen, J. R. Reynolds, S. R. Marder, *J. Mater. Chem.* **2010**, *20*, 123.
- [86] M. X. Chen, X. Crispin, E. Perzon, M. R. Andersson, T. Pullerits, M. Andersson, O. Inganas, *Appl. Phys. Lett.* **2005**, *87*, 252105.
- [87] H. Yi, R. G. Johnson, A. Iraqi, D. Mohamad, R. Royce, D. G. Lidzey, *Macromol. Rapid Commun.* **2008**, *29*, 1804.
- [88] G. Li, R. Zhu, Y. Yang, *Nature Photonics*, **2012**, *6*, 153.
- [89] P. Peumans, A. Yakimov, S. R. Forrest, *J. Appl. Phys.*, **2003**, *93*, 3693.

- [90] P. Peumans, V. Bulovic, S. R. Forrest, *J. Appl. Phys.*, **2000**, 76, 2650.
- [91] P. Peumans, V. Bulovic, S. R. Forrest, *J. Appl. Phys.*, **2000**, 76, 3855.
- [92] A. K. Ghosh, D. L. Morel, T. Feng, R. F. Shaw, C. A. Rowe Jr., *J. Appl. Phys.* **1974**, 45, 230.
- [93] C. W. Tang, *Appl. Phys. Lett.* **1986**, 48, 183.
- [94] S. Shafian, Y. Jang, K. Kim, *Opt. Express*, **2015**, 23, A936.
- [95] G. Yu, J. Gao, J. C. Hummelen, F. Wudl, A. J. Heeger, *Science*, **1995**, 270, 1789.
- [96] W. Cao, J. Xue, *Energy Environ. Sci.*, **2014**, 7, 2123.
- [97] A. J. Heeger, *Adv. Mater.*, **2014**, 26, 10.
- [98] N. S. Sariciftci, D. Braun, C. Zhang, V. I. Srdanov, A. J. Heeger, G. Stucky, F. Wudl, *Appl. Phys. Lett.*, **1993**, 62, 585.
- [99] A. Tayebbeh, N. Lia, C. J. Brabec, *Energy Environ. Sci.*, **2013**, 6, 2390.
- [100] C.-C. Chen, W.-H. Chang, K. Yoshimura, K. Ohya, J. You, J. Gao, Z. Hong, Y. Yang, *Adv. Mater.*, **2014**, 26, 5670.
- [101] E. Bundgaard, F. C. Krebs, *Sol. Energ. Mat. Sol. Cells.*, **2007**, 91, 954.
- [102] T. J. Savenije, *Organic solar cells*, Delft University of Technology, **2014**.
- [103] J. Lin, N. Oder, M. L. Nakarmi, J. Y. Lin, H. X. Jiang, *Appl. Phys. Lett.*, **2006**, 89, 213510.
- [104] N. Martino, D. Ghezzi, F. Benfenati, G. Lanzani, R. M. Antognazza, *J. Mater. Chem. B.*, **2013**, 1, 3768.
- [105] K.-J. Baeg, M. Binda, D. Natali, M. Caironi, Y.-Y. Noh, *Adv. Mater.*, **2013**, 25, 4267.

- [106] L. Dou, Y. Yang, J. You, Z. Hong, W.-H. Chang, G. Li, Y. Yang, *Nat. Commun.*, **2014**, *5*, 1.
- [107] P. M. Allemond, A. Koch, F. Wudl, Y. Rubin, F. Diederich, M. M. Alvarez, S. J. Anz, R. L. Whetten, *J. Am. Chem. Soc.*, **1991**, *113*, 1050.
- [108] D. Wrobel, A. Graja, *Coord. Chem. Rev.*, **2011**, *255*, 2555.
- [109] C. J. Brabec, S. E. Shaheen, C. Winder, N. S. Sariciftci, P. Denk, *Appl. Phys. Lett.*, **2002**, *80*, 1288.
- [110] M. M. Wienk, J. M. Kroon, W. J. H. Verhees, J. Knol, J. C. Hummelen, P. A. van Hal, R. A. J. Janssen, *Angew. Chem. Int. Ed.*, **2003**, *42*, 3371.
- [111] G. Li, V. Shrotriya, J. Huang, Y. Yao, T. Moriarty, K. Emery, Y. Yang, *Nature Mater.*, **2005**, *4*, 864.
- [112] M. L. Ma, C. Y. Yang, X. Gong, K. Lee, A. J. Heeger, *Adv. Funct. Mater.*, **2005**, *15*, 1617.
- [113] D. Muhlbacher, M. Scharber, M. Morana, Z. Zhu, D. Waller, R. Gaudiana, C. Brabec, *Adv. Mater.*, **2006**, *18*, 2884.
- [114] J. Peet, J. Y. Kim, N. E. Coates, W. L. Ma, D. Moses, A. J. Heeger, G. C. Bazan, *Nature Mater.*, **2007**, *6*, 497.
- [115] N. Blouin, A. Michaud, M. Leclerc, *Adv. Mater.*, **2007**, *19*, 2295.
- [116] S. H. Park, A. Roy, S. Beaupre, S. Cho, N. Coates, J. S. Moon, D. Moses, M. Leclerc, K. Lee, A. J. Heeger, *Nature Photon.*, **2009**, *3*, 297.
- [117] Y. Y. Liang, Y. Wu, D. Feng, S.-T. Tsai, G. Li, L. Yu, *J. Am. Chem. Soc.*, **2009**, *131*, 56.

- [118] Y. Y. Liang, D. Feng, Y. Wu, S.-T. Tsai, G. Li, C. Ray, L. Yu, *J. Am. Chem. Soc.*, **2009**, *131*, 7792.
- [119] H. Y. Chen, J. Hou, S. Zhang, Y. Liang, G. Yang, Y. Yang, L. Yu, Y. Wu, G. Li, *Nature Photon.*, **2009**, *3*, 649.
- [120] Z. He, B. Xiao, F. Liu, H. Wu, Y. Yang, S. Xiao, C. Wang, T. P. Russell, Y. Cao, *Nature Photon.*, **2015**, *9*, 174.
- [121] J.-D. Chen, C. Cui, Y.-Q. Li, L. Zhou, Q.-D. Ou, C. Li, Y. Li, J.-X. Tang, *Adv. Mater.*, **2015**, *27*, 1035.
- [122] S. Qu, H. Tian, *Chem. Commun.*, **2012**, *48*, 3039.
- [123] Z. Qiao, Y. Xu, S. Lin, J. Peng, D. Cao, *Synth. Met.*, **2010**, *160*, 1544.
- [124] M. Tantiwiwat, A. Tamayo, N. Luu, X.-D. Dang, T.-Q. Nguyen, *J. Phys. Chem. C*, **2008**, *112*, 17402.
- [125] J. Li, Y. Zhao, H. S. Tan, Y. Guo, C.-A. Di, G. Yu, Y. Liu, M. Lin, S. H. Lim, Y. Zhou, H. Su, B. S. Ong, *Sci. Rep.*, **2012**, *2*, 754.
- [126] L. Dou, W.-H. Chang, J. Gao, C.-C. Chen, J. You, Y. Yang, *Adv. Mater.*, **2012**, *25*, 825.
- [127] Q. M. Zhou, Q. Hou, L. Zheng, X. Deng, G. Yu, Y. Cao, *Appl. Phys. Lett.*, **2004**, *84*, 1653
- [128] A. Gadisa, *Adv. Funct. Mater.*, **2007**, *17*, 2836.
- [129] F. Huang, K.-S. Chen, H.-L. Yip, S. K. Hau, O. Acton, Y. Zhang, J. Luo, A. K.-Y. Jen, *J. Am. Chem. Soc.*, **2009**, *131*, 13886.
- [130] H. Y. Chen, J. Hou, A. E. Hayden, H. Yang, K. N. Houk, Y. Yang, *Adv. Mater.*, **2010**, *22*, 371.

- [131] C. Duan, A. Furlan, J. J. van Franeker, R. E. M. Willems, M. M. Wienk, R. A. J. Janssen, *Adv. Mater.*, **2015**, *27*, 4461.
- [132] T. Y. Chu, J. Lu, S. Beaupre, Y. Zhang, J.-R. Pouliot, S. Wakim, J. Zhou, M. Leclerc, Z. Li, J. Ding, Y. Tao, *J. Am. Chem. Soc.*, **2011**, *133*, 4250.
- [133] Y. J. He, H. Y. Chen, J. H. Hou, Y. F. Li, *J. Am. Chem. Soc.*, **2010**, *132*, 1377.
- [134] G. J. Zhao, Y. J. He, Y. F. Li, *Adv. Mater.*, **2010**, *22*, 4355.
- [135] A. L. Roes, E. A. Alsema, K. Blok, M. K. Patel, *Prog. Photovolt: Res. Appl.*, **2009**, *17*, 372.
- [136] T. Ameri, N. Li, C. J. Brabec, *Energy Environ. Sci.*, **2013**, *6*, 2390.
- [137] J. You, C.-C. Chen, Z. Hong, K. Yoshimura, K. Ohya, R. Xu, S. Ye, J. Gao, G. Li, Y. Yang, *Adv. Mater.*, **2013**, *25*, 3973.
- [138] C.-C. Chen, W.-H. Chang, K. Yoshimura, K. Ohya, J. You, J. Gao, Z. Hong, Y. Yang, *Adv. Mater.*, **2014**, *26*, 5670.
- [139] X. Gong, M. Tong, Y. Xia, W. Cai, J. S. Moon, Y. Cao, G. Yu, C.-L. Shieh, B. Nilsson, A. J. Heeger, *Science*, **2009**, *325*, 1665.
- [140] K. S. Nalwa, Y. Cai, A. L. Thoeming, J. Shinar, R. Shinar, S. Chaudhary, *Adv. Mater.*, **2010**, *22*, 4157.
- [141] P. E. Keivanidis, S.-H. Khong, P. K. H. Ho, N. C. Greenham, R. H. Friend, *Appl. Phys. Lett.*, **2009**, *94*, 173303.
- [142] J. B. Wang, W. L. Li, B. Chu, C. S. Lee, Z. S. Su, G. Zhang, S. H. Wu, F. Yan, *Org. Electron.*, **2011**, *12*, 34.
- [143] J. Qi, X. Zhou, D. Yang, W. Qiao, D. Ma, Z. Y. Wang, *Adv. Func. Mater.*, **2014**, *24*, 7605.

- [144] X. Hu, Y. Dong, F. Huang, X. Gong, Y. Cao, *J. Phys. Chem. C*, **2013**, *117*, 6537.
- [145] Y. Yao, Y. Liang, V. Shrotriya, S. Xiao, L. Yu, Y. Yang, *Adv. Mater.*, **2007**, *19*, 3979.
- [146] G. Qian, J. Qi, J. A. Davey, J. S. Wright, Z. Y. Wang, *Chem. Mater.*, **2012**, *24*, 2364.
- [147] K. Bange, T. Gamble, *Adv. Mater.*, **1990**, *2*, 10.
- [148] D. R. Rosseinsky, R. J. Mortimer, *Adv. Mater.*, **2001**, *13*, 783.
- [149] D. Li, G. Qian, Z. Y. Wang, *Syn. Metals*, **2014**, *189*, 26.

Chapter 2 Design, Synthesis, Characterization of Soluble-to-Insoluble Diketopyrrolopyrrole based Polymers and Their Use in Multilayer Devices

2.1 Introduction

Most conjugated polymers that have been explored for device applications are ideally made by solution process. They are feasibly prepared for large-area fabrication of thin films and tailor designed to have the desired properties such as bandgap, and charge transport [1,2]. Conjugated polymers are widely used as active materials in polymer light-emitting diodes (LEDs), thin film transistors (TFTs), field-effect transistors (FETs), solar cells, photodetectors, and radio-frequency identification RFID tags [3-9].

Over the years, device development becomes more focused on multilayer architectures and tandem cells due to advantages of a greater range of light harvest, better controlled charge separation/recombination and overall higher efficiency [10]. A typical device with a diode structure comprises of the active layer, electron-transporting layer (ETL) and hole-transporting layer (HTL) between the anode and cathode. (Fig. 2.1) [11].

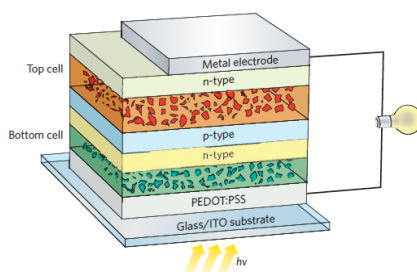


Figure 2.1: Tandem cell configuration (Adapted with permission from Ref. 10)

In a tandem device, the two or more active layers are used and separated by the interlayers. For device fabrication, each layer of polymer thin film is routinely spin coated or cast from the polymer solution in common organic solvents such as chloroform, tetrahydrofuran (THF), toluene, chlorobenzene and N,N-dimethylformamide (DMF) [12,13]. How to process the top layer of polymer film in a multilayer device without dissolving or disturbing the polymer layer below becomes a practical issue. A common method to address this issue is to select solvent pair that selectively dissolves one of the two polymers. For example, an organo-soluble emissive polymer was spin coated on the PEDOT:PSS layer and a water-soluble ETL was then coated on the top of the emissive layer [14]. Another method involves layer-by-layer assembly, which relies on electrostatic interaction between poly-anion and poly-cation on charged surface [15,16]. A more general method involves the crosslinking treatment, in which the first layer of polymer film is thermally, chemically or photochemically crosslinked to become solvent-resistant and then the second layer of polymer film is coated [17-20].

Diketopyrrolopyrrole (DPP) is electron deficient and widely used as the electron acceptor unit in the donor-acceptor polymers. Its planer conjugated bicyclic structure allows for a strong π - π interaction. Furthermore, by using a spacer such as thiophene, steric repulsion can be diminished, which leads to backbone coplanarity and good charge transport properties. Due to these characteristics, DPP-containing polymers have been explored for use in solar cells, OFET and other electronic devices [21,22]. Typically, the DPP moiety can be functionalized due to different reactive sites

and is usually subjected to N or O-substituted alkyl chain in order to impart the solubility, thus enabling a solution-based processing (Fig. 2.2) [23].

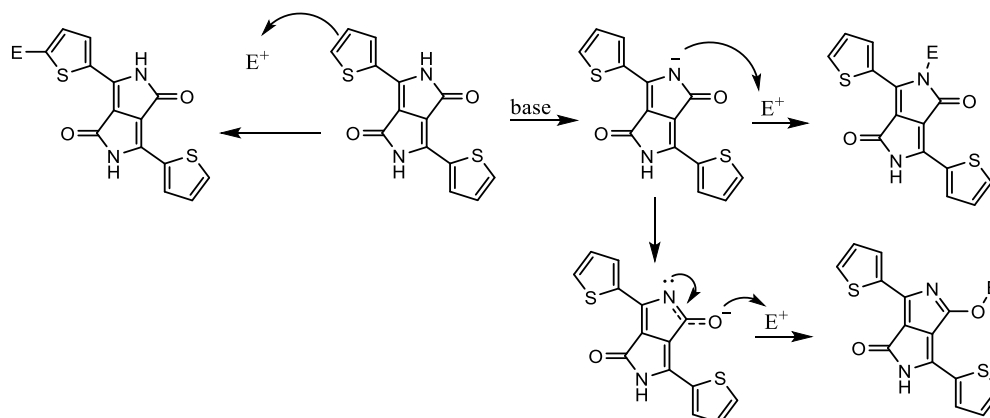


Figure 2.2: Functionalization of DPP

In this work, we intend to explore a simple way to change the polymer solubility and demonstrate the use of soluble-to-insoluble polymers in solution-based process for fabrication of multilayer polymer films. It is known that the *N-tert*-butyloxycarbonyl (BOC) protecting group for amine or alcohol can be thermally cleaved at approximately 180 °C [24]. Therefore, the N-substitution of BOC group on the DPP moiety should ensure a good solubility of polymers. Removal of the BOC group would result in a decrease in solubility since the resulting unsubstituted lactam units enable stronger interchain interaction through the hydrogen-bond network [24]. The electron-withdrawing effect of the lactam unit supplies a strong electron affinity and interconnected hydrogen bonding between the lactam units favors the molecule into a physically cross-linked structure in the solid state (Fig. 2.3). This in turn leads to shorter distance between the molecule planes resulting in stronger π - π molecular orbital interaction and exciton coupling effects [25]. Accordingly, we have synthesized and

studied a series of the BOC-substituted DPP-containing polymers with different donor units.

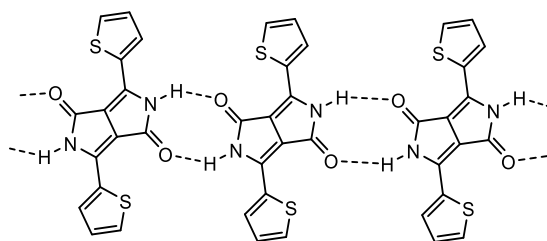
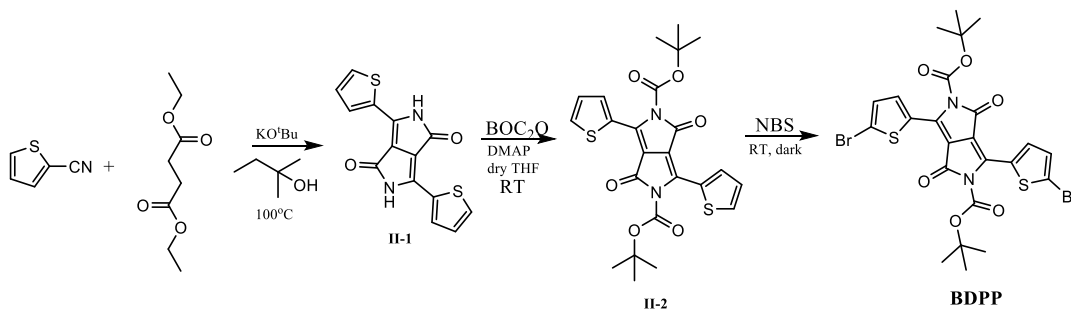


Figure 2.3: Hydrogen bonds between the DPP units in the solid state

2.2 Results and discussions

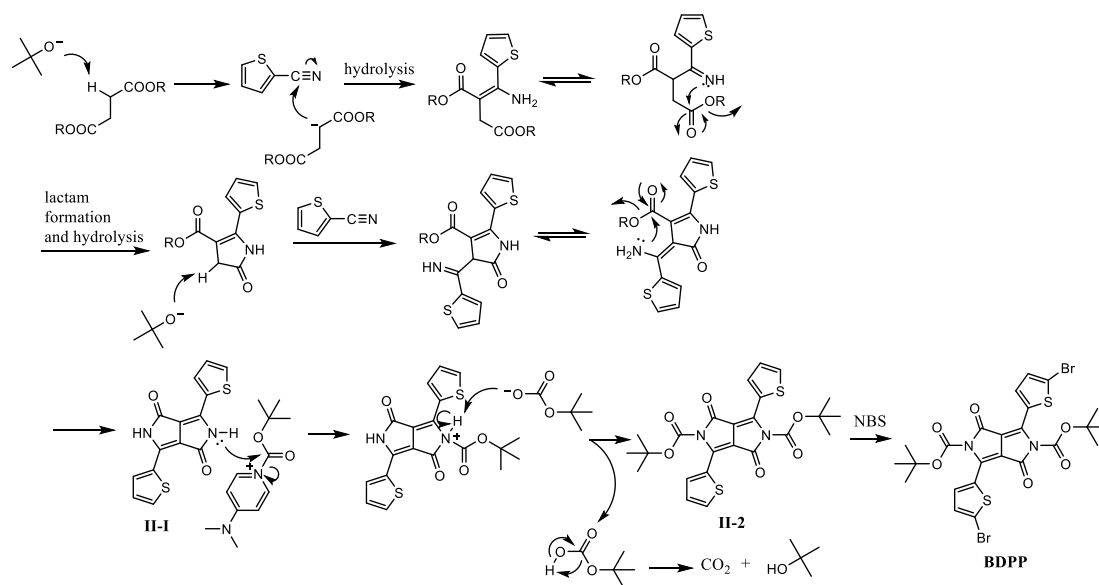
2.2.1 Synthesis of acceptor monomer



Scheme 2.1: Synthesis of **BDPP**

The synthetic route towards **BDPP** is shown on Scheme 2.1. In a one-pot reaction with 2-thiophenecarbonitrile and diethyl succinate under basic condition gives a red solid, **II-1**, at a high yield. Protection of the γ -lactam nitrogen can be accomplished in dry THF using di-*tert*-butyl dicarbonate (BOC_2O) with small amount of *N,N*-dimethylpyridin-4-amine (DMAP) acting as a catalyst. The subsequent carbamate product, **II-2**, is readily soluble in common organic solvents due to the polar BOC group, whereas the DPP compound was only soluble in DMF or DMSO. Bromination of **II-2** was done using NBS to give the **BDPP** monomer and serves as a

key building block for the construction of the polymer series [26]. The mechanism of **BDPP** is shown on Scheme 2.2.



Scheme 2.2: Mechanisms of reactions involved in the synthesis of **BDPP**

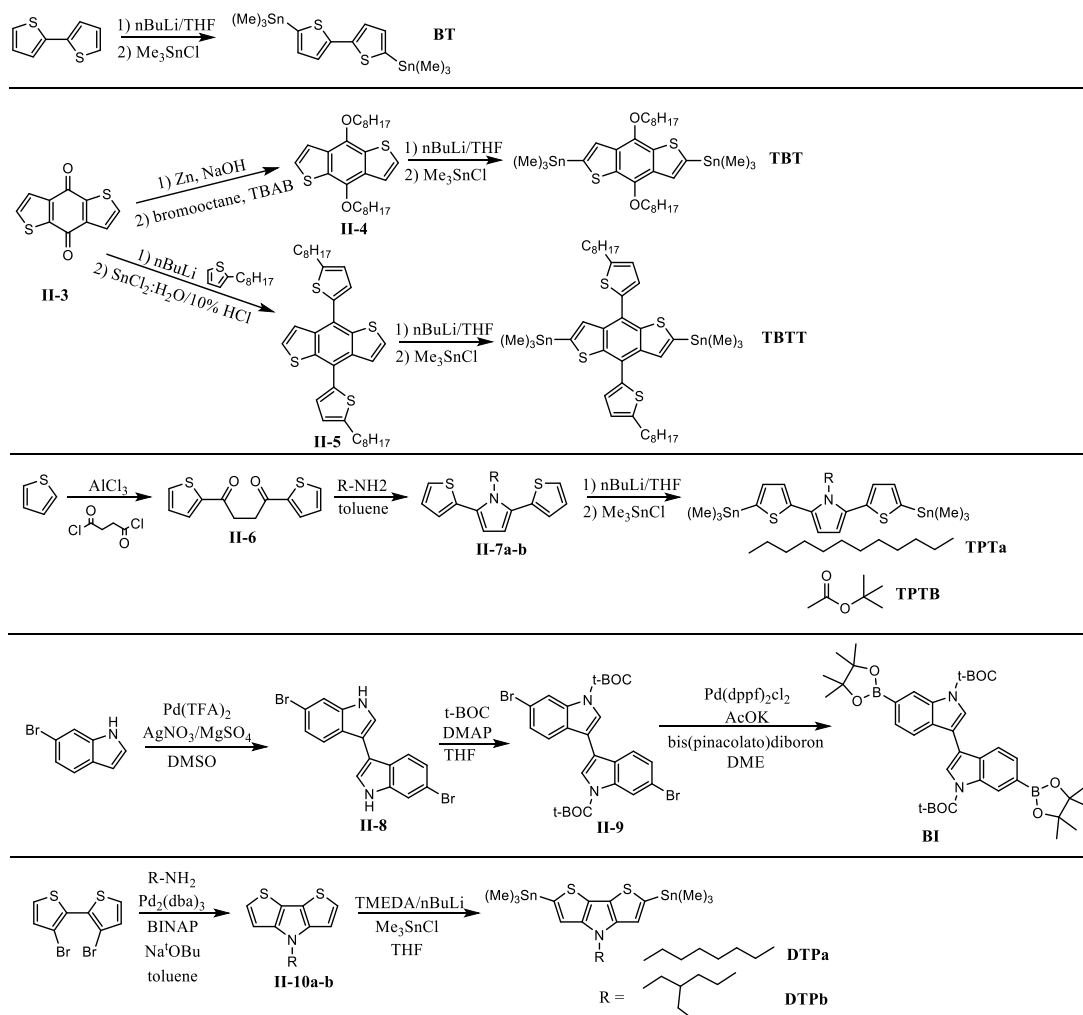
In the presence of a strong base, the α -proton on the succinate is removed to generate the resonance stabilized enolate which acts as nucleophile attacking the electron rich carbonitrile to form a secondary aldimine. The Schiff base then attacks the ester carbonyl to form iminium ion which is then hydrolyzed to form the γ -lactam. The α -proton from the subsequent lactam is removed by the base followed by nucleophilic attack on a second carbonitrile species to form the aldimine compound which then results in the formation of the second lactam and cyclization. In the protection of the lactam, DMAP attacks the carbonyl site on BOC_2O resulting in a carbamate pyridinium species. The DPP nitrogen then attacks the carbonyl of the pyridinium ion regenerating the DMAP. A free tert-butyl carbonate picks up a proton

from the protonated DPP amine which then decomposes to carbon dioxide and t-butyl alcohol.

2.2.2 Synthesis of donor monomers

Syntheses of different donor monomers containing the units: 2,2'-bithiophene, benzo[1,2-*b*:4,5-*b'*]dithiophene, 2,5-di(thiophen-2-yl)-pyrrole, 3,3'-biindole, 4,8-di(thiophen-2-yl)benzo[1,2-*b*:4,5-*b'*]dithiophene and dithieno[3,2-*b*:2',3'-*d*]pyrrole are shown on Scheme 2.3. 2,2-Bithiophene is commercially available and the subsequent organotin, **BT**, was synthesized using n-butyllithium to form the dilithinated intermediate and then transmetalation occurs with the presence of organotin chloride. Synthesis of **TBT** and **TBTT** is done in two different routes starting from compound **II-3**, in the first route, reduction of the ketone was done using zinc powder and then O-alkylation occurs using alkyl halide to afford **II-4**. In the second route, tin chloride was used to reduce the quinone in a condensation reaction [27]. **TPT** donors were derived from Friedel-Crafts acylation of thiophene and then condensation with alkyl amine or ammonium acetate results in **II-7a/b** [28-30]. Finally, following the previous the method for the formation of the organotin compound affords the donors **TBT**, **TBTT** and **TPTa/B**. The 3,3-biindole, **II-8**, was synthesized by Pd-catalyzed direct C-H dimerization and using the Miyarura borylation reaction the subsequent boron ester compound, **BI**, was made [31]. Indole analogues are well known heteroaromatic compounds and have the π -conjugated planar structure. In a recent report, the use of biindole in dye-sensitized solar cells has achieved a power conversion efficiency of

6.54% [32]. Monomer **DTP** was synthesized via Buchwald-Hartwig amination followed by formation of the organotin [33-34].

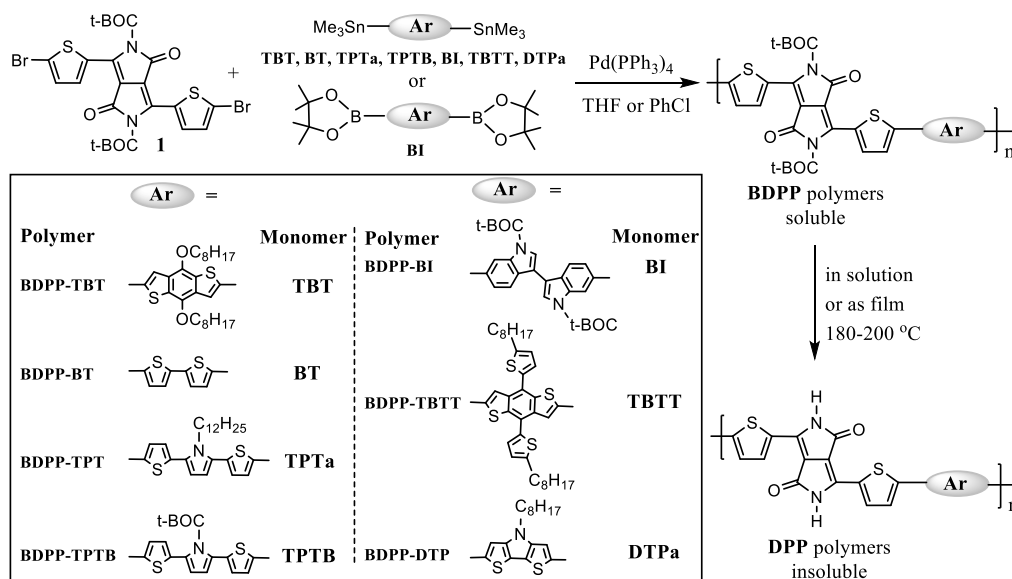


Scheme 2.3: Synthesis of donor monomers **BT**, **TBT**, **TBTT**, **TPTa**, **TPTB**, **BI**, **DTPa-b**.

2.2.3 Synthesis of D-A polymers

Polymers **BDPP-TBT**, **BDPP-BT**, **BDPP-TPTa**, **BDPP-TPTB** and **BDPP-DTP** were synthesized by the Stille cross-coupling reaction under inert atmosphere

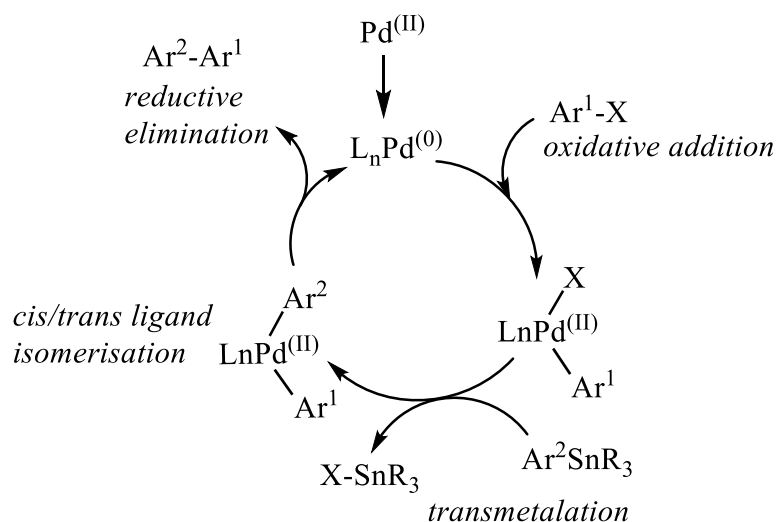
using palladium catalyst and **BDPP-BI** was synthesized via the Suzuki cross-coupling reaction (Scheme 2.4).



Scheme 2.4: Synthesis of soluble BDPP-based polymers and conversion to insoluble DPP-based polymers

Palladium-catalyzed cross-coupling reaction, which includes Suzuki cross-coupling and Stille cross-coupling, is among the most powerful and versatile synthetic methods for carbon-carbon bond formation. The reactions have a broad scope and tolerant to wide range of functionality. The catalytic cycle for the cross-coupling reaction of organometallics contains five main sequences: activation, oxidative addition, transmetalation, cis/trans ligand isomerization and reductive elimination (Scheme 2.5). In the first step of the cycle, Pd(II) is reduced to the activated Pd(0) complex followed by oxidative addition of Ar¹-halide compound to afford a stable trans-σ-palladium (II) complex and is often the rate-determining step in a catalytic cycle. It is called oxidative addition because the oxidation state of the transition metal changes from 0 to II in the

process. The palladium (II) intermediate then undergoes transmetalation. The nucleophile (Ar^2) is transferred from the organometallic reagent to the palladium (II) complex, this is followed by *cis-trans* isomerization where the *trans*-adduct isomerizes to the *cis* intermediate. The steric hindrance of the isomerization forces a reductive elimination to give the product ($\text{Ar}^1\text{-Ar}^2$) and the palladium (0) catalyst is regenerated for another cycle.



Scheme 2.5: General catalytic cycle of palladium-catalyzed cross-coupling

Due to the nature of Lewis acid of the organo-tin bromide by-product and increased temperature in the coupling reaction, partial cleavage of the BOC groups during the polymerization can occur. Thus, it is necessary to reintroduce the BOC group after polymerization in each repeat unit to ensure good solubility of the polymers in common organic solvents such as chloroform, THF and chlorobenzene. The coupling reactions worked relatively well with polymer **BDPP-TBT** having the highest yield of 77% (Table 2.1). The polymers were purified by Soxhlet extraction to remove any starting materials and also low molecular weight oligomers. Molecular weights and

polydispersity indices (PDI) of the polymers were determined by gel permeation chromatography (GPC) relative to polystyrene standards (Table 2.1). **BDPP-BT** has a higher molecular weight of 475.4 kg/mol with a PDI of 2.05. **BDPP-TBT**, **TPTb** and **BI** have molecular weight of 103.6 kg/mol, 100.0 kg/mol and 90.5 kg/mol, respectively. Comparing to these four polymers, **BDPP-TPTa** and **TBTT** has the lowest molecular weight of 3.1 kg/mol and 4.83 kg/mol, respectively. **BDPP-DTPa** was not measured due to solubility issues.

Table 2.1: Yields, molecular weights and PDI of BDPP polymers.

Reaction	Stille cross-coupling					Suzuki cross-coupling	
	BT	TBT	TPTa	TPTB	TBTT	DTPa	BI
BDPP- polymers							
Yield (%)	69	77	67	47	62	54	41
Mw (kg/mol)	475.4	103.6	3.1	100.0	4.83	-	90.5
PDI	2.05	2.08	1.36	2.24	1.44	-	3.4

2.2.4 Characterization

2.2.4.1 Cleavage of the BOC group

The BOC group can be readily cleaved by either thermolysis or by strong acid [35]. Considering the fabrication of multilayer films in device, thermolysis is a preferred method over the acid hydrolysis as the latter requires extra workup to remove the acid and may cause contamination or damage to the device. Experimentally, thermolysis can be done using spin-coated polymer film on glass substrate and free-standing film or by heating the polymer in a high-boiling solvent. Thus, BDDP-based polymers in 1,2,4-trichlorobenzene (TCB) were subjected to heating at approximately

180 °C for 10 minutes and the resulting DPP-based polymers precipitated out of the reaction solution (Scheme 2.4). Furthermore, removal of the BOC group of these polymers as thin films coated on glass or ITO electrode can be effectively done by direct heating. The thermally treated films maintain the film integrity and become highly resistant to most organic solvents at ambient temperatures, which is suitable for subsequent solution-coating of another layer of polymer film.

Infrared spectroscopic study further confirms a facile conversion of BDPP- to DPP- based compounds (Fig. 2.4, Appendix B). Upon heating of BDPP powders in KBr pellet at 180 °C for 1 min, there was an increase of broadness at around 3000 cm^{-1} and loss of 1745 cm^{-1} (red line) suggesting the loss of the BOC group and the presence of lactam (N-H). Furthermore, we observe a shift of the carbonyl peak from 1650 to 1600 cm^{-1} . An interesting note, we see an intensity increase at 2330 cm^{-1} (blue line) is due to CO_2 as a by-product from removal of the BOC group that was trapped in the KBr pellet. Similar trend was observed for the BDPP- and DPP-based polymers (Appendix B).

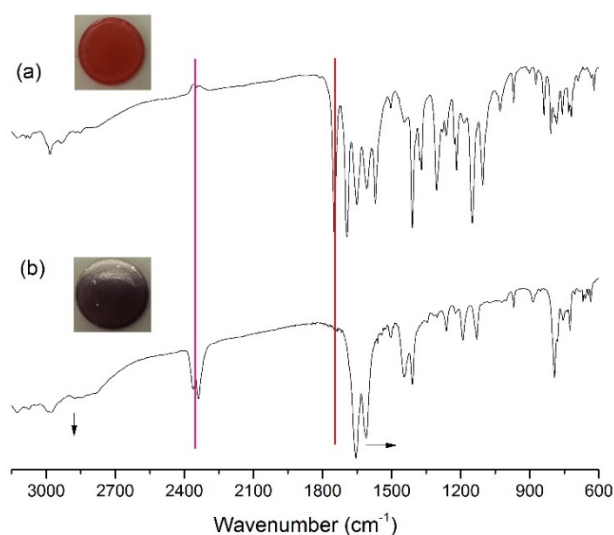


Figure 2.4: Infrared spectroscopy of (a) BDPP and (b) DPP units

Due to poor solubility, the chemical structures of DPP-based polymers were only confirmed with the most soluble polymer **DPP-TBTT** (Fig. 2.5). Proton NMR was done in tetrachloroethane- D_2 (TCE) to confirm the change between BDPP and DPP polymer. The BDPP show good solubility in TCE, where the peaks ranging from 0.25 to 2.3 ppm corresponds to the aliphatic chain and the aromatic protons ranging from 6.3 to 7.5 ppm. The BOC group is found overlapping with the alkyl chain at 0.67 ppm. After the BOC group was cleaved, the solubility decreased drastically, however the presence of the alkyl group is still evident, along with the aromatic protons and increased sharpness at 0.67 ppm.

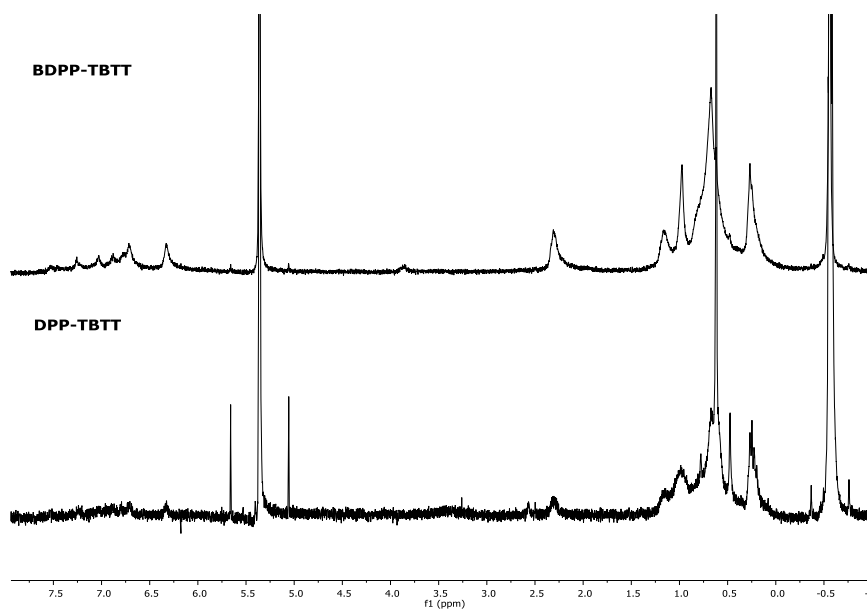


Figure 2.5. 1H NMR (300 MHz) of **BDPP-TBTT** (top) and **DPP-TBTT** (bottom) in tetrachloroethane- D_2

The solubility of BDPP- and DPP-based polymers was tested in chloroform (Table 2.2). **BDPP-TPTa**, **BDPP-TPTB** and **BDPP-TBTT** showed the best solubility due to the long alkyl chain and rotational flexibility on the TPT and TBTT moiety.

Polymers **BDPP-BT**, **BDPP-TBT** and **BDPP-DTPa** are less soluble due to chain rigidity. Conversely, polymer **BDPP-BI** is partially soluble in chloroform. Solubility of polymer **BDPP-DTPa** is much lower than the other polymers due to the large conjugated backbone giving the molecule a highly planar structure and an ability to pack well, which prevents it from being readily dissolved in solvents. Furthermore, the lack of branched aliphatic side chains causes a low solubility. In comparison, the solubility of DPP polymers decreased dramatically and only **DPP-TBT** had the highest solubility of 4.6 mg/mL in chloroform among all.

Table 2.2. Solubility in chloroform (mg/mL) of BDPP- and DPP-based polymers at ambient temperature.

Donor Unit	BT	TBT	TPTA	TPTB	BI	TBTT	DTPA
BDPP series	9.2	10	23	8.6	7.0	25	4.0
DPP series	0.4	1.0	2.2	0.6	0.8	4.6	<0.1

2.2.4.2 Thermal stability

Since thermal stability of polymers is an important factor for potential applications, it is often determined by thermogravimetric analysis (TGA). TGA measures the changes in the weight loss of a sample as a function of temperature and time. Fig 2.6 and Appendix C shows the decomposition characteristics and the data is summarized in Table 2.3. All the polymers have two stages of decomposition. First, a sharp drop starting at 160 °C to 180 °C, which signifies the loss of the BOC group. For polymers **BDPP-TBT** and **-TPT** there is a 15% weight loss. Whereas, **BDPP-BT** show a 20% weight loss, due to BOC group having more significant weight to the polymer. The second stage is the true decomposition temperature (T_d) with a loss of 5% weight

mass.

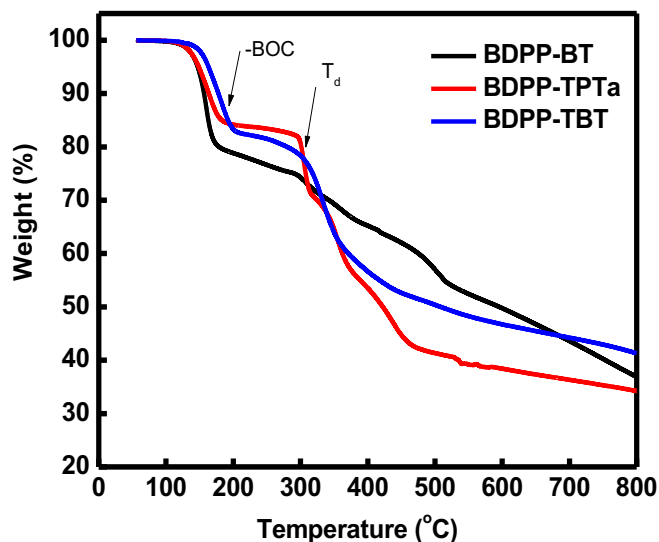


Figure 2.6: TGA of **BDPP-BT**, **BDPP-TPT** and **BDPP-TBT**

All the polymers have the T_d above 250 °C, thus suitable for device fabrication. During different stages of fabrication, the devices need to be annealed to a certain temperature to remove solvent and improve morphology. Researchers usually choose temperature above the glass transition temperature (T_g), a reversible transition in amorphous material to glassy or rubber-like state. This allows the polymer chain to rotate to a more favorable conformation which in turn optimizes the morphology of device and performance. Since the polymers need to be heated at 180 °C, it serves the purpose of cleaving the BOC group and optimization of the film.

Table 2.3: Thermal stability of BDPP-based polymers

Donor unit	BT	TBT	TPTA	TPTB	BI	TBTT	DTPA
Decomposition temperature (t_d , °C)	292	308	301	225	325	274	263

2.2.4.3 Absorptions of BDPP and DPP Polymers

The UV-vis absorption spectra were taken at room temperature before and after thermolysis. All of the polymers show several absorption bands at the short and long wavelength (Table 2.4, Fig. 2.7). By adopting donor-acceptor polymerization the λ_{\max} ranging from 500 to 700 nm, with different intensity, is attributed to the intramolecular charge transfer (ICT) between DPP unit and donor segment. The absorption at lower wavelength is due to π - π^* transition band. In comparison with **BDPP-BI** and **BDPP-BT** whose maximal absorptions (λ_{\max} , film) at 585 and 596 nm respectively, polymers **BDPP-TBT**, **BDPP-TPTa**, **BDPP-TPTB**, **BDPP-TBTT** and **BDPP-DTP** show more red-shift, with λ_{\max} at 666, 660, 630, 620 and 660 nm, respectively. This can be accounted by the better conjugation system and planarity of the donor group. We see a slight blue-shift for most polymers when the BOC is cleaved both in solution and more evident on film. All the polymers except for **DPP-BI** and **DPP-TBTT** (on film) showed blue-shift ranging from 10-70 nm. The blue-shift can be caused by the formation of less ordered amorphous packing, where the backbone of the polymer is twisted, however still retaining the hydrogen bonding. Furthermore, with the removal of the electron-withdrawing BOC may lead to a raised LUMO level, hence the increased optical band gap. Polymer **DPP-BI** showed a red shift approximately of 25 nm, whereas **DPP-TBTT** showed only a red shift of 5 nm. This could be due to improved coplanarity of the polymer backbone and chain packing order.

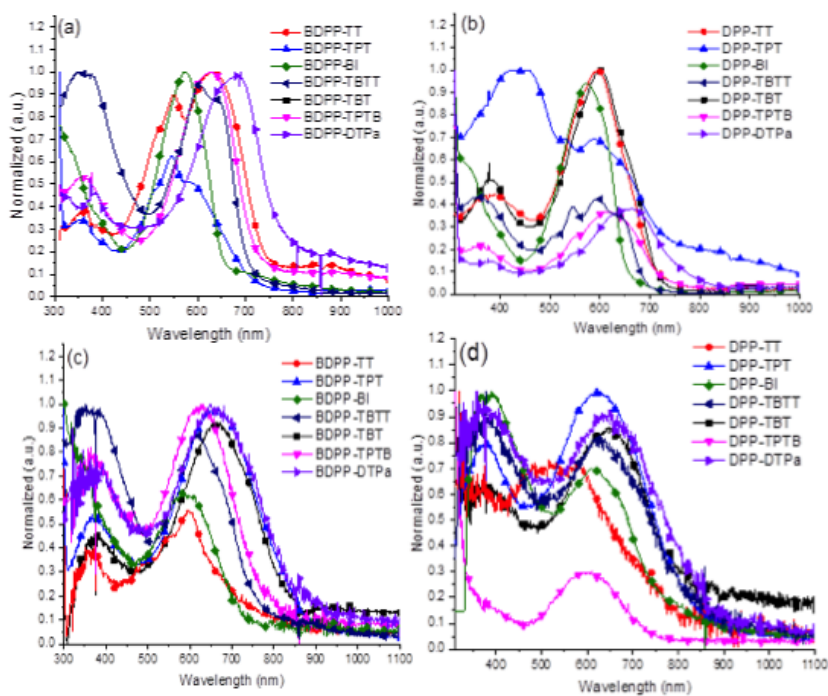


Figure 2.7: Absorption spectra of polymers in 1,2,4-trichlorobenzene (a) at room temperature, (b) after heating at 180 °C, (c) film at room temperature (d) film after heating at 180 °C

Table 2.4: Absorption of BDPP and DPP polymers

Polymer	$\lambda_{\text{abs}}(\text{nm})^{\text{a}}$ solution		$\lambda_{\text{abs}}(\text{nm})^{\text{b}}$ film	
Donor Unit	BDPP series	DPP series	BDPP series	DPP series
TBT	590	600	666	650
BT	631	600	596	525
TPTa	543	592	660	620
TPTB	625	617	630	600
BI	570	575	585	611
TBTT	603	597	620	625
DTP	681	666	660	650

^{a)} In 1,2,4-trichlorobenzene; ^{b)} Spin-coated on glass

2.2.4.4 Solvatochromism and Halochromism

Due to the presence of hydrogen bonding on the lactam moiety, the DPP-based polymers may exhibit solvatochromism and halochromism (Fig. 2.8). Therefore, polymers **DPP-BI** and **DPP-TPTB** were subjected to spectroscopic studies in different solvents and the presence of acid or base. A hypsochromic shift was observed when using a polar solvent (i.e., propylene carbonate) and there was a bathochromic shift when using a less polar TCB or CHCl_3 . In more polar solvents intermolecular hydrogen bonding is more predominate, conversely, in less polar solvents intramolecular hydrogen bonding is dominate. Furthermore, when the polymers are in an acidic medium, such as camphorsulfonic acid (CSA) in TCB, there is a large broadening and slight redshift of the peak. This is due to the protonation of the lactam and the donor unit. Protonation of the acceptor would increase the electron withdrawing ability and causes a red shift, however protonation on the donor, would cause a blue shift [36]. Furthermore, when using triethylamine (TEA) we also see broadening in the peak. This suggest that when the DPP is deprotonated, the negative charge is resonance stabilized on the oxygen atom and may form ionic interaction with protonated trimethylamine. This in turn would weaken electronic coupling between the oxygen atom and azo ring [37]. With the low pKa value, deprotonation of the DPP polymer would provide a feasible method to cross-linking.

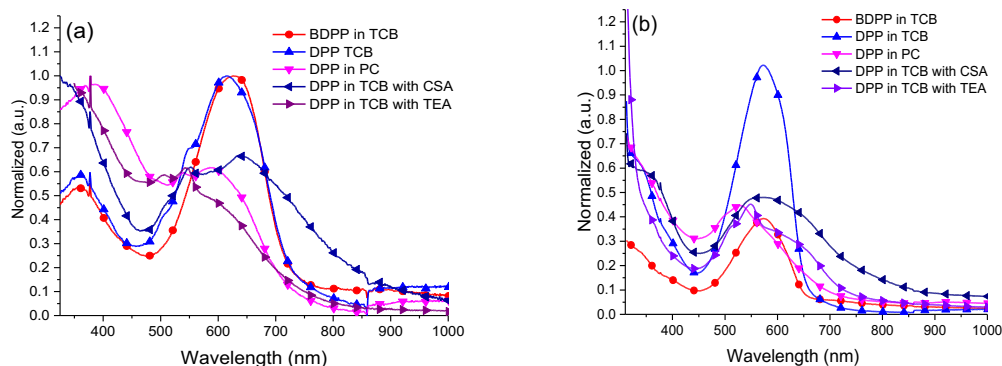


Figure 2.8: Absorption spectra of (a) DPP-TPTB and (b) DPP-BI in different solvents and reagents. TCB: 1,2,4-trichlorobenzene, PC: propylene carbonate, CSA: camphorsulfonic acid, TEA: triethylamine

2.2.4.5 Electrochemical Property

The redox potentials of the BDPP-based polymers were determined by cyclic voltammetry. The results show that all the polymers are electrochemically active (Fig. 2.9 and Table 2.5). The HOMO and LUMO levels were calculated from its oxidation and reduction potential, although, the reduction potentials were not apparent for most polymers, except for **BDPP-TBT** and **BDPP-TPTB**, it can be calculated from the optical energy gap. The polymers as thin films show an optical energy band gap ranging from 1.30 to 1.60 eV. The DPP series also shows similar trend as the BDPP series, where the reduction potential is not apparent. Comparing the BDPP and DPP series, all the polymers, except BI and TBTT, shows higher optical band gap ranging from 1.33 to 1.60 eV. TBTT has a larger planar conjugated structure and thus can form π - π stacking much easier, thus decreasing the band gap [38].

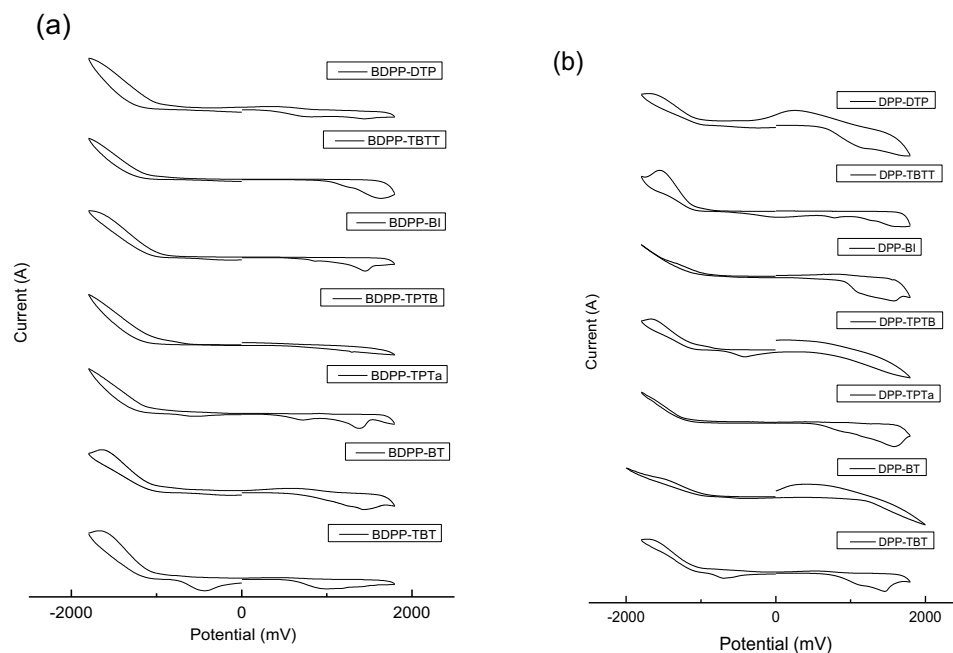


Figure 2.9: CV of polymers on ITO in 0.1 M Bu₄NPF₆ in acetonitrile at scan rate of 100 mV/s (a) with BOC (b) without BOC

Table 2.5: Electrochemical properties of BDPP and DPP polymers

Polymer	HOMO (eV)	LUMO (eV)	E _g (eV)	HOMO (eV) ^a	LUMO (eV) ^a	E _g (eV) ^a	E _g (opt., eV) ^b film	E _g (opt., eV) ^b film
Donor Unit	BDPP series	BDPP series	BDPP series	DPP series	DPP series	DPP series	BDPP series	DPP series
TBT	-4.98	-3.62	1.36	-5.46	-4.00	1.46	1.43	1.49
BT	-5.36	-3.96 ^c	-	-4.57 ^c	-3.05	-	1.40	1.50
TPTa	-4.87	-3.57 ^c	-	-5.10	-3.76 ^c	-	1.30	1.34
TPTB	-5.18 ^e	-3.70	-	-5.17 ^c	-3.56	-	1.48	1.60
BI	-5.04	-3.44 ^c	-	-5.35	-3.96 ^c	-	1.60	1.39
TBTT	-5.47	-4.02 ^c	-	-4.01	-2.78	1.23	1.45	1.37
DTP	-4.87	-3.55 ^c	-	-5.42	-4.09 ^c	-	1.32	1.33

^a) For thin films, calculated from $E(\text{HOMO}) = -(E_{\text{ox}} + 4.34)$ (eV) $E(\text{LUMO}) = -(E_{\text{red}} + 4.34)$ (eV). The energy gap (E_g) is derived from the HOMO subtracting the LUMO. ^b) Optical energy gap calculated from the absorption onset. $E_g = 1240/\lambda$ (onset, nm) ^c) Calculated from optical band gap.

2.2.5 Preparation and characterization of multilayer films

Due to the soluble-to-insoluble modification of the acceptor unit, these polymers are ideal for making solution-processable multilayer films for use in organic electronic devices. Fabrication of a multilayer films were made using polymer **DPP-BI** as the bottom layer and **PDPP-F** (λ_{max} at 522 nm) as the top layer (Fig. 2.11). The top layer is used for two reason, first, as a higher band gap polymer to absorb lower wavelength and second to fill any cracks and holes produced at the bottom layer when the film is heated at 200 °C. The film was prepared using 1:3 ratio blend of polymer to PCBM onto a pre-cleaned glass at 1500 rpm. The films were heated at 180 °C for 10 min to remove any residual solvent and cleave the BOC group and thus rendering the polymer layer insoluble and undisturbed. The films were then analyzed via UV-Visible spectroscopy, showing the presence of the polymer and polymer blend at λ_{max} of 600 and 482 nm, respectively. The UV shows no change in absorbance nor any shift, thus overlapping the BOC polymer at room temperature and after cleavage. The top layer, **PDPP-F**, was spin-coated at 1500 rpm for 60 seconds. What was observed is that the 1:1 ratio blend film did not retain as much PCBM, possibly due to the solvent washing it away. However, when increasing the PCBM ratio to 3:1, we see some retention. The results were similar when doing both static and dynamic dispersive spin coating. AFM was done to further demonstrate the capability of multilayer formation. AFM study shows a very smooth surface of PCBM and **DPP-BI** polymer blend with an average roughness of 0.5 nm (Fig. 2.10). After **PDPP-F** was spin-coated, the average surface roughness increased to 15 nm. To demonstrate the difference of surface smoothness and to show the contrast between the two layers, Teflon tape was used to cover portion

of **DPP-BI** polymer film and the top layer was added via dynamic dispersive spin coating.

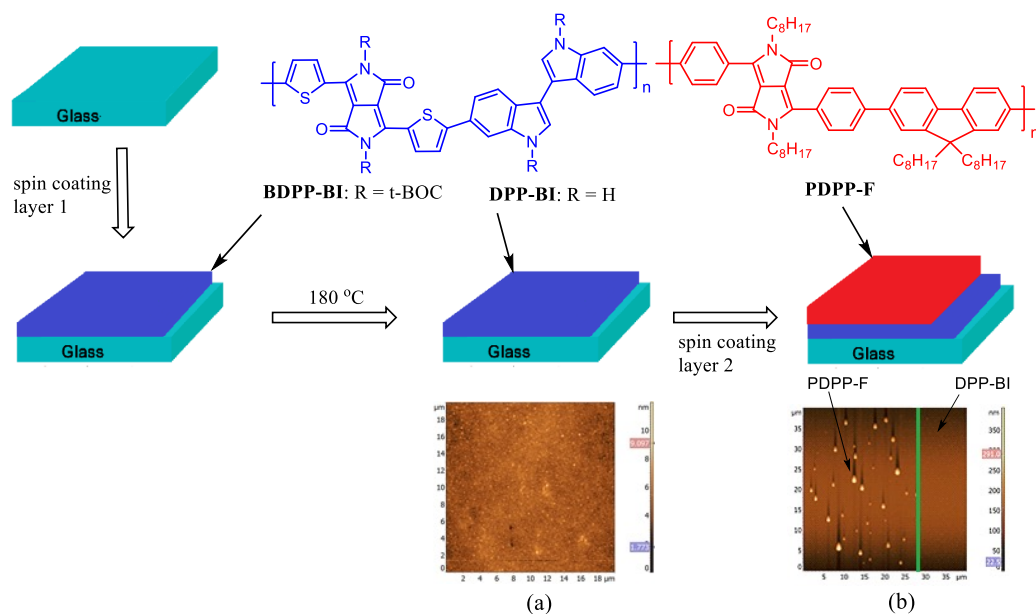


Figure 2.10: Multilayer film fabrication (a) AFM of **DPP-BI** (roughness ~ 0.5 nm) (b) AFM of **PDPP-F** spin coated on top of partially covered **DPP-BI** layer. Left shows droplet like **PDPP-F** (roughness ~ 15 nm) and right showing bottom layer of **DPP-BI**.

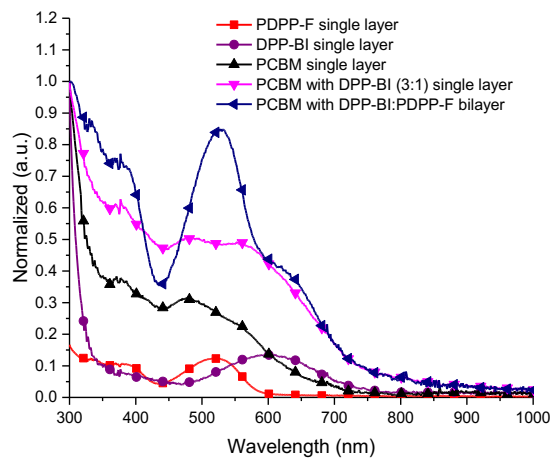


Figure 2.11: Absorption of the films of **DPP-BI** (~ 60 nm), **PDPP-F** (~ 75 nm) and bilayer **DPP-BI** (bottom layer) with **PDPP-F** (top layer).

2.2.5.1 Organic field effect measurements

OFET transistor uses an electric field to control electrical conductivity in a organic semiconductor material. OFET operates as a capacitor and it is commonly used for weak-signal amplification. In OFET, there are three essential components, the source, the drain and the gate. The current flows along the semiconductor path which is called the channel. Between the semiconductor material there are two electrodes, at one end there is the source and at the other end it is the drain. The direction of the charge carrier in the channel is from the source to the drain. The gate works to control the charge induced into the channel (Fig 2.12). A dielectric material is an electrical insulator that can be polarized by an applied electric field and it is used to separate the drain and source electrodes from the gate. Most commonly used insulator material is silicon dioxide and gate material as silicon. Metals such as silver, gold, copper and titanium are used as contact materials.

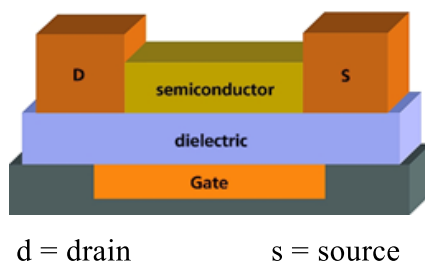


Figure 2.12: Typical configuration of organic field-effect transistor.

In a p-type OFET, a negative voltage greater in magnitude than the threshold voltage of the semiconductor material is applied between the gate and the source, this causes holes (positive carriers) flow from the source to the drain. Conversely, for n-type OFET, a positive voltage is applied causing electron carriers built up along the channel. As the magnitude of the drain-source voltage is increased, the current also

increases until a threshold, “pinch-off”, is reached, where the drain current with saturated at its maximum value [39]. OFET research generally seeks to optimize two important values, the carrier mobility and the on/off current ratio. The carrier mobility is proportional to the semiconducting material. The on/off current ratio is the ratio of the saturation current when V_{GS} (gate-source voltage) is high to the leakage current when V_{GS} is zero. The on/off ratio indicates the ability of the device to shut down. The carrier mobility can be calculated from the following equation in linear mode [40]:

$$\mu_h = \frac{I_{IDS}L}{WC_{OX}V_{DS}[(V_{GS} - V_{TH}) - \frac{V_{DS}}{2}]}$$

I_{IDS} = output current

L = channel length

W = channel width

V_{DS} = drain-source voltage

V_{GS} = gate voltage

V_{TH} = threshold voltage

C_{OX} = insulator capacitance

The interest in OFETs has grown immensely in recent years due to the performances of OFETs competing with amorphous silicon (a-Si) with mobilities of $0.5\text{-}1\text{ cm}^2\text{V}^{-1}\text{s}^{-1}$ and on/off ratio of $10^6\text{-}10^8$. Rubrene holds the distinction of organic material with the highest hole carrier mobility reaching up to $40\text{ cm}^2\text{V}^{-1}\text{s}^{-1}$. This is comparable to that of best poly-silicon devices [41]. DPP-based polymer, **DPP-TT** (Fig. 2.13), achieved record high hole mobility for p-type material of $10.5\text{ cm}^2\text{V}^{-1}\text{s}^{-1}$, with on/off ratio of 10^6 [42]. More recently, a thionoisindigo-naphthalene polymer

(PTIIG-Np) have reached unprecedented mobility of $14.4 \text{ cm}^2\text{V}^{-1}\text{s}^{-1}$ which exceeds benchmark values for amorphous silicon semiconductor [43].

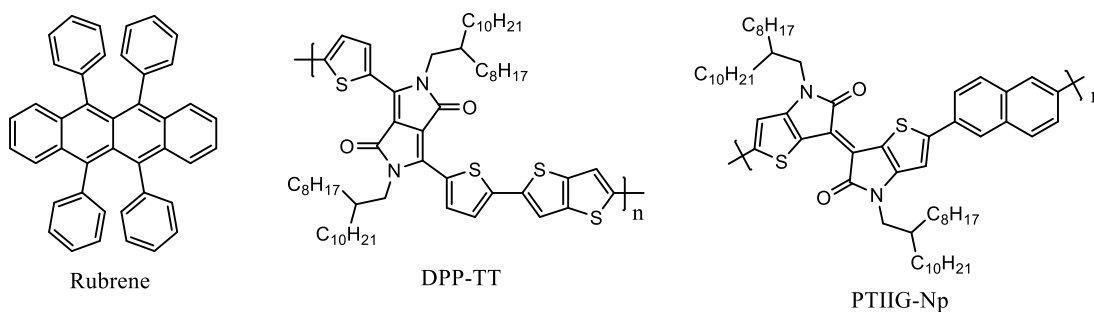


Figure 2.13: Organic semiconducting materials used for OFET

Polymer **BDPP-TPTa/B**, **BDPP-BI** and **BDPP-TBTT** were tested for their transistor performance. However, only **BDPP-TPTa** was characterized. **BDPP-TPTB** and **BDPP-BI** were not able to be coated on the silicon wafer substrate and **BDPP-TBTT** no performance was observed. Several devices were prepared in top-contact bottom-gate configuration (Fig. 2.12) by spin-coating on SiO₂/Si substrate. The films were annealed at 60 °C and 200 °C for 30 minutes under nitrogen protection. The OFET properties of **DPP-TPTa** is summarized on Table 2.6 and 2.7. The V-shape transfer characteristic is observed in hole-enhancement ($V_{DS} = -100 \text{ V}$) (Fig. 2.14). **BDPP-TPTa** exhibited at best performance of $7.4 \times 10^{-5} \text{ cm}^2\text{V}^{-1}\text{s}^{-1}$ and average mobility of $5.9 \times 10^{-5} \text{ cm}^2\text{V}^{-1}\text{s}^{-1}$. Whereas, after annealing at 200 °C, DPP-TPT polymer exhibited slightly higher mobility, with average mobility of $8.9 \times 10^{-5} \text{ cm}^2\text{V}^{-1}\text{s}^{-1}$ and best performance was observed at $1.0 \times 10^{-4} \text{ cm}^2\text{V}^{-1}\text{s}^{-1}$. Despite the poor overall performances in the devices, which might be due to poor crystallinity of the polymer chain, there is an increase of mobility after removing the BOC group. This can be

accounted for more densely packed polymer π -planar backbone after thermal cleavage, facilitating the charge transport of holes.

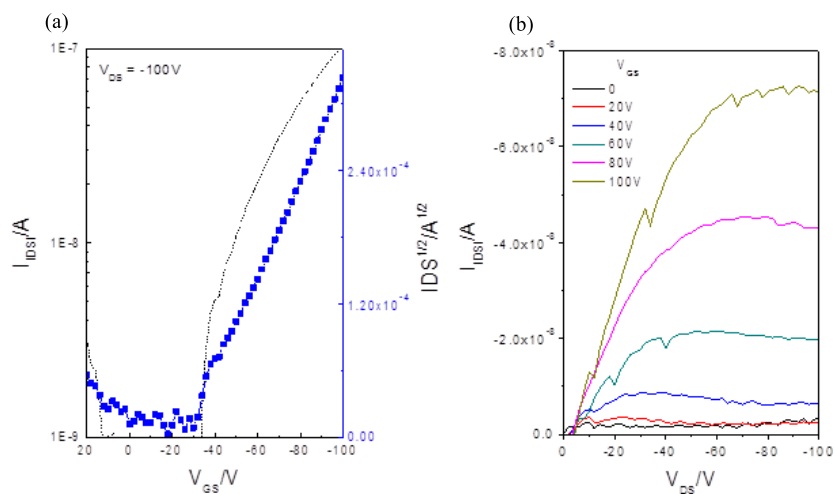


Figure 2.14: Transfer (a) and output (b) characteristics of OFET based on polymer **DPP-TPTa**

Table 2.6: Hole motilities of **BDPP-TPTa**

Device	Annealing after 60 °C			Annealing after 200 °C		
	Hole mobility ($\text{cm}^2\text{V}^{-1}\text{s}^{-1}$)	V_{TH} (V)	V_{DS} (V)	Hole mobility ($\text{cm}^2\text{V}^{-1}\text{s}^{-1}$)	V_{TH} (V)	V_{DS} (V)
1	7.4×10^{-5}	-33.2	-100	9.6×10^{-5}	-25.8	-100
2	6.8×10^{-5}	-35.0	-100	1.0×10^{-4}	-28.0	-100
3	4.5×10^{-5}	-31.7	-100	8.2×10^{-5}	-26.7	-100
4	5.1×10^{-5}	-29.8	-100	8.2×10^{-5}	-27.4	-100
5	5.8×10^{-5}	-37.1	-100	8.3×10^{-5}	-27.2	-100

Table 2.7: Average and best hole mobility of **BDPP-TPTa**

Device	Average mobility ($\text{cm}^2\text{V}^{-1}\text{s}^{-1}$)	Best mobility ($\text{cm}^2\text{V}^{-1}\text{s}^{-1}$)
After annealing at 60 °C	5.9×10^{-5}	7.4×10^{-5}
After annealing at 200 °C	8.9×10^{-5}	1.0×10^{-4}

2.2.5.2 X-ray diffraction analysis

To determine the molecular packing of polymer thin films before and after thermal cleavage, the X-ray diffraction (XRD) analysis was carried out. XRD is a powerful tool to determine crystal structure and molecular packing. Using Bragg's law:

$$n\lambda = 2d\sin\theta$$

where, n is the order, λ is the wavelength of the x-ray generated, d is the lattice spacing and θ is the diffraction degree, the d -space between the polymer lattice can be determined. XRD was done on polymers **BDPP-BT/TBT/TPT** with BOC group and after thermal cleavage. Polymers **BDPP-BT** and **BDPP-TPTa** did not show any crystallinity, suggesting the polymers are completely amorphous, whereas, **BDPP-TBT** showed crystallinity. As shown in Fig. 2.15, the spin-coated thin film exhibits a sharp primary diffraction peak at $2\theta = 5.05^\circ$, which arises from the ordered interlayer stacking of the polymer and corresponds to a $d(001)$ -spacing of 1.75 nm. Upon thermal cleavage by annealing at 200°C for 20 min, the deprotected-polymer exhibits a primary diffraction peak at $2\theta = 5.45^\circ$, corresponding to a $d(001)$ -spacing of 1.62 nm. The slightly reduced $d(001)$ -spacing indicates that π -planar distance might be shortened, which is beneficial to charge transport. The presence of the smaller d -spacing value suggests the strong intermolecular interaction forces between fused ring moieties (DPP) and the thiophene segments comprising the DPP backbone.

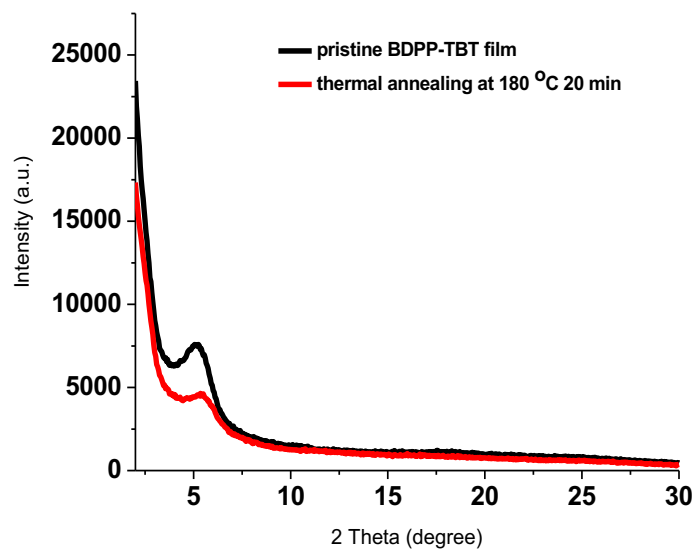


Figure 2.15: Out-of-plane X-ray diffraction of **BDPP-TBT** (black) and **DPP-TBT** (red)

2.2.5.3 EQE and dark current measurements

Several single-layer devices were designed using polymers **BDPP-BT**, **TBT** and **TPT**. Four devices were made according to the following device structure (Fig. 2.16):

Device A: **BDPP-TBT**:**[60]PCBM** (1:2 weight ratio)

Device B: **BDPP-BT**:**[60]PCBM** (1:2 weight ratio)

Device C: **BDPP-TPTa**:**[60]PCBM** (1:2 weight ratio)

Device D: **P3HT**:**BDPP-TBT**:**[60]PCBM** (1:1:4 weight ratio)

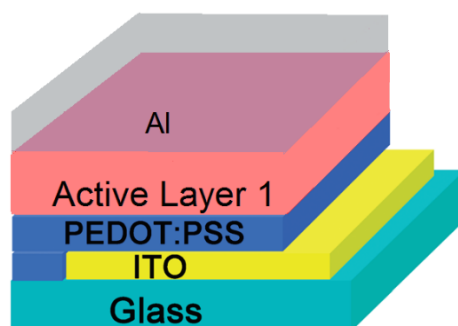


Figure 2.16: Device architecture

The devices were characterized before and after thermal annealing at 200 °C for 10 min under nitrogen atmosphere. Absorption spectra, EQE and dark current were measured on the four devices before and after thermal treatment (Appendix D). We observe increase of intensity of absorption at 450 nm region, which is due to reorganizing the intermolecular packing of the fullerene and polymer blend. The EQE and dark current for the four devices are summarized on Table 2.8. Before thermal annealing the devices exhibit high dark current, showing similar range. However after cleaving off the BOC group, the dark current is lowered, with device C having the lowest with 5.10×10^{-13} A/cm² at -0.1 V. The four devices show two maximum EQE region, in the UV and visible. This overlaps with the absorption spectra, having two strong peaks in UV and visible region. However, the devices show low photon conversion, with device C and D exhibiting the highest EQE of 13.8 and 19.5 % in 350 nm region and approximately 6% at 650 nm. After thermal cleavage, we observe a hypsochromic shift in the EQE and lower conversion. There are several reasons for the overall low performance, first, even with the BOC, the solubility of the polymer were not ideal, therefore formation of thick film is difficult and thus hindering efficient photon absorption. Secondly, the molecular weight of the polymers are relatively low, research have shown that with

increased molecular weight of polymers correlates to better charge carrier mobility, film morphology and overall device performance [44, 45].

Table 2.8: Summary of EQE and Dark current for the devices A-D

Device	Before Annealing		After Annealing	
	Maximum EQE (%) at 0 V	Dark Current at - 0.1 V(A/cm ²)	Maximum EQE (%) at 0 V	Dark Current at - 0.1 V(A/cm ²)
A	8.5 (345 nm), 4.5 (650 nm)	1.66x10 ⁻⁶	5 (350 nm), 3 (625 nm)	1.31x10 ⁻⁸
B	5.4 nm (340 nm), 3.3 (475 nm)	3.34x10 ⁻⁷	6.5 (360 nm), 6.1 (475 nm)	2.17x10 ⁻⁹
C	13.8 (350 nm), 5.98 (645 nm)	4.24x10 ⁻⁶	5.9 (350 nm), 4.0 (510 nm)	5.10x10 ⁻¹³
D	19.5 (355 nm), 15.8 (475 nm), 5.4 (650 nm)	2.34x10 ⁻⁷	7.8 (345 nm), 2.6 (615 nm)	1.42x10 ⁻⁹

2.3 Conclusion

A series of soluble BDPP-containing polymers bearing thermally cleavable BOC group were synthesized. They absorb spectral region from 300-900 nm. They show reasonable solubility prior to cleavage and after thermal cleavage they are completely insoluble. Multilayer films were easily processed by spin-coating and show good retention of PCBM, thus making them excellent candidate for multi-layer material.

2.4 Experimental

2.4.1 Materials

Tetrahydrofuran (THF, Aldrich) was dried by refluxing over sodium solid and benzophenone. *N,N*-dimethylformamide (DMF, Aldrich) was dried under molecular sieves overnight and then redistilled. Toluene (Aldrich) was dried by refluxing over

calcium hydride. Other chemicals and reagents purchased from Aldrich, TCI, Combi-Blocks Catalog, Biofine Product List and OChem Product List were used directly without further purification. (6,6)-phenyl C₆₁ butyric acid methyl ester (PCBM) was purchased from American Dye Source.

2.4.2 Measurements

Fisher-John's melting point apparatus was used for recording the melting points of all the synthesized compounds by thin disc method. Care was taken to ensure that the heating was done at a steady rate. The melting points were not corrected. ¹H and ¹³C NMR spectra were recorded on a Bruker Avance Digital 300 and 400 MHz (300, 400 and 75, 100 MHz for ¹H and ¹³C NMR, respectively). Resonances were quoted on the δ scale relative to tetramethylsilane (TMS, $\delta = 0$) as an internal standard. For ¹H-NMR spectra, the following abbreviations have been used: s = singlet, d = doublet, t = triplet, q = quartet, m = multiplet. Infrared measurements were performed on a Varian 1000 FT-IR Scirinitar spectrophotometer. The bands were expressed in cm⁻¹. Mass spectra were measured with a Micromass Quattro LC ESI (EI). The UV-Vis spectra were recorded on a Perkin-Elmer Lambda 900 UV-Vis-NIR spectrometer at room temperature. Cyclic voltammetry (CV) was performed using a BAS 100B/W electrochemical workstation. Spectral grade acetonitrile was used as the solvent under an argon atmosphere, and 0.1 M tetrabutylammonium hexafluorophosphate was used as the supporting electrolyte. A platinum wire was used as working electrode, a platinum wire was used as counter-electrode, and Ag/AgCl electrode was used as reference electrode. All measurements were done using a scan rate of 100 mV s⁻¹ at

room temperature. The topography was obtained using an Ntegra (NTMDT, Russia) atomic force microscope in a semi-contact mode in air at 23 °C with 512×512 points per image. A $100 \times 100 \mu\text{m}^2$ scanner (Ntegra) and cantilevers with rotated monolithic silicon tips were used for all topographic measurements. The typical scan rate was 0.5 Hz. AFM images were further processed by Nova image processing software. Thermogravimetric analysis was performed on a TA Instruments Q50 apparatus under a nitrogen atmosphere. Gel permeation chromatography (GPC) analysis was conducted on a PL-GPC 220 system with polystyrene as standard and tetrahydrofuran (THF) as eluent. X-ray diffraction (XRD) measurements were performed on a D8 Focus diffractometer at a scan rate of 0.6 min^{-1} in the 2θ range from 2° to 35° with graphite-monochromated $\text{Cu K}\alpha$ radiation ($\lambda = 0.15405 \text{ nm}$).

2.4.3 Solubility test

BDPP polymers were added in 1 mL of chloroform and stirred at ambient temperature until saturation. The solution was then filtered by gravity and the undissolved polymer was dried, weighed and subtracted from the total amount added to determine solubility.

BDPP-polymer powder was heated at 180°C under nitrogen for 10 minutes to remove BOC group. The resulting DPP polymers were stirred in 1 mL of chloroform at ambient temperature for 30 minutes and filtered by gravity, dried and weighed. The undissolved powder was subtracted from total amount added to determine solubility.

2.4.4 Film Preparation

2.4.4.1 Multilayer preparation

A solution of polymer **DPPB-BI** and PCBM in a weight ratio of 1:3 was prepared (10 mg in 3.0 mL of chloroform). The solution was filtered through 0.25-micron filter and then spin-coated onto a clean glass plate (microscope slide, 25 × 25 × 1 mm) at a spin rate of 1500 rpm using the Chemat Technology Spin-Coater KW-4B. The films were then annealed at 180 °C for 5 minutes under nitrogen. The average film thickness was ~60 nm, as measured using Ntegra (NTMDT, Russia) atomic force microscope (AFM). Polymer **PDPP-F** (5 mg in 3.0 mL of chloroform) was then spin-coated onto the thermally treated **DPP-BI** film. A separate film was prepared with **BDPP-BI** and PCBM (1:3 w/w). Teflon tape was used to cover portion of the film and then **PDPP-F** (5 mg in 3 mL of chloroform) was spin-coated on top. Thermal annealing on the top layer was not done to show contrast between the bottom and the top layer. The films were analyzed using UV-Vis spectrophotometer and AFM. The two multilayer films were prepared with a configuration as follows:

- (a) Glass/**DPP-BI**:PCBM(1:3)/**PDPP-F**
- (b) Glass/**DPP-BI**:PCBM(1:3) partially covered by Teflon/**PDPP-F**

2.4.4.2 EQE device fabrication

A mixture of polymer and (6,6)-phenyl C₆₁ butyric acid methyl ester (PCBM) in a weight ratio of 1:2 was dissolved in chlorobenzene with a concentration of 20 mg mL⁻¹ and stirred under nitrogen atmosphere at RT for more than 12 h. Indium tin oxide (ITO) coated glass substrates were cleaned, sequentially, by ultrasonic treatment in

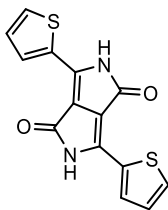
detergent at 60°C for 2 h, washed with de-ionized water, blow dried with nitrogen, and then dried in an oven at 110°C for 0.5 h. After UV–ozone treatment for 15 min, the ITO-coated slides was spin coated with poly(3,4-ethylenedioxythiophene) doped with poly(styrenesulfonate) (PEDOT:PSS) at 3500 rpm for 60 s, followed by heating at 120 °C for 30 min, forming a film of about 30 nm thickness. The active layer in 80 nm thickness was deposited by spin-coating of the solution at a speed of 800 rpm for 60 s. Al was deposited by thermal evaporation. The active device area is defined by a shadow mask to be 16 mm². The four devices were prepared with a configuration as follows:

- (a) ITO/PEDOT:PSS/**BDPP-TBT**:PCBM/Al
- (b) ITO/PEDOT:PSS/**BDPP-TT**:PCBM/Al
- (c) ITO/PEDOT:PSS/**BDPP-TPTB**:PCBM/Al
- (d) ITO/PEDOT:PSS/**P3HT:BDPP-TBT**:PCBM (1:1:4)/Al

Measurements were done on the device at ambient temperature and after thermal annealing at 200°C for 10 minute under nitrogen atmosphere.

2.4.5 Synthesis

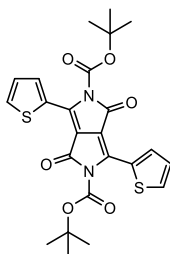
3,6-Di(thiophen-2-yl)-2,5-dihydropyrrolo[3,4-c]pyrrole-1,4-dione (II-1).



In a 250 mL three-neck round-bottom flask flushed with argon, potassium t-butoxide (5.50 g, 50.0 mmol) was dissolved in 150 mL of 2-methyl-2-butanol and heated to 100 °C. Thiophene-2-carbonitrile (5.00 g, 45.8 mmol) was then added,

followed by dropwise addition of diethyl succinate (3.3 mL, 20.0 mmol) over 1.5 h. The reaction mixture was then heated to 130 °C and stirred overnight. The reaction mixture was then poured into a mixture of methanol (500 mL) and acetic acid (25 mL). The red precipitate was filtered and washed with methanol and dried to give compound **1** as red solid (5.0 g, 83% yield). m.p. 293.0 °C (lit.⁵ m.p 292-296 °C); ¹H NMR (300 MHz, DMSO-d₆): 11.34 (s, 2H), 8.22 (d, *J* = 3.7 Hz, 2H), 7.95 (d, *J* = 4.1 Hz, 2H), 7.46 (d, *J* = 4.0 Hz, 2H). ¹³C NMR (75 MHz, DMSO-d₆) 162.10, 136.64, 133.17, 131.78, 131.25, 129.20, 109.00, 49.04; IR (KBr, cm⁻¹): 3127-2990 (ν_{N-H}), 1646 (ν_{C=O}), 1603 (ν_{C=C}).

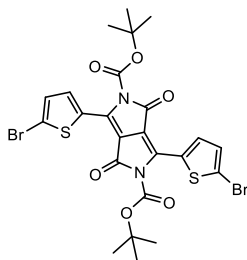
Di-tert-butyl 1,4-dioxo-3,6-di(thiophen-2-yl)pyrrolo[3,4-*c*]pyrrole-2,5(1H,4H)-dicarboxylate (II-2).



Under an atmosphere of argon in a 100 mL round bottom flask mixture of compound **1** (2 g, 6.66 mmol), di-*tert*-butyl dicarbonate (4.4 g, 20 mmol) and 10% DMAP was stirred in 50 mL of dry THF and stirred for 24 h. The solvent was removed under vacuum and flash chromatography was done using CHCl₃ in silica to give golden brown solid (1.8 g, 54%). ¹H NMR (400 MHz, CDCl₃) δ 8.24 (dd, *J* = 3.9, 1.2 Hz, 2H), 7.65 (dd, *J* = 5.0, 1.1 Hz, 2H), 7.21 (dd, *J* = 5.0, 3.9 Hz, 1H), 1.61 (s, 9H). ¹³C NMR (101 MHz, CDCl₃) δ 159.01 (s), 149.77 (s), 148.76 (s), 137.89 (s), 133.88 (s), 131.76 (s), 129.63 (s), 128.03 (s), 110.23 (s), 85.87 (s), 27.67 (s). IR (KBr Plate, cm⁻¹): 3088-

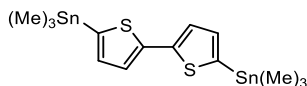
2936 (ν_{C-H}) 1746 ($\nu_{C=O}$ TBOC) 1712 ($\nu_{C=O}$) 1593 ($\nu_{C=C}$).

Di-*tert*-butyl 3,6-bis(5-bromothiophen-2-yl)-1,4-dioxopyrrolo[3,4-*c*]pyrrole-2,5(1H,4H)-dicarboxylate (BDPP).



In a round bottom flask, compound **2** (1.2 g, 2.4 mmol) was dissolved in 30 mL of $CHCl_3$ and bubbled with argon for 20 min. Then NBS (0.896 g, 5.03 mmol) was slowly added portion wise. The solution was then stirred overnight in dark. The solution was then concentrated and precipitated out in methanol to give brown solid (0.9 g, 57%). 1H NMR (400 MHz, $CDCl_3$) δ 8.09 (d, $J = 4.2$ Hz, 2H), 7.17 (d, $J = 4.2$ Hz, 2H), 1.64 (s, 18H). ^{13}C NMR (101 MHz, $CDCl_3$) δ 159.01 (s), 149.77 (s), 148.76 (s), 137.89 (s), 133.88 (s), 131.76 (s), 129.63 (s), 128.03 (s), 110.23 (s), 106.57 (s), 85.87 (s), 27.67 (s).

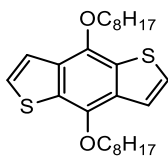
5,5'-Bis(trimethylstannyl)-2,2'-bithiophene (BT).



In a flame-dried 3-neck 50 mL round bottom flask flushed with argon, bithiophene (1 g, 6 mmol) was dissolved in 30 mL dry THF. The solution is then cooled to $-78^\circ C$ using acetone/dry ice batch. 2.5 M *n*BuLi (5 mL, 12.5 mmol) was added drop wise and stirred for 1/2 hour and then brought to room temperature and stirred for

additional 1/2 hour. It was then brought to -78°C and then 1 M trimethyltin chloride solution (12.5 mL, 12.5 mmol) was added drop wise and stirred for 1 hour and then overnight at room temperature. The solvent was removed by vacuum and then extracted with CH_2Cl_2 , the organic layer was washed with water, brine and dried over Na_2SO_4 . The solvent was removed under vacuum and the crude solid was recrystallized in ethanol to give white needle (2.1 g, 70%). ^1H NMR (400 MHz, CDCl_3) δ (ppm) 7.29 (d, $J = 3.3$ Hz, 2H), 7.10 (d, $J = 3.3$ Hz, 2H), 0.40 (s, 18H). ^{13}C NMR (75 MHz, CDCl_3) δ (ppm) 143.01, 137.05, 135.85, 124.85, -8.21.

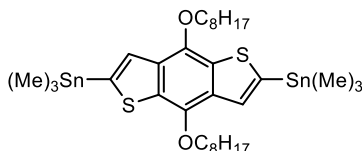
4,8-Bis(octyloxy)benzo[1,2-*b*:4,5-*b'*]dithiophene (II-4)



To a 100 mL flame-dried two-necked flask was added benzo[1,2-*b*:4,5-*b'*]dithiophene-4,8-dione 8 (2.0 g, 9.1 mmol), zinc dust (1.56 g, 24 mmol) and NaOH aqueous solution (30 mL, 20%). The mixture was heated to reflux for 1 h. Then, octyl bromide (4.4 g, 23 mmol) and a catalytic amount of tetrabutylammonium bromide (TBAB) were added into the flask. After being refluxed for 12 h, the mixture was poured into 150 mL of cold water, and extracted by CHCl_3 three times. The combined organic layers were washed with water and dried over anhydrous Na_2SO_4 . Column chromatography on silica gel using a mixture of acetone and hexane (3:7 v/v) as the eluent yielded the title compound **II-4** as a white solid (3.45 g, 85% yield). ^1H NMR (300 MHz, CDCl_3) δ (ppm) 7.50 (d, $J = 5.5$ Hz, 2H), 7.38 (d, $J = 5.5$ Hz, 2H), 4.30 (t, $J = 6.6$ Hz, 4H), 2.01 – 1.79 (m, 4H), 1.69 – 1.50 (m, 4H), 1.50 – 1.22 (m, 16H), 1.01 – 0.85 (m,

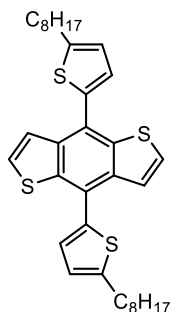
6H). ^{13}C NMR (75 MHz, CDCl_3) δ (ppm) 144.52, 131.61, 130.15, 125.97, 120.31, 73.97, 31.84, 30.55, 29.43, 29.30, 26.09, 22.67, 14.12.

(4,8-Bis(octyloxy)benzo[1,2-*b*:4,5-*b'*]dithiophene-2,6-diyl)bis(trimethylstannane)
(TBT)



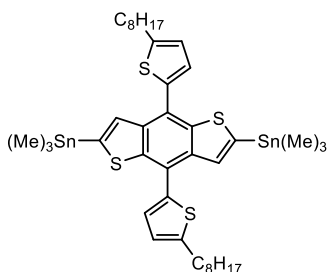
Compound **II-4** (1 g, 2.2 mmol) was dissolved in 25 mL of anhydrous THF under argon protection. The solution was cooled to $-78\text{ }^\circ\text{C}$ and 1.9 mL of *n*-butyllithium solution (4.75 mmol, 2.5 M in hexane) was added dropwise. The reaction mixture was stirred at this temperature for 1 h and allowed to warm to room temperature over 1 h, at which point it was stirred for an additional hour. Then the mixture was again cooled to $-78\text{ }^\circ\text{C}$ and trimethyltin chloride solution (4.5 mL, 4.5 mmol, 1 M in THF) was added dropwise. The mixture was allowed to warm to room temperature and stirred overnight. The reaction was quenched with 50 mL of cold water and extracted with CHCl_3 three times. The organic extraction was washed by water and then dried by anhydrous Na_2SO_4 . After removal of the solvent under vacuum, the residue was recrystallized of the crude product from methanol yielded colorless needle crystal (1.4 g, 81%). ^1H NMR (300 MHz, CDCl_3) δ (ppm) 7.54 (s, 2H), 4.32 (t, $J = 6.5$ Hz, 4H), 2.00 – 1.79 (m, 4H), 1.74 – 1.52 (m, 4H), 1.52 – 1.25 (m, 16H), 1.02 – 0.84 (m, 6H), 0.47 (s, 18H). ^{13}C NMR (75 MHz, CDCl_3) δ (ppm) 140.48, 134.03, 132.98, 128.02, 73.60, 31.87, 30.55, 29.46, 29.36, 26.13, 22.71, 14.14, -8.31.

4,8-Bis(5-octylthiophen-2-yl)benzo[1,2-*b*:4,5-*b'*]dithiophene (II-5)



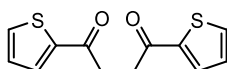
In a two-neck oven-dried round-bottom flask purged with argon, *n*-butyllithium (2.5 M, 4.2 mL) was added dropwise to a solution of 2-octylthiophene (1.90 g, 9.50 mmol) in 25 mL of dry THF at 0 °C. After one hour, **II-4** (1.00 g, 4.50 mmol) was added and the reaction continued for an additional hour at reflux. After cooling to room temperature, a solution of SnCl₂ (4.50 g) in 20% aqueous hydrochloride was added and the mixture was stirred for 1.5 hour before pouring into ice water. The mixture was extracted with CHCl₃ twice (2 x 100 mL) and the combined organic phase was dried over Na₂SO₄. After removal of solvent the crude product was recrystallized in ethanol to give compound **II-5** as yellow needle (1.70 g, 64%). ¹H NMR (300 MHz, CDCl₃) δ (ppm) 7.67 (d, *J* = 5.7 Hz, 2H), 7.47 (d, *J* = 5.7 Hz, 2H), 7.31 (d, *J* = 3.5 Hz, 2H), 6.93 (d, *J* = 3.5 Hz, 2H), 2.94 (t, *J* = 7.6 Hz, 4H), 1.79 (dd, *J* = 15.2, 7.6 Hz, 4H), 1.52 – 1.24 (m, 20H), 0.92 (t, *J* = 6.8 Hz, 6H); ¹³C NMR (75 MHz, CDCl₃) δ (ppm) 147.16, 136.98, 136.52, 127.77, 127.44, 124.17, 123.44, 31.76, 30.27, 29.31, 22.69, 14.13.

(4,8-Bis(5-octylthiophen-2-yl)benzo[1,2-*b*:4,5-*b'*]dithiophene-2,6-diyl)bis(trimethylstannane) (TBTT)



In an oven dried round bottom flask flushed with argon, compound **12** (0.5g, 0.86 mmol) was dissolved in dry THF and then brought to -78 °C and then 2.5 M of n-butyllithium (0.76 mL) was added drop-wise and stirred for 10 min and then brought to 0°C and stirred for additional 30 min. The solution was then cooled back to -78°C and 1 M trimethyltin chloride (1.9 mL) was added drop-wise and then the solution was brought to room temperature and stirred overnight. The solution was extracted with ether three times and dried over Na₂SO₄. The crude product was used for the next step without purification (0.80 g, 100% yield). ¹H NMR (300 MHz, CDCl₃) δ (ppm) 7.70 (s, 2H), 7.33 (d, *J* = 3.5 Hz, 4H), 6.94 (d, *J* = 3.5 Hz, 4H), 3.02 – 2.86 (m, 4H), 1.81 (dt, *J* = 15.1, 7.5 Hz, 4H), 1.31 (t, *J* = 10.9 Hz, 20H), 0.91 (t, *J* = 6.7 Hz, 6H), 0.41 (s, 18H). ¹³C NMR (75 MHz, Chloroform-*d*) δ (ppm) 143.10, 140.48, 134.03, 132.98, 128.02, 73.60, 31.87, 30.55, 29.46, 29.36, 26.13, 22.71, 14.14, -8.31.

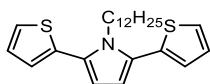
1,4-Di(thiophen-2-yl)butane-1,4-dione (II-6)



In a flame dried 250 mL round bottom flask, AlCl₃ (15 g, 112.5 mmol) was suspended in 100 mL CH₂Cl₂. A mixture of succinyl dichloride (7.0 g, 45.4 mmol) and

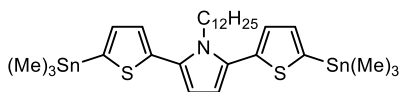
thiophene (9.5 g, 112.5 mmol) in 25 mL CH₂Cl₂ was added drop wise. The reaction was stirred for 4 hours, after which the mixture was poured into ice and concentrated HCl. The organic phase was washed three times with 25 mL NaHCO₃ and then with brine and dried over MgSO₄. After evaporation of the solvent, the green solid was recrystallized in ethanol to give a silver solid (11 g, 97%). ¹H NMR (400 MHz, CDCl₃) δ (ppm) 7.84 (dd, *J* = 3.8, 1.1 Hz, 2H), 7.67 (dd, *J* = 5.0, 1.0 Hz, 2H), 7.17 (dd, *J* = 4.9, 3.8 Hz, 2H), 3.42 (s, 4H).

1-Dodecyl-2,5-di(thiophen-2-yl)-1*H*-pyrrole (II-7a)



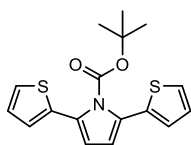
In a flame-dried 150 mL round bottom flask, compound **II-6** (6 g, 24 mmol) was dissolved in 70 mL dry toluene and 3 mL of propionic acid. dodecylamine (5 g, 27 mmol) was then added and the solution was refluxed for 3 days using Dean-Stark trap to remove water. The solvent was then removed by vacuum and then extracted using CH₂Cl₂. It was washed with three times 25 mL of NaHCO₃, water and brine. The organic layer was dried over MgSO₄. CH₂Cl₂ was removed under vacuum and the resulting oil was purified by silica gel flash chromatography using hexane. The resulting oil was crystallized out using ethanol to give a light yellow needle (7 g, 77%). ¹H NMR (400 MHz, CDCl₃) δ (ppm) 7.34 (dd, *J* = 4.8, 1.6 Hz, 2H), 7.13 – 7.07 (m, 4H), 6.36 (s, 2H), 4.22 – 4.08 (m, 2H), 1.58 (q, *J* = 5.7, 3.6 Hz, 2H), 1.38 – 1.06 (m, 18H), 0.91 (t, *J* = 6.9 Hz, 3H). ¹³C NMR (101 MHz, CDCl₃) δ (ppm) 135.04, 128.28, 127.23, 125.89, 125.18, 110.72, 45.15, 31.93, 31.15, 29.67 – 29.29, 28.91, 26.38, 22.70, 14.14.

1-Dodecyl-2,5-bis(5-(trimethylstannyl)thiophen-2-yl)-1H-pyrrole (TPTa)



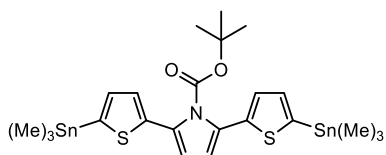
In a flame-dried 3-neck 50 mL round bottom flask flushed with argon, compound **6** (1 g, 2.5 mmol) was dissolved in 20 mL dry THF. The solution is then cooled to -78°C using acetone/dry ice batch. 2.5 M nBuLi (2.2 mL, 5.5 mmol) was added drop wise and stirred for 1 hour and then brought to room temperature and stirred for additional 1 hour. It was then brought to -78°C and then 1 M trimethyltin chloride solution (5.5 mL, 5.5 mmol) was added drop wise and stirred for 1 hour and then overnight at room temperature. The solvent was removed by vacuum and then extracted with CH_2Cl_2 , the organic layer was washed with water, brine and dried over Na_2SO_4 . The solution was concentrated and flash chromatography was done using neutral Al_2O_3 with hexane as eluent. The solvent was removed to give a greenish oil and stored in dark under argon (1.2 g, 66%). ^1H NMR (400 MHz, CDCl_3) δ (ppm) 7.32 (td, $J = 4.5$, 1.4 Hz, 1H), 7.23 – 7.16 (m, 1H), 7.10 (dt, $J = 3.1$, 2.6 Hz, 2H), 6.34 (d, $J = 3.1$ Hz, 2H), 4.14 (dd, $J = 13.6$, 5.9 Hz, 2H), 1.21 (d, $J = 46.5$ Hz, 20H), 0.90 (t, $J = 6.8$ Hz, 3H), 0.42 (s, 3H). ^{13}C NMR (75 MHz, CDCl_3) δ (ppm) 127.21, 126.66, 125.72, 125.04, 110.76, 110.39, 45.16, 31.93, 31.17, 29.64, 29.53, 29.42, 29.36, 26.39, 22.70, 14.14, -8.19.

Tert-butyl 2,5-di(thiophen-2-yl)-1H-pyrrole-1-carboxylate (IIb)



In a flame-dried single round bottom flask flushed with argon, a mixture of compound **5** (3.05 g, 12.2 mmol) and ammonium acetate (9.40 g, 12.2 mmol) was stirred in 25 mL acetic acid and 6 mL acetic anhydride. The solution was refluxed for 24 hours. After the reaction was cooled to room temperature, the mixture was extracted with CHCl₃ and was washed with three times 25 mL of NaHCO₃, water and brine. The organic layer was dried over MgSO₄. To the resulting solution, di-*tert*-butyl dicarbonate (4.4 g, 20 mmol) and catalytic amount of DMAP was added and stirred for 6 hours, after which the solution was washed with water and brine. CHCl₃ was removed under vacuum and the resulting solid was purified by silica gel flash chromatography using hexane:ethylacetate (9:1 v/v) to give light beige solid (3 g, 74%). ¹H NMR (400 MHz, CDCl₃) δ 7.34 (dd, *J* = 5.0, 1.3 Hz, 2H), 7.12 – 7.04 (m, 4H), 6.34 (s, 2H), 1.28 (s, 9H). ¹³C NMR (75 MHz, CDCl₃) δ 149.38, 134.55, 128.67, 127.17, 126.75, 125.60, 113.74, 84.46, 27.19.

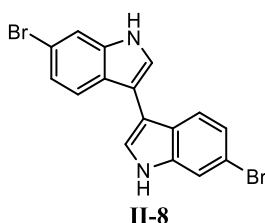
***Tert*-butyl 2,5-bis(5-(trimethylstannyl)thiophen-2-yl)-1*H*-pyrrole-1-carboxylate (TPTB)**



A mixture of TMEDA (0.21 mL, 1.40 mmol) and compound **8** (0.20g, 0.603 mmol) in dry THF was brought to -78°C and nBuLi (0.760 mL, 1.90 mmol) was added dropwise and stirred for 30 min and then stirred for 0°C for 30 min. The solution was then brought to -78°C and 1.0 M Sn(Me)₃Cl (1.3 mL, 1.3 mmol) was added dropwise and stirred for 1 hour and then at room temperature overnight. The solution was extracted with ether

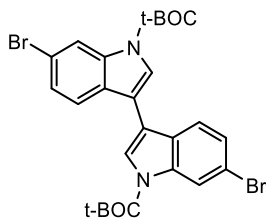
and washed with ice/NH₃Cl, brine and dried over Na₂SO₄. The solvent was removed under vacuum and the product was purified by Al₂O₃ column using hexane:ethyl acetate (8:2 v/v) to afford a yellow oil (100%, 0.4g). ¹H NMR (300 MHz, CDCl₃) δ 7.20 (d, *J* = 3.2 Hz, 2H), 7.14 (d, *J* = 3.3 Hz, 2H), 6.32 (s, 2H), 1.27 (s, 9H), 0.40 (s, 18H).

6,6'-Dibromo-1*H*,1'*H*-3,3'-biindole (II-8)



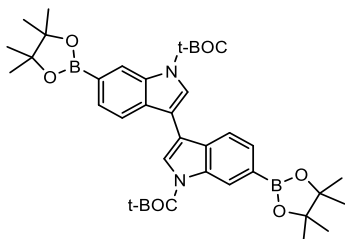
Pd(TFA)₂ (0.300 g, 0.90 mmol) was added into a solution of 6-bromoindole (2.00 g, 10.0 mmol) in 25 mL of DMSO in an oven-dried flask. Then anhydrous MgSO₄ (3.61 g, 30.0 mmol) was added and followed by AgNO₃ (1.87 g, 11.0 mmol). The reaction mixture was stirred at 20 °C for 24h under argon. After the completion the reaction was quenched with water and extracted with EtOAc (4 x 25 mL)/ DCM (4 x 25 mL). The combined organic layer was washed with brine and dried over anhydrous MgSO₄. The solvent was removed and the product was purified on silica gel with hexane:ethyl acetate (7:3 v/v) to give a brown solid (1.9 g, 48%). ¹H NMR (400 MHz, DMSO-*d*₆) δ (ppm) 11.36 (s, 2H), 7.75 – 7.58 (m, 6H), 7.18 (dd, *J* = 8.5, 1.9 Hz, 2H).

Di-*tert*-butyl 6,6'-dibromo-1*H*,1'*H*-[3,3'-biindole]-1,1'-dicarboxylate (II-9)



Then di-*tert*-butyl dicarbonate (1.46 g, 6.7 mmol) and catalytic amount of DMAP was added to a solution of the brown compound (1g, 2.6 mmol) in THF and stirred for 4 hours. After which the solvent was removed under vacuum and purified by silica gel using hexane:ethyl acetate (8:2 v/v) to give a brown solid (2.6g, 90%). ¹H NMR (300 MHz, DMSO-*d*₆) δ (ppm) 8.34 (d, *J* = 1.8 Hz, 2H), 7.98 (s, 2H), 7.64 (d, *J* = 8.5 Hz, 2H), 7.51 (dd, *J* = 8.5, 1.8 Hz, 2H), 1.67 (s, 18H). HRMS (ESI-TOF): Calc. 590.32. Found 613.0193 m/z (+ Na).

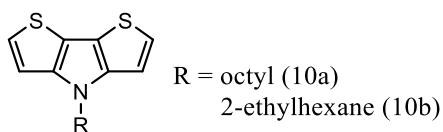
Di-*tert*-butyl 6,6'-bis(4,4,5,5-tetramethyl-1,3,2-dioxaborolan-2-yl)-1*H*,1'*H*-[3,3'-biindole]-1,1'-dicarboxylate (BI)



In a dry one-neck round bottom flask, the resulting compound (1 g, 1.7 mmol), potassium acetate (0.42 g, 4.3 mmol) and bis(pinacolato)diboron (1.1 g, 4.3 mmol) was dissolved in 25 mL DME and bubbled with argon for 10 min. After which 5% Pd(dppf)₂Cl₂ (0.07 g) was added and the solution was refluxed overnight. After cooling, the solution was quenched with water and extracted with CHCl₃ and dried over Na₂SO₄.

After vacuum removal of the solvent, the dark oil was purified via silica gel using hexane:ethyl acetate (8:2 v/v) to afford a beige solid (69%, 0.8 g). ^1H NMR (300 MHz, CDCl_3) δ 8.75 (s, 2H), 7.90 (s, 2H), 7.72 (s, 4H), 1.73 (s, 18H), 1.39 (s, 24H). ^{13}C NMR (75 MHz, CDCl_3) δ 149.58, 135.40, 131.99, 128.78, 124.55, 122.01, 119.59, 113.66, 83.81, 28.17, 24.92. IR (NaCl, cm^{-1}): 1737 [$\nu_{\text{C=O(ester)}}$], 1606 ($\nu_{\text{C=C}}$). m.p. 220-223°C. Calculated Elemental Analysis: C, 66.68%; H, 7.36%; N, 4.09%. Measured Elemental Analysis: C, 66.10%; H, 6.95%; N, 3.87%. HRMS (ESI-TOF): Calc. 684.44. Found 707.3652 m/z (+ Na).

4-Alkyl-4H-dithieno[3,2-b:2',3'-d]pyrrole (II-10a/b)



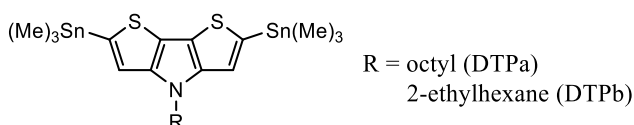
In a dry round bottom flask flushed with argon, dibromobithiophene (1.05 g, 3.24 mmol) $\text{Pd}_2(\text{dba})_3$:BINAP: Na^tOBu (0.05:0.15:2) and alkyl-amine (0.55 mL, 3.3 mmol) was dissolved in toluene and the solution was bubbled with argon for further 10 min. The mixture was then refluxed overnight. After cooling the solution to ambient temperature, it was washed with water twice extracted with CH_3Cl and dried over Na_2SO_4 . After removal of the solvent under vacuum, the crude product was purified under silica gel using hexane:ethyl acetate (8:2 v/v) to afford a brown oil.

4-Octyl-4H-dithieno[3,2-b:2',3'-d]pyrrole (II-10a) (0.85 g, 90%). ^1H NMR (300 MHz, CDCl_3) δ (ppm) 7.15 (d, $J = 5.3$ Hz, 2H), 7.02 (d, $J = 5.3$ Hz, 2H), 4.21 (t, $J = 7.0$ Hz, 2H), 1.87 (q, $J = 7.1$ Hz, 2H), 1.42 – 1.18 (m, 10H), 0.88 (t, $J = 6.7$ Hz, 3H).

^{13}C NMR (75 MHz, CDCl_3) δ 122.75, 110.95, 47.44, 31.78, 30.37, 29.21, 29.13, 27.01, 22.61, 14.08.

4-(2-Ethylhexyl)-4*H*-dithieno[3,2-*b*:2',3'-*d*]pyrrole (II-10b) (0.90 g, 95%). ^1H NMR (300 MHz, CDCl_3) δ (ppm) 7.14 (d, $J = 5.3$ Hz, 2H), 7.00 (d, $J = 5.3$ Hz, 2H), 4.08 (dd, $J = 7.3, 4.1$ Hz, 2H), 2.03 – 1.91 (m, 1H), 1.46 – 1.19 (m, 8H), 1.01 – 0.81 (m, 6H). ^{13}C NMR (75 MHz, CDCl_3) δ 145.28, 122.69, 111.07, 51.34, 40.47, 30.66, 28.68, 24.04, 22.98, 14.03, 10.68.

4-Alkyl-2,6-bis(trimethylstannyl)-4*H*-dithieno[3,2-*b*:2',3'-*d*]pyrrole (DTPa/b)



In an oven-dried round-bottom flask, compound **14** (0.20 g, 0.69 mmol) was dissolved in a hexane and brought to 0 °C. Then TMEDA (.26 mL, 1.73 mmol) and *n*-butyllithium (2.5 M, 0.70 mL, 1.73 mmol) added and stirred for 2 hours at 0 °C. Then trimethyltin chloride (1.45 mL, 1.45 mmol) was added and brought to ambient temperature and stirred overnight. The solution was extracted with ether and dried over Na_2SO_4 . The solvent was removed to give a dark brown oil, the crude product was used for the next step without purification.

4-Octyl-2,6-bis(trimethylstannyl)-4*H*-dithieno[3,2-*b*:2',3'-*d*]pyrrole (DTPa) (0.43 g, 100%) ^1H NMR (300 MHz, CDCl_3) δ (ppm) 7.02 (s, 2H), 4.20 (t, $J = 7.1$ Hz, 2H), 1.90 (t, $J = 7.2$ Hz, 2H), 1.29 (d, $J = 10.8$ Hz, 10H), 0.89 (t, $J = 6.3$ Hz, 3H), 0.42 (s,

18H). ^{13}C NMR (75 MHz, CDCl_3) δ (ppm) 147.85, 122.48, 117.89, 110.99, 57.62, 47.42, 47.39, 45.83, 31.81, 30.43, 30.40, 29.20, 29.15, 27.00, 22.64, 14.10, 1.03, -8.12.

4-(2-Ethylhexyl)-2,6-bis(trimethylstannyl)-4*H*-dithieno[3,2-*b*:2',3'-*d*]pyrrole

(DTPb) (0.43 g, 100%) ^1H NMR (300 MHz, CDCl_3) δ 6.98 (s, 2H), 4.07 (dd, $J = 7.3$, 4.6 Hz, 2H), 3.82 – 3.67 (m, 2H), 1.96 – 1.76 (m, 3H), 1.34 (tq, $J = 12.4$, 6.9, 5.6 Hz, 10H), 0.92 (dt, $J = 9.9$, 7.4 Hz, 8H), 0.42 (s, 17H).

General synthesis of polymers by the Stille cross-coupling reaction.

In a flame-dried 25-mL round-bottom flask under an argon atmosphere, organotin monomer and DPP monomer in 1:1 mole ratio were dissolved in 8 mL of chlorobenzene. The solution was bubbled with argon for 30 min and then 10 mol % of $\text{Pd}(\text{PPh}_3)_4$ was added and solution was heated to 110 °C and stirred for 48 hours. After cooling, the polymer was precipitated out in methanol and filtered. The polymer was purified via Soxhlet extraction (hexane and acetone) to give dark solid. The polymer was then suspended in dry THF with di-*tert*-butyl dicarbonate and a small amount of DMAP was added and stirred overnight. The solution was then precipitated in 250 mL of methanol and filtered to give the target polymer.

General synthesis of polymers by the Suzuki-cross coupling reaction.

In a flame-dried 25-mL round-bottom flask under an argon atmosphere, boron ester monomer and DPP monomer in 1:1 mole ratio were dissolved in 6 mL of THF and 4 mL of 2 M K_2CO_3 aqueous solution. The solution was bubbled with argon for 30

min and then 10 mol% of Pd(PPh₃)₄ was added and solution was heated to reflux and stirred for 48 hours. After cooling, the polymer was precipitated out in methanol/water mixture and filtered. The polymer was purified via Soxhlet extraction (hexane and acetone) to give dark solid. The polymer was then suspended in dry THF with di-tert-butyl dicarbonate and a small amount of DMAP was added and stirred overnight. The solution was then precipitated in 250 mL of methanol and the target polymer was collected by filtration.

Polymer **BDPP-TBT**.

Dark blue solid (77% yield). ¹H NMR (300 MHz, CDCl₃): 8.32 (dd, *J* = 11.0, 4.1 Hz, 7H), 7.68 (d, *J* = 6.6 Hz, 8H), 7.53 (s, 4H), 7.41 (s, 8H), 4.32 (d, *J* = 6.7 Hz, 24H), 1.93 (s, 31H), 1.61 (d, *J* = 27.8 Hz, 59H), 1.38 (d, *J* = 19.1 Hz, 109H), 0.92 (s, 41H). ¹³C NMR (100 MHz, CDCl₃) 159.02 (s), 148.85 (s), 144.42 (s), 134.83 (s), 134.47 (s), 126.14 (s), 118.64 (s), 86.15 (s), 73.94 (s), 52.38 (s), 31.85 (s), 30.52 (s), 29.36 (d, *J* = 13.4 Hz), 27.76 (s), 26.01 (s), 22.67 (s), 14.12 (s). IR (KBr, cm⁻¹): 1739 [ν_{C=O} (ester)], 1697 (ν_{C=O}), 1590 (ν_{C=C}).

Polymer **BDPP-TT**.

Dark black solid (69% yield). ¹H NMR (300 MHz, CDCl₃): 8.21 (dd, *J* = 69.9, 5.2 Hz, 1H), 7.11 (dd, *J* = 39.5, 4.7 Hz, 1H), 1.64 (s, 7H). IR (KBr, cm⁻¹): 1739 [ν_{C=O} (ester)], 1653 (ν_{C=O}), 1594 (ν_{C=C}).

Polymer BDPP-TPT.

Dark blue solid (67% yield). ^1H NMR (300 MHz, CDCl_3): 8.33 (t, $J = 4.3$ Hz, 3H), 7.42 – 7.29 (m, 9H), 7.11 (d, $J = 4.7$ Hz, 6H), 7.06 – 7.00 (m, 5H), 6.48 – 6.32 (m, 7H), 4.29 – 4.13 (m, 7H), 1.66 (d, $J = 10.4$ Hz, 26H), 1.66 – 1.40 (m, 33H), 1.35 – 1.08 (m, 74H), 0.88 (t, $J = 6.8$ Hz, 14H). ^{13}C NMR (100 MHz, CDCl_3) 159.08 (s), 149.01 (s), 136.52 (s), 135.66 (s), 135.42 (s), 134.60 (s), 127.74 (s), 127.32 (s), 126.11 (d, $J = 12.7$ Hz), 125.51 (s), 124.26 (s), 111.34 (d, $J = 16.1$ Hz), 85.99 (s), 64.97 (d, $J = 11.1$ Hz), 45.40 (s), 31.90 (s), 31.13 (s), 29.74 – 28.48 (m), 27.76 (s), 26.38 (s), 22.68 (s), 14.11 (s). IR (KBr, cm^{-1}): 1739 [$\nu_{\text{C=O}}$ (ester)], 1653 ($\nu_{\text{C=O}}$), 1597 ($\nu_{\text{C=C}}$).

Polymer BDPP-TPTB.

Dark blue solid (47% yield). ^1H NMR (300 MHz, CDCl_3): 8.32 (s, 6H), 7.36 (d, $J = 7.4$ Hz, 9H), 7.07 (d, $J = 6.6$ Hz, 21H), 6.39 (dd, $J = 15.4, 4.1$ Hz, 14H), 1.67 (s, 54H), 1.57 (s, 93H). IR (KBr, cm^{-1}): 1739 [$\nu_{\text{C=O}}$ (ester)], 1644 ($\nu_{\text{C=O}}$), 1594 ($\nu_{\text{C=C}}$).

Polymer BDPP-BI.

Dark blue solid (41% yield). ^1H NMR (300 MHz, CDCl_3): 8.62 (s, 2H), 8.42 – 8.34 (m, 2H), 7.92 (d, $J = 11.6$ Hz, 3H), 7.74 (t, $J = 7.2$ Hz, 4H), 7.64 (d, $J = 7.1$ Hz, 3H), 7.52 (d, $J = 4.1$ Hz, 2H), 1.78 (s, 17H), 1.69 (s, 14H), 1.56 (s, 25H). IR (KBr, cm^{-1}): 1739 [$\nu_{\text{C=O}}$ (ester)], 1680 [$\nu_{\text{C=O}}$ (ester)], 1566 ($\nu_{\text{C=C}}$).

Polymer BDPP-TBTT.

Dark greenish blue solid (62% yield). ^1H NMR (300 MHz, CDCl_3): 8.37 – 8.17

(m, 9H), 7.86 (s, 8H), 7.68 – 7.57 (m, 11H), 7.49 (d, $J = 6.7$ Hz, 23H), 6.96 (s, 16H), 4.53 (d, $J = 5.4$ Hz, 6H), 2.95 (s, 38H), 1.73 (d, $J = 47.0$ Hz, 59H), 1.62 (d, $J = 19.8$ Hz, 61H), 1.37 (d, $J = 25.5$ Hz, 230H), 0.92 (s, 81H). ^{13}C NMR (100 MHz, CDCl_3) 147.50 (s), 136.43 (s), 128.09 (d, $J = 41.8$ Hz), 124.38 (s), 38.14 (s), 32.25 – 31.63 (m), 31.63 – 31.44 (m), 30.76 – 30.07 (m), 30.07 – 28.52 (m), 23.05 – 22.02 (m), 14.50 – 13.29 (m), 1.20 – 0.82 (m). IR (KBr, cm^{-1}): 1739 [$\nu_{\text{C=O}}$ (ester)], 1648 ($\nu_{\text{C=O}}$), 1597 ($\nu_{\text{C=C}}$).

Polymer **BDPP-DTP**.

Dark blue solid (54% yield) ^1H NMR (300 MHz, CDCl_3): 8.25 (s, 1H), 8.22 – 8.15 (m, 1H), 7.02 (d, $J = 3.4$ Hz, 2H), 4.27 – 4.13 (m, 4H), 1.89 (s, 6H), 1.68 (s, 12H), 1.57 (s, 36H), 1.30 (t, $J = 10.2$ Hz, 23H), 0.96 – 0.80 (m, 8H). IR (KBr, cm^{-1}): 1739 [$\nu_{\text{C=O}}$ (ester)], 1644 ($\nu_{\text{C=O}}$), 1594 ($\nu_{\text{C=C}}$).

Reference

- [1] H. Dong, H. Zhu, Q. Meng, X. Gong, W. Hu, *Chem. Soc. Rev.*, **2012**, *41*, 1754.
- [2] K.-J. Baeg, M. Binda, D. Natali, M. Caironi, Y.-Y. Noh, *Adv. Mater.*, **2013**, *25*, 4267.
- [3] N. T. Kalyani, S. J. Dhoble, *Rnew. Sust. Energ. Rev.*, **2012**, *16*, 2696.
- [4] H. Klauk, *Chem. Soc. Rev.*, **2010**, *39*, 2643.
- [5] L. Torsi, M. Magliulo, K. Manoli, G. Palazzo, *Chem. Soc. Rev.*, **2013**, *42*, 8612.
- [6] Y. Lin, Y. Li, X. Zhan, *Chem. Soc. Rev.*, **2012**, *41*, 4245.
- [7] J. Nelson, *Mater. Today*, **2011**, *14*, 462.
- [8] P. Peumans, A. Yakimov, S. R. Forrest, *J. Appl. Phys.*, **2003**, *93*, 3693.

- [9] A. Dodabalapur, *Mater. Today*, **2006**, *9*, 24.
- [10] G. Li, R. Zhu, Y. Yang, *Nat. Photon.* **2012**, *6*, 153.
- [11] K. Kawano, N. Ito, T. Nishimori, J. Sakai, *Appl. Phys. Lett.* **2006**, *88*, 073514.
- [12] S. Sista, Z. Hong, L. Chen, Y. Yang, *Energy Environ. Sci.* **2011**, *4*, 1606.
- [13] S. Sista, M.-H. Park, Z. Hong, Y. Wu, J. Hou, W. L. Kwan, G. Li, Y. Yang, *Adv. Mater.* **2010**, *22*, 380.
- [14] W. Ma, P.K. Iyer, X. Gong, B. Liu, D. Moses, G.C. Bazan, A. J. Heeger, *Adv. Mater.*, **2005**, *17*, 274.
- [15] M. V. Twigg, J.T. Richardson, *Chem. Eng. Res. Des.* **2002**, *80*, 183
- [16] Z. Liang, O. M. Cabarcos, D. L. Allara, Q. Wang, *Adv. Mater.* **2004**, *16*, 823.
- [17] M. C. Tria, K.-S. Liao, N. Alley, S. Curran, R. Advincula. *J. Mater. Chem.* **2011**, *21*, 10261.
- [18] B. K. Kuila, P. Formanek, M. Stamm, *Nanoscale*, **2013**, *5*, 10849.
- [19] Q. Wei, T. Becherer, P.-L. M. Noeske, I. Grunwald, R. Haag, *Adv. Mater.*, **2014**, *26*, 2688.
- [20] X. Gong, M.-H. Tong, S. H. Park, M. Liu, A. Jen, A. J. Heeger, *Sensors*, **2010**, *10*, 6488.
- [21] J. C. Bijleveld, V. S. Gevaerts, D. Di Nuzzo, M. Turbiez, S. G. J. Mathijssen, D. M. de Leeuw, M. M. Wienk, R. A. J. Janssen, *Adv. Mater.*, **2010**, *22*, E242.
- [22] J. C. Bijleveld, B. P. Karsten, S. G. J. Mathijssen, M. M. Wienk, D. M. de Leeuw, R. A. J. Janssen, *J. Mater. Chem.*, **2011**, *21*, 1600.
- [23] B. Zhao, K. Sun, F. Xue, J. Ouyang, *Organic Electronics*, **2012**, *13*, 2516.
- [24] J. S. Zambounis, Z. Hao, A. Iqbal, *Nature*, **1997**, *388*, 131.

- [25] J. Mizuguchi, *J. Phys. Chem. A*, **2000**, *104*, 1817.
- [26] A. B. Tamayo, B. Walker, T.-Q. Nguyen. *J. Phys. Chem. C*. **2008**, *112*, 11545.
- [27] J. Warnan, A. E. Labban, C. Cabanetos, E. T. Hoke, P. K. Shukla, C. Risko, J.-L. Bredas, M. D. McGehee, P. M. Beaujuge. *Chem. Mater.*, **2014**, *26*, 2299.
- [28] E. Yildiz, P. Camurlu, C. Tanyeli, I. Akhmedov, L. Toppare. *J. Electroanal. Chem.*, **2008**, *612*, 247.
- [29] H. Wynberg, J. Metselaar. *Synth. Commun.*, **1984**, *14*, 1.
- [30] A. R. Sorensen, L. Overgaard, I. Johannsen. *Synth. Met.*, **1993**, *55*, 1626.
- [31] Y. Li, W.-H. Wang, S.-D. Yang, B.-J. Li, C. Feng, Z.-J. Shi. *Chem. Commun.*, **2010**, *46*, 4553.
- [32] X. Qian, H.-H. Gao, Y.-Z. Zhu, L. Lu, J.-Y. Zheng. *RSC Adv.* **2015**, *5*, 4368.
- [33] G. Koeckelberghs, L. D. Cremer, W. Vanormelingen, W. Dehaen, T. Verbiest, A. Persoons, C. Samyn. *Tetrahedron*. **2005**, *61*, 687.
- [34] S. J. Evenson, M. J. Mumm, K. I. Pokhodnya, S. C. Rasmussen. *Macromolecules*. **2011**, *44*, 835.
- [35] B. Jolicoeur, E. E. Chapman, A. Thompson, W. D. Lubell. *Tetrahedron*. **2006**, *62*, 11531.
- [36] G. Qian, J. Qi, J. A. Davey, J. S. Wright, Z. Y. Wang. *Chem. Mater.*, **2012**, *24*, 2364.
- [37] B. Zhao, K. Sun, F. Xue, J. Ouyang. *Organic Electronics*. **2012**, *13*, 2516.
- [38] J. Hou, M. H. Park, S. Zhang, Y. Yao, L. M. Chen, J. H. Li, Y. Yang. *Macromolecules*. **2008**, *41*, 6012.
- [39] R. F. Pierret, *Semiconductor Device Fundamentals*. Reading, Massachusetts:

Addison Wesley Longman, **1996**, 525-732.

- [40] A. F. Stassen, R. W. I. de Boer, N. N. Iosad, A. F. Morpurgo, *Applied Physics Letters*, **2004**, *85*, 3899.
- [41] T. Hasegawa, J. Takeya, *Sci. Technol. Adv. Mater.*, **2009**, *10*, 024314.
- [42] J. Li, Y. Zhao, H. S. Tan, Y. Guo, C.-A. Di, G. Yu, Y. Liu, M. Lin, S. H. Lim, Y. Zhou, H. Su, B. S. Ong, *Sci. Rep.*, **2012**, *2*, 754.
- [43] G. Kim, S.-J. Kang, G. K. Dutta, Y.-K. Han, T. J. Shin, Y.-Y. Noh, C. Yang, *J. Am. Chem. Soc.*, **2014**, *136*, 9477.
- [44] Z. Xiao, K. Sun, J. Subbiah, T. Qin, S. Lu, B. Purushothaman, D. J. Jones, A. B. Holmes, W. W. H. Wong, *Polym. Chem.*, **2015**, *6*, 2312.
- [45] C. Liu, K. Wang, X. Hu, Y. Yang, C.-H. Hsu, W. Zhang, S. Xiao, X. Gong, Y. Cao, *ACS Appl. Mater. Interfaces*, **2013**, *5*, 12163.

Chapter 3 Transformation of Diketopyrrolopyrrole Polymers into Dithioketopyrrolopyrrole (DTPP) and Diazapentalene (DAP) Polymers and their Use in Visible-near Infrared Photodetectors

3.1 Introduction

Organic photodetectors (OPDs) have been extensively studied recently due to their great advantages, which include flexibility, large-area detection, light weight, mechanical flexibility and low cost fabrication [1-4]. OPDs sensing in the UV-visible have variety of commercial application such as image sensing, telecommunication and bio sensing. These devices show large spectral response, high external quantum efficiency (EQE) and great detectivity, however sensing in the near-infrared (NIR) region have been difficult due to the poor design of organic material thus leading to poor exciton formation from incident photons [5-7]. In a recent publication reported by Gong *et al.* showed large spectral absorption in the UV-NIR region (300-1450 nm) with very high detectivity reaching greater than 10^{12} Jones ($\text{cmHz}^{1/2}\text{W}^{-1}$) and linear dynamic range over 100 decibels [8]. Diketopyrrolopyrrole (DPP) is an important chromophore which exhibit weather resistance and thermal stability and it is widely used as starting material for many device archetypes [9]. They have particularly been used for OTFT, OPV and OLED. Such semiconductors have achieved very high hole mobility reaching up to $10.5 \text{ cm}^2\text{V}^{-1}\text{s}^{-1}$ and power conversion efficiency (PCE) reaching up to 8.62% [10-11]. DPP has a planer bicyclic ring consisting of cross conjugation of vinylogous amidic and vinylogous hydrazine units. Upon thioamidation using Lawesson's reagent (LR) and subsequent alkylation, the compound is converted to 2,5-diazapentalene (DAP).

DAP has a red-shift in the absorption, decreasing the HOMO and LUMO gap. Computational calculation was done on the chromophores showing the energy gap in the order of DPP > PPO > DAP, and their HOMO levels gradually decreasing in order from DPP to PPO to DAP. This is due to lack of electron donation from nitrogen on to the π -orbitals of the diene system (Fig. 3.1) [12].

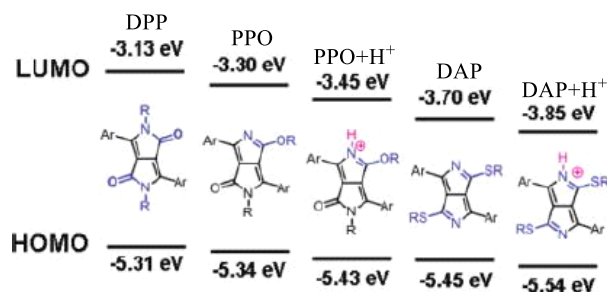


Figure 3.1: Energy level of DPP, PPO and DAP (Adapted with permission from Ref.

12)

Furthermore, due to the more basic property of the thiolactam, it can easily undergo acid-base reaction, thus polymers containing DAP moiety produce thermochromic and halochromic characteristics (Fig. 3.2). Under acid condition, these polymers have a bathochromic shift up to 160 nm, reaching into the NIR region and are able to change color in the visible and NIR spectral region (500-1200 nm) at the transition temperature around 50-60 °C [12, 13].

Also, these polymers show good photovoltaic response from 400-1100 nm with EQE of 13% and detectivity of 2.3×10^{10} Jones at 800 nm [2].

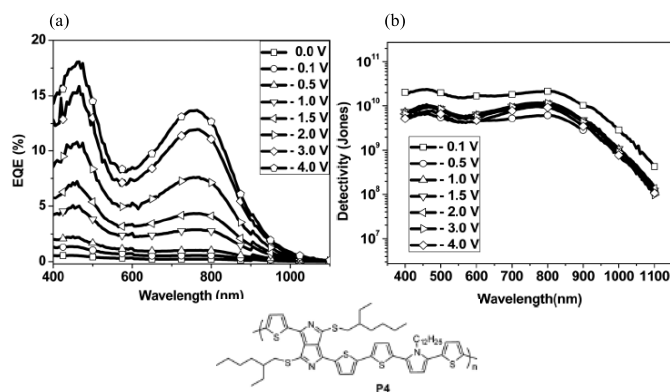


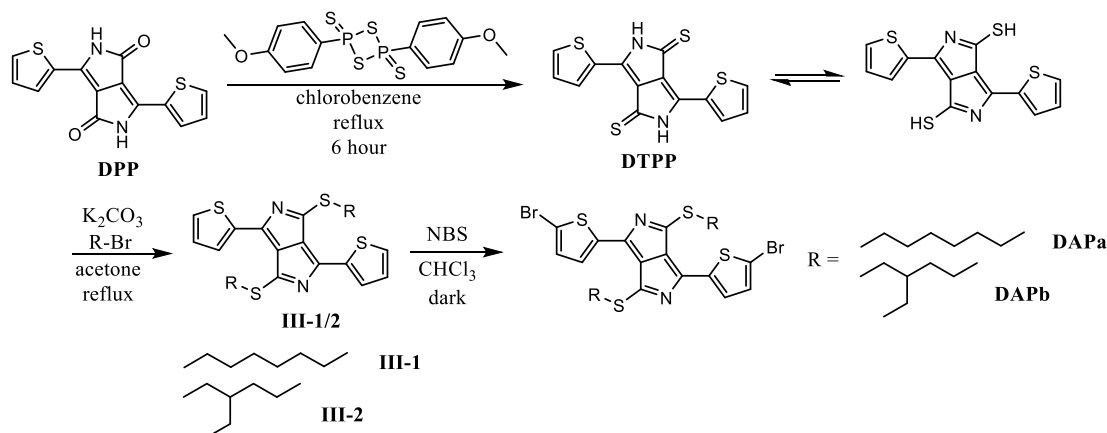
Figure 3.2: Photodetectors properties of **P4** (a) EQE (b) Detectivity (Adapted with permission from Ref. 2)

In this chapter we will demonstrate multilayer device architecture for photodetector application using a series of DPP polymers, discussed in chapter 1, and DAP polymers in a to absorb a larger spectral region. We are interested in the formation of the hydrogen bond network, which in turn will enhance the intermolecular charge-carrier hopping and build multilayer architecture by spin-coating without the use of vapour deposition. To generate the hydrogen bonding without sacrificing the solubility during the film formation, a solubilizing protecting group, *tert*-butoxycarbonyl (BOC), is introduced to the DPP unit in polymers. The BOC group can thermally be cleaved at approximately 180 °C to reanimate the hydrogen-bond network [14]. We will also demonstrate chemical transformation of DPP polymers to form their thiolactam analogue and study their photodetector performance.

3.2 Results and discussion

3.2.1 Synthesis of DTPP and DAP monomer

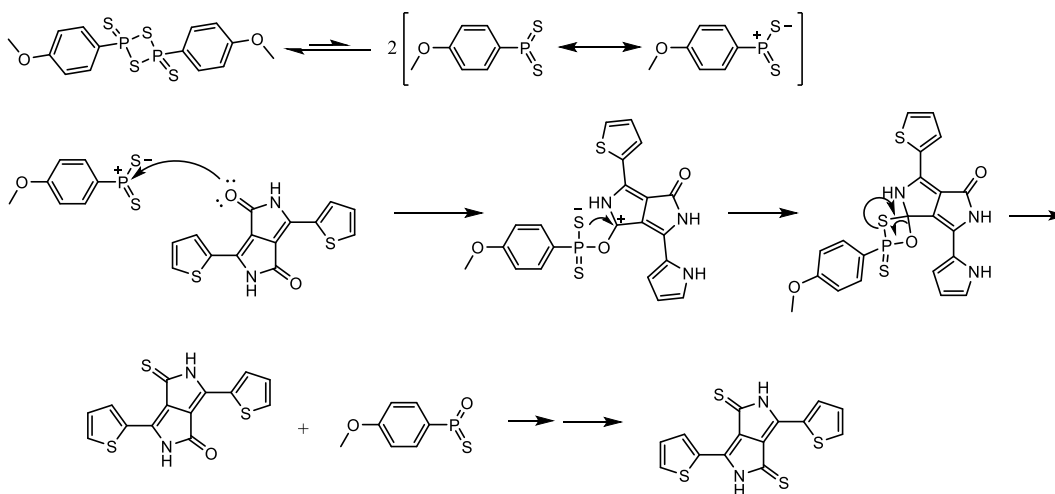
Syntheses of DAP monomers are shown on Scheme 3.1. Thionation of DPP unit is done using LR in chlorobenzene at reflux for 6 hours. The completion of the reaction is determined when the solution turns from dark red to dark green. The DTPP solid is extracted with hot methanol to remove residual phosphorus-containing compound, which decomposes the DTPP compound if it is not purified. Thioalkylation is readily done under base medium and the alkylated product, **III-1**, is purified by flash chromatography since decomposition is observed in silica gel. Bromination, under dark, of the subsequent product affords the monomer. Two different DAP monomers were synthesized, DAPa, which contains a straight alkyl chain and DAPb, which has a branched chain for higher degree of solubility. The monomers are soluble in common organic solvents such as CHCl_3 , THF and chlorobenzene.



Scheme 3.1: Synthesis of **DAPa** and **DAPb**

The mechanism for the formation of the thiolactam is shown on Scheme 3.2. Lawesson's reagent in solution is in equilibrium with a more reactive dithiophosphine ylide. The reaction with a carbonyl compound gives rise to a thioxaphosphetane

intermediate. The driving force in the next step is the formation of a stable P=O bond in a cyclo-reversion mechanism that resembles the Wittig reaction. Reactions of ketones, amides, lactams and lactones with LR are relatively faster than that of esters.

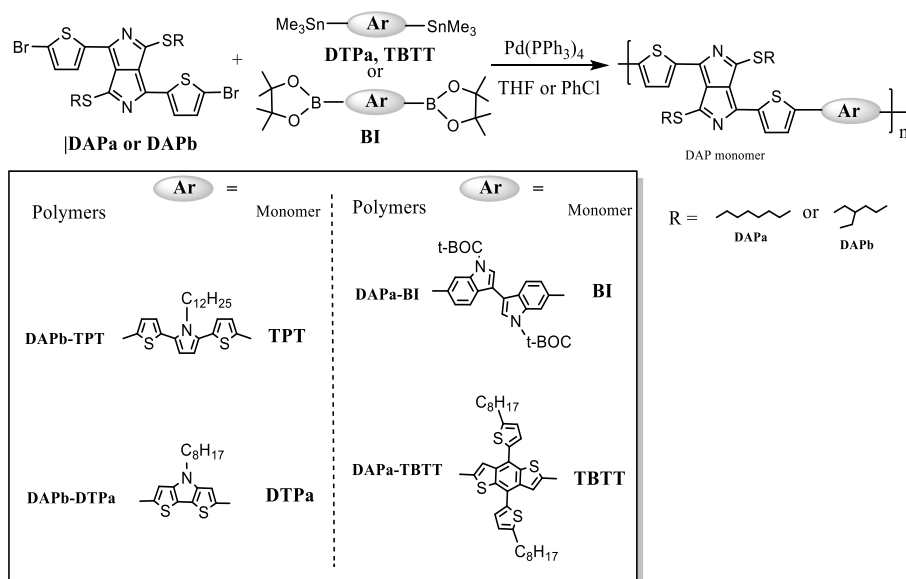


Scheme 3.2: Mechanism of Lawesson's reagent reaction with DPP

3.2.2 Synthesis of DAP polymers

Various electron donors were used, dithieno[3,2-*b*:2',3'-*d*]pyrrole (DTP), bis(2-thienyl)-*N*-alkyl-pyrrole (TPT), benzo[1,2-*b*:4,5-*b'*]dithiophene, 4,8-bis(5-alkyl-2-thienyl) (TBTT) and 3,3-biindole (BI). DTP is receiving a great deal of attention as an electron donor due to large planarity of the rigid and fused ring structure, which leads to better intermolecular charge carrier [15-16]. TBTT is also a strong donor and have shown good PCE performance of 9.35% in photovoltaic devices [17]. TPT and BI are relatively new donors and have shown good promise in organic solar cell and PDs application [2, 18-20]. The subsequent DAP-polymers were synthesized by Stille or Suzuki cross-coupling reaction and were purified by Soxhlet extraction. The polymers

were soluble in common organic solvents such as chloroform, dichloromethane and tetrahydrofuran. Polymer **DAPb-TPT** was previously synthesized.



Scheme 3.3: Synthesis of DAP polymers

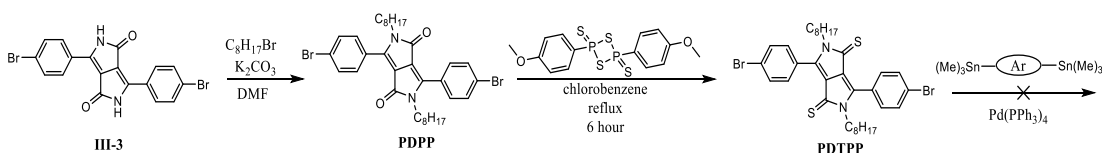
Molecular weights and polydispersity indices (PDI) of the polymers were determined by gel permeation chromatography (GPC) relative to polystyrene standards (Table 3.1). **DAPb-DTP** and **DAPa-TBTT** have higher molecular weight of 960.4 and 884.4 kg/mol with a PDI of 1.84 and 1.71, respectively. Whereas, **DAPa-BI** has a molecular weight of 653.6 kg/mol and PDI of 1.68. All three polymers have relatively very high molecular with small dispersity, which is ideal for device performance.

Table 3.1. Molecular weights and PDI of polymers.

Polymer	M_w (kg/mol)	PDI
DAPb-DTP	9.60×10^2	1.84
DAPa-TBTT	8.84×10^2	1.71
DAPa-BI	6.53×10^2	1.68

3.2.3 PDTTP polymer reaction

Scheme 3.3 shows the possible synthetic route for polymerization of PDTTP monomer. Alkylation of **III-3** is done by alkyl halide in base followed by purification column chromatography to give pure product PDPP. This is followed by thionation by LR. Polymer reaction was done with known organotin donors, however, no polymerization was observed. This could be due to palladium poisoning by the thiolactam or photodegradation of the PDTTP monomer. Therefore, a different synthetic route was taken.



Scheme 3.4: DTPP polymerization

Sulfur plays an important role in changing the catalytic properties of palladium catalyst [21]. For example, sulfur was identified to be a critical contaminant for the catalytic combustion of methane to carbon dioxide. Partial deactivation of palladium was observed from sulfur-containing gases. Studies also have shown irreversible poisoning of the Pd component in a SO_2/Pd interaction on three-way catalysts system [22-25]. Figure 3.3 demonstrates a possible DPP-Pd complex which competes with the polymerization cycle.

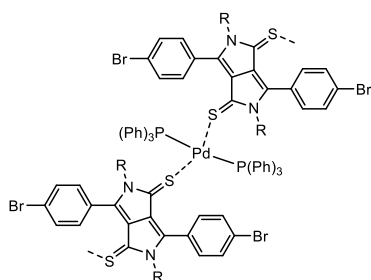
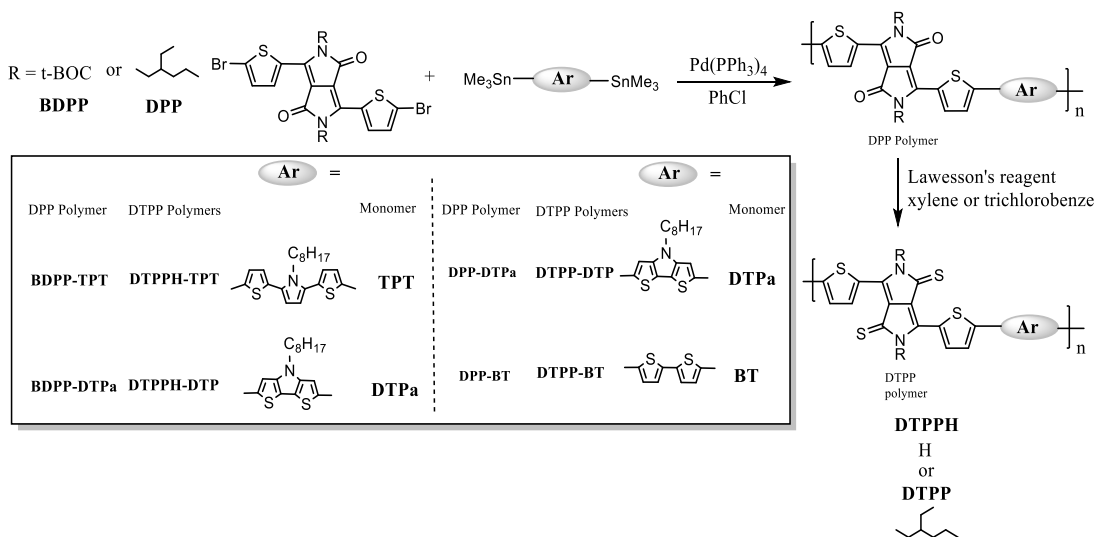


Figure 3.3: Possible Pd complex with PDTTP

The alternate synthetic route involves polymer transformation of DPP- or BDPP-based polymer (Scheme 3.4). Two DPP-based polymers were synthesized using Stille cross-coupling reaction with donor DTPa and BT. The polymers were characterized by proton NMR, which displayed the expected resonances peaks. They are readily soluble in common organic solvents, although DPP-BT showed limited solubility. The DTPP polymers were synthesized according to method previously described. BDPP polymers were heated in trichlorobenzene at 180 °C to remove the BOC group, whereas, DPP polymers is dissolved in xylene and then reacted with LR until there was a change of color. The exchange of the carbonyl oxygen for sulfur was determined by infrared analysis. The DTPP polymers were purified via Soxhlet extraction to remove the phosphorus by-products.



Scheme 3.5: Synthesis of DTPP polymers

3.2.4 IR Characterization

Infrared analysis of the DAP polymers shows similar peaks apart from **DAPa-BI** (Fig. 3.4), which contains the BOC group on the BI donor unit arising at 1730 cm⁻¹

¹. Furthermore, there are two weak bands composing of N-C-S and C-S peaks, arising at 786 and 690 cm^{-1} , respectively [26, 27].

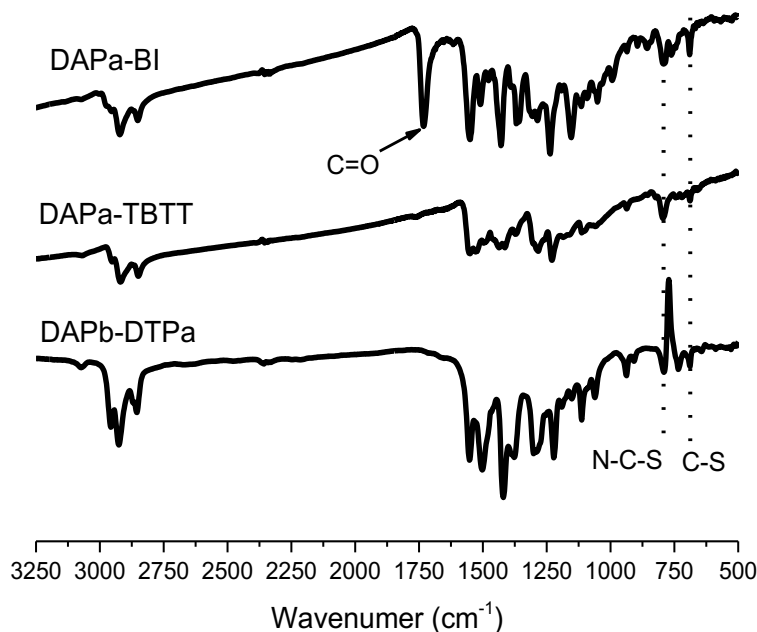


Figure 3.4: IR spectra of DAP polymers in KBr pellet.

IR analyses of **PDPP** and **PDTTP** monomers (Fig. 3.5) were done to confirm their conversion. The progression was determined by the disappearance of the C=O stretch at 1670 cm^{-1} and the appearance of the new N-C=S and C=S at 1380 and 1035 cm^{-1} . Similarly, the same trend was observed for the DTPP polymers. Polymer **DTPP-DTP** was fully converted to the thiolactam, with the lack of the ketone peak. Whereas, the **DTPP-BT** and **DTPH-TPT** were only partial converted, showing slight presence of the ketone peak at 1640 cm^{-1} .

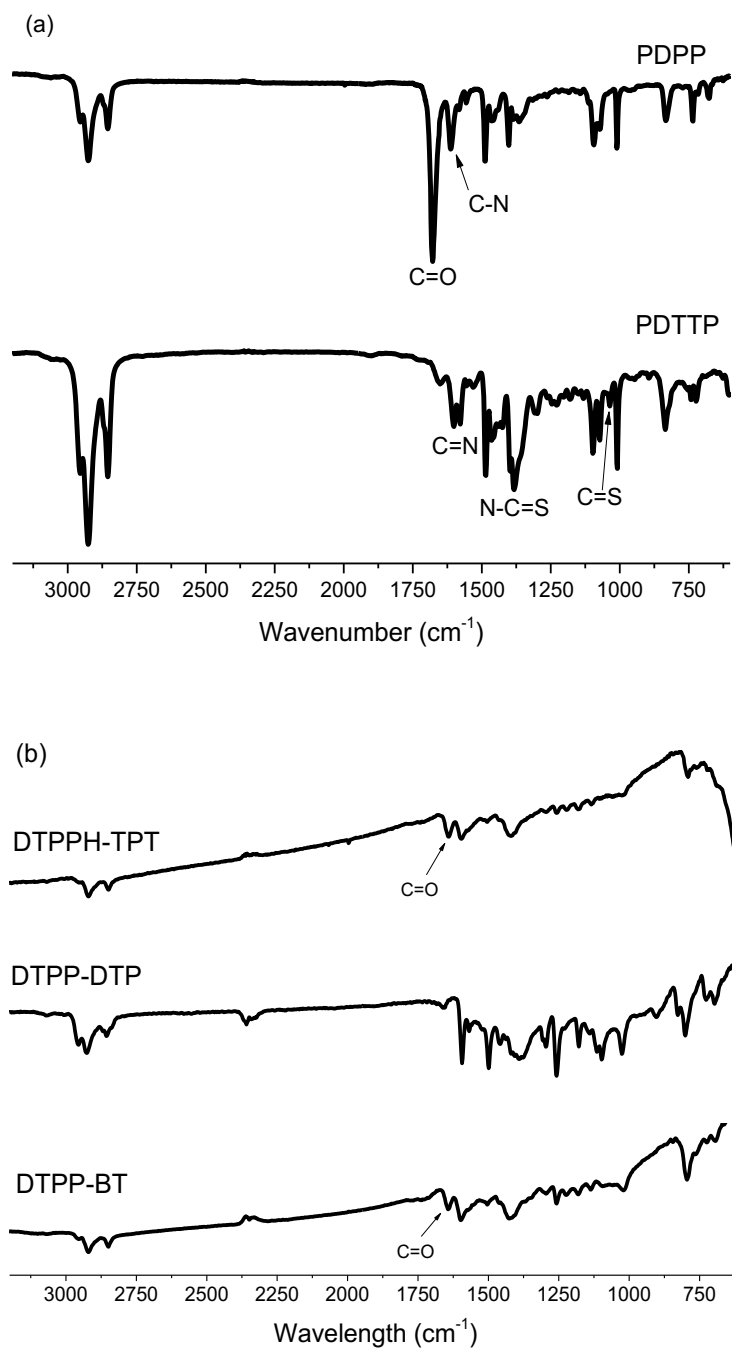


Figure 3.5: IR spectra of (a) **PDPP** and **PDTTP** monomers on NaCl (b) **DTPP** polymers KBr pellet

While studying the **PDTTP/DTTP** monomer and polymers, we noticed bleaching or loss of pigmentation when left in solution without any protection against air and light. Powder samples, however, did not show any degradation. Photodegradation of the **PDTTP** monomer was also explored via IR analysis (Fig. 3.6), a solution of **PDTTP** was allowed to sit at ambient temperature and exposed to incandescent light till solution turned yellow. Due to the low stability of the thiolactam, we observe new peaks, predominately, alcohol peak at 3300 cm^{-1} and ketone peak at 1650 cm^{-1} . This could have explained by photochemical oxidation of the thiolactam by oxygen. There are different possible pathways for degradation, first forming sulphine intermediate linkage (750 cm^{-1}) and then formation of sulfoxide (1075 cm^{-1}). Reacting with another oxygen molecule and the loss of sulfur monoxide would regenerate the carbonyl peak. An alternate pathway involves four membered cyclic C-O-O-S ring (1250 cm^{-1}) and then loss of sulfur monoxide to generate the carbonyl or ring cleavage to form hydroxyl group [28, 29].

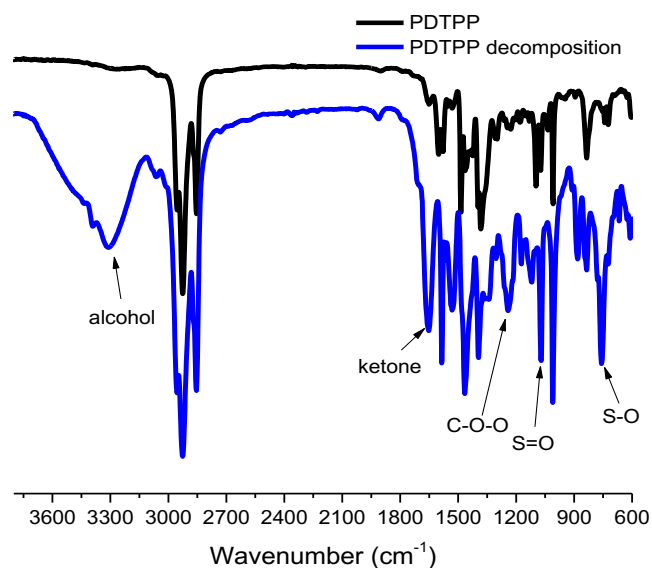
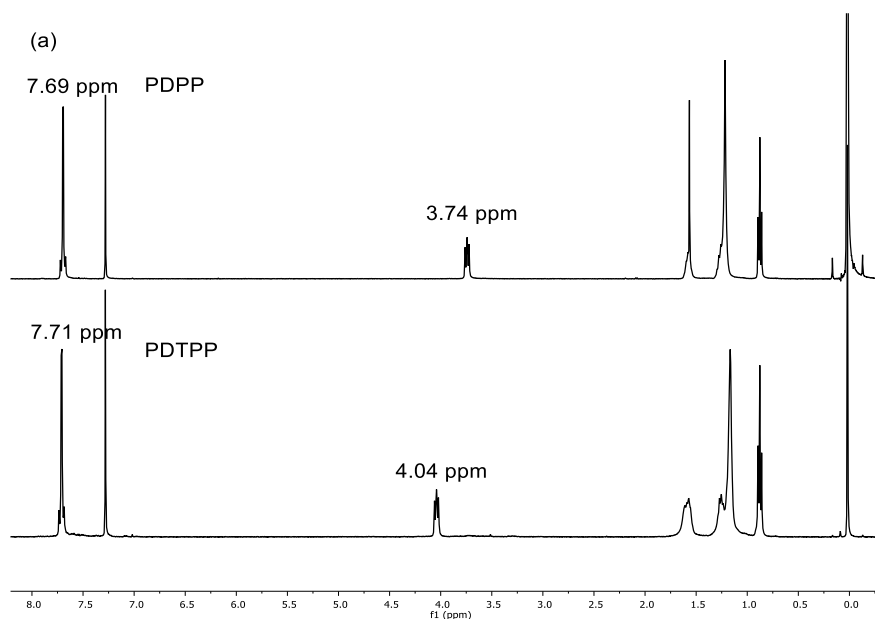


Figure 3.6: IR spectra of DTTP photodegradation

3.2.5 NMR Characteristics of PDTTP and DTPP-polymers

PDTTP was characterized by ^1H NMR and ^{13}C NMR spectroscopy. In the ^1H NMR spectra (Fig. 3.7), **PDPP** displayed all the expected resonances with no discernible peaks. The proton resonances both in the aliphatic region (0.88-1.57 ppm) due to alkyl chains and the aromatic region (7.69 ppm) due to the phenylene ring. In ^{13}C spectra, the carbonyl carbon arises at 162 ppm. In **PDTTP** there is no change to aliphatic proton, however, the proton assigned to N-CH₂ of **PDPP** core arises at 3.74 ppm, whereas, in **PDTTP** that proton is deshielded (4.04 ppm) due to stronger magnetic field caused by removal of electron density by sulfur atom. Similarly, the thiolactam is also found more downfield (177 ppm) compared to the γ -lactam.



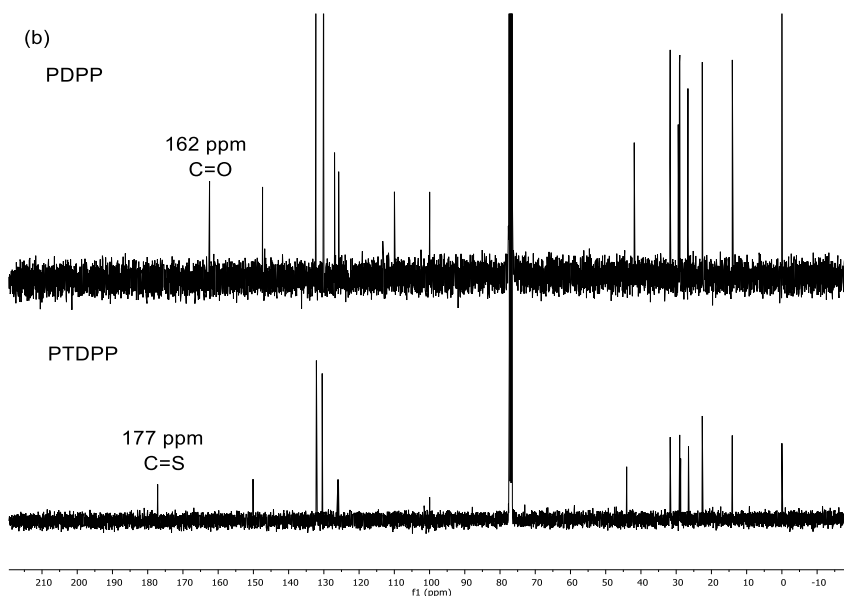
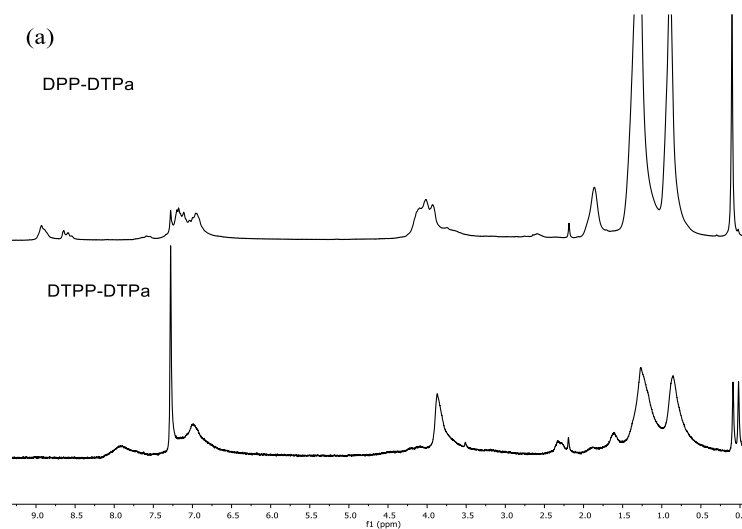


Figure 3.7: ^1H NMR (a) and ^{13}C spectra (b) of PDPP and PDTDP in CDCl_3

We see similar observation with polymers **DTPP-BT** and **DTPa** (Fig. 3.8). For both polymers, the aromatic region differs from the DPP polymers. We also observe the downfield of N- CH_2 peak, which is more evident in **DTPP-BT**. Because of the high degree of overlap, peak assignments of polymers are impossible in both aliphatic and aromatic regions.



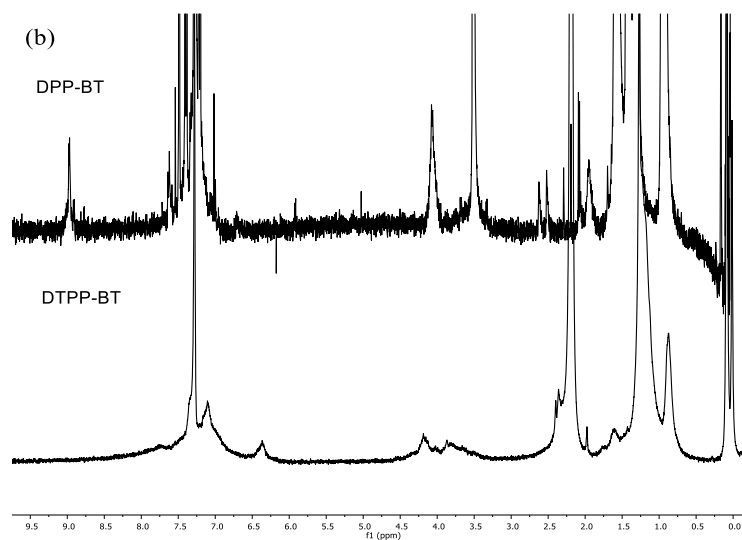
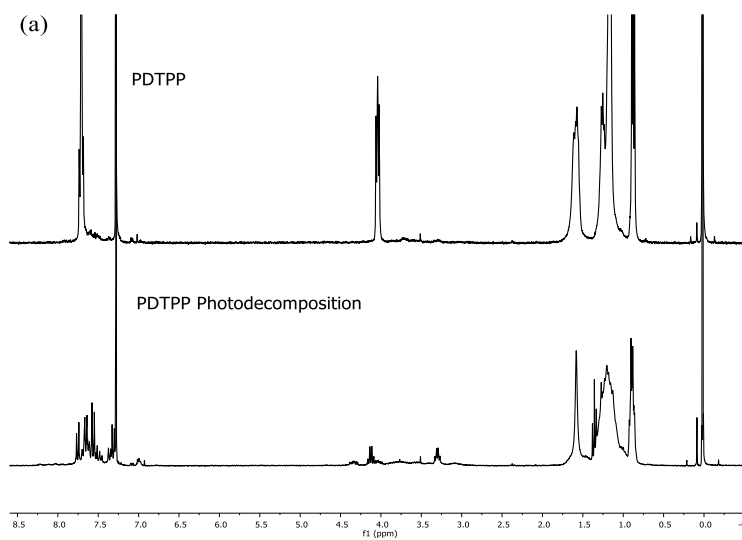


Figure 3.8: ^1H NMR of (a) **DPP-** and **DTPP-DTPa** (b) **DPP-** and **DTPP-BT** in CDCl_3 .

Proton and carbon NMR were taken of **PDTPP** after photodecomposition (Fig. 3.9). In the proton NMR, we observe splitting from phenylene proton to new aromatic peaks. Furthermore, we observe a slight downfield shift in N-CH_2 peak. What is more significant is the disappearance of the C=S peak at 177 pm. This further signifies the proposed mechanism of photodecomposition.



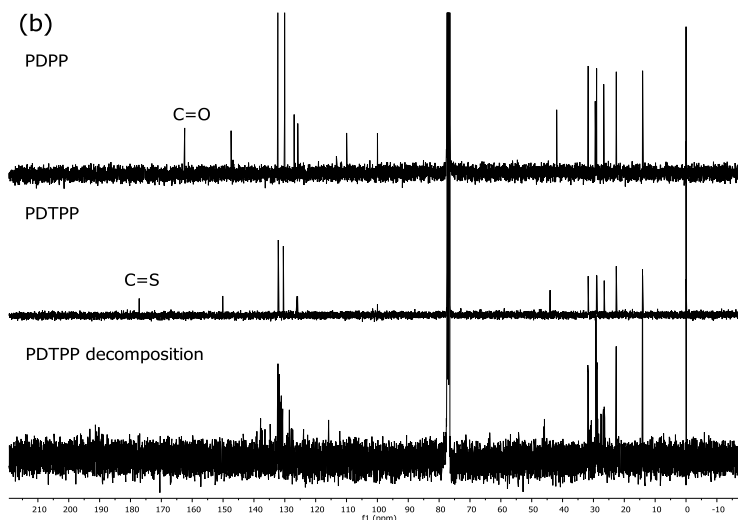


Figure 3.9: (a) ^1H NMR of **PTDPP** before and after decomposition (b) ^{13}C NMR of **PTDPP** before and after decomposition in CDCl_3 .

3.2.6 Absorption Characterization

3.2.6.1 Optical properties of DAP polymers

The optical properties of the DAP polymers were studied and are shown on Fig. 3.10 and summarized on Table 3.2. The polymers have two absorption peaks first assigned to the π - π^* transition of the conjugated polymer backbone, ranging from 350 to 530 nm. We also observe n - π^* transition for **DAPa-BI** at around 375 nm. The λ_{max} of DAP-based polymers show more red shift, compared to BDPP polymers, ranging from 685 to 830 nm in solution. This is attributed to the intramolecular charge transfer (ICT) between DAP and donor segments. The polymers containing DTP donor unit shows a broader absorption compared to the other donors, ranging from 550 to 850 nm for DPP polymer and 600 to 1600 nm for DAP polymer. This is due to combination of strong contribution of π - π^* electronic transition and donor-acceptor internal charge transfer, along with better orientation of the π - π interchain interaction [30, 31]. The

absorption spectra of the polymers in thin films show bathochromic shift compared to solution and all the thin films spectra are slightly broader, indicating stronger intermolecular interaction in the solid state. The relatively small shift of chromism is probably due to rigid conformation of polymers both in the solution and in the solid state.

Table 3.2. UV-vis absorptions of polymers.

Polymer	λ_{abs} (nm) in solution	λ_{abs} (nm) Film
DAPa-BI	375/480/700	400/470/740
DAPa-TBTT	400/730	450/750
DAPb-DTPa	450/830	445/890
DAPb-TPT	415/730	450/800

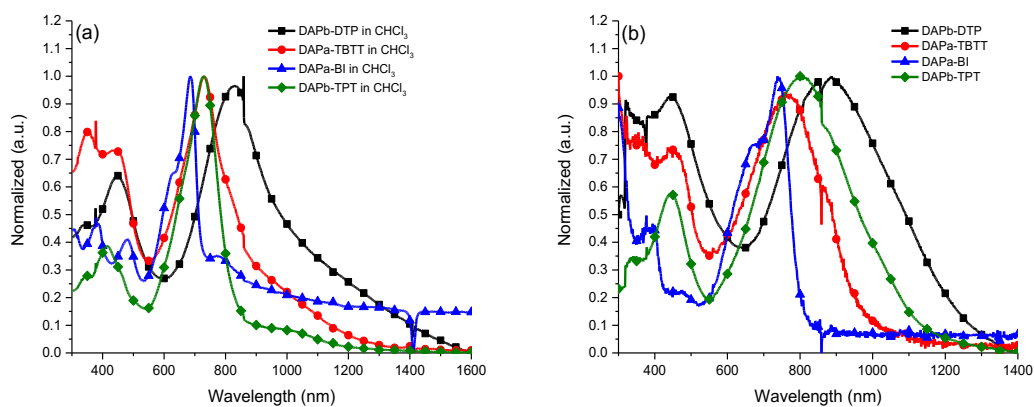


Figure 3.10: Absorption spectra of DAP polymers (a) in solution CHCl_3 (b) spin-coated on glass film.

Due to the more basic lactam in the DAP unit, acid-base reaction can occur. When the DAP polymers were treated with camphorsulfonic acid (CSA) in CHCl_3 , the absorption is red-shifted 220, 200, 115 and 50 nm for DTP, TPT, TBTT and BI,

respectively (Fig. 3.11). This is due to the increased π -donation, DTP>TPT>TBTT>BI, into the decreased electron deficient DAP+H⁺ acceptor unit. Similarly, when **DAPb-DTPa** and **TPT** films was submerged in 0.1 M CSA in MeOH, there is a 210 nm red shift. Furthermore, there is an increase of broadness ranging from 700 to 2000 nm.

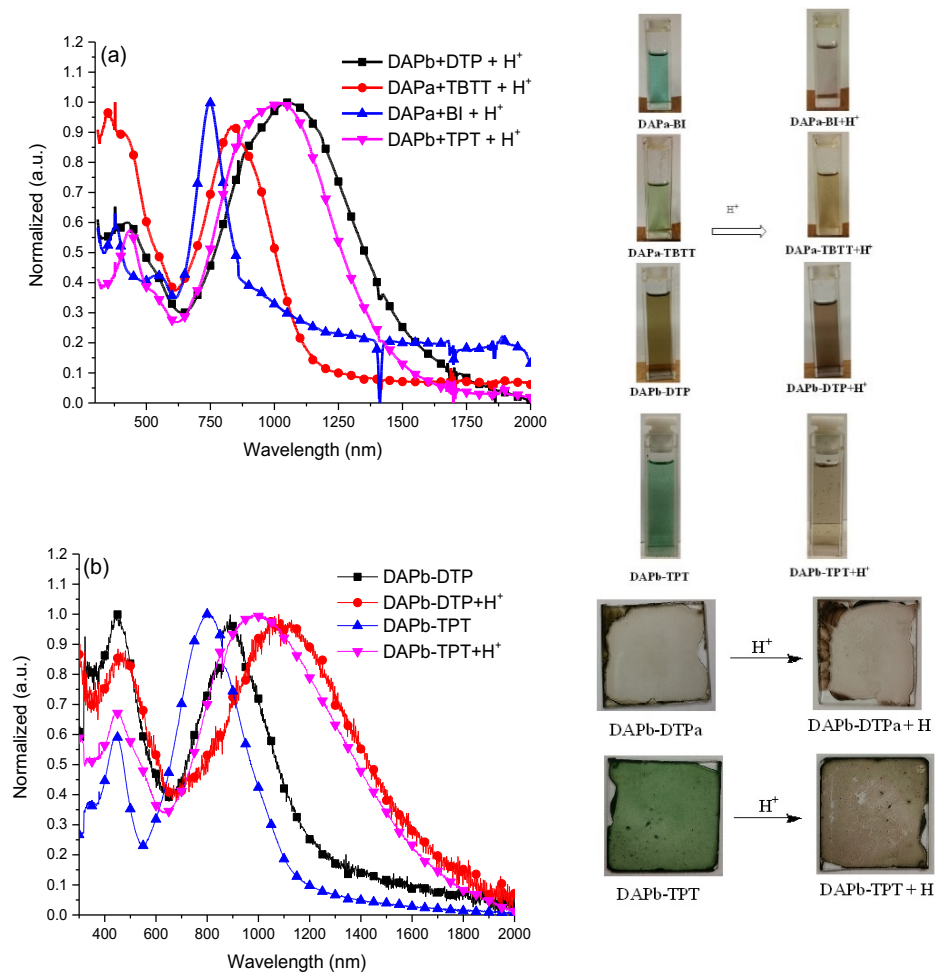


Figure 3.11: (a) Absorption of DAP polymers in CHCl₃ with CSA (b) Film absorption of **DAPb-DTPa** at room temperature and submerged in 0.1 M CSA in MeOH.

3.2.6.2 Optical properties of DTPP polymers

The optical properties of PDTPP and DTPP-based polymers were studied (Fig. 3.12-3.13). **PDTPP** was obtained as dark powder and were soluble in chloroform, toluene, THF and other organic solvents, whereas, **DTPP-DTPa** and **DTPP-BT** were slightly soluble in THF, chloroform, trichlorobenzene. Polymer **DTPPH-DTPa** and **DTPPH-TPT** showed extremely low solubility in common organic solvents. **PDPP** in chloroform show a yellow solution and upon thionation (blue solution in CHCl_3) we observe bathochromic shift from λ_{max} 480 nm to 603 nm. The fluorescence displays an emission at 540 nm with excitation at 430 nm, showing a Stokes shift of 60 nm. However, the thiolactam monomer and polymers displays no fluorescence due to the quenching by the sulfur atom. An interesting note, there is a decrease of molar absorptivity going from lactam to thiolactam, suggesting lower extinction coefficient. For photovoltaic materials, absorption coefficient is an important factor, it determines how far into a material light, at specific wavelength, can penetrate before it is absorbed. The absorption coefficient is related to extinction coefficient from the following formula:

$$\alpha = \frac{4\pi k}{\lambda}, \text{ where } \alpha \text{ is absorption coefficient and } k \text{ is extinction coefficient}$$

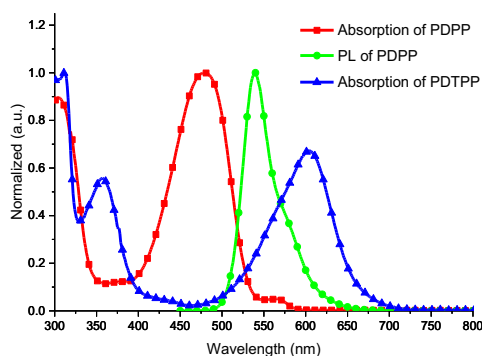


Figure 3.12: Optical properties of converted **PDPP** to **PDTPP** (10^{-5} M in CHCl_3)

The DPP polymers generally have bathochromic shift compared to PDPP, this is due to donor-acceptor interactions between thiophene and DPP core unit is more predominate than that of phenylene unit. Similar trend is observed when DPP- and BDPP-polymers are converted to the thiolactam. Polymer **DPP-BT** show broad absorption from 400 to 1200 nm, with λ_{max} peak at 670 nm. After partial conversion of the polymer, we observe a slight red shift to 710 nm. Similarly, **BDPP-** and **DPP- DTPa** show approximately 122 and 57 nm red shift, respectively. **BDPP-TPT** displays the largest bathochromic shift of all the polymers, approximately 172 nm.

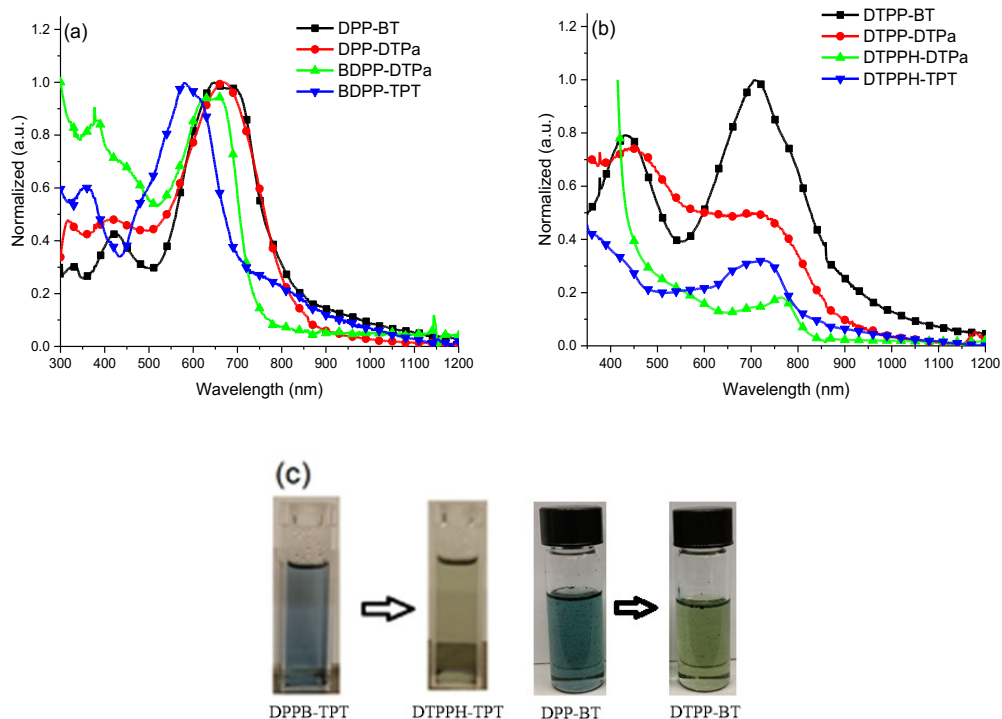


Figure 3.13: Optical properties of converted DPP to DTPP polymers in TCB.

Table 3.3: Optical summary of converted PDPP and DPP-based polymers in TCB.

Polymer	λ_{\max} (nm) in solution of ketone	λ_{\max} (nm) in solution of thioketone
PDPP	480	360/603
DPP-BT	425/670	432/710
DPP-DTPa	423/668	450/725
BDPP-TPT	363/558	730
BDPP-DTPa	384/642	764

3.2.6.3 Photodegradation of PDTTP and DTTP Polymers

The photodecomposition was studied quantitatively by exposing to incandescent light bulb (spectral range from 400-1000 nm) over period of time and measuring decrease of optical absorption. **PDTTP** was studied in two different solvents, CHCl_3 and THF (Fig. 3.14). In both solvents, the spectra indicate a decrease of the peak at 600 nm. Within 5 minutes of exposure, there is a drastic decrease of absorption. In THF, the spectral change involves two isobestic points at 500 and 378 nm, indicating photoreaction involving in a single step transition. Plotting $\ln(A_t/A_0)$ where, A_t = absorbance at given time and A_0 = absorbance at $t = 0$, vs. time for irradiation leads at exponential decay plot. Thus plotting a regression line, we can determine mean lifetime (τ) and decay rate (λ) using the following formulas:

$$N(t) = N_0 e^{-\frac{t}{\tau}}$$

$$\tau = \frac{1}{\lambda}$$

Thus, it was determined the mean lifetime of **PDTTP** in CHCl_3 was 8.78 min and decay rate of 0.114 min^{-1} , where as in THF, the mean lifetime is 13.9 min and decay rate of 0.0718 min^{-1} .

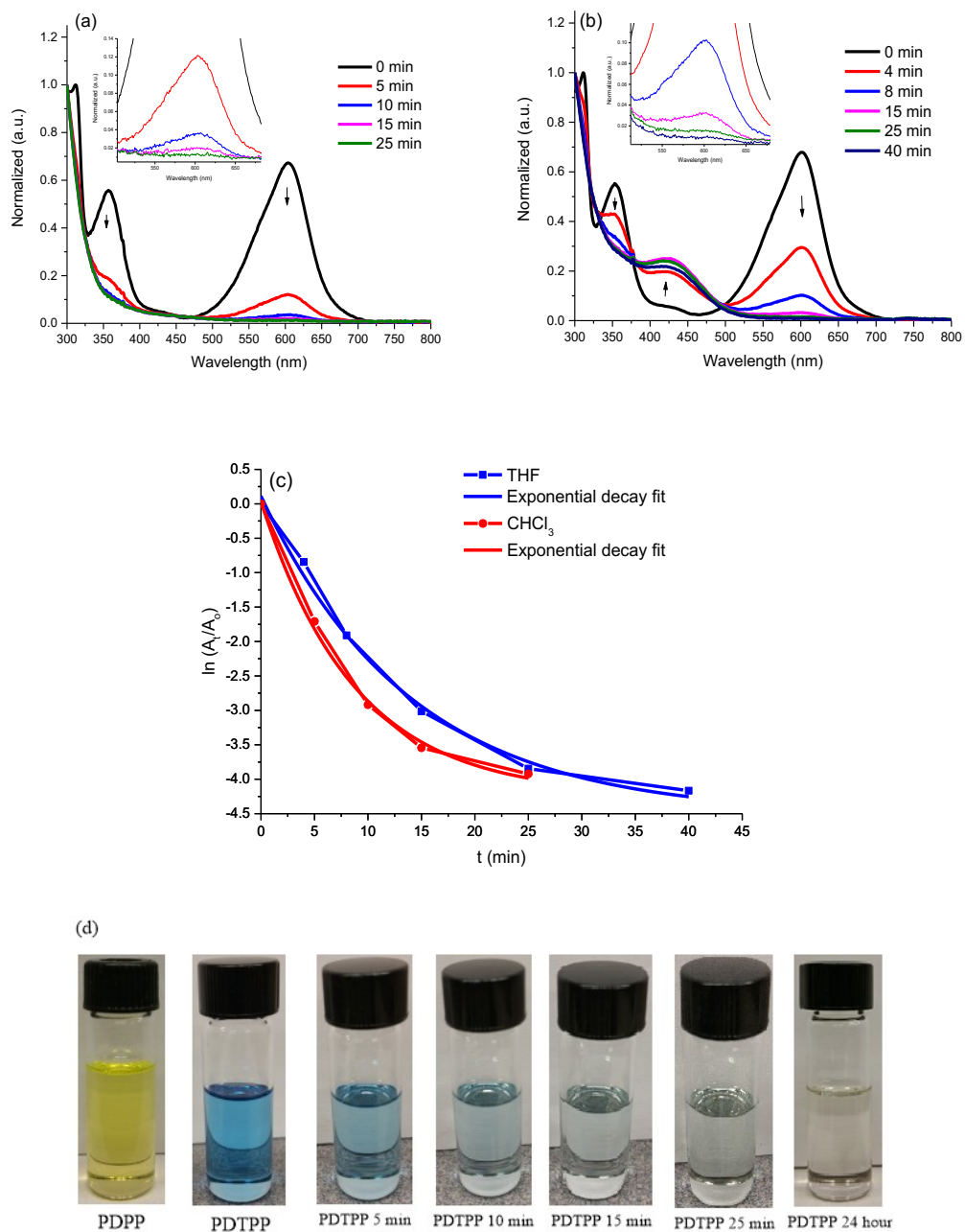
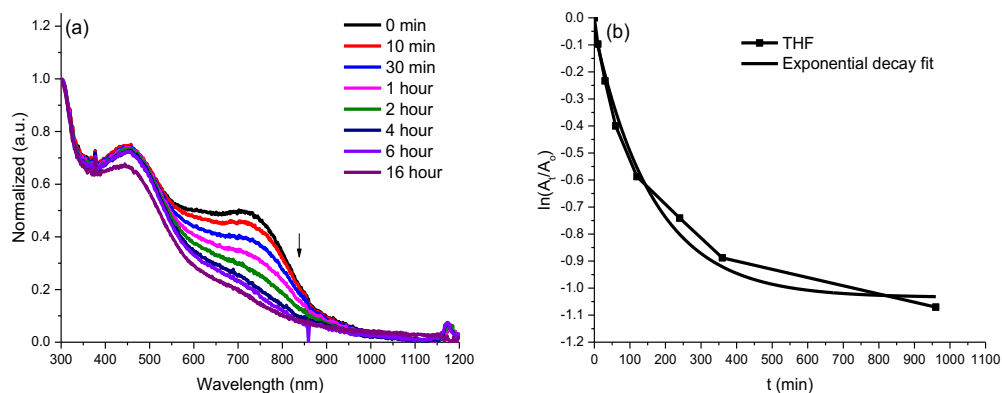


Figure 3.14: Photodegradation of PDTTP (10^{-5} M) (a) in CHCl_3 (b) THF (c) Plot of $\ln(A_t/A_0)$ vs. time for determination of rate constants k (d) Photographic images of the solution vs. time

Photodecomposition behavior of **DTPP-DTPa** show similar trend compared to **PDTPP** monomer (Fig. 3.15), except photodegradation is much slower and without an isobestic point. This indicates that exposure to light may involve several chemical reactions. As expected, the mean lifetime is much high for the polymer at 166.5 min (2.77 hours) with a decay rate of $6.01 \times 10^{-3} \text{ min}^{-1}$. This is probably due to strong donor-acceptor character of the polymer which prevents energy transfer from the DTP unit into the DPP core, thus contributing to higher photostability. **DTPP-BT** exhibit different characteristic when exposed to white light (Fig. 3.15c). Compared to **DTPP-DTPa**, where the absorption peak arising from the ICT decreases and π - π transition band increases, that phenomenon is not present for BT polymer. Instead, we observe a slight broadness in the near-infrared region, slight hypsochromic shift and increase in the π - π transition. Since the polymer is partially converted, it overall resists to photo decomposition.



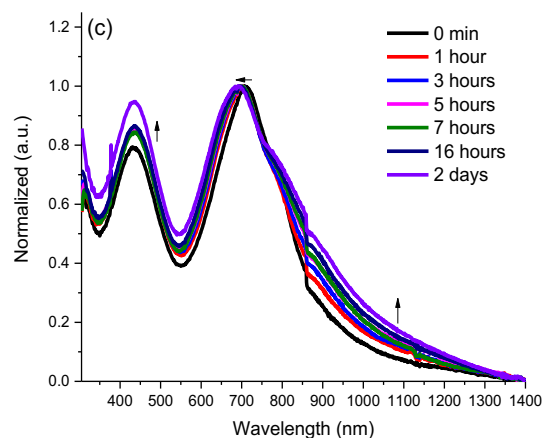


Figure 3.15: Photodegradation of **DTTP-DTPa** (10^{-5} M) (a) in THF (b) Plot of $\ln(A_t/A_0)$ vs. time for determination of rate constants k (c) Photostability of **DTTP-BT** (10^{-5} M)

Studies have shown that photodecomposition of DPP-polymers proceed in two processes, the first step which is the absorption of light by the DPP core chromophore and is usually a slow process. In the second step, much rapid process, addition light absorption by co-monomer and subsequently energy transfer to the DPP core. Therefore, the latter effect favors the rapid decomposition. Since, **PDTPP** does not exhibit a donor-acceptor characteristic, the energy absorbed by the phenylene spacer increases decomposition [32].

3.2.7 Thermal Characterization

Since the polymers are to be used in OPDs, the thermal stability is one of the major factors that needs to be determined. Polymers were characterized by thermogravimetric analysis (TGA) and differential scanning calorimetry (DSC) (Fig. 3.16). The DAP polymers have high decomposition temperature (T_d) above 250 °C,

thus being suitable for the device fabrication. Similarly, **DAPa-BI**, in which the BOC contributes to approximately 20% weight of the polymer, has a T_d of 257 °C after 5% weight loss. DSC is a good tool to determine physical transformation of material such as glass transition state (T_g) or crystallization temperature (T_c). It is essential during the fabrication of the devices that the polymers films are annealed at certain temperature so that the polymers are at ideal conformation. All polymers are amorphous based on the evidence of no crystallization peaks in DSC, this is due to the presence of the bulky aliphatic chains in the donor and acceptor core. This hinders the packing of the conjugated backbones. The glass transition states were not observed in the polymers. However, we do observe transition for **DAPa-BI** at 180 °C, which is due to the loss the BOC group from the biindole backbone.

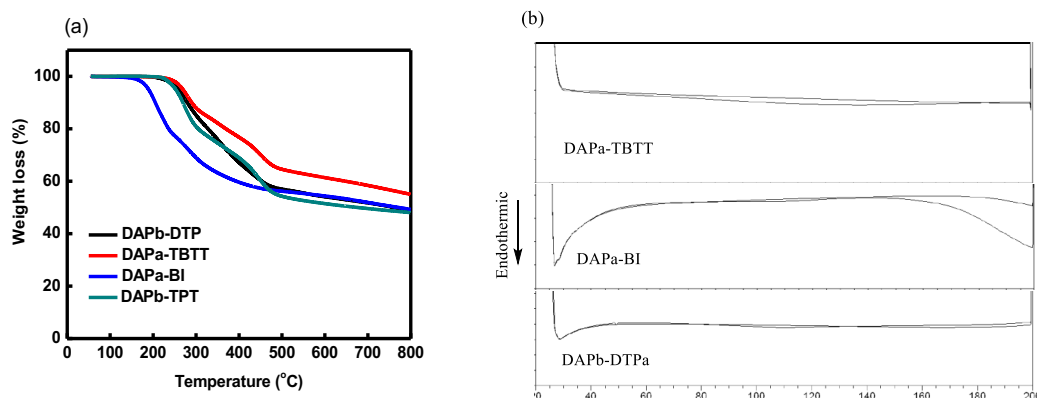


Figure 3.16: (a) TGA and (b) DSC of DAP polymers

Polymer **DTPP-BT** showed the highest thermal stability with T_d of 290 °C. Conversely, the rest of the polymers has lower T_d of 250 °C. When compared to **DPPB-TPT** and **DPPB-DTP**, the DTPP polymers showed lower thermal stability, this could be due to overall lower stability of the thiolactam backbone.

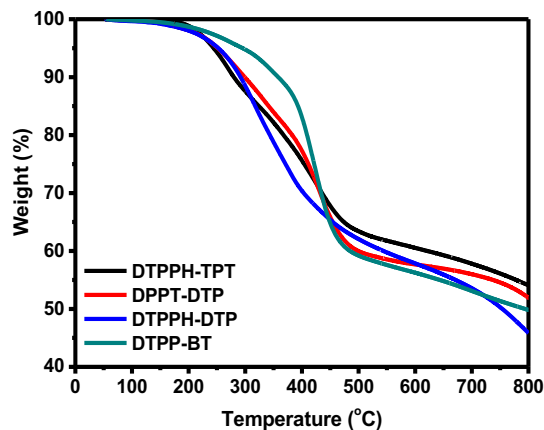


Figure 3.17: TGA of DTPP polymers

3.2.8 Electrochemical Characterization and Band Gap Calculation

3.2.8.1 DAP polymers

Electrochemical cyclic voltammetry (CV) was performed to determine the HOMO and LUMO energy levels of the polymers. Platinum wire was used as a counter electrode, Ag/Ag⁺ was used as a reference electrode and were calibrated with ferrocene/ferrocenium (Fc/Fc⁺) redox couple. The oxidation of Fc/Fc⁺ was measured to be 0.44 V and the absolute redox potential is -4.8 eV below vacuum [2]. Thus, the HOMO and LUMO values can be calculated according to the following equation:

$$E_{\text{HOMO/LUMO}} = -e(E_{\text{ox/red}} + 4.36) \text{ (eV)}$$

From the onset oxidation potential E_{ox} and onset reduction potential E_{red} , the HOMO and LUMO levels as well as the band gap E_g were calculated and listed in Table 3.4. The DAP polymers show reduction potential; however, the oxidation potentials are not evident except for polymer **DAPb-DTPa** (Fig. 3.18). From the onset of the reduction potential the lowest unoccupied molecular orbital (LUMO) energy levels are calculated to be -4.28, -4.23 and -4.10 eV for **DAPa-BI**, **DAPa-TBTT** and **DAPb-DTPa**,

respectively. The LUMO level of the polymers are in optimal position for effective exciton dissociation with regards to that of PCBM LUMO level (-4.2 eV) [33]. The HOMO level, which can be calculated from the optical band-gap for polymers **DAPa-BI** and **DAPa-TBTT**, are -5.70 and -5.28 eV. Whereas, the HOMO level for polymer **DAPb-DTPa** evident on CV curve at -4.86 eV. The corresponding band-gap of **DAPb-DTPa** is 0.76 eV, which is significantly lower than that of the other DAP polymers. Changing the donor from BI to DTPa, we observe both HOMO and LUMO deepening, this occurrence is owed to stronger interaction between adjacent DTP units in the chain.

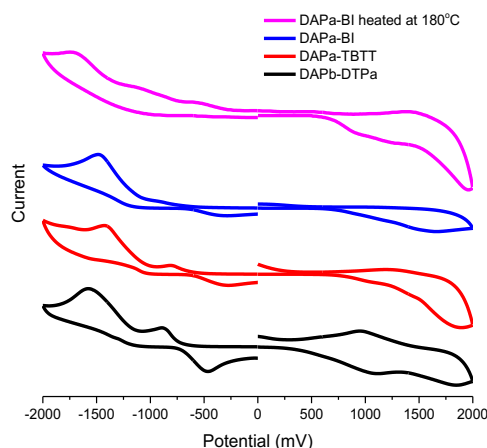


Figure 3.18: Cyclic voltammetry of DAP polymers on ITO in 0.1 M Bu_4NPF_6 in acetonitrile at scan rate of 100 mV/s

Table 3.4: Electrochemical properties and band gaps of polymers

Polymer	HOMO (eV) ^(a)	LUMO (eV) ^(a)	Band gap (eV) ^(b)
DAPa-BI	-5.70 ^(d)	-4.28	1.42 ^(c)
DAPa-TBTT	-5.38 ^(d)	-4.23	1.15 ^(c)
DAPb-DTPa	-4.86	-4.10	0.76

(a) For thin films, calculated from $E(\text{HOMO}) = -(E_{\text{ox}} + 4.36)$ (eV) $E(\text{LUMO}) = -(E_{\text{red}} + 4.36)$ (eV). (b) The energy gap (E_g) is derived from the HOMO subtracting the LUMO. (c) Optical energy gap calculated from the absorption onset. $E_g = 1240/\lambda$ (onset, nm). (d) Calculated from optical band gap.

3.2.8.2 DTPP polymers

CV of polymers **DPPDTPa/BT** and **DTPP-DTPa/BT** were done before and after conversion. The DPP polymers show redox potential, with **DPP-DTPa** having a HOMO level at -4.48 eV, LUMO level at -2.72 eV and band gap of 1.76 eV. Once converted, the HOMO level deepens to -4.58 eV, as well as the LUMO also decreasing to -2.54 eV. However, despite the lowering of both HOMO and LUMO levels, the band gap increases to 2.04 eV, which is probably due to increasing absorption in UV region. Similarly, **DPP-BT** has a HOMO level at -4.85 eV, LUMO level at -3.27 eV and band gap of 1.58 eV. The LUMO level of **DTPP-BT** is measured at -2.84 eV, which is slightly higher compared to other thiolactam analogue. However, the HOMO level (-4.06 eV) of **DTPP-BT** is not evident and thus calculated from the optical band gap (1.22 eV).

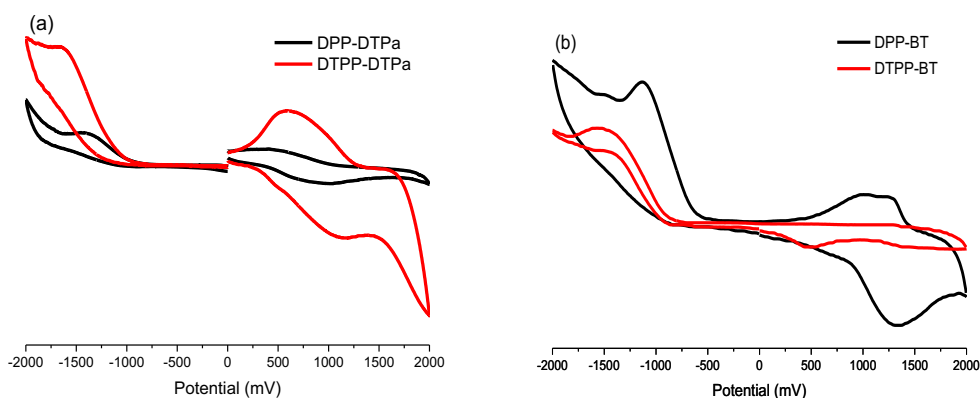


Figure 3.19: Cyclic voltammetry of (a) **DPP/DTPP-DTPa** (b) **DPP/DTPP-BT** on ITO in 0.1 M Bu_4NPF_6 in acetonitrile at scan rate of 100 mV/s

3.2.9 Polymer Photodetectors

3.2.9.1 Single-layer photodetector based on DAP polymers

Photodetector properties of single-layer DAP polymers were studied. The basic device configuration of ITO/PEDOT:PSS (30 nm)/active layer (80 nm)/Al (100 nm) was used. The active layers were composed of DAP polymer and PC[61]BM in an optimized weight ratio of 1:3. The current density-voltage (J-V) characteristic of the polymers are summarized on Table 3.5. Asymmetry behavior is observed under reverse and forward bias with the polymers showing relatively low dark current and **DAPa-TBTT** showing the lowest dark current of $9.97 \times 10^{-9} \text{ A cm}^{-2}$. The absorption profile of the films and EQE curve (Fig. 20a) correlates to efficient photon absorbed in the visible to near-infrared region. Polymers **DAPb-TPT** and **DAPb-DTPa** shows superior response to photon absorption in the near-infrared reaching up to 25% (760 nm) and 24% (900 nm) at -2 V bias, respectively. Furthermore, **DAPb-DTPa** show average EQE of 17% from 300-1000 nm. Equally, the responsivity is expressed a function of the wavelength of the incident radiation in the following equation:

$$R = n \frac{q}{hf} \approx \frac{\lambda_{\mu m}}{1.23985 (\mu m \times \frac{W}{A})}$$

where, n is the quantum efficiency, q is the electron charge, f is the frequency of the optical signal, and h is Planck's constant. Therefore, **DAPb-TPT** and **DAPb-DTPa** demonstrates maximum responsivity of 156 (770 nm) and 176 (920 nm) mA W^{-1} . The detectivity, calculated in Jones ($\text{cm}\sqrt{\text{Hz}}/\text{W}$), measures relative noise levels present in

the device. The higher the detectivity, the better the device can detect signal from noise. All the polymers show detectivity above 10^{11} Jones at -0.1 V bias from visible to near infrared region. However, when applying higher voltage, we observe lower detectivity due to lower film stability (Appendix D). Polymers **DAPb- TPT/DTPa** display the highest stability, although having lower detectivity at -2 V, approximately 5x lower for DTPa and 10x lower for TPT.

Table 3.5: Performance of OPDs based on single-layer DAP polymers

Polymer	Dark current ($A\ cm^{-2}$) ^(a)	Responsivity ($mA\ W^{-1}$) ^(b)	Detectivity (Jones) ^(c)
DAPa-BI	1.12×10^{-8}	36 (710 nm)	6.01×10^{11}
DAPa-TBTT	9.97×10^{-9}	21 (770 nm)	1.15×10^{12}
DAPb-DTPa	2.49×10^{-8}	174 (920 nm)	9.98×10^{11}
DAPb-TPT	1.85×10^{-7}	156 (770 nm)	9.59×10^{11}

(a) Dark current under bias of -0.1V (b) Responsivity at -2 V reverse bias (c) Detectivity at -0.1 V reverse bias at 800 nm

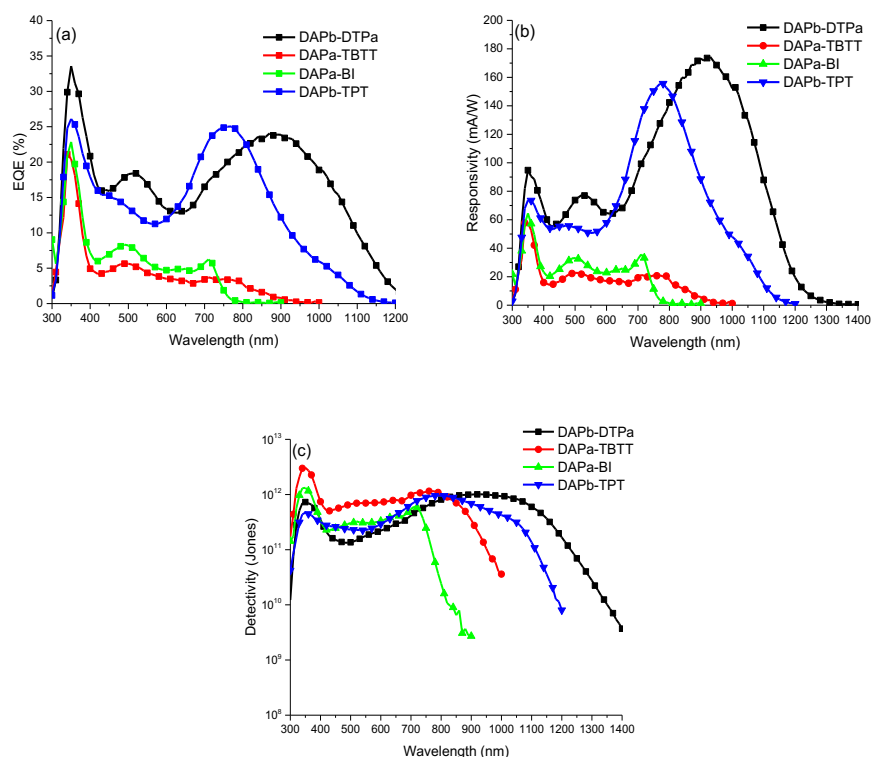


Figure 3.20: Photodetector properties of DAP polymers (a) EQE at -2 V bias (b) responsivity at -2 V bias (c) detectivity at -0.1 V bias.

We also developed ternary blend devices using BDPP and DAP polymers. Adopting a multi-layer stack has become a serious technical challenge, such as processing of a sturdy intermediate layer, coupling of appropriate active layer as well as the optimizing the layer's thickness. Recently, a new strategy has been adopted keeping in mind of tandem cell design. This design, organic ternary devices, contains a host wide bandgap polymer, NIR sensitizer and acceptor molecule (Fig. 3.21) [34]. The ternary approach would improve the photon-harvesting limit while removing the intermediate layer required in a tandem cell, thus would result in a higher EQE in a single junction cell.

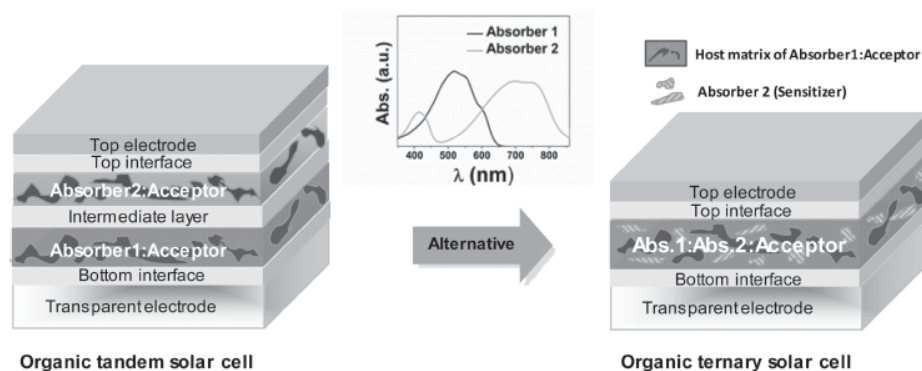


Figure 3.21: Difference between tandem cells and ternary blend (Adapted with permission from Ref. 34)

There are two mechanisms on how a ternary cell functions. The first proposed mechanism is the cascade charge transfer (Fig. 3.22a), where the HOMO level of the sensitizer (low bandgap) material is deeper than the host material (large bandgap). Due to this arrangement, excitons are generated in both sensitizer and host material. The electrons cascade down to the LUMO of the acceptor (PCBM). Whereas the hole is

transferred to the HOMO of host material and then to the anode [34]. The second proposed mechanism is the parallel-like charge transfer (Fig. 3.22b); this method uses two or more materials with different band gaps but have similar polarity. Excitons are generated in the donor materials and the electrons and holes are transferred to their respective electrodes.

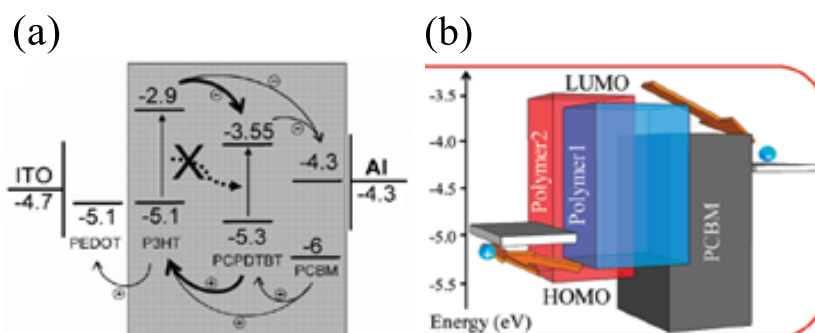


Figure 3.22: Mechanism of ternary blend (a) cascade charge transfer (Adapted with permission from Ref. 35) (b) parallel-like charge transfer (Adapted with permission from Ref. 36)

The devices we designed are based on polymers with similar polarity thus having efficient miscibility. We used polymers **BDPP-TPT** and **BDPP-TBTB** as the host material and **DAPb-TPT** as the near infrared sensitizer. Two devices were made using the following architecture:

Device A: ITO/PEDOT:PSS/**BDPP-TPTB**:**DAPb-TPT**:PCBM/Al

Device B: ITO/PEDOT:PSS/**BDPP-TPT**:**DAPb-TPT**:PCBM/Al

The active layers were composed of blended BDPP and DAP polymer and PC[61]BM at a weight ratio of 1:1:3 in chlorobenzene. The films were then thermally annealed to remove any residue solvent and also cleave to the BOC group from the BDPP polymer.

This would insure a hydrogen bonded network between the free N-H from the DPPB and the nitrogen of thiolactam DAP polymer, thus improving charge carrier. The dark current for the devices are at 10^{-8} A/cm² at -0.1 V bias, which is relatively low. With increasing bias, we observe an increase of dark current, reaching up to 10^{-5} A/cm² at -2 V for Device A, although, Device B show lower dark current at -2 V, 10^{-7} A/cm² (Fig. 23a). There are two maximum photon absorption peaks, first one in the UV region (350 nm), which is more predominate, having reached EQE of 25% for Device A and 10% for Device B. The second absorption, which in the near infrared region (800 nm), reaching 7% for Device A and 1.7% for Device B at -2 V bias (Fig 23b). The low EQE could be due to high recombination effect, which can be caused by poor film formation. Furthermore, green light is absorbed in the bulk of the device and a low diffusion length can affect the collection probability and ultimately reduce the quantum efficiency. Concurrent with the EQE absorption peak, the responsivity shows maximum of 47 mA/W for Device A and 11.2 mA/W for Device B at -2 V bias. Device A also shows higher detectivity, 1.3×10^{11} Jones, although tailing off as reaching above 900 nm. Device B show more stability ranging from 300 to 1200 nm. Furthermore, with increasing bias voltage Device B is relatively more stable, whereas Device A the detectivity significantly reduces (Fig 23d).

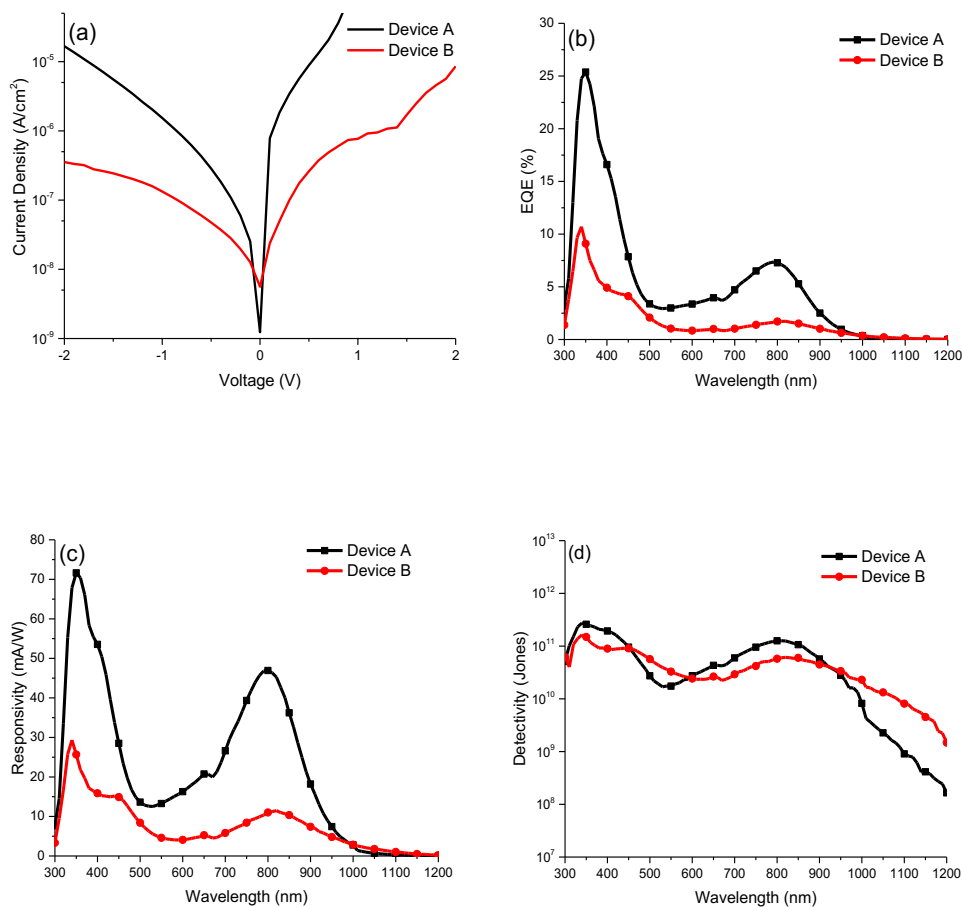


Figure 3.23: Photodetector properties of ternary blend Device A: **BDPP-TPTB:DAPb-TPT** and Device B: **BDPP-TPT:DAPb-TPT** (a) current-density voltage (J-V) characteristics (b) EQE at -2 V bias (c) responsivity at -2 V bias (d) detectivity at -0.1 V bias.

3.2.9.2 Multilayer photodetector performances of DPP-DAP polymers

Different devices based on multilayer structure were designed (Fig. 3.24).

The basic configuration is as follows:

ITO/PEDOT:PSS/active layer 1:PCBM/active layer 2:PCBM/Al.

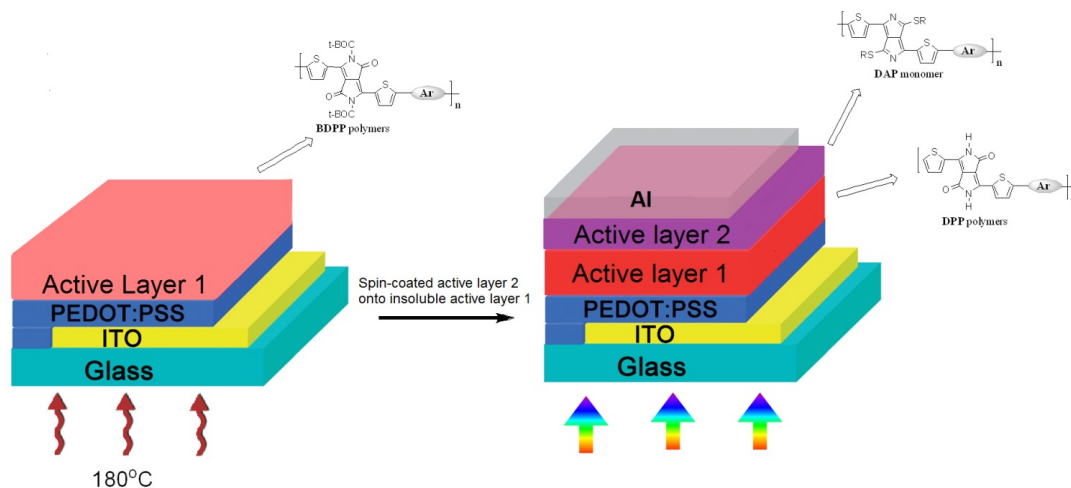


Figure 3.24: Multilayer device configuration

Six devices were developed with different active layer 1 and 2. The devices were postulated with the most promising polymers and the photodetector properties are summarized on Table 3.6. The devices are based on the following polymers:

Device A: **DPP-BT:DAPb-TPT**

Device B: **DPP-TPTB:DAPb-TPT**

Device C: **DPP-BI:DAPb-TPT**

Device D: **DPP-DTPa:DAPb-DTP**

Device E: **DPP-DTPa:DAPa-TBTT**

Device F: **DPP-BI:DAPa-BI**

Active layer 1 is composed of soluble-DPP polymer and (6,6)-phenyl C₆₁ butyric acid methyl ester (PCBM) in a weight ratio of 1:3. It is then spun-coated on top of the buffer layer and then annealed at 180°C to render the polymer insoluble and trapping the PCBM in the polymer matrix. Active layer 2, which contains the DAP polymer and PCBM at 1:3 weight ratio, is then spun-coated on top of

active layer 1. Active layer 1 is aimed for spectral response in the wide band-gap region, whereas, active layer 2 is aimed for low band-gap region.

Table 3.6. Photodetector properties of multilayer devices.

Devices	EQE ^A	R ^D	J _d ^D	D ^{*E}
A	25%	147.7	3.4x10 ⁻⁷	8.9x10 ¹¹
B	14%	86.1	1.4 x10 ⁻⁷	8.3x10 ¹¹
C	20%	117.9	9.2 x10 ⁻⁸	9.2x10 ¹¹
D	20%, 25% ^b	177.6	3.6 x10 ⁻⁸	8.9x10 ¹¹
E	4%	17.5	2.8 x10 ⁻⁸	7.6x10 ¹¹
F	4.5% ^c	26.7 ^c	6.24x10 ⁻⁹	1.83x10 ¹¹

^aat 750 nm at -2 V bias ^bat 900 nm at -2 V bias ^cat 710 nm at -2 V bias ^dResponsivity (mA W⁻¹) at 750 nm for device a-c, e and 900 nm for device d at bias -2 V. ^dDark current (A cm⁻²) at 0.1 V bias ^eSpecific detectivity (Jones) at 750 nm for device a-c, e and 900 nm for device d at bias -0.1 V bias.

The dark current density-voltage (J - V) characteristics under reverse and forward biases were measured (Appendix D). The devices show asymmetry characteristic and devices A-C show similar dark current, whereas, device D, E and F show lower current, due to better film formation. The devices based on the selective polymer combinations exhibit photovoltaic response from 400 to 1400 nm. The devices show high responsivity in two spectral region 400 to 550 nm and 650 to 1000 nm (Fig. 3.25a) which correlates to the strong intense absorption in those regions. The polymers exhibit high responsivity with increase applied bias (0, -0.1, -0.5, -1 and -2 V) (Appendix D), which is due field-induced exciton dissociation.

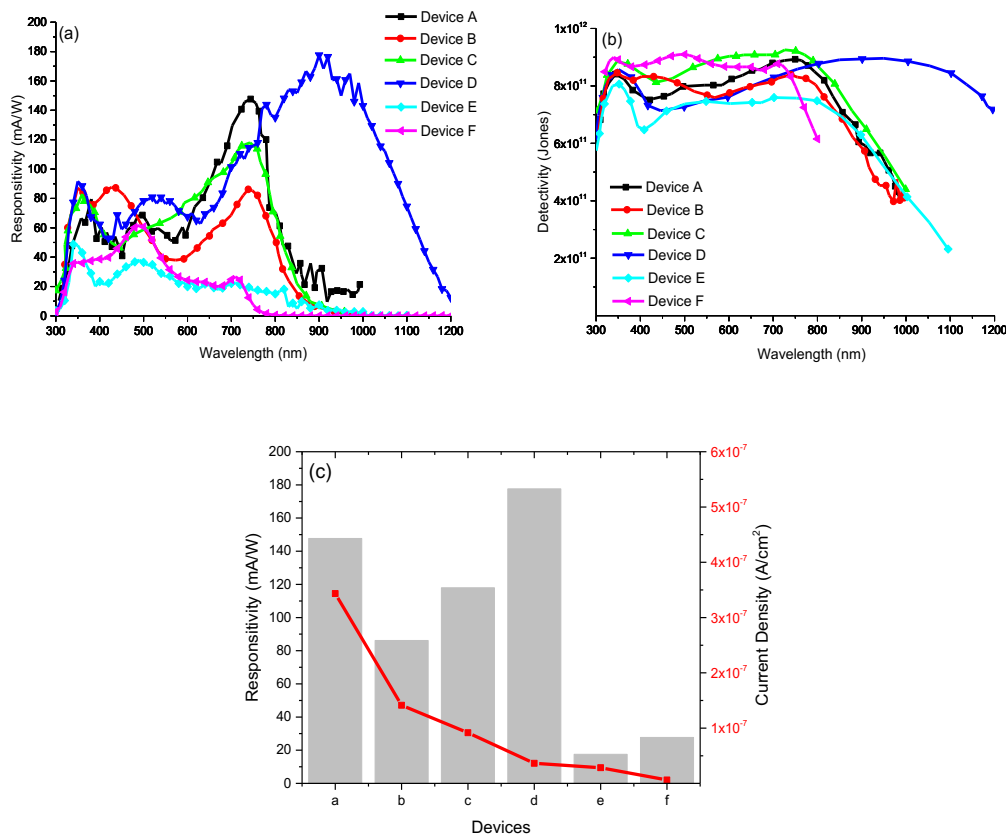


Figure 3.25: Photodetector properties of multilayer devices (a) Spectral responsivity of devices **A-F** under -2 V bias (b) Specific detectivity of devices **A-F** under voltage of -0.1 V. (c) Responsivity (bar) at 750 nm for devices **A-C, E, F** and at 900 nm for device **D**. Dark current density (squared line) under -0.1 V bias.

Device D exhibits the highest responsivity, peaking at 117.6 mA/W at 900 nm, which is one of the highest reported in the near infrared region. The specific detectivity based on the devices show high detectivity in the 10^{11} Jones region with a broad spectral response ranging from 400-1100 nm (Fig. 3.25b). The different variations in the detectivity are due to dark current, polymer morphology, and the quality of the device architecture. Device C, D and F show the most stability with low variation with

increased applied biases (Appendix). Device D shows high detectivity from 400 nm to 1200 nm reaching up to 8.9×10^{11} Jones.

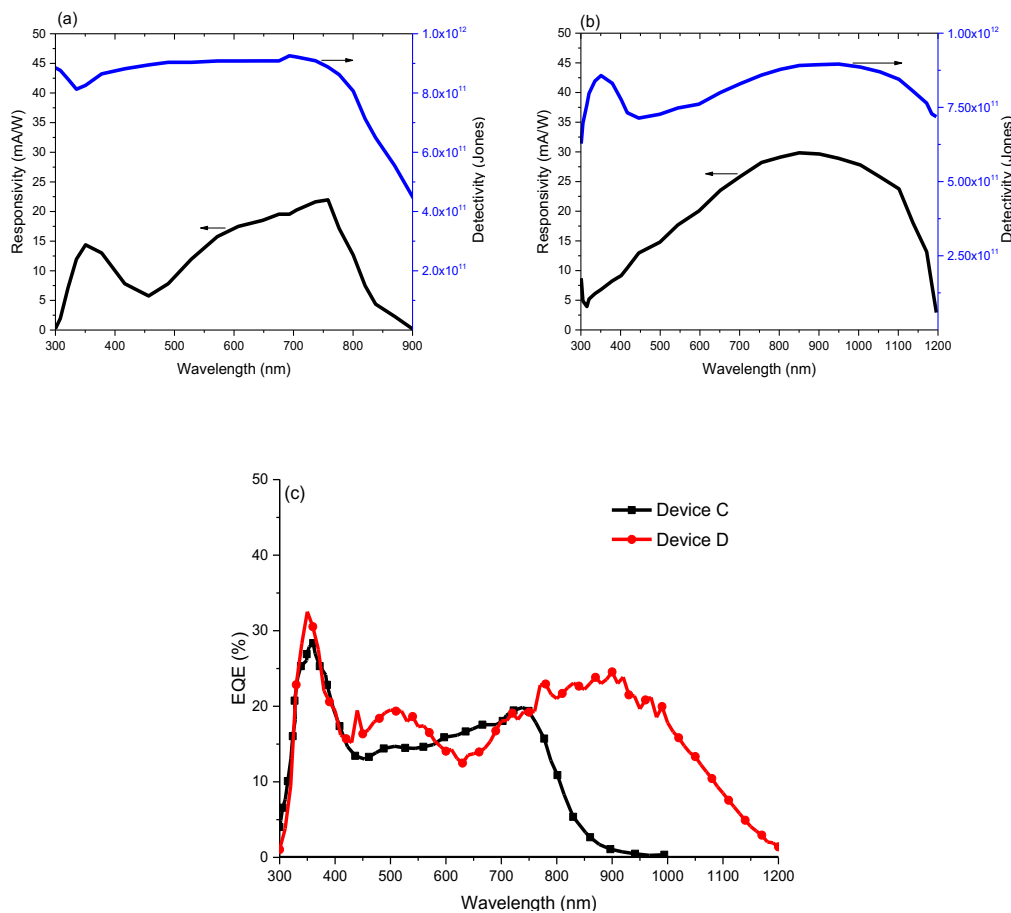


Figure 3.26: Photodetector response for Device C and D (a) Detectivity/responsivity at -0.1 V bias for device C. (b) Detectivity/responsivity at -0.1 V bias for device D. (c) External quantum efficiency profile for device C and D at -2 V.

3.2.9.3 Photodetector based on DTPP polymers

Despite the poor photostability of the DTPP polymers, we fabricated devices based on **DTPP-DTPa** and **DTPP-BT**. As expected the devices showed poor stability with increasing voltage. Which is likely due to purity of the polymers. Soxhlet extraction were done to remove the phosphine oxide by products, however, residual

amount still remained. This would drastically diminish the device performances. Although the dark current was reasonably low for **DTPP-DTPa**, in the nano A/cm^2 , **DTPP-BT** showed symmetrical curve, which is not ideal for photodetector device. When the device was applied with -100 mV voltage, we observe extreme fluctuation, resulting in a destabilized device.

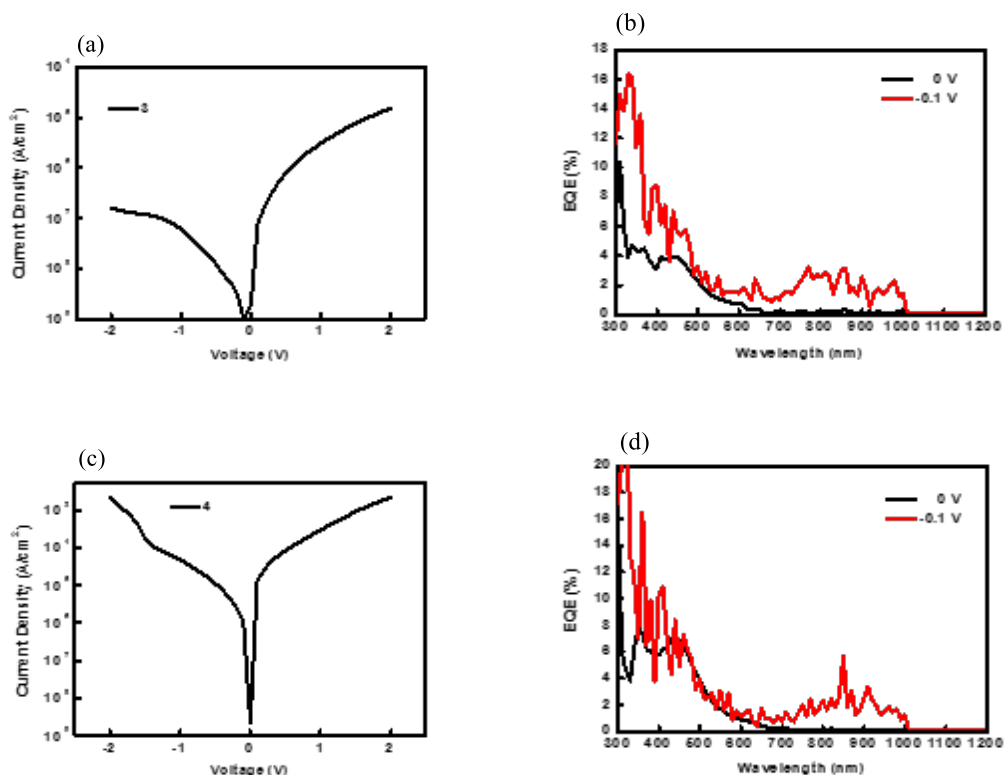


Figure 3.27: Photodetector performance of DTPP polymers (a) J-V curve of **DTPP-DTPa** (b) EQE of **DTPP-DTPa** (c) J-V curve of **DTPP-BT** (d) EQE of **DTPP-BT**

3.3 Conclusion

Three new DAP polymers were successfully synthesized by Stille and Suzuki cross-coupling and were fully characterized. These polymers exhibit narrow band gap, with the lowest reaching 0.76 eV, and show UV-Vis and NIR spectral response from

350 to 1300 nm. Furthermore, successful conversion of DPP- and BDPP – based polymers to their thiolactam were demonstrated and were confirmed by IR and NMR. The converted polymers show a bathochromic shift, however show photodegradation over time, thus not suitable for device. Single and multilayer devices were developed to study photoactivity of DAP and BDPP polymers. In the multilayer configuration BDPP polymers were used as the active layer 1, which has a spectral response at the higher wavelength. After thermal treatment, the active layer 1 is rendered insoluble and the lower band gap polymer, DAP polymer, can be spin coated. Different combination of BDPP and DAP polymers were explored, with **DPP-DTPa** and **DAPb-DTPa** showing the best result.

3.4 Experimental

3.4.1 Materials

Tetrahydrofuran (THF, Aldrich) was dried by refluxing over sodium solid and benzophenone. N,N-dimethylformamide (DMF, Aldrich) was dried under molecular sieves overnight and then redistilled. Toluene (Aldrich) was dried by refluxing over calcium hydride. Other chemicals and reagents purchased from Aldrich, TCI, Combi-Blocks Catalog, Biofine Product List and OChem Product List were used directly without further purification.

3.4.2 Instruments

Gel permeation chromatography (GPC) analysis was conducted on a PL-GPC 220 system with polystyrene as standard and 1,2,4-trichlorobenzene as eluent at 150 °C.

Thermogravimetric analysis (TGA) measurements were performed on a PerkinElmer Thermal Analysis Instruments Pyris Diamond TG from 50 to 800 °C at a heating rate of 10 °C/min under a continuous nitrogen flow. Differential scanning calorimetry (DSC) measurements were performed on a TA-DSC Q100 (TA Instruments) from 20 to 250 °C at a heating rate of 10 °C/min under a continuous nitrogen flow.

3.4.3 Photodegradation measurement of PDTPP and DTPP Polymers

A 10^{-5} M solution was prepared from PDTPP/DTPP polymer using 10 mL of dry THF and CHCl_3 in dark. The absorption spectrum was measured prior to exposure to light. In a closed box at ambient condition, the solution was then exposed to a 40-watt incandescent light bulb with color temperature of 2700 K and wavelength ranging from 500 to 2000 nm at distance of 50 cm. Absorption spectrum was then measured at different time intervals.

3.4.4 Multilayer device fabrication and characterization

A mixture of polymer and (6,6)-phenyl C_{61} butyric acidmethylester (PCBM) in a weight ratio of 1:3 was dissolved in chlorobenzene with a concentration of 20 mg mL^{-1} and stirred under nitrogen atmosphere at RT for more than 12 h. Indium tin oxide (ITO) coated glass substrates were cleaned, sequentially, by ultrasonic treatment in detergent at 60°C for 2 h, washed with de-ionized water, blow dried with nitrogen, and then dried in an oven at 110°C for 0.5 h. After UV–ozone treatment for 15 min, the ITO-coated slides was spin coated with poly(3,4-ethylenedioxythiophene) doped with poly(styrenesulfonate) (PEDOT:PSS) at 3500 rpm for 60 s, followed by heating at

120°C for 30 min, forming a film of about 30 nm thickness. The active layer in 80 nm thickness was deposited by spin-coating of the solution at a speed of 800 rpm for 60 s. Al was deposited by thermal evaporation. The active device area is defined by a shadow mask to be 16 mm². The five devices were prepared with a configuration as follows:

- (a) ITO/PEDOT:PSS/**DPP-TT**:PCBM/**DAPb-TPT**:PCBM/Al
- (b) ITO/PEDOT:PSS/**DPP-TPTB**:PCBM/**DAPb-TPT**:PCBM/Al
- (c) ITO/PEDOT:PSS/**DPP-BI**:PCBM/**DAPb-TPT**:PCBM/Al
- (d) ITO/PEDOT:PSS/**DPP-DTP**:PCBM/**DAPb-DTP**:PCBM/Al
- (e) ITO/PEDOT:PSS/**DPP-DTP**:PCBM/**DAPa-TBTT**:PCBM/Al
- (d) ITO/PEDOT:PSS/**DPP-BI**:PCBM/**DAPa-BI**:PCBM/Al

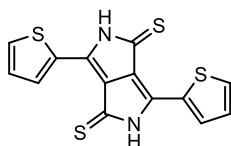
Measurements were done in ambient conditions. EQE measurements was done using a tungsten lamp (250 W) and a monochromator chopped at 160 Hz with a lock-in amplifier (SR830, Stanford Research Systems) to remove background noise. The reference was a calibrated Si photodiode (S1337-1010BQ, Hamamatsu, calibrated by the National Institute of Metrology of China) with known EQE spectra. Reverse bias on the device was provided by a Keithley 236 Source Measure Unit. For the dark current measurement, current–voltage characteristics were recorded using a Keithley 236 source measurement unit. The devices were shielded in a metal case to prevent electrostatic interference. Assuming that the shot noise from the dark current is a major contributor or factor, the specific detectivity (D^*), one of the most important figures of merits for PDs, is expressed as [8, 12]:

$$D^* = R/(2qJ_d)^{1/2} = (J_{ph}/J_{light})/(2qJ_d)^{1/2} \text{ (Jones),}$$

where R is the responsivity, a ratio of photocurrent (J_{ph}) to incident-light intensity (J_{light}), q is the absolute value of electron charge (1.6×10^{19} Coulombs), and J_d is the dark current density ($A \text{ cm}^{-2}$).

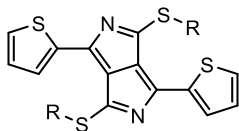
3.4.4 Synthesis

3,6-Di(thiophen-2-yl)-2,5-dihydropyrrolo[3,4-c]pyrrole-1,4-dithione (DTPP)



DPP (3.00 g, 10.0 mmol), previously synthesized, Lawesson's reagent (8.10 g, 20.0 mmol) and chlorobenzene (100 mL) were added to flame dried one neck round-bottomed flask. The mixture was bubbled with argon for 15 min at room temperature and then stirred at 135 °C for 8 hours. The color of the solution turned red to dark green in 6 hours' time. The solution mixture was precipitated in 400 mL methanol and filtered. The precipitate was washed with methanol and Soxhlet extraction was done using ethanol to remove any phosphate by-products. The desired thiolactam intermediate was obtained as a dark green solid and stored under dark and argon (3.1 g, 93%). ^1H NMR (300 MHz, $\text{DMSO-}d_6$) δ (ppm) 12.82 (s, 2H), 9.00 (dd, $J = 3.9, 1.2$ Hz, 2H), 8.06 (dd, $J = 4.9, 1.1$ Hz, 2H), 7.39 (dd, $J = 5.0, 3.9$ Hz, 2H). ^{13}C NMR (75 MHz, $\text{DMSO-}d_6$) δ (ppm) 174.82, 140.67, 133.42, 133.15, 132.74, 129.07, 114.08. IR (KBr, cm^{-1}): 3176-3095 ($\nu_{\text{N-H}}$), 1583, 1407 ($\nu_{\text{C=C}}$), 1181 ($\nu_{\text{C=N=S}}$), 1022 ($\nu_{\text{C=S}}$).

1,4-Bis(alkylthio)-3,6-di(thiophen-2-yl)pyrrolo[3,4-c]pyrrole (III-1/2)



In a one neck round bottom flask, the mixture of **DTPP** (2 g, 6.02 mmol), alkylbromide (13 mmol) and anhydrous powdered K_2CO_3 (2.8 g, 20 mmol) and acetone (100 mL) was purged with argon for 15 minutes. The reaction was then stirred at reflux overnight. The reaction solvent was removed by vacuum and the crude compound was extracted with chloroform. The solvent was concentrated and the product was purified by column chromatography (silica gel, hexane-ethyl acetate, 1:9, v/v). A dark green flaky solid was obtained.

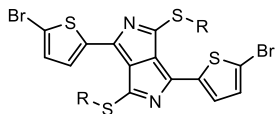
1,4-Bis(octylthio)-3,6-di(thiophen-2-yl)pyrrolo[3,4-c]pyrrole (III-1) (2.5 g, 75%).

1H NMR (400 MHz, $CDCl_3$) δ (ppm) 8.08 (dd, $J = 3.9, 1.0$ Hz, 2H), 7.64 (dd, $J = 5.0, 1.0$ Hz, 2H), 7.35 – 7.23 (m, 2H), 3.50 (t, $J = 7.4$ Hz, 4H), 1.89 (p, $J = 7.4$ Hz, 2H), 1.60 – 1.44 (m, 2H), 1.45 – 1.22 (m, 20H), 0.97 – 0.83 (m, 6H). ^{13}C NMR (101 MHz, Chloroform-*d*) δ (ppm) 166.78, 152.18, 139.14, 132.57, 132.41, 131.95, 128.94, 32.36, 31.82, 29.68, 29.18, 29.12, 28.93, 22.65, 14.10.

1,4-Bis((2-ethylhexyl)thio)-3,6-di(thiophen-2-yl)pyrrolo[3,4-c]pyrrole (III-2) (2.1

g, 63%). 1H NMR (300 MHz, $CDCl_3$) δ (ppm): 8.12 (d, 2H, $J = 3.9$ Hz), 7.64 (d, 2H, $J = 5.0$ Hz), 7.33–7.24 (m, 2H), 3.65–3.45 (m, 4H), 1.96–1.74 (m, 2H), 1.66–1.25 (m, 16H), 1.11–0.81 (m, 12H).

1,4-Bis(5-bromothiophen-2-yl)-3,6-bis(alkylthio)pyrrolo[3,4-c]pyrrole (DAPa/b)



Compound III-1/2 (1.5 g, 2.69 mmol) was dissolved in dry chloroform in round bottom flask and flushed with argon for 15 minutes. NBS (1.07 g, 6 mmol) was added portion at a time and the solution was stirred at room temperature in the dark overnight. The chloroform was removed and the crude product was precipitated in methanol and filtered to give a dark green solid.

1,4-Bis(5-bromothiophen-2-yl)-3,6-bis(octylthio)pyrrolo[3,4-*c*]pyrrole (DAPa)

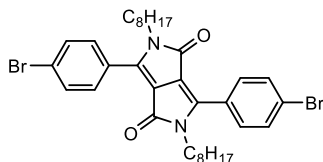
(1.2 g, 62%). ^1H NMR (300 MHz, CDCl_3) δ (ppm) 7.78 (d, $J = 4.1$ Hz, 2H), 7.22 (d, $J = 4.1$ Hz, 2H), 3.46 (t, $J = 7.4$ Hz, 4H), 1.86 (p, $J = 7.3$ Hz, 4H), 1.58 – 1.22 (m, 20H), 1.01 – 0.81 (m, 6H). ^{13}C NMR (75 MHz, Chloroform-*d*) δ (ppm) 166.52, 150.99, 140.65, 132.66, 132.15, 131.54, 121.19, 99.98, 32.54, 31.85, 29.68, 29.20, 29.12, 28.91, 22.68, 14.14, 1.03. HRMS: calcd. 714.70, found 715.0425.

1,4-Bis(5-bromothiophen-2-yl)-3,6-bis((2-ethylhexyl)thio)pyrrolo[3,4-*c*]pyrrole

(DAPb) (1.05 g, 54%). ^1H NMR (300 MHz, CDCl_3) δ (ppm) 7.82 (d, 2H, $J = 4.1$ Hz), 7.23 (d, 2H, $J = 4.1$ Hz), 3.60–3.41 (m, 4H), 1.89–1.73 (m, 2H), 1.61–1.27 (m, 16H), 1.06–0.87 (m, 12H).

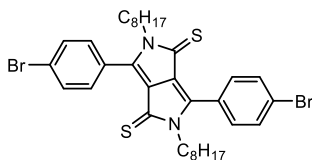
3,6-Bis(4-bromophenyl)-2,5-dioctyl-2,5-dihydropyrrolo[3,4-*c*]pyrrole-1,4-dione

(PDPP)



III-3 (2.50 g, 5.60 mmol), previously synthesized, K_2CO_3 (1.93, 14 mmol) and 18-crown-6 (10 mg) were added in a round bottom flask and flushed with argon. After which, 1-bromooctane (2.90 g, 15 mmol) and 50 mL of DMF was added and heated at 120 °C. The reaction was stirred overnight. The solution was cooled and extracted with chloroform and washed with water and the organic phase was dried over anhydrous $MgSO_4$. The crude product was purified by column chromatography (hexane-ethyl acetate, 9:1, v/v). The bright orange solid was obtained (1.13 g, 30%). 1H NMR (400 MHz, $CDCl_3$) δ (ppm) 7.80 – 7.60 (m, 8H), 3.83 – 3.63 (m, 4H), 1.57 (s, 4H), 1.22 (s, 20H), 0.88 (t, $J = 7.0$ Hz, 6H). ^{13}C NMR (101 MHz, $CDCl_3$) δ (ppm) 162.44, 147.40, 132.26, 130.06, 126.97, 125.80, 109.96, 99.98, 41.91, 31.70, 29.42, 29.07, 28.97, 26.66, 22.59, 14.07. HRMS: calcd. 670.53, found 671.1704.

3,6-Bis(4-bromophenyl)-2,5-dioctyl-2,5-dihydropyrrolo[3,4-c]pyrrole-1,4-dithione (PDTPP)



PDPP (1.00 g, 1.49 mmol) was dissolved in chlorobenzene (50 mL) and bubbled with argon for 10 minutes. Lawesson's reagent (1.21 g, 2.98 mmol) was added and heated to 135 °C and stirred under dark for 7 hours, the solution turned from yellow to blue. The solution was cooled and the product was precipitated out of methanol. The

crude product was purified using flash chromatography under dark to give a blue solid (0.6 g, 57%). ^1H NMR (400 MHz, CDCl_3) δ (ppm) 7.82 – 7.62 (m, 8H), 4.04 (dd, $J = 9.0, 6.5$ Hz, 4H), 1.59 (d, $J = 17.5$ Hz, 4H), 1.21 (dt, $J = 29.0, 4.5$ Hz, 20H), 0.88 (t, $J = 7.0$ Hz, 6H). ^{13}C NMR (101 MHz, CDCl_3) δ (ppm) 177.18, 150.11, 132.12, 130.48, 126.01, 125.87, 125.80, 99.97, 44.05, 31.70, 29.00, 28.86, 28.73, 26.50, 22.60, 14.09. HRMS: calcd. 702.65, found 703.1357.

General synthesis of DAP polymers by the Stille-cross coupling reaction.

In a flame-dried 25 mL round-bottom flask flushed with argon, organotin compound and monomer 2 were dissolved in 8 mL of chlorobenzene. The solution was bubbled with argon for addition 15 min. and then 10% $\text{Pd}(\text{PPh}_3)_4$ were added and the solution was stirred under dark at 110 °C for 48 hours. After cooling to room temperature, the polymers were precipitated in methanol and filtered. The polymers were purified via Soxhlet extraction (acetone and hexane) to give dark solid.

General synthesis of DAP polymer by the Suzuki-cross coupling reaction.

In a flame-dried 25 mL round-bottom flask under an argon atmosphere, boron ester monomer and DAP monomer in 1:1 mole ratio were dissolved in 6 mL of THF and 4 mL of 2 M K_2CO_3 aqueous solution. The solution was bubbled with argon for 30 min and then 10 mol% of $\text{Pd}(\text{PPh}_3)_4$ was added and solution was heated to reflux and stirred for 48 hours. After cooling, the polymer was precipitated out in methanol/water mixture and filtered. The polymer was purified via Soxhlet extraction (hexane and acetone) to give dark solid.

Polymer **DAPb-DTP**. Dark green-brown solid. (0.1078 g, 51%). ^1H NMR (300 MHz, CDCl_3) δ (ppm) 7.08 (s, 2H), 4.13 (d, $J = 34.7$ Hz, 1H), 3.56 (d, $J = 51.8$ Hz, 1H), 2.96 (s, 1H), 1.86 (s, 2H), 1.37 (d, $J = 57.9$ Hz, 20H), 0.95 (d, $J = 41.9$ Hz, 14H).

Polymer **DAPa-TBTT**. Dark green solid. (0.3440 g, 90%). ^1H NMR (300 MHz, CDCl_3) δ (ppm) 7.06 – 6.81 (m, 4H), 3.50 (s, 2H), 2.97 (s, 4H), 1.87 (s, 7H), 1.46 (d, $J = 71.6$ Hz, 39H), 0.90 (s, 14H).

Polymer **DAPa-BI**. Dark green solid. (0.27 g, 95%). ^1H NMR (300 MHz, CDCl_3) δ (ppm) 8.73 – 8.61 (m, 1H), 8.12 (d, $J = 5.4$ Hz, 1H), 7.95 (s, 1H), 7.81 – 7.67 (m, 2H), 7.66 – 7.59 (m, 1H), 3.67 – 3.46 (m, 3H), 1.93 (d, $J = 8.1$ Hz, 3H), 1.86 – 1.70 (m, 9H), 1.59 (d, $J = 13.2$ Hz, 6H), 1.50 – 1.24 (m, 11H), 0.97 – 0.81 (m, 4H).

Polymer **DPP-DTPa**. Dark blue solid. (0.30 g, 79%). ^1H NMR (300 MHz, CDCl_3) δ (ppm) 8.98 (t, $J = 4.5$ Hz, 1H), 7.75 – 7.59 (m, 1H), 7.48 (d, $J = 4.3$ Hz, 1H), 7.21 – 6.84 (m, 3H), 4.10 (s, 8H), 1.97 (s, 2H), 1.70 (d, $J = 49.1$ Hz, 17H), 1.27 (s, 34H), 0.89 (d, $J = 2.6$ Hz, 20H).

Polymer **DPP-BT**. Dark blue solid. (0.21 g, 78%). ^1H NMR (400 MHz, CDCl_3) δ (ppm) 7.49 (d, $J = 2.4$ Hz, 1H), 7.40 (d, $J = 8.6$ Hz, 1H), 7.21 (dd, $J = 8.6, 2.4$ Hz, 3H), 4.07 (s, 1H), 3.51 (d, $J = 4.6$ Hz, 4H), 1.59 (s, 20H), 1.27 (s, 4H), 0.94 (dd, $J = 13.2, 7.3$ Hz, 3H).

General synthesis of DTPP polymers.

In a flame dried round bottom flask, DPP (0.2 mmol) or BDPP polymer is dissolved in 8 mL of xylene or trichlorobenzene. For BDPP polymers, in trichlorobenzene, the solution was initially heated to 180 °C for 15 minutes and then brought to room temperature. Lawesson's reagent (0.4 mmol) was added and the solution was bubbled with argon. The reaction mixture was heated to 150 °C under dark overnight. The solution was brought to room temperature and the polymer was precipitated out of methanol and filtered. The polymers were purified Soxhlet extraction (ethanol) to give pure product.

Polymer **DTPP-BT**. Dark brown solid. (0.12 g, 83%). ¹H NMR (300 MHz, CDCl₃) δ (ppm) 7.28 (s, 8H), 7.11 (s, 3H), 6.37 (s, 1H), 4.18 (s, 2H), 3.78 (t, *J* = 32.3 Hz, 2H), 2.19 (s, 38H), 1.07 (d, *J* = 119.1 Hz, 27H).

Polymer **DTPP-DTPa**. Dark brown solid. (0.15 g, 88%). ¹H NMR (300 MHz, CDCl₃) δ (ppm) 7.90 (s, 1H), 6.99 (s, 3H), 3.86 (s, 4H), 2.26 (d, *J* = 39.0 Hz, 1H), 1.61 (s, 2H), 1.26 (s, 7H), 0.86 (s, 5H).

Polymer **DTPPH-DTPa**. Dark brown solid. (0.10 g, 80%). Due to poor solubility NMR was not taken.

Polymer **DTPPH-TPT**. Dark brown solid. (0.11 g, 75%). Due to poor solubility NMR was not taken.

Reference

- [1] Y. Yao, Y. Y. Liang, V. Shrotriya, S. Q. Xiao, L. P. Yu, Y. Yang, *Adv. Mater.*, **2007**, *19*, 3979.
- [2] G. Qian, J. Qi, Z. Y. Wang, *J. Mater. Chem.*, **2012**, *22*, 12867.
- [3] G. Yu, K. Pakbaz, A. J. Heeger, *Appl. Phys. Lett.* **1994**, *64*, 3422-3424.
- [4] T. P. Osedach, A. Iacchetti, R. R. Lunt, T. L. Andrew, P. R. Brown, G. M. Akselrod, V. Bulovic, *Appl. Phys. Lett.*, **2012**, 101.
- [5] E. H. Sargent, *Adv. Mater.*, **2005**, *17*, 515.
- [6] S. Kim, Y. T. Lim, E. G. Soltesz, A. M. De Grand, J. Lee, A. Nakayama, J. A. Parker, T. Mihaljevic, R. G. Laurence, D. M. Dor, L. H. Cohn, M. G. Bawendi, J. V. Frangioni, *Nat. Biotechnol.*, **2004**, *22*, 93.
- [7] M. Ettenberg, *Adv. Imaging*, **2005**, *20*, 29.
- [8] X. Gong, M. Tong, Y. Xia, W. Cai, J. S. Moon, Y. Cao, G. Yu, C.-L. Shieh, B. Nilsson, A. J. Heeger, *Science*, **2009**, *325*, 1665.
- [9] Z. Hai, A. Iqbal. *Chem. Soc. Rev.* **1997**, *26*, 203.
- [10] Y. Li, P. Sonar, L. Murphy, W. Hong. *Energy Environ. Sci.*, **2013**, *6*, 1684.
- [11] L. Dou J. You, J. Yang, C.-C. Chen, Y. He, S. Murase, T. Moriarty, K. Emery, G. Li, Y. Yang, *Nature Photonics*, **2012**, *6*, 180.
- [12] G. Qian, J. Qi, J. A. Davey, J. S. Wright, Z. Y. Wang, *Chem. Mater.*, **2012**, *24*, 2364.
- [13] G. Qian, Z. Y. Wang, *Adv. Mater.*, **2012**, *24*, 1582.
- [14] J. S. Zambounis, Z. Hao, A. Iqbal. *Nature*. **1997**, *388*, 131.

- [15] S. L. Evenson, T. M. Pappenfus, M. C. R. Delgado, K. R. Radke-Wohlers, J. T. L. Navarrete, S. C. Rasmussen, *Phys. Chem. Phys.*, **2012**, *14*, 6101.
- [16] Y. Honsho, A. Saeki, S. Seki, *International Journal of Spectroscopy*, **2012**, *2012*, 7 pages.
- [17] S. Zhang, L. Ye, W. Zhao, D. Liu, H. Yao, J. Hou, *Macromolecules*, **2014**, *47*, 4653.
- [18] X. Qian, H.-H. Gao, Y.-Z. Zhu, L. Lu, J.-Y. Zheng, *RSC Adv.*, **2015**, *4*, 4368.
- [19] J. Qi, L. Ni, D. Yang, X. Zhou, W. Qiao, M. Li, D. Ma, Z. Y. Wang, *J. Mater. Chem. C*, **2014**, *2*, 2431.
- [20] A. Dhanabalan, J. K. J. van Duren, P. A. van Hal, J. L. J. van Dongen, R. A. J. Janssen, *Adv. Funct. Mater.*, **2001**, *11*, 255.
- [21] P. Albers, J. Pietsch, S. F. Parker, *J. Mol. Catal. A: Chem.*, **2001**, *173*, 275.
- [22] T.-C. Yu, H. Shaw, *Appl. Catal. B*, **1998**, *18*, 105.
- [23] D. L. Mowery, M. S. Graboski, S. Michael, T. R. Ohno, R. L. McCormick, *Appl. Catal. B*, **1999**, *21*, 157.
- [24] J. K. Lampert, M. K. Shahjahan, R. J. Farrauto, *Appl. Catal. B*, **1997**, *14*, 211.
- [25] D. D. Beck, J. W. Sommers, *Stud. Surf. Sci. Catal.*, **1995**, *96*, 721.
- [26] C. N. R. Rao, R. Venkataraghavan, T. R. Kasturi, *Canadian Journal of Chemistry*, **1964**, *42*, 36.
- [27] C. N. R. Rao, R. Venkataraghavan, *Spectrochimica Acta*, **1962**, *18*, 541.
- [28] N. Ramnath, V. Ramesh, V. Ramamurth, *J. Org. Chem.*, **1983**, *48*, 214.

- [29] S. Tamagaki, K. Hotta, *J. C. S Chem. Comm.*, **1980**, 187, 598.
- [30] V. Tamilavan, M. Song, S. Kim, R. Agneeswari, J.-W. Kang, M. H. Hyun, *Polymer*, **2013**, 54, 3198.
- [31] S. C. Rasmussen, S. J. Evenson, *Prog. Polym. Sci.*, **2013**, 38, 1773.
- [32] S. Wood, J. Wade, M. Shahid, E. Collado-Fregoso, D. D. C. Bradley, J. R. Durrant, M. Heeney, J.-S. Kim, *Energy Environ. Sci.*, **2015**.
- [33] P. W. M. Blom, V. D. Mihailetschi, L. J. A. Koster, D. E. Markov, *Adv. Mater.*, **2007**, 19, 1551.
- [34] T. Ameri, P. Khoram, J. Min, C. J. Brabec, *Adv. Mater.*, **2013**, 25, 4225.
- [35] L. Yang, H. Zhou, S. C. Price, W. You, *J. Am. Chem. Soc.*, **2012**, 134, 5432.
- [36] M. Koppe, H.-J. Egelhaaf, G. Dennler, M. C. Scharber, C. J. Brabec, P. Schilinsky, C. N. Hoth, *Adv. Funct. Mater.*, **2010**, 20, 338.

Chapter 4 Synthesis and Characterization of Cross-linkable Functionalized Isoindigo-carbazole Polymers for Use in Photovoltaic Devices as Hole Blocking Layer

4.1 Introduction

Ever since the first discovery of electrically conductive polymers in 1977, a great deal of research has gone into conjugated polymer-based optoelectronics [1]. To date, organic-based light emitting diodes (OLED) are commercially available with excellent performance and polymer-based photovoltaic devices (PV) have reached unprecedented efficiency over 9% [2, 3]. Exploitation of the peculiar properties of conjugated polymers are being addressed and commercial development of polymer PVs are being explored [4]. Following conjugated polymer/fullerene bulk heterojunction solar cells, much effort has been made in order to improve device performances, stability and efficiency. Main development for improvement have been focused on synthesizing new polymers used in the active layer, optimizing device structure and film morphology. The most common device structure comprises a transparent electrode such as indium tin oxide (ITO) or fluorine-doped tin oxide (FTO) on glass or plastic substrate covered by a thin layer of hole transporting layer, such as poly(3,4-ethylenedioxythiophene)-poly(styrenesulfonate) (PEDOT:PSS). The active layer, composed of a blend of donor polymer and acceptor fullerene, is deposited typically from solution by means of spin-coating, ink jet, spray coating, doctor blading, etc. [5-8]. The final component of the device is a thin metal layer with low work function (Al, Ca/Al, LiF/Al) which is deposited by vacuum deposition. The work

function difference between the two electrodes provides a built-in potential that provides a driving force for the photo-generated electrons and hole to their respective electrodes. This type of device structure can offer good performance such as the power conversion efficiency (PCE) around 9% [3]. Despite having good efficiency, this process is less than optimal for large scale reproducibility. There are several drawbacks; first, due to the required energy level alignment among all the device components, a low work function electrode (e.g., Al) is required on top of the device for electron extraction. However, low work function metal readily undergoes fast oxidation when exposed to air, ultimately losing their conductivity and converting working devices into faulty ones [9]. Furthermore, PEDOT:PSS is inherently acidic in nature, which is detrimental to the underlying metal oxide layer and thus degrades more quickly [10, 11]. Finally, the widely used polymer/fullerene blend undergoes vertical phase separation during the film formation, with the fullerene phase mainly concentrated at the bottom of the film and the polymer phase is concentrated at the top of the film. Thus, the film with a vertical phase structure is far from ideal, where the fullerene should concentrate at the top facing the low-work function electrode [12, 13]. This issue could be addressed by reversing the collection process, collecting holes at the top electrode and electron by the bottom electrode. In this structure, the top metal electrode would have a high work function like silver or gold, thus eliminating the oxidation problem, while the bottom electrode should be a transparent electron conducting layer such as zinc oxide (ZnO) or titanium oxide (TiO_x) which eliminates the problem arising from the acidic PEDOT:PSS on ITO or FTO (Fig. 4.1) [14].

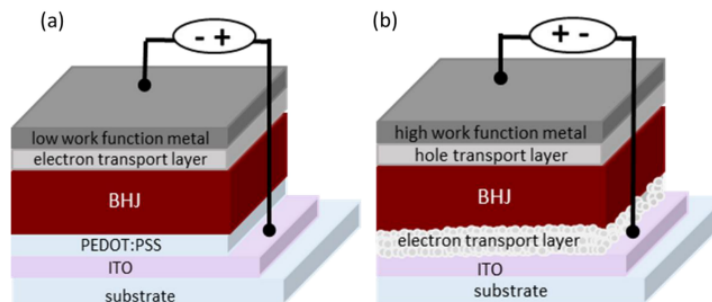


Figure 4.1: Device architecture of (a) conventional (b) inverted (Adapted with permission from Ref. 14)

The inverted structure was first exploited for use in the fabrication of OLED and typically referred as “upside-down” structure and been recently used in field for photovoltaics [15-17]. After these pioneering works, it has been demonstrated that the inverted structure can outperform their counterpart conventional cell [18, 19]. Recently an inverted structure has reached the PCE of 9.2% [20].

Stability and performance of these devices have been under great scrutiny. Due to imbalance of hole, electron fluxes and poor charge injection into the electrodes, there has been a great deal of studies devoted to interfacial engineering to improve performances. In a conventional device, PEDOT:PSS is applied as electron blocking layer (hole transfer layer), that is the energy barrier between the conduction band of the PEDOT:PSS and the LUMO level of the donor material is very high, thus blocking electron to reach the electrode. At the same time, the energy barrier between valence band and HOMO level of the donor should be lower, thus passing holes from the donor to the electrode [21]. Furthermore, PEDOT:PSS smoothens the surface of ITO which decreases the shunt current effect [22]. Similarly, a hole blocking layer (HBL) (electron transfer layer) can be added on metal electrode side. A HBL serves a buffer layer to prevent damage to the active layer caused by evaporation of the metal cathode and

hinders diffusion of metal atoms through the active layer [23]. Additionally, HBL blocks the hole injection from the cathode, thus preventing recombination cathode/organic layer interface [24, 25]. One of the most commonly used hole blocking materials is bathocuproine (BCP) (Fig. 4.2). BCP has a wide band gap with a deep HOMO level (7 eV) and has widely been used in organic solar cells and photodetectors [24-29]. Other materials such as nanostructured titanium dioxide (TiO₂), zinc oxide (ZnO) and lithium fluoride (LiF) also have been employed as a hole-blocking layer [30-34]. However, these inorganic materials are made into a very thin layer via several deposition techniques such as sol-gel or nanoparticle (NP) deposition [35,36]. Making these thin films have become a technical challenge and solution-processed interface layer is often preferred over vacuum process.

Zhou et al. recently reported the use of polyethylenimine (PEI) as a hole-blocking interlayer and demonstrated that the material can shift the work function and allows an air-stable material to be used in place of more reactive Ca [37].

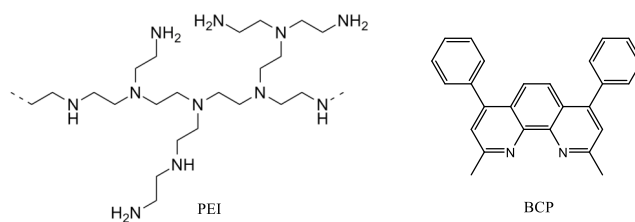


Figure 4.2: Bathocuproine (BCP) and Polyethylenimine (PEI)

In a recent finding, Udum et al. reported an inverted bulk-heterojunction based on cross-linked PEI with different ether cross-linkers. The cross-linked layer is more solvent resistant compared to pristine PEI layer and shows improvement in reproducibility of the device fabrication process. Furthermore, device efficiency showed slight improvement [38]. Other amine-based compounds such as carbazole and

triphenylamine have been used for a HBL material. Poly(N-vinylcarbazole) (PVK) has been used in OLED devices to improve luminous efficiency [39, 40].

Lactam-containing dyes such as diketopyrrolopyrole, isoindigo and benzodipyrrolidone have been extensively studied as acceptor units for donor-acceptor polymers [41-43]. Isoindigo has become one of the most important building blocks for D-A polymers due to its synthetic versatility and have been applicable for OPV and OFET uses [44-47]. Isoindigo is the isomeric analogue of the commonly known indigo dye. Historically, indigo is a natural dye extracted from plants and often associated with the dye used in blue jeans. In a recent finding reported by Deng et al., a polymer composed of dithienocarbazole and isoindigo showed good phase separation with PCBM and the inverted solar cell device based on it showed best PCE of 8.2% [48].

Indole is another important heterocyclic compound which widely been used for drug-discovery studies due to their bioactivity against microbes [49]. Conversely, polyindole is an electroactive polymer which is commonly obtained by electrochemical oxidation of indole using either FeCl_3 or CuCl_2 . Polyindole have fairly good thermal stability, high redox activity, slow degradation compared to polypyrrole and have electrical conductivity close to 0.1 S cm^{-1} [50-53]. Polyindole have been subjected to variety of application, especially Li-ion battery application, which shows great promise [54]. Along with oxidative polymerization, indole can also undergo direct C-H oxidative dimerization via palladium catalyst which serves as precursor for variety of synthetic products [55].

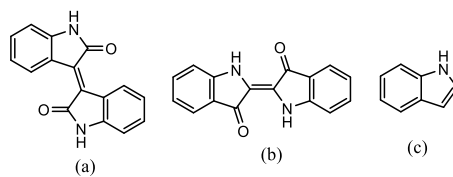
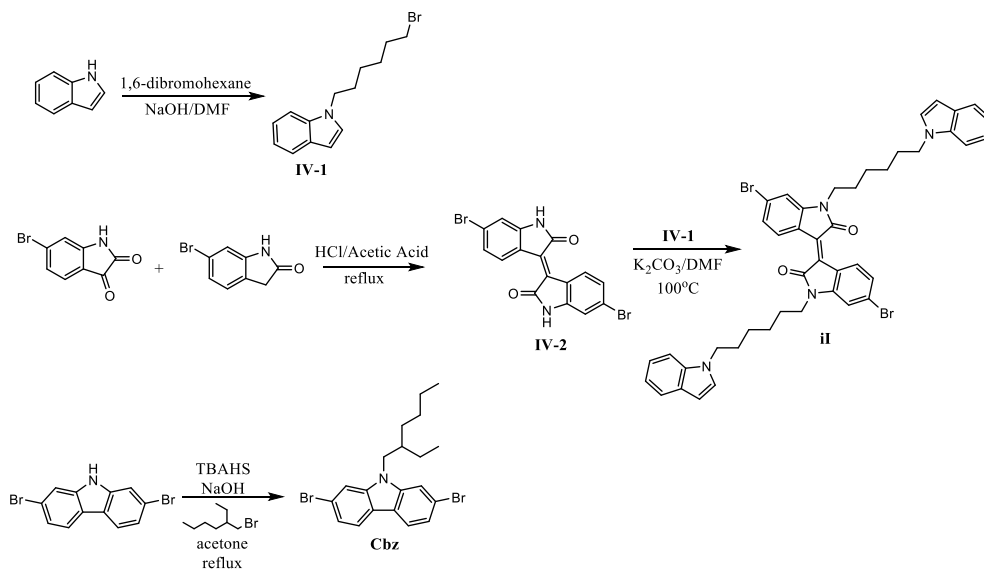


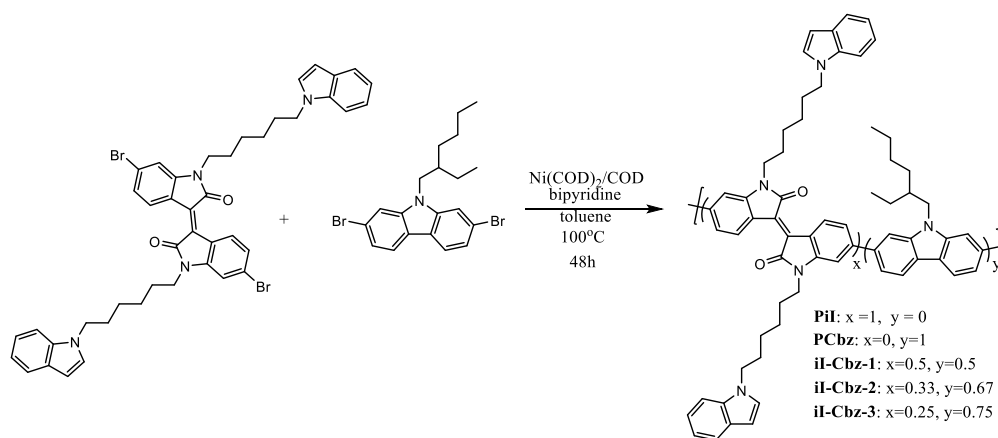
Figure 4.3: Structure of (a) isoindigo (b) indigo (c) indole

Herein, we developed N-substituted isoindigo with alkylated indole and polymerized with a different ratio of carbazole. The polymers were chemically cross-linked, direct indole C-H linking, rendering it insoluble and thus making it resistant to solvent. The effect of a different amount of carbazole on the optical and electrochemical properties were investigated.

4.2 Results and discussions

4.2.1 Syntheses of polymers





Scheme 4.1: Syntheses of polymers **PiI**, **PCbz**, **iI-Cbz-1**, **iI-Cbz-2** and **iI-Cbz-3**

The polymer syntheses are shown in Schemes 4.1. Indole is alkylated with 1,6-dibromohexane to afford compound **IV-1**, which is used to alkylate the isoindigo (**IV-2**). Isoindigo can be conveniently synthesized, with high yield, by acid catalyzed condensation reactions from commercially available oxindole and isatin [56]. The unsubstituted isoindigo shows limited solubility in common organic solvents, although, it can be improved with by placing various alkyl chain on the amide nitrogen atom. In our case, we use compound **IV-1**, which can be chemically cross-linked via palladium catalyst. The monomer **Cbz** was synthesized according to previous method [57]. The polymers were synthesized by Yamamoto cross-coupling reaction. The nickel-catalyzed coupling reaction have been widely used in recent years due to more selectivity of aryl halide coupling [58, 59]. Homopolymers **PiI** and **PCbz** were synthesized as reference. Whereas, the random copolymers were synthesized in a one pot reaction at different mole ratio of monomer **Cbz**.

4.2.1.1 Crosslinking of polymers

The crosslinking procedure was followed according to literature method [60]. Li et al. reported direct 3,3'-C-H transformation by using palladium catalyst and silver nitrate as an initiator (Fig. 4.4).

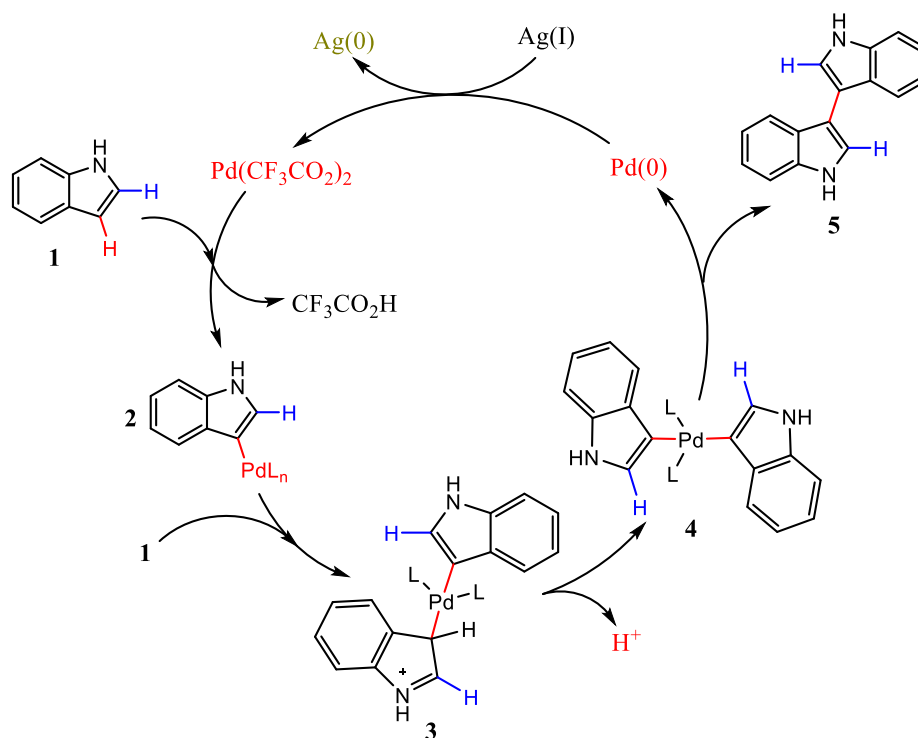


Figure 4.4: Proposed catalytic pathway for 3,3'-biindole

The plausible pathway suggests an electrophilic substitution of compound **1** with the Pd-catalyst, then the intermediate **2** attacks compound **1** again via electrophilic substitution to form intermediate **3**. With the loss of a proton, reductive elimination and reanimation of Pd(0), the oxidative 3,3'-linked biindole, **5**, is formed. The subsequent Pd(0) catalyst is oxidized by an silver atom to Pd(II), and ultimately restarting the catalytic cycle. This coupling is conventionally done in solution, ideally in a polar solvent such as DMSO or DMF.

Using the same concept, we were able to do 3,3'-indole coupling on film. This is accomplished by spin coating a mixture of isoindigo co-polymer with of Pd(TFA)₂ (20% mole ratio) and AgNO₃ (2 mole eq.) in THF on a glass substrate and then heated at 80°C under dark and argon overnight. The resulting cross-linked polymers are insoluble in common organic solvents such as CHCl₃, CH₂Cl₂ and THF. Similarly, a drop-cast film can accomplish the equal results (Fig. 4.5). More detailed procedure is explained in the experimental section.

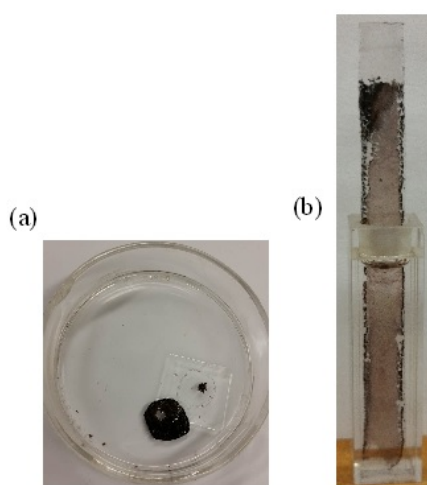


Figure 4.5: Cross-linked polymer **iI-Cbz-1** submerged in CHCl₃ (a) drop-cast (b) spin-cast film

4.2.2 IR characterization

IR analysis of pre-crosslinked polymers were done with thin films of polymers cast on the NaCl salt plates. As shown in Fig. 4.6a, the **iI-Cbz** polymers contains the distinct lactam group arising from isoindigo, showing an intense C=O peaks at 1700 cm⁻¹. As the content of carbazole increases from polymer **iI-Cbz-1** to **iI-Cbz-3**, the intensity of band at 1700 cm⁻¹ decreases as well. This observation proves that carbazole was successfully copolymerized into the polymer with isoindigo and the ratio between

the monomers is related to feed ratio of the carbazole. IR analysis was also done on cross-linked polymers using ATR technique. An increase broadness at 1650 cm^{-1} was observed, suggesting an overlap of the lactam peak and the aromatic C=C peak. We also observe increased broadness in the fingerprint region at 1100 cm^{-1} .

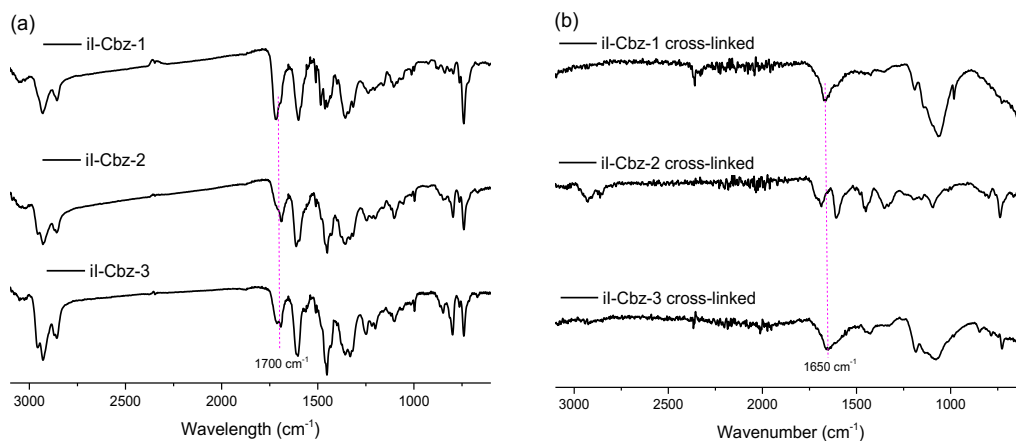


Figure 4.6: IR spectra of polymers **iI-Cbz-1**, **iI-Cbz-2** and **iI-Cbz-3** (a) before crosslinking on NaCl plate (b) after crosslinking by ATR-IR

4.2.3 NMR characterization

All polymers were characterized by ^1H NMR and ^{13}C NMR spectroscopy. The ^1H NMR spectra display proton resonances both in the aliphatic region (0-4.5 ppm) due to alkyl chains and the aromatic region (6.5-9.0 ppm) due to the conjugated backbone of the polymers. Because of high degree of overlapping of the peaks, assignments of the peaks are nearly impossible in these two regions, although, important information can be obtained from those regions. The protons arising from N-CH₂ groups from **PCbz** is slightly more downfield, 4.24-4.37 ppm, compared to N-CH₂ in **PiI**, 3.73-4.09 ppm. These protons exhibit resonance peaks with less overlapping. (Fig. 4.7).

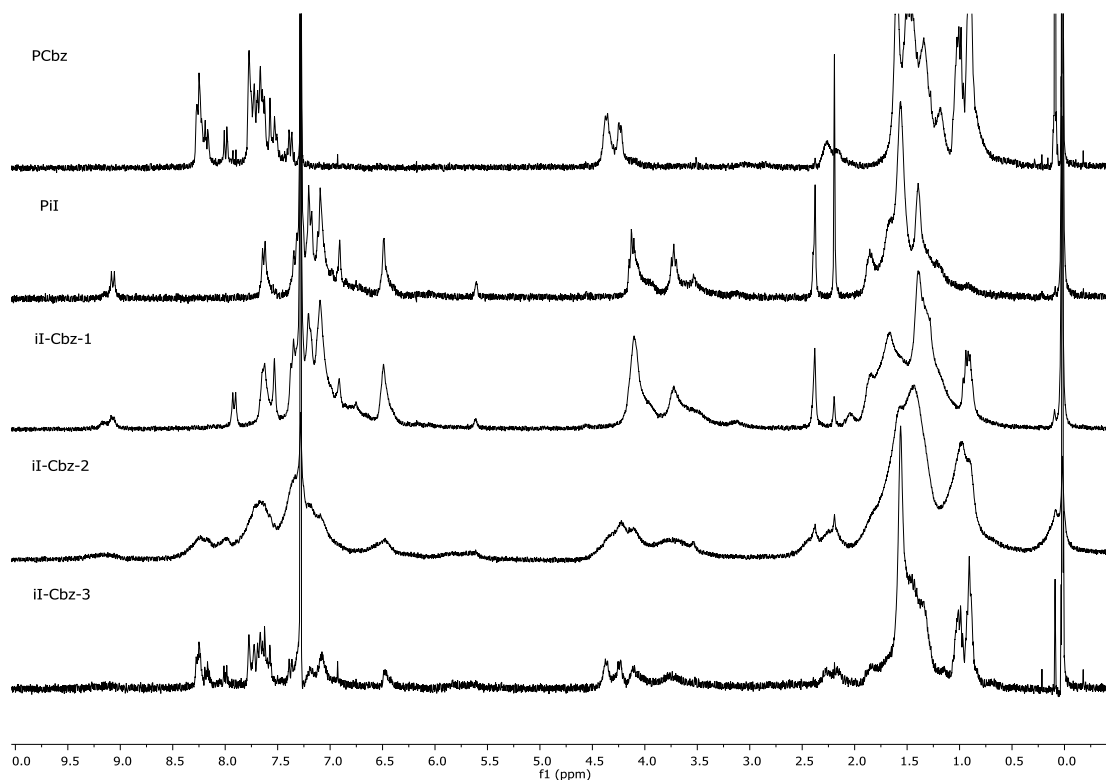


Figure 4.7. ^1H NMR spectra of polymer **PCbz**, **PiI**, **ii-Cbz-1**, **ii-Cbz-2** and **ii-Cbz-3** in CDCl_3 .

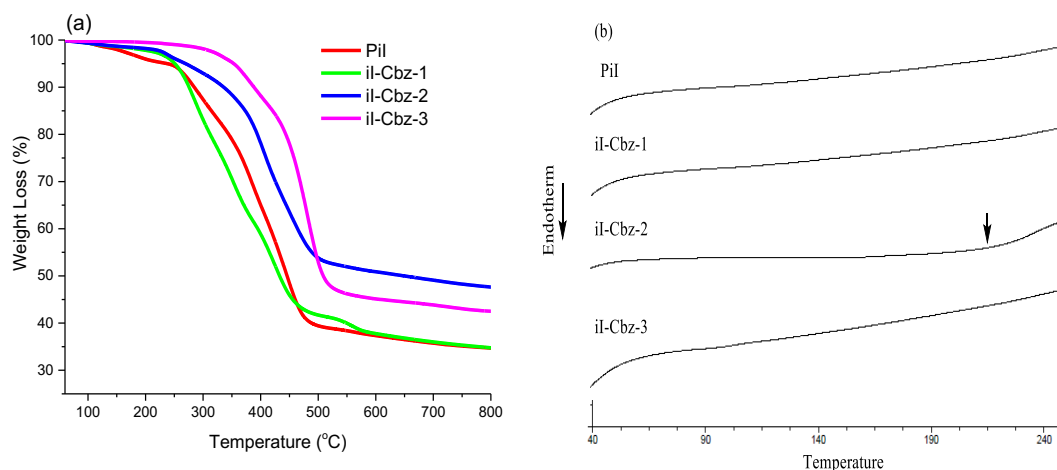
Quantitative study of the polymer structures can be achieved by comparing the integration of the two N-CH_2 peaks. The data are summarized in Table 4.1. After calculation, the actual percentage of Cbz in the polymer was obtained. The percentage of Cbz content in polymer **ii-Cbz-1** could not be calculated due to the absence of the N-CH_2 from Cbz group, there is however, remnant of the CH_3 peak (1.0 ppm) from Cbz unit. For polymers **ii-Cbz-2** and **3**, comparing with the calculated ratio and the NMR ratio, the amount of Cbz in the polymer was found to be slightly higher. The reason is probably due to the lower reactivity of **ii** monomer. This is probably caused by the lower purity of the monomer, which is evident on the NMR spectrum (Appendix A). Therefore, lower reactivity of monomer can result in lower molecular weight of the polymers.

Table 4.1. The ratio of **Cbz** to **il** in polymers **il-Cbz-1**, **il-Cbz-2** and **il-Cbz-2**.

Polymer	Cbz:il feed ratio	Cbz (%) Calculated	H _{Cbz} :H _{il} by ¹ H NMR	Cbz:il in polymer	Cbz (%) in polymer
il-Cbz-1	1:1	50	-	-	-
il-Cbz-2	2:1	67	2:4.16	2:0.69	74
il-Cbz-3	3:1	75	2:3.69	3:0.62	82

4.2.4 Thermal analysis

Polymers were characterized by thermogravimetric analysis (TGA) and differential scanning calorimetry (DSC) (Fig. 4.8). The data are summarized in Table 4.3.

**Figure 4.8:** Thermal properties of polymers (a) TGA (b) DSC

TGA showed thermal stability above 250 °C at 5% weight loss for most polymers, with polymer **PiI** being the least thermally stable (237 °C) and **il-Cbz-3** being the most stable (353 °C). Likewise, with increasing **Cbz** monomer content an increase of the thermal stability was observed. Study have shown that with increasing carbazole

content in a polymer produced higher thermal stability, which is likely due to the rigidity in the polymer chain [61]. Based on DSC graphs, there is no evidence of crystallization, thus all the polymers are considered amorphous. We do observe a glass transition peak for polymer **il-Cbz-2** at 215 °C. Typically, during fabrication the polymer films require to be annealed above the T_g temperature for optimized film morphology, therefore, having a very high T_g temperature is not always ideal.

Table 4.2. Thermal properties of polymers

Polymer	Decomposition Temperature (T_d)	Glass Transition Temperature (T_g)
Pil	237 °C	-
il-Cbz-1	251 °C	-
il-Cbz-2	268 °C	215 °C
il-Cbz-3	353 °C	-

4.2.5 Absorption

The absorption spectra of the polymers in chloroform and as film are shown in Figure 4.9. **PCbz** has only one λ_{max} at 368 nm, which is assigned to the π - π^* transition of the conjugated backbone. Conversely, the spectrum of **Pil** displays two bands, the first one contributed by the π - π^* transition occurs at 400 nm and the second weaker band at 500 nm is attributed from the ICT. The absorption spectra of the polymer thin films showed red shift and became broadened compared to those in solution, due to interchain intermolecular interaction in the solid state. However, the relatively small red-shift indicates that the long side chains prevent effective interchain interaction in the solid state. Subsequently, after cross-linking, the ICT band attributed from the D-A

have diminished. Furthermore, polymer **il-Cbz-3**, which contains a highest content of Cbz unit, show a slight hypsochromic shift of 10 nm.

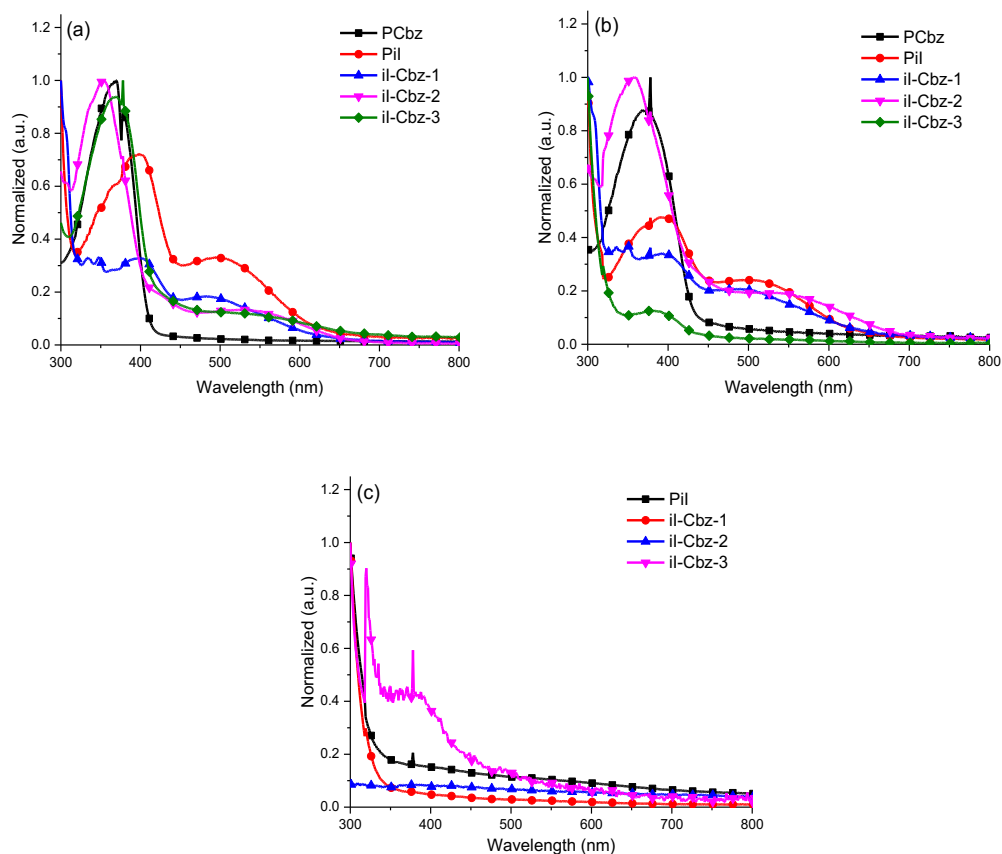
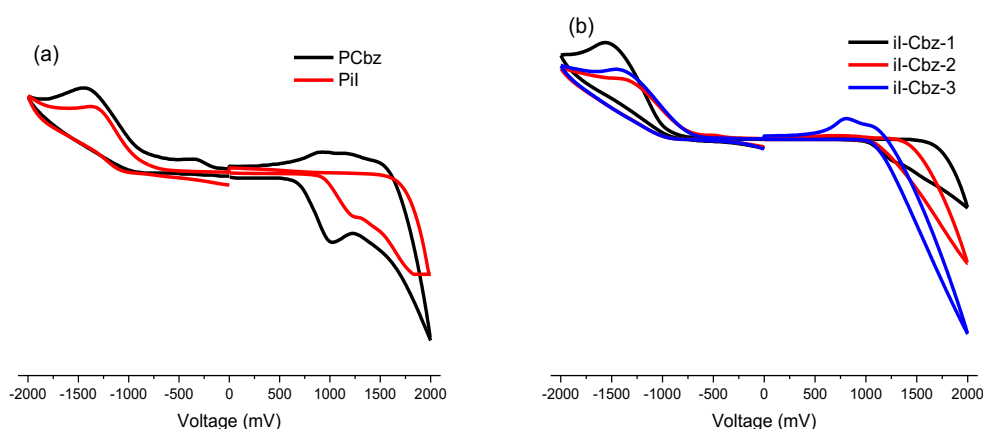


Figure 4.9: Absorption spectra of polymers (a) in CHCl_3 (b) as film (c) as film after cross-linking

4.2.6 Electrochemical property and band gaps

Electrochemical cyclic voltammetry (CV) was performed to determine the HOMO and LUMO energy levels of the polymers before and after crosslinking. From the value of onset oxidation potential E_{ox} and onset reduction potential E_{red} , the HOMO and LUMO levels were extrapolated. The band gap E_g were calculated and listed in

Table 4.3, as well as energy diagram based on these values (Figure 4.11). Prior to cross-linking, the data show that **PiI** has a LUMO level of -3.42 eV, and a band gap of 2.04 eV. The oxidation potentials were not evident for polymers **il-Cbz- 2** and **3**, therefore the HOMO levels was calculated from the optical band-gap. After increasing the Cbz monomer content in the co-polymer, we observe a slight decrease of the LUMO level. This is because LUMO level of the D-A polymer is determined by the electron withdrawing ability of the acceptor. Introduction of donor Cbz has an impact on lowering the LUMO level, due to an increase of D-A characteristic in the polymer. After cross-linking, the polymers show redox potential, with polymer **PiI** having the lowest HOMO, highest LUMO level and an increase of band gap by 0.13 eV. We also observe a decrease of the LUMO level of the co-polymers, leveling around -3.65 eV. Furthermore, with an increase content of Cbz unit, we observe an increase of the HOMO level. This results in a decrease of the band gap for **il-Cbz- 1, 2** and **3**. This is likely due to increased packing order and immobility of the acceptor unit in the film matrix.



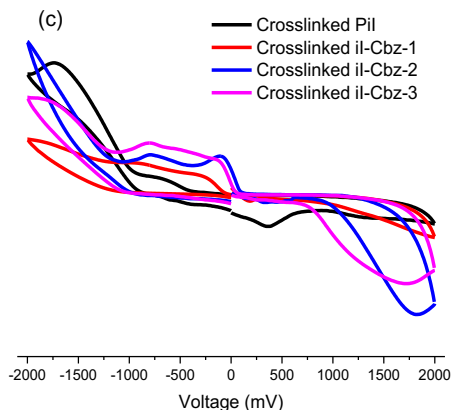


Figure 4.10: CV of polymers (a) **PCbz** and **Pil** (b) **il-Cbz-1**, **il-Cbz-2** and **il-Cbz-3**
(c) crosslinked **Pil**, **il-Cbz-1**, **il-Cbz-2**, **il-Cbz-3**

Table 4.3. Electrochemical properties and band gaps of polymers.

Polymer	HOMO (eV) ^(a)	LUMO (eV) ^(a)	Band gap (eV) ^(b)	Optical band gap (eV) ^(c)
PCbz	-5.12	-3.38	1.74	2.82
Pil	-5.46	-3.42	2.04	1.95
il-Cbz-1	-5.62	-3.38	2.24	1.95
il-Cbz-2	-5.35 ^(d)	-3.40	-	1.95
il-Cbz-3	-6.32 ^(d)	-3.46	-	2.86
Crosslinked Polymer	HOMO (eV) ^(a)	LUMO (eV) ^(a)	Band gap (eV) ^(b)	
Pil	-5.51	-3.34	2.17	
il-Cbz-1	-5.50	-3.65	1.85	
il-Cbz-2	-5.32	-3.68	1.64	
il-Cbz-3	-5.18	-3.63	1.55	

^(a) The potentials were measured from the onset of the CV curves. The CV of compounds were measured on thin film ITO in a 0.1 mol/L Bu₄NPF₆/acetonitrile solution, calculated from E(HOMO) = -(E_{ox} + 4.34) (eV) E(LUMO) = -(E_{red} + 4.34) (eV). ^(b) The energy gap (E_g) is derived from the HOMO subtracting the LUMO. ^(c) Optical energy gap calculated from the absorption onset. E_g = 1240/λ (onset, nm). ^(d) Calculated from optical band gap.

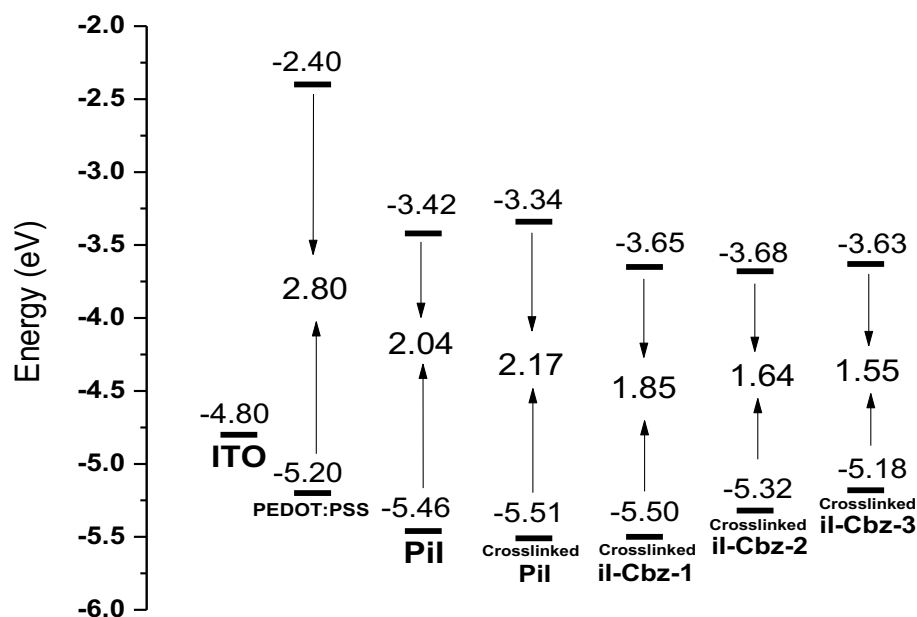


Figure 4.11. Energy levels of cross-linked polymers

4.3 Conclusion

A series of co-polymers with N-alkylated indole-isoindigo with different ratio of carbazole were successfully synthesized. Using Pd catalyst, the polymers were chemically cross-linked and thus rendering them insoluble. The polymers show absorption band from 350 to 600 nm, which diminished after cross-linking. Cross-linked **PiI** show an increase of the LUMO level and lowering of the HOMO level. Whereas, polymers **il-Cbz- 1, 2, and 3** showed a decrease in band gap. Therefore, polymer **PiI** would be prime candidate in replacing PEDOT:PSS.

4.4 Experimental

4.4.1 Materials

Tetrahydrofuran (THF) was dried by refluxing over sodium solid and

benzophenone. N,N-Dimethylformamide (DMF) was dried under molecular sieves overnight and then redistilled. Toluene was dried by refluxing over calcium hydride. Other chemicals and reagents purchased from Aldrich Chemicals and other commercial sources and were used directly without further purification.

4.4.2 Instruments

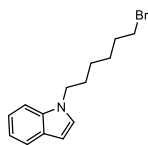
Mass spectra were measured with a Micromass Quattro LC ESI (EI).

4.4.3 Cross-linking procedure

A mixture of 10 mg of polymer, 20% mol eq. of Pd(TFA)₂, and 2 mol eq. of AgNO₃ dissolved in 4 mL of dry THF and bubbled with argon for 15 minutes. The solution mixture was vigorously stirred during that duration. A glass slide (3 cm x 3 cm) was sonicated in soap water, distilled water and then air dried. After which, the solution mixture was spin-coated on the glass substrate at 1000 rpm and heated on hot plate under nitrogen at 80 °C for 8 hours. The film was then cooled to room temperature and washed with methanol. Various test was then performed to determine the degree of cross-linking.

4.4.4 Synthesis

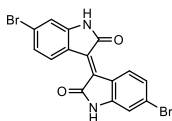
1-(6-Bromohexyl)-1*H*-indole (IV-1)



A mixture of indole (2.50 g, 21.3 mmol), KOH (1.43 g, 25.56 mmol) and 1,6-

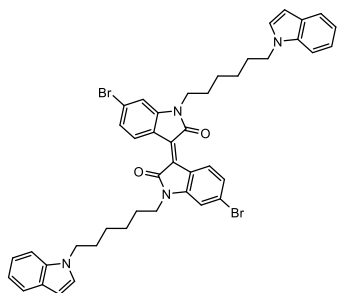
dibromohexane (15,62 g, 64.2 mmol) in dry DMF (100 mL) was stirred at room temperature for 48h under argon. The reaction mixture was diluted with water (100 mL) and extracted with chloroform (3 x 25mL). The combined organic phase was washed with brine, dried over MgSO₄, and concentrated. The residue was purified by chromatography with hexane-acetone (19:1 v/v) to give a pale green oil (4.51 g, 76% yield). ¹H NMR (300 MHz, CDCl₃) δ 7.72 – 7.63 (m, 1H), 7.38 (dq, J = 8.2, 0.9 Hz, 1H), 7.30 – 7.19 (m, 1H), 7.18 – 7.08 (m, 2H), 6.53 (dd, J = 3.1, 0.8 Hz, 1H), 4.16 (t, J = 7.0 Hz, 2H), 3.41 (t, J = 6.7 Hz, 2H), 1.98 – 1.78 (m, 4H), 1.59 – 1.43 (m, 2H), 1.36 (dd and dd, J = 14.0, 8.7, 5.8, 1.6 Hz, 2H). ¹³C NMR (75 MHz, CDCl₃) δ 137.24, 129.12, 127.48, 122.48, 122.19, 115.08, 112.61, 101.22, 50.40, 40.01, 30.65, 28.61, 24.00, 23.13, 14.15, 10.65.

(E)-6,6'-Dibromo-[3,3'-biindolinylidene]-2,2'-dione (IV-2)



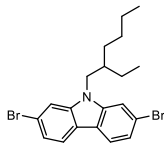
6-Bromooxindole (5.33 g, 23.6 mmol) and 6-bromoisatin (5.00 g, 23.6 mmol) were dissolved in 125 mL of acetic acid with 1.2 mL of 12 M HCl for 24 hours. The solution was cooled at room temperature and dropped in 1 L of water and filtered. The brown solid was washed with water and 100 mL of methanol. The crude product was triturated in 150 mL of ethyl acetate for 1 hour. The product was then cooled and filtered to afford a dark brown solid (9.91 g, 89% yield). ¹H NMR (300 MHz, DMSO-*d*₆) δ 11.11 (s, 2H), 9.01 (s, 2H), 7.10 (d, J = 54.1 Hz, 4H).

(E)-1,1'-bis(6-(1*H*-indol-1-yl)hexyl)-6,6'-dibromo-[3,3'-biindolinylidene]-2,2'-dione (II)



6,6'-Dibromoisindigo (0.75 g, 1.78 mmol), anhydrous potassium carbonate (0.62 g, 4.5 mmol) and compound **IV-1** (1.00 g, 3.57 mmol) were mixed in 25 mL dry DMF and heated to 100 °C under argon atmosphere. The resulting mixture was reacted for 18 hours and poured into water and extracted with chloroform (3 x 25 mL). The organic phases were combined, washed with brine and dried of sodium sulfate. The solvent was evaporated under reduced pressure and a red viscous oil was obtained. The product was purified over a short silica column using hexane as the first eluent and then with mixture of hexane and acetone (8:2 v/v) to afford a red solid (1.10 g, 78% yield). ¹H NMR (300 MHz, CDCl₃) δ 9.07 (d, *J* = 8.6 Hz, 2H), 7.64 (d, *J* = 7.8 Hz, 2H), 7.34 (d, *J* = 8.2 Hz, 2H), 7.25 – 7.15 (m, 4H), 7.15 – 7.05 (m, 4H), 6.90 (d, *J* = 1.9 Hz, 2H), 6.49 (d, *J* = 3.2 Hz, 2H), 4.13 (t, *J* = 7.0 Hz, 4H), 3.71 (t, *J* = 7.2 Hz, 4H), 1.95 – 1.76 (m, 4H), 1.68 (d, *J* = 6.8 Hz, 6H), 1.40 (dd, *J* = 7.6, 3.8 Hz, 10H). ¹³C NMR (75 MHz, CDCl₃) δ 167.74, 145.62, 131.20, 127.70, 125.22, 121.35, 120.95, 119.19, 111.27, 109.29, 100.97, 46.25, 40.04, 30.11, 27.28, 26.70, 26.62. IR (NaCl plate, cm⁻¹): 1693 (ν_{C=O}), 1600 (ν_{C=C}). M.P. 98-100°C. HRMS (ESI)(M+H): Calc. 819.66, Found: 819.1583.

2,7-Dibromo-9-(2-ethylhexyl)-9H-carbazole (Cbz)



A mixture of 2,7-dibromo-9H-carbazole (2.00 g, 6.15 mmol), 2-ethylhexyl bromide (1.22 g, 6.32 mmol), tetrabutylammonium hydrogensulfate (0.07 g) and sodium hydroxide (0.30 g, 7 mmol) was dissolved in 100 mL of acetone and refluxed overnight. The solvent was then removed under reduced vacuum. The residue was extracted with chloroform (3 x 35 mL), washed with brine and dried under sodium sulfate. The solvent was removed by reduced vacuum and the residue oil was purified by column chromatography on silica gel using hexane:acetone (9:1 v/v) to give a white solid (2.10 g, 78% yield). ^1H NMR (300 MHz, CDCl_3) δ 7.88 (d, $J = 8.3$ Hz, 2H), 7.51 (d, $J = 1.6$ Hz, 2H), 7.35 (dd, $J = 8.3, 1.6$ Hz, 2H), 4.18 – 3.90 (m, 2H), 2.03 (dq, $J = 12.3, 5.6$ Hz, 1H), 1.48 – 1.20 (m, 8H), 0.92 (dt, $J = 9.4, 7.3$ Hz, 6H). ^{13}C NMR (75 MHz, CDCl_3) δ 141.80, 122.49, 121.39, 119.63, 112.26, 47.64, 39.12, 30.77, 28.55, 24.32, 23.04, 14.03, 10.89.

General synthesis of Yamamoto cross-coupling.

Under an argon atmosphere, a solution of **Cbz**, **iI**, $\text{Ni}(\text{COD})_2$ (3 mol eq.), COD (3 mol eq.) and 2,2'-bipyridine (3 mol eq.) was stirred in 8 mL of toluene at 90 °C. The reaction mixture was stirred under dark for 48 hours. After cooling, the mixture was precipitated in 200 mL of methanol/acetone/1 M HCl (1:1:1) solution and stirred for additional half hour. The precipitate was filtered and the polymers were purified in Soxhlet extraction using acetone and hexane. The polymers were extracted using

chloroform, after which it was concentrated under reduced vacuum and re-precipitated in methanol to give a beige to reddish solid.

Polymer **PCbz**. 0.686 mmol of **Cbz** was used. Pale beige solid. Yield: 0.15 g, 80%. ^1H NMR (300 MHz, CDCl_3) δ 8.22 (dd, $J = 22.3, 4.9$ Hz, 2H), 7.83 – 7.33 (m, 5H), 4.30 (d, $J = 37.8$ Hz, 2H), 2.22 (d, $J = 27.0$ Hz, 1H), 1.77 – 1.09 (m, 14H), 0.96 (d, $J = 32.7$ Hz, 7H). ^{13}C NMR (75 MHz, CDCl_3) δ 142.15, 140.14, 122.10, 121.86, 121.42, 120.57, 119.17, 107.95, 47.47, 39.56, 31.17, 30.97, 28.91, 24.50, 23.15, 14.08, 11.03.

Polymer **PiI**. 0.190 mmol of **iI** was used. Red solid. Yield: 0.102 g, 85% yield. ^1H NMR (300 MHz, CDCl_3) δ 9.07 (d, $J = 8.5$ Hz, 2H), 7.63 (d, $J = 7.7$ Hz, 5H), 7.27 – 6.83 (m, 25H), 6.49 (s, 5H), 4.13 (t, $J = 7.6$ Hz, 9H), 3.73 (d, $J = 8.6$ Hz, 6H), 1.98 – 1.07 (m, 62H). ^{13}C NMR (101 MHz, CDCl_3) δ 135.87, 128.53, 127.70, 125.22, 121.34, 120.94, 119.18, 109.28, 100.96, 46.24, 30.09, 26.69, 26.61.

Polymer **iI-Cbz-1**. 0.177 mmol of **Cbz** and 0.177 mmol of **iI** was used. Reddish-brown solid. Yield: 0.260 g, 82%. ^1H NMR (300 MHz, CDCl_3) δ 9.08 (s, 1H), 7.91 (d, $J = 8.2$ Hz, 1H), 7.58 (d, $J = 29.2$ Hz, 5H), 7.23 (q, $J = 32.6, 24.9$ Hz, 23H), 6.60 – 6.40 (m, 3H), 4.10 (s, 8H), 3.72 (s, 6H), 2.10 – 0.67 (m, 40H). ^{13}C NMR (75 MHz, CDCl_3) δ 128.54, 127.71, 122.51, 121.34, 120.93, 119.18, 112.30, 109.29, 100.96, 47.69, 46.25, 40.04, 30.10, 28.54, 27.32, 26.70, 26.62, 26.28, 24.32, 23.03, 10.89.

Polymer **ii-Cbz-2**. 0.354 mmol of **Cbz** and 0.177 mmol of **ii** was used. Reddish-brown solid. Yield: (0.38 g, 80%). ^1H NMR (300 MHz, CDCl_3) δ 9.15 (s, 1H), 8.45 – 6.73 (m, 23H), 6.49 (s, 2H), 4.70 – 3.22 (m, 9H), 2.29 (d, $J = 56.4$ Hz, 5H), 1.99 – 0.62 (m, 43H). ^{13}C NMR (75 MHz, CDCl_3) δ 127.71, 122.13, 121.42, 120.94, 120.55, 119.15, 112.09, 109.31, 108.14, 107.96, 100.91, 47.59, 46.24, 39.34, 30.96, 30.09, 28.72, 26.68, 24.40, 23.09, 14.04, 10.95.

Polymer **ii-Cbz-3**. 0.531 mmol of **Cbz** and 0.177 mmol of **ii** was used. Beige solid. Yield: (0.48 g, 75%). ^1H NMR (300 MHz, CDCl_3) δ 8.21 (d, $J = 24.7$ Hz, 2H), 7.85 – 7.47 (m, 4H), 7.08 (s, 8H), 6.47 (s, 1H), 4.31 (d, $J = 37.7$ Hz, 2H), 4.10 (s, 1H), 2.27 (s, 2H), 1.56 (s, 21H), 1.20 – 0.73 (m, 7H). ^{13}C NMR (75 MHz, CDCl_3) δ 142.16, 121.86, 120.60, 120.57, 112.09, 109.32, 107.96, 39.56, 31.17, 30.06, 28.91, 24.50, 23.15, 14.08, 11.04.

References

- [1] H. Shirakawa, E. J. Louis, A. G. MacDiarmid, A. G. Chaing, A. J. Heeger, *J. Chem. Soc. Chem. Commun.*, **1977**, 578.
- [2] R. F. Service, *Science*, **2011**, 332, 293.
- [3] M. Scharber, N. S. Sariciftci, *Prog. Polym. Sci.*, **2013**, 38, 1929.
- [4] M. Jorgensen, J. E. Carle, R. R. Sondergaard, M. Lauritzen, N. A. Dagnaes-Hansen, S. L. Byskov, T. R. Andersen, T. T. Larsen-Olsen, A. P. L. Bottiger, B. Andreasen, L. Fu, L. Zuo, Y. Liu, E. Bundgaard, X. Zhan, H. Chen, F. C. Krebs, *Sol. Energy Mater. Sol. Cells*, **2013**, 119, 84.

- [5] B. Tremolet de Villers, C. J. Tassone, S. H. Tolbert, B. J. Schwartz, *J. Phys. Chem. C*, **2009**, *113*, 18978.
- [6] M. Sanyal, B. Schmidt-Hansberg, M. F. G. Klein, A. Colsmann, C. Munuera, A. Vorobiev, U. Lemmer, W. Schabel, H. Dosch, E. Barrena, *Adv. Energy Mater.*, **2011**, *1*, 363.
- [7] C. N. Hoth, S. A. Choulis, P. Schilinsky, C. J. Brabec, *J. Mater. Chem.*, **2009**, *19*, 5398.
- [8] W. Nie, R. Coffin, J. Liu, C. M. MacNeill, Y. Li, R. E. Noffle, D. L. Carroll, *Int. J. Photoenergy*, **2012**, *2012*.
- [9] G. Li, R. Zhu, Y. Yang, *Nature Photonics*, **2012**, *6*, 153.
- [10] Y. H. Kim, S. H. Lee, J. Noh, S. H. Han, *Thin Solid Films*, **2006**, *510*, 305.
- [11] M. P. De Jong, L. J. van Ijzendoorn, M. J. A. de Voigt, *Appl. Phys. Lett.*, **2000**, *77*, 2255.
- [12] K. H. Yim, Z. Zheng, R. H. Friend, W. T. S. Huck, J. S. Kim, *Adv. Funct. Mater.*, **2008**, *18*, 2897.
- [13] E. Pavlopoulou, G. Fleury, D. Deribew, F. Cousin, M. Geoghegan, G. Hadziioannou, *Org. Electron*, **2013**, *14*, 1249.
- [14] H.-J. Wang, C.-P. Chen, R.-J. Jeng, *Materials*, **2014**, *7*, 2411.
- [15] D. R. Baigent, R. N. Marks, N. C. Greenham, R. H. Friend, S. C. Maratti, A. B. Holmes, *Appl. Phys. Lett.*, **1994**, *65*, 2636.
- [16] A. C. Arias, M. Granstrom, D. S. Thomas, K. Petritsch, R. H. Friend, *Phys. Rev. B*, **1999**, *60*, 1854.
- [17] T. Nyberg, *Synth. Met.*, **2004**, *140*, 281.

- [18] T. Ameri, G. Dennler, C. Waldauf, P. Denk, K. Forberich, M. C. Scharber, C. J. Brabec, K. Hingerl, *J. Appl. Phys.*, **2008**, *103*, 084506.
- [19] J. Yuan, X. Huang, H. Dong, J. Lu, T. Yang, Y. Li, A. Gallagher, W. Ma, *Org. Electron.*, **2013**, *14*, 635.
- [20] Z. He, C. Zhong, S. Su, M. Xu, H. Wu, Y. Cao, *Nature Photonics*, **2012**, *6*, 591.
- [21] S. Lattante, *Electronics*, **2014**, *3*, 132.
- [22] H. Derouiche, V. Djara, *Sol. Energy Mater. Sol. Cells*, **2007**, *91*, 1163.
- [23] H. Derouiche, H. B. Miled, A. B. Mohamed, *Phys. Status Solidi. A*, **2010**, *207*, 479.
- [24] P. Peumans, V. Bulovic, S. R. Forrest, *Appl. Phys. Lett.*, **2000**, *76*, 3855.
- [25] J. Qi, L. Ni, D. Yang, X. Zhou, W. Qiao, D. Ma, Z. Y. Wang, *J. Mater. Chem. C*, **2014**, *2*, 2431.
- [26] D. F. O'Brien, M. A. Baldo, M. E. Thompson, S. R. Forrest, *Appl. Phys. Lett.*, **1999**, *74*, 442.
- [27] S. Heutz, P. Sullivan, B. M. Sanderson, S. M. Schultes, T. S. Jones, *Sol. Energy Mater. Sol. Cells*, **2004**, *82*, 299.
- [28] J. Qi, J. Han, X. Zhou, D. Yang, J. Zhang, W. Qiao, D. Ma, Z. Y. Wang, *Macromolecules*, **2015**, *48*, 3941.
- [29] J. Qi, X. Zhou, D. Yang, W. Qiao, D. Ma, Z. Y. Wang, *Adv. Funct. Mater.*, **2014**, *24*, 7605.
- [30] J. Y. Kim, S. H. Kim, H.-H. Lee, K. Lee, W. Ma, X. Gong, A. J. Geeger, *Adv. Mater.*, **2006**, *18*, 572.

- [31] J. Gilot, I. Barbu, M. M. Wienk, R. A. Janssen, *Appl. Phys. Lett.*, **2007**, *91*, 113520.
- [32] K. Lee, J. Y. Kim, S. H. Park, S. H. Kim, S. Cho, A. J. Heeger, *Adv. Mater.*, **2007**, *19*, 2445.
- [33] J. Y. Kim, S. H. Kim, H.-H. Lee, K. Lee, W. Ma, X. Gong, A. J. Heeger, *Adv. Mater.*, **2006**, *18*, 572.
- [34] C. J. Brabec, S. E. Shaheen, C. Winder, N. S. Sariciftci, P. Denk, *Appl. Phys. Lett.*, **2002**, *80*, 1288.
- [35] A. K. K. Kyaw, X. W. Sun, C. Y. Juang, G. Q. Lo, D. W. Zhao, D. L. Kwong, *Appl. Phys. Lett.*, **2008**, *93*, 221107.
- [36] M. A. Ibrahim, H. Y. Wei, M. H. Tsai, K. C. Ho, J. J. Shyue, C. W. Chu, *Sol. Energy Mater. Sol. Cells*, **2013**, *108*, 156.
- [37] Y. Zhou, C. Fuentes-Hernandez, J. Shim, J. Meyer, A. J. Giordano, H. Li, P. Winget, T. Papadopoulos, H. Cheun, J. Kim, M. Fenoll, A. Dindar, W. Haske, E. Najafabadi, T. M. Khan, H. Sooudi, S. Barlow, S. Graham, J.-L. Bredas, S. R. Marder, A. Kahn, B. Kippelen. *Science*, **2012**, *336*, 327.
- [38] Y. Udum, P. Denk, G. Adam, D. H. Apaydin, A. Nevsad, C. Teichert, M. S. White, N. S. Sariciftci, M. C. Scharber, *Organic Electronics*, **2014**, *15*, 997.
- [39] J.-W. Lee, J.-K. Kim, Y.-S. Yoon, *Chin. J. Chem.*, **2010**, *28*, 115.
- [40] Y.-J. Xia, J. Lin, C. Tang, K. Yin, G.-Y. Zhong, G. Ni, B. Peng, F.-X. Gan, W. Huang, *J. Phys. D: Appl. Phys.*, **2006**, *39*, 4987.
- [41] S. Qu, H. Tian, *Chem. Commun.*, **2012**, *48*, 3039.
- [42] R. Stalder, J. Mei, J. R. Reynolds, *Macromolecules*, **2010**, *43*, 8348.

- [43] W. Cui, J. Yuen, F. Wudl, *Macromolecules*, **2011**, *44*, 7869.
- [44] S. Holliday, J. E. Donaghey, I. McCulloch, *Chem. Mater.*, **2014**, *26*, 647.
- [45] J. Mei, Y. Dio, A. L. Appleton, L. Fang, Z. Bao, *J. Am. Chem. Soc.*, **2013**, *135*, 6724.
- [46] J. D. Yuen, F. Wudl, *Energy Environ. Sci.*, **2013**, *6*, 392.
- [47] R. Stalder, J. Mei, K. R. Graham, L. A. Estrada, J. R. Reynolds, *Chem. Mater.*, **2014**, *26*, 664.
- [48] Y. Deng, J. Liu, J. Wang, L. Liu, W. Li, H. Tian, X. Zhang, Z. Xie, Y. Geng, F. Wang, *Adv. Mater.*, **2014**, *26*, 471.
- [49] N. K. Kaushik, N. Kaushik, P. Attri, N. Kumar, C. H. Kim, A. K. Verma, E. H. Choi, *Molecules*, **2013**, *18*, 6620.
- [50] D. Billaud, E. B. Maarouf, E. Hannecart, *Mater. Res. Bull.*, **1994**, *29*, 1239.
- [51] D. Billaud, E. B. Maarouf, E. Hannecart, *Synt. Met.*, **1995**, *69*, 571.
- [52] P. S. Abthagir, K. Dhanalakshmi, R. Saraswathi, *Synt. Met.*, **1998**, *93*, 1.
- [53] R. Lazzaroni, A. D. Pryck, C. Debaisieux, J. Riga, J. Verbist, J. L. Bredas, J. Delhalle, J. M. Andre, *Synt. Met.*, **1987**, *21*, 189.
- [54] C. Zhijiang, Y. Guang, *Synt. Met.*, **2010**, *160*, 1902.
- [55] Z. Liang, J. Zhao, Y. Zhang, *J. Org. Chem.*, **2010**, *75*, 170.
- [56] J. Mei, K. R. Graham, R. Stalder, J. R. Reynolds, *Org. Lett.*, **2010**, *12*, 660.
- [57] A. Iraqi, I. Wataru, *Chem. Mater.*, **2004**, *16*, 442.
- [58] T. Yamamoto, S. Wakabayashi, K. Osakada, *J. Organomet. Chem.*, **1992**, *428*, 223.
- [59] H. Asakura, T. Shishido, T. Tanaka, *J. Phys. Chem. A*, **2012**, *116*, 4029.

- [60] Y. Li, W.-H. Wang, S.-D. Yang, B.-J. Li, C. Feng, Z.-J. Shi, *Chem. Commun.*, **2010**, *46*, 4553.
- [61] N. H. Nordin, N Othman, Z. Ahmad, *Adv. Mat. Research*, **2013**, *747*, 733.

Chapter 5 Electrochromic Study of Benzothiadiazole Based Polymers

5.1 Introduction

Electrochromism is a unique characteristic that is displayed by some materials by reversibly changing colors when a surge of electrical charged is applied. Such materials can be used to construct electrochromic devices, depending on the specific applications. An electrochromic device changes light transmission when a voltage is applied and thus one can control the amount of light passing through it. Such examples include electrochromic windows by changing its opacity from transparent to translucent or vice versa. Traditional electrochromic material includes, tungsten oxide (WO_3), iridium dioxide (IrO_2), titanium dioxide (TiO_2), polyaniline, polyacetylene and many other conjugated polymers [1]. Organic materials such as viologens and metallophthalocyanines came in development and showed greater advantages over inorganic compounds. These include coloration efficiency, fast switching ability, multiple colors and fine-tuning of the band gap [2-4].

These advantages are due to alterations of the backbone of the polymers. Substitution in the conjugated polymer's backbone with more electron donating group has incredible influence on the electrical, electrochemical and optical properties [5]. These influences include the change of coloration efficiency which is defined as the relationship between injected/ejected charge as a function of electrode area and the change in optical density unit. Studies showed the coloration efficiency is far better in materials made of organic backbone ($30\text{-}700\text{ cm}^2\text{C}^{-1}$) than those of inorganic material ($10\text{-}50\text{ cm}^2\text{C}^{-1}$). This shows that using organic electrochromic materials increases

efficiency by one order magnitude over inorganic materials. The wide range of coloration efficiency values in conducting polymers is a very good example for the enhancement of polymer properties by backbone modification [2].

In electrochromic materials, electrochemical reduction and oxidation activates a reversible change in the reflected or transmitted light, which is the essence of electrochromism. The stability of the electrochromic materials when switching between the different oxidation states is essential for a practical use of these organic materials. Electrochromic materials should switch between their reduced and oxidized states with good efficiency, or be able to switch to different oxidation states that display different colors with efficient lifetime. Compared to inorganic electrochromic materials, organic polymers are very promising in terms of their stability upon multiple switching. As an example, a sealed polymeric electrochromic device under an inert atmosphere could be switched 180 000 times with only 6% loss of its total 75% optical contrast [6].

Until recently, no green colored conducting polymer had been reported due to the difficulty in achieving the absorptions required in the visible region to reflect the green color. The discovery of green organic polymers to the additive primary color was a step forward for the commercialization of these materials. The discovery was reported in 2004 along with the electrochemical and optical properties of the green conjugated polymer. The great stability of this polymer was demonstrated after 10000 double potential steps, which makes it a prime candidate for completion of the RGB circle [7]. Studies done by the Reynold group on conjugated polymers showed that changing the backbone can produce many different colored polymers and using different polymers in their neutral, intermediate and doped states can also produce a different variety of

colors [4]. Furthermore, the theory of color mixing defines that by subtracting or adding two different colors can produce a new color. Accordingly, it is possible to obtain all colors required for commercial electrochromic applications from conjugated polymers [8].

The spectroelectrochemistry of electrochromic polymers showed that tuned polymers can produce different spectra in the ultraviolet, visible and NIR regions. High and low band gap polymers have π - π^* transitions in the UV and NIR regions, respectively. Our eyes are sensitive to certain range of wavelength and not all optical changes in π - π^* transitions can be followed with the naked eye. Polymers that contain high band gap have their π - π^* transitions in the UV region are more sought out for application uses due to their absorption changes in the visible region, this correspond to low energy charge carriers (polarons and bipolarons) [9]. Majority of conjugated polymers have a band gaps between 1.0 and 2.5 eV and usually present their π - π^* transitions in the visible region. However, efforts have been focused on obtaining NIR materials due to variety of applications such as optical fiber-based telecommunication (specifically 850 nm, 1310 nm and 1550 nm), optical attenuator, data storage, thermal control, aerospace and military camouflage [10-17]. Active studies of the spectroelectrochemistry of conducting polymers have showed that there are other advantages over inorganic electrochromics material. Most of the non-organic electrochromic materials only switch between two oxidation states (neutral and oxidized); conducting organic polymers are able to be controlled between these two extreme oxidation states with a certain applied potential. This shows that single polymeric electrochromic film can produce different absorptions at different oxidation

states, resulting in different tones of the same color, or even different colors, with small variations in the applied electrical voltages. Figure 5.1 demonstrates this phenomenon of a widely studied organic polymer, PEDOT.

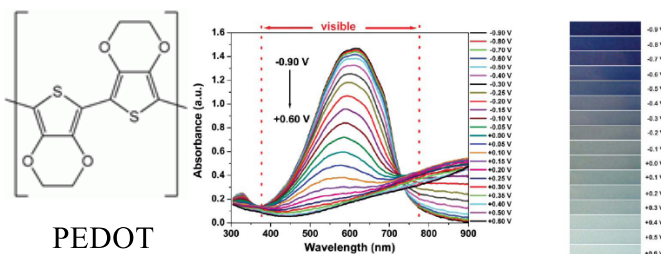


Figure 5.1: Structure of PEDOT and spectroelectrochemical properties (Adapted with permission from Ref. 1)

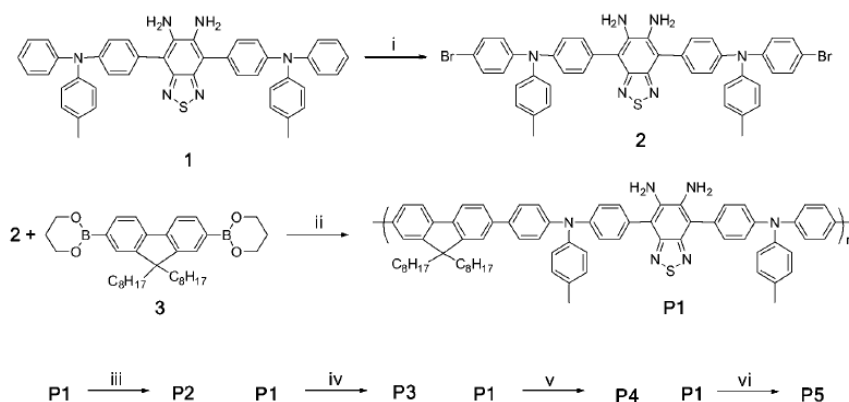
PEDOT is a conducting polymer based 3,4-ethylenedioxythiophene monomer. PEDOT and derivatives have potential application such as field-effect transistors, electroluminescent devices, solar cells, photochemical resists, nonlinear optic devices, batteries, diodes, and chemical sensors [18-21]. The electrochromic properties of PEDOT are used to manufacture windows and mirrors, which can become opaque or reflective when a potential is applied [22]. Studies have shown that adopting electrochromic windows in commercial homes could save billions of dollars per year in air conditioning costs [23].

The donor-acceptor concept predicts that polymers with repeating unit, which is composed of a donor with a high lying energy level and an acceptor with low lying energy level have small band gaps and wide valence and conduction bands. The concept works on the idea that the polymer valence bands form energetically near the HOMO of the donor and that the conduction forms in the region of the LUMO of the acceptor. Band formation requires strong interaction between the fragments, and this interaction

is inversely proportionally to the energy difference between the fragment orbitals [24, 25].

Benzo[1,2-*c*:4,5-*c'*]bis([1,2,5]thiadiazole (BBTD) and its derivatives are strong electron accepting units, which are suitable for designing low band gap donor-acceptor material used as the active component in transistor, photovoltaic and NIR photodetector devices. Previous investigation of D- π -A- π -D NIR chromophore series containing BBTD and its selenium analogues show low band-gap in nature contributed by quinoidal characteristic due to the electron-deficient imine nitrogen and electron delocalization by incorporating different donors. The corresponding polymers containing BBT or structurally related acceptors can gradually change the LUMO level, from the hypervalent sulfur atom, and absorb at different wavelengths and show various colors [26-32].

A series of low band gap polymers containing BBT were synthesized by Gang et al. and their structures were fully characterized by ^1H NMR and FT-IR. Because most of low band gap compounds with electron acceptors are unstable in alkaline solution and readily attacked by nucleophiles, it is still a challenge to synthesize high-molecular-weight low-band-gap polymers. The polymers were synthesized from a precursor polymer, **P1**, Scheme. 5.1 and Fig. 5.2, because the 1,2-diaminophenylene group is stable in Suzuki coupling reaction and it can be easily converted to electron-deficient groups such as thiadiazolo-quinoxaline, thiadiazolo-phenazin, benzobisthiadiazole and selenadiazolo-benzothiadiazol, corresponding to polymers **P2-P5** [33].



Scheme 5.1: Synthetic routes to polymers **P1-P5**. *Reagents and conditions:* (i) Bu_4NBr_3 , CH_2Cl_2 , 25°C , 3h (ii) $\text{Pd}(\text{PPh}_3)_4$, K_2CO_3 (aq, 2 M), toluene, Aliquat 336, 95°C , 24h (iii) 1,4-dioxane-2,3-diol, AcOH, 60°C , overnight (iv) 1,4-dioxane-2,3-diol, AcOH, 60°C , overnight (v) PhNSO , TMSCl , pyridine, 80°C , overnight (vi) SeO_2 , THF, reflux, 4h.

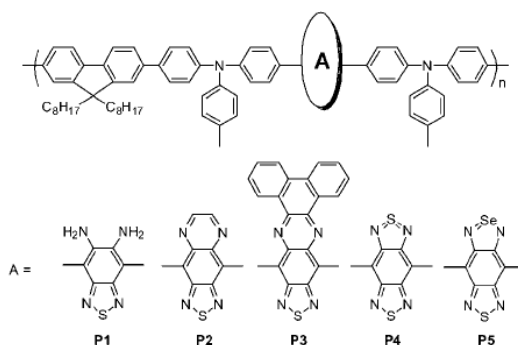


Figure 5.2: Structures of **P1-P5**

It was reported that BBTD acceptor strength can be increased via intermolecular or intramolecular interaction by addition of either of a Lewis acid or other electron-acceptor species. Gang et al. showed that adding boron trifluoride (BF_3) adduct can lead to bathochromic shift in absorption by 426 nm and it was found that BF_3 binds to the nitrogen atom on the thiadiazole, which effectively pulls electron density away from the BBTD unit. This, ultimately, enhances the intramolecular charge transfer (ICT)

transition between peripheral donor and acceptor core. Additionally, there is a synergistic lowering of the absolute energies of the two frontier molecular orbitals, thus narrowing the band gap [26]. However, fabrication of optoelectronic devices containing Lewis acid would be impractical due to corrosive nature of the acid. Therefore, a different approach on improving ICT would be introducing intramolecular hydrogen bonding (IHB). Introduction of pyrrole spacer with BBTD have shown to contribute similar effect of adding a Lewis acid. IHB have exhibited a bathochromic shift by 183 nm, suggesting that partial removal of electron density from the BBT core [26]. However, there are only few reported polymers with pyrrole spacer exhibiting IHB with benzothiadiazole (BTD) core. Although, these polymers show narrow band gap and low oxidation potential, their synthesis are tedious, employing electropolymerization, only micrograms of the polymer can be synthesized and the molecular weight of these polymers tend to low [34, 35].

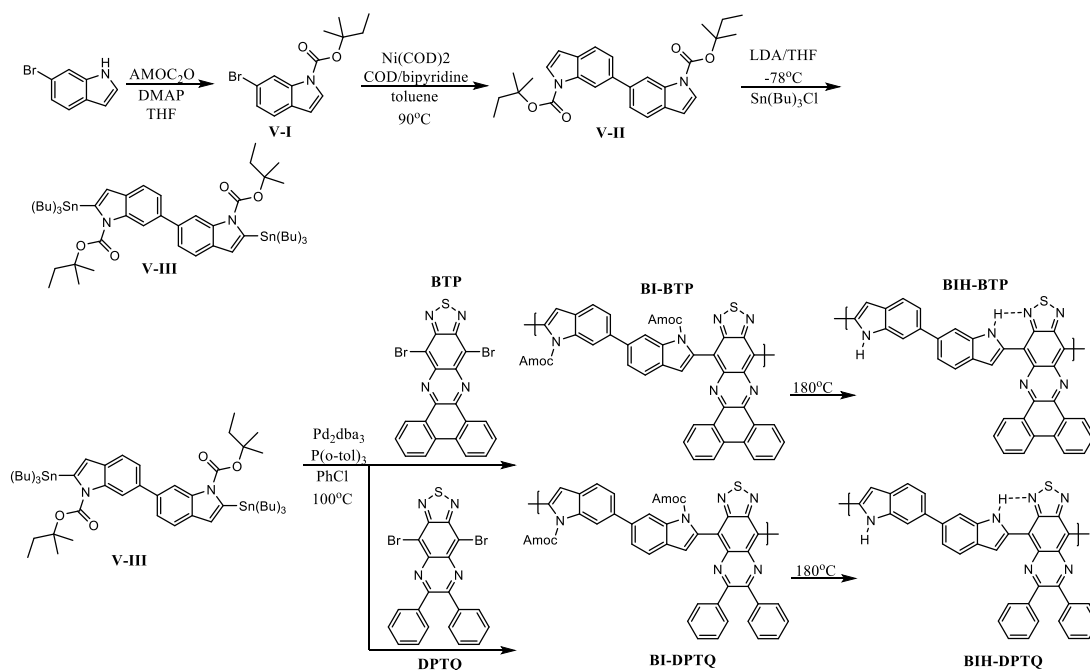
Using donor-acceptor approach a series of low band gap polymers were constructed which show green color in their neutral state. In this chapter, electrochromic cells were prepared for adaptive camouflage for military purpose, and to determine the redox chemistry, efficiency of coloration, operating voltage, and switching capabilities using organic polymers.

5.2 Results and discussions

5.2.1 Synthesis of benzothiadiazolo-based donor-acceptor polymers bearing thermally cleavable group

We employed **BTP** and **DPTQ** core with thermally cleavable moiety on indole.

Polymer synthesis was accomplished by polymerizing compound **V-III** and **BTP/DPTQ** (Scheme 5.2). Previously, we incorporated *tert*-butyloxycarbonyl group in our DPP compounds, although those polymers showed reasonable solubility, optimal film formation was not reached. Therefore, a slightly larger, yet still volatile, group was introduced, di-*tert*-pentyl dicarbonate (Amoc), to the biindole donor. First, protection of 6-bromoindole was accomplished identical to that of DPP-BOC, using catalytic amount of DMAP; the Amoc group was employed with high yield. This is followed by Yamamoto cross-coupling using Ni(COD)₂ and bipyridine to afford compound **V-II**. It is worth noting, Amoc group should be employed before the coupling reaction, the amine on the indole will bind to the nickel complex producing by-products. The subsequent organotin compound, **V-III**, was synthesized according to literature procedure [36]. Polymerization was achieved via Stille cross coupling using palladium catalyst. Despite the bulkier Amoc group, the polymer still has limited solubility, with fair solubility in CHCl₃, chlorobenzene, dichlorobenzene and partial solubility in THF. Molecular weights and polydispersity indices (PDI) of the polymers were determined by gel permeation chromatography (GPC) relative to polystyrene standards. **BI-BTP** has a weight of 4.77×10^3 Daltons with PDI of 1.4 and **BI-DPTQ** has a molecular weight of 5.22×10^3 Daltons with PDI of 1.9.



Scheme 5.2: Synthesis of polymers **BI-BTP** and **BI-DPTQ**

5.2.2 IR Characteristic

IR analysis of **BI-BTP/DPTQ** were done using KBr pellet before and after thermal cleavage. As shown in Figure 5.3, both polymers contain the ester from Amoc group arising with intense C=O peaks at 1735 cm⁻¹ along with the aromatic C=C peaks at 1610 cm⁻¹. After thermal cleavage, we observe CO₂ peak arising at 2330 cm⁻¹, due to the decomposition of tert-pentyl carbonate to carbon dioxide and 2-methylbutene. The volatile 2-methylbutene is not evident in the IR due to overlapping with C=C peak.

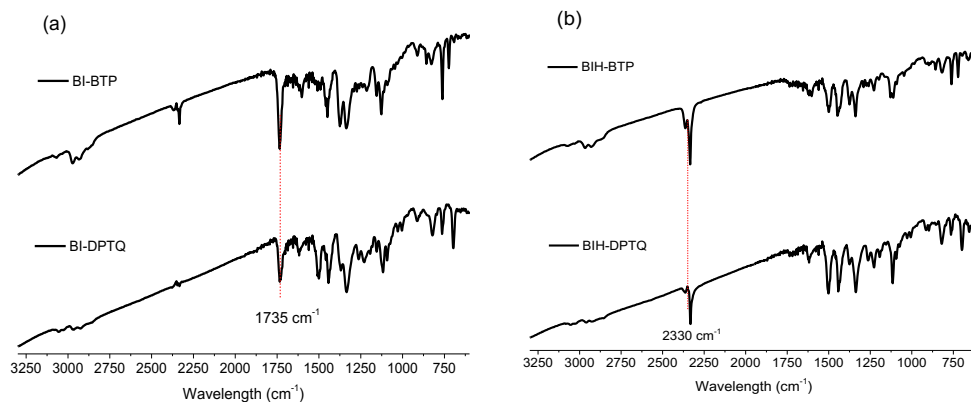


Figure 5.3: IR spectra of polymers (a) **BI-BTP** and **BI-DPTQ** (b) **BIH-BTP** and **BIH-DPTQ** in KBr pellet.

5.2.3 Thermal properties

The two polymers initially show decomposition with approximately 30% and 40% weight loss for **BI-DPTQ** and **BI-BTP**, respectively. This is due to the cleavage of the Amoc group at 190 °C. Subsequently, with the loss of the cleavable group, polymer **BI-DPTQ** has a 5% weight loss at 284 °C. Similarly, **BI-BTP** has 5% weight loss at 270 °C. DSC show parallel to that of TGA, with concavity occurring at 190 °C due to loss of the Amoc group. In a repetitive cycle, no glass transition or crystallization peak is observed, indicating amorphous state for the polymers.

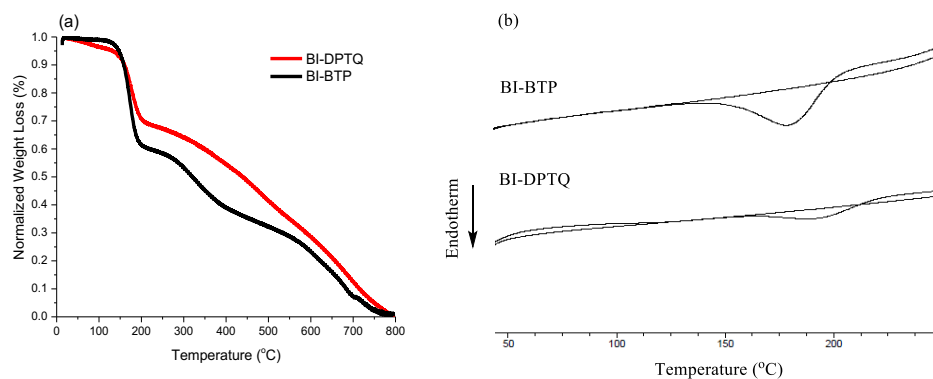


Figure 5.4: Thermal stability of **BI-BTP** and **BI-DPTQ** (a) TGA (b) DSC.

5.2.4 Absorption properties

The absorption and photoluminescence of polymers **P1-P5** were recorded in chlorobenzene, Figure 5.5. Without a strong acceptor, **P1** absorbs with maximum (λ_{\max}) at 440 nm and emits at 558 nm, which is due to the π - π^* and n- π^* transition. In comparison, owing to the presence of electron-withdrawing groups, the maximum absorption and emission wavelengths of polymers **P2-P5** are red-shifted dramatically to near infrared region, Table 5.1. The UV-visible spectrum shows absorption ranging from 620 to 820 nm. The electronic absorption spectra of the four polymers display two discrete bands (Fig. 5.5a): the bands in the short wavelength region plus the shoulders ranging from 300–450 nm attributed to the $\pi - \pi^*$ and n- π^* transitions of the conjugated aromatic segments, and the region in long wavelength region are due to the intramolecular charge transfer (ICT) transitions between the donors and the acceptors. The maximum absorption wavelength (λ_{\max} abs) diverges in the order of **P1** < **P2** < **P3** < **P4** < **P5**. We observe a 90 nm red-shift in λ_{\max} abs of **P3** relative to **P2**, due to the extension of the conjugation length in the [1,2,5]thiadiazolo[3,4-i]dibenzo[a,c]phenazine (TDP) core. Furthermore, replacement of sulfur atom by selenium atom led to a further red-shift (**P5** vs. **P4**), due to the polarization effect of selenium atom [37]. It is worth noting that **P3** absorbs at 380 and 720 nm, with a valley at 503 nm and has a leaf green color (Fig. 5.5c). Contrast to absorption spectra, the emission spectra in solution just show only one peak in the visible, while the rest of the polymers emits in the near infrared spectral region. The emission wavelengths of **P1-P5** vary in the same trend as for the absorption. Polymers **P2-P5** demonstrate a large Stokes shift, which further confirms the presence of a strong ICT in these polymers. In

association with the solution absorption spectra, the absorption maxima of the polymer films are red-shifted by 7–87 nm, indicating the presence of intermolecular π - π interaction and rigid backbone packing. Additionally, the fluorescence spectra of the polymer films display several peaks, which could be due to the vibronic bands and intermolecular charge transfer bands. The longest emission wavelength reaches 1280 nm, falling in the telecommunication window. Contrasting to many NIR dyes, the polymers films **P2–P5** emit strongly in the NIR spectral region, thus, they can potentially be used in NIR light emitting diodes (LEDs).

Table 5.1: Characterizations of Polymers **P1-P5**

	λ_{abs} max[nm] ^a	$\lambda_{\text{PL max}}$ [nm] ^a	Stokes shifts [nm] ^a	Bandgap [eV] ^b	E_{onset} [V]	HOMO [eV] ^d	LUMO [eV] ^e
P1	371,440(sh) ^c	558	187	2.67	0.31	-4.67	-2.00
P2	608	950	342	1.71	N/A	N/A	N/A
P3	697	1020	323	1.50	0.63	-4.99	-3.28
P4	714	1060	346	1.44	0.52	-4.88	-3.38
P5	814	1105	291	1.29	0.51	-4.87	-3.58

^a Measured in chlorobenzene, excitation wavelengths are at their maximum absorption wavelengths. ^b

Optical band gap, estimated from the onset wavelength of optical absorption spectra. ^c Shoulder peak.

^d Calculated using $E_{\text{HOMO}} = -e(E_{\text{ox}} + 4.36)$ with oxidation potential of ferrocene/ferrocenium at 0.44 V to the Ag/Ag⁺ electrode. The redox potential of Fc/Fc⁺ has absolute energy level of -4.8 eV [38, 39].

^e Calculated from the HOMO level and optical band-gap.

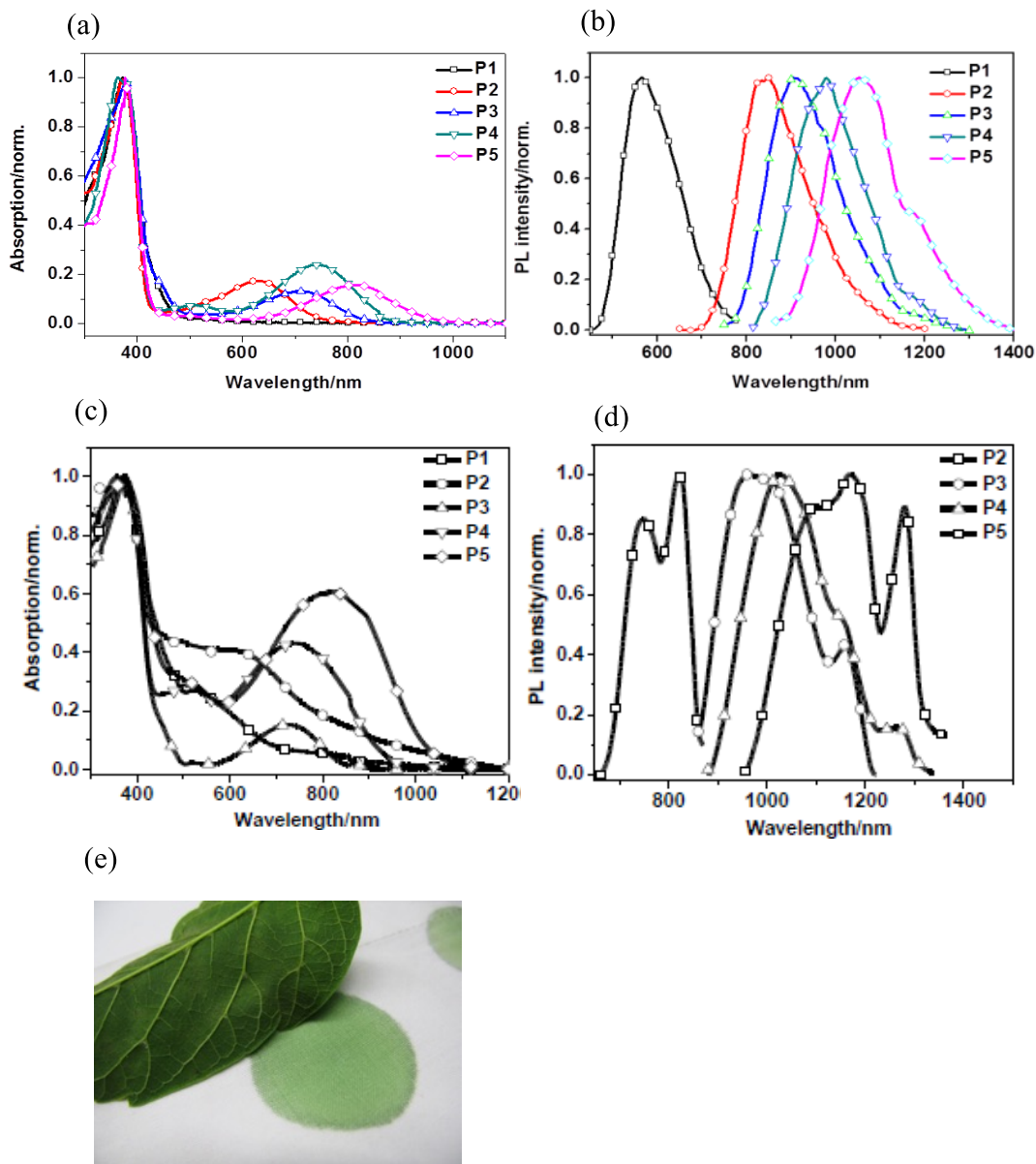


Figure 5.5: (a) Normalized absorption (b) fluorescence emission spectra of five polymers **P1-P5** in chlorobenzene (c) normalized absorption on film (d) fluorescence emission on film of **P1-P5** (e) leaf-color of **P3** (Reproduced from Ref. 33 with permission from The Royal Society of Chemistry)

The absorption studies on **BI-BTP** and **BI-DPTQ** were done in solution and film are shown on Fig. 5.6. Similar to polymers **P1-P5**, they show two strong bands,

first in the 400 nm region and second, in the visible-near infrared region. **BI-BTP** has a λ_{\max} of 705 nm in solution, 725 nm in film and tailing from 1100 nm. **BI-DPTQ** shows a more bathochromic shift compared to **BI-BTP**, with λ_{\max} 780 nm in solution, 800 nm in film and tailing from 1100 nm. Despite having a more rigid fused acceptor core, **BI-BTP** is slightly blue-shifted compared to **BI-DPTQ**. This can be accounted due to a lower molecular weight of **BI-BTP**. As expected, after thermal cleavage of the Amoc group we observe a bathochromic shift in both solution and film. We observe approximately 120 nm shift in solution and 140 nm shift in film for **BIH-DPTQ**. Whereas, for **BIH-BTP** a 205 nm shift in solution and 265 nm shift in film is observed. The improved ITC enhancement is more evident for **BIH-BTP** due to higher degree of structural conformation in the solid state thus leading to lowering of the frontier orbital due to the pulled electron density from the acceptor core.

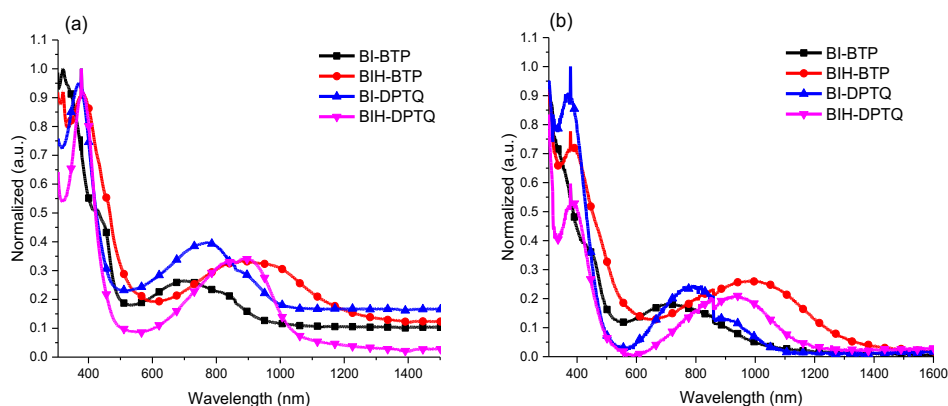


Figure 5.6: Normalized UV of **BI(H)-BTP** and **BI(H)-DPTQ** (a) in TCB (b) thin glass film.

Table 5.2: Absorption characteristic of **BI(H)-BTP** and **BI(H)-DPTQ**

	λ_{abs} max[nm] solution	λ_{abs} max[nm] film	Bandgap [eV] ^a	Optical Bandgap [eV] ^b	HOMO [eV] ^c	LUMO [eV] ^c
BI-BTP	705	725	0.63	1.13	-5.42	-4.79
BIH-BTP	910	990	0.66	0.89	-5.32	-4.66
BI-DPTQ	780	800	0.59	1.13	-5.34	-4.75
BIH-DPTQ	900	940	0.89	1.03	-5.49	-4.60

a) Electrochemical band gap using onset potentials; b) Calculated from onset wavelength of absorption film spectra, $E_g = 1240/\lambda$ c) HOMO/LUMO = $-(E_{\text{ox/red}} + 5.13)$ eV [40, 41]

5.2.5 Electrochemical properties and band gaps

The electrochemical properties of polymers **P1–P5** (except for **P2** due to poor solubility) were determined by cyclic voltammetry (CV) and the data are summarized in Table 5.1. A solution, 10 mg/mL concentration, containing the polymer in chlorobenzene was prepared and spun-coated on ITO-coated glass slides, which serves as the working electrode. The slide was heated to remove any residual solvent, CV was performed in a 0.1 M Et_4NClO_4 electrolyte in acetonitrile with Pt wire counter electrode and Ag/Ag⁺ reference electrode. The cyclic voltammograms of **P1** and **P3–P5** are shown in Appendix C. The polymers exhibit excellent reversibility of electrochemical characteristics and they can be used as electrochromic materials. Two quasireversible waves are observed for all the polymers in the oxidation region, which are attributed to the oxidation of triphenylamine (TPA) segments, and the two electrons are removed successively from the two nitrogen atoms to form radical cation (polarons) (Fig. 5.7). Due to the strong electron-donating TPA and amino groups, the precursor polymer **P1** exhibits a low onset oxidation potential ($E_{\text{onset}}^{\text{ox}}$) at 0.31 V and the HOMO level of -4.67 eV, which corresponds with previously reported polymers containing TPA and NMe_2 groups [42]. Due to the presence of the D- π -A- π -D structure in **P3–P5**, their

onset oxidation potentials increase and HOMO levels decrease about 0.3 eV. Accordingly, the band-gap levels of **P2–P5** are in the range of 1.3–1.7 eV. The reversible transition between neutral and reduced states was not observed. This is potentially due to permanent structural change in the backbone of the polymer when the polymers are reduced.

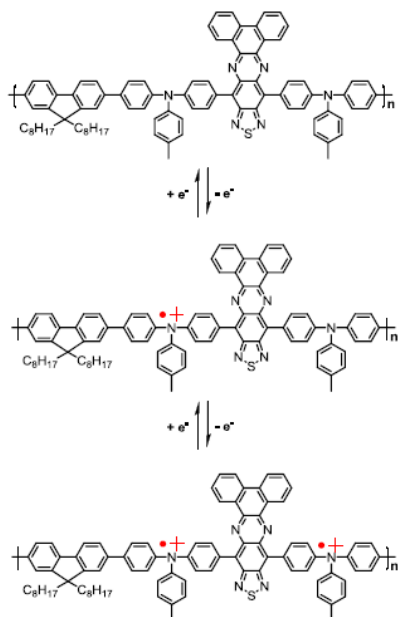


Figure 5.7: The neutral, radical cation and dication states during redox process of polymer **P3**. (Reproduced from Ref. 33 with permission from The Royal Society of Chemistry)

The electrochemical properties of **BI-BTP** and **BI-DPTQ** on thin film were investigated at ambient temperature and after thermal cleavage using square-wave voltammetry. The results are summarized in Table 5.2. The HOMO/LUMO levels were extrapolated from the onset potentials of the oxidation and reduction curve. The LUMO levels of the polymers range from -4.79 to -4.60 eV. As expected we observe lowering of the LUMO level after thermal cleavage of the Amoc group, which is attributed to

the more electron deficient acceptor due to the hydrogen bonding network. Ideally, an effective approach to lowering the band gap would be incorporating a less electron-rich donor (low-lying HOMO level). Since the donor unit has an increase of electron density upon thermal cleavage, we should expect the HOMO level to rise. This is seen for **BIH-DPTQ** but not for **BIH-BTP**. For both cases, even with the bathochromic shift, the bandgap rises.

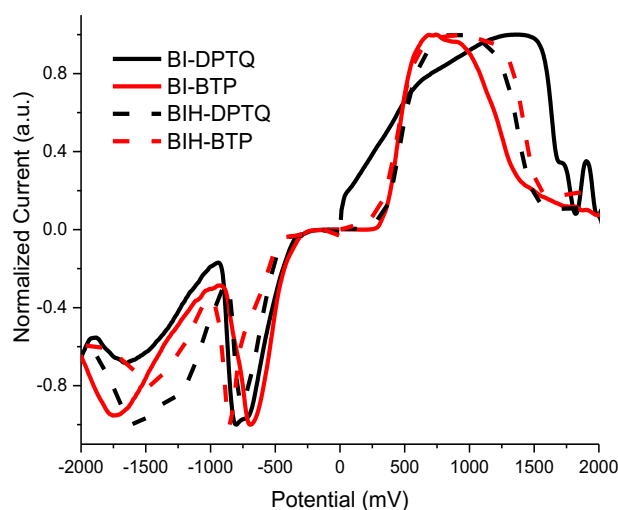


Figure 5.8: Normalized square-wave voltammetry of **BI(H)-BTP** and **BI(H)-DPTQ**.

5.2.6 Electrochromic properties of the chromophores

P1-P5 were studied for electrochromic properties, Fig. 5.9, with **P3** extensively studied due to the camouflage capability of the surrounding environment. The polymers are electrochromic, changing from orange, blue, green, grey and dark gold in the neutral state to grey or sienna in the oxidized state. When the polymer film is completely oxidized, it turns to a dark green color. Neutral polymer film absorb in the visible region, upon oxidation, π - π^* transition decreases with an increasing of a broad peak outside the visible region at longer wavelength in the NIR region (1150 nm), corresponding to

low energy charge carriers. For **P1**, it's color change from orange to gray in the oxidized state.

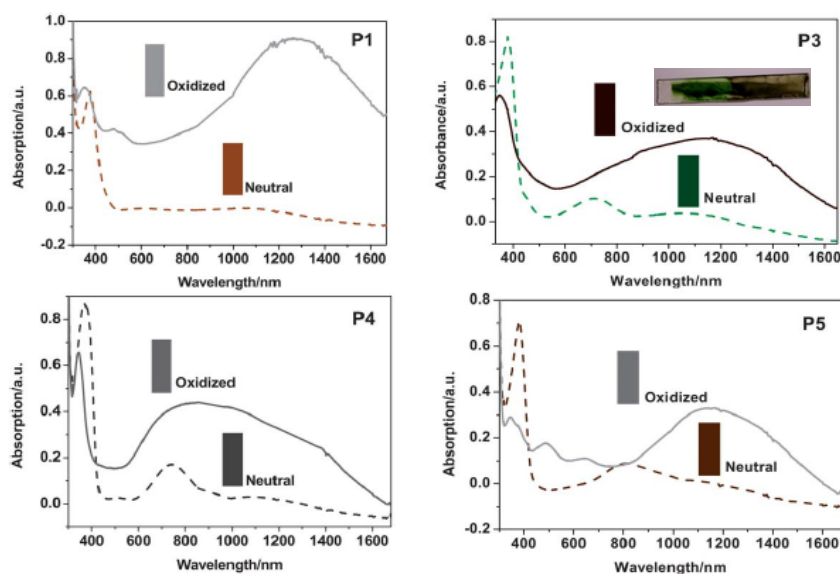


Figure 5.9: UV/Vis/NIR absorption spectra of polymer **P1** and **P3-P5** thin films on ITO-coated glass substrate (in CH_3CN with 0.1 M Et_4NClO_4 as the supporting electrolyte) at neutral (dashed) and oxidized (solid). (Reproduced from Ref. 33 with permission from The Royal Society of Chemistry)

The green polymer **P3** was subjected to more extensive study for its visible and NIR electrochromism. When oxidized the polymer is tuned to a very deep green color shown on Fig. 5.9. This makes a prime candidate for military camouflage application. From the electrochemical properties, very little potential is required to fully oxidize the polymer to attenuate in the NIR region. Most of the inorganic electrochromic materials are able to only switch between two oxidation states (neutral and oxidized), EC polymers are able to jump between two extreme oxidation states with applied potentials. This allows single polymeric electrochromic film produce different absorptions at

different oxidation states, resulting in different tones of the same color, or even different colors, with small variations in the applied electrical voltages [8]. When the applied voltage increases from 0.0 V to 1.0 V, the π - π^* absorption band at 380 nm decreases gradually (Fig. 5.10a) and at the same time, a new broad band appears in the NIR region at about 1160 nm, due to the formation of radical cations (polarons) in the main chain. The reflectance is coherent with the p-doping absorption (Fig. 5.10b). With an increasing applied voltage, there's a decrease of reflectance in the NIR region and also a decrease in UV-Visible region. **P3**, along with **P1-P5**, are fully conjugated organic polymers, as the oxidation level is consistently increased, charged carriers balanced with counter ions are created on the backbone (3° amine group). The low energy-gap polymer is as oxidative generated via p-doping which allows the formation of radical cations (polarons) and further dications (bipolarons) the absorption can be transferred into the near-infrared region with depletion of the ground-state transition in the visible region. The ability of the backbone to form a stable quinoidal geometry, as well as the position of the bipolaronic transition relative to the visible region, governs the transmissivity of the fully oxidized state.

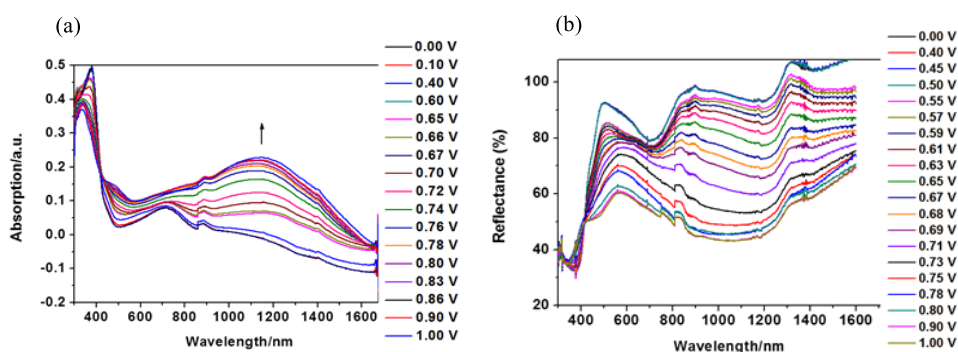


Figure 5.10: p-Doping (a) absorption a **P3** film on ITO-coated glass slide from 0 V to 1 V (b) reflectance of a **P3** film on ITO-coated glass slide in front of reference mirror

from 0 V to 1 V. (Reproduced from Ref. 33 with permission from The Royal Society of Chemistry)

The rate of change in transmittance upon oxidation/neutral states provides a direct evaluation of the switching ability of a material. The transmittance of the film of polymer **P3** coated on ITO glass was monitored at the telecommunication wavelengths of 1310 nm and 1550 nm, respectively, while the potential was switched between 0.0 V and 1.0 V (vs. Ag wire) using square wave potentiometry. Fig. 5.11 shows the electrochromic switching; the percent transmittance was monitored at 1310 and 1550 nm at 36 and 30 %, respectively, for **P3**. The response time from the neutral to oxidized state or vice versa was found to be 2.0 s for 95% of full optical recovery. The optical contrast showed nearly constant after hundreds of cycles switch, indicating robust and excellent stability.

The transmittance properties can be used to determine the coloration efficiency of the polymer via the following formula [43]:

$$CE(\lambda) = \Delta OD(\lambda) / Q_d \text{ (cm}^2/\text{C)}$$

$$\Delta OD(\lambda) = \log[\%T_b(\lambda) / \%T_c(\lambda)]$$

where T_b is the transmittance of the neutral state and T_c is the transmittance of the oxidized state. It is obtained by determining the injecting/ejected charge as a function of the electrode area (Q_d) and the change in optical density (ΔOD) during a redox step of the devices. The coloration efficiency of **P3** at 1310 and 1550 nm are 479 and 232 cm^2/C , respectively. A large efficiency would exhibit a large change in transmittance with a small increase in charge. Furthermore, optical attenuation (A) can be calculated

from:

$$A = 10 \times \Delta OD/L$$

Where L is the thickness (μm) of the electrochromic active layer. The optical attenuation of P3 is calculated to be $44 \text{ dB } \mu\text{m}^{-1}$ at 1310 nm and $21 \text{ dB } \mu\text{m}^{-1}$ at 1550 nm , which is comparable to those of PEDOT film [44].

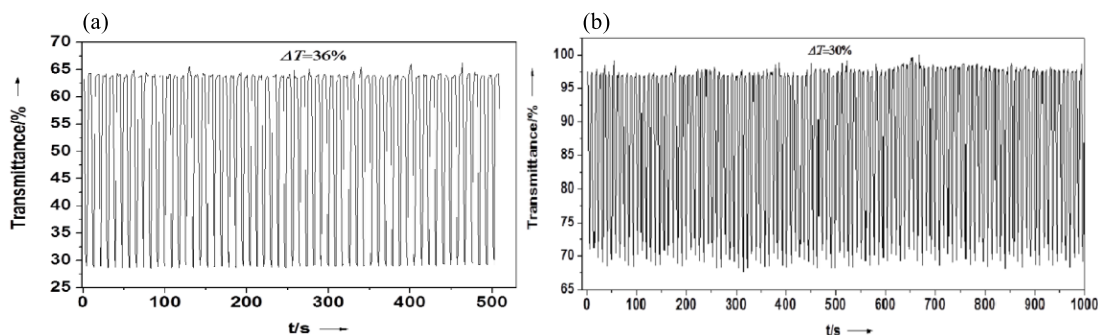


Figure 5.11: Changes in optical transmission of film of **P3** at (a) 1310 nm (b) 1550 nm over time with stepping potentials between $+1.0 \text{ V}$ and 0 V (Reproduced from Ref. 33 with permission from The Royal Society of Chemistry)

5.2.7 OTFT measurements

With the minor difference in the HOMO/LUMO levels of **BI-BTP/DPTQ** suggests they may be capable of ambipolar charge transport. The polymers were evaluated in bottom gate contact configuration and the results are summarized in Table 5.3 and Appendix D. Both polymers showed ambipolar behavior, with **BI-BTP** showing average mobility of $3.87 \times 10^{-5} \text{ cm}^2 \text{V}^{-1} \text{s}^{-1}$ for p-type operation and $2.2 \times 10^{-5} \text{ cm}^2 \text{V}^{-1} \text{s}^{-1}$ for n-type operation, while **BI-DPTQ** show mobility of $6.1 \times 10^{-5} \text{ cm}^2 \text{V}^{-1} \text{s}^{-1}$ for p-type operation and $5.4 \times 10^{-5} \text{ cm}^2 \text{V}^{-1} \text{s}^{-1}$ for n-type operation. After thermal cleavage, there is a slight increase in mobility for both p-type and n-type operation, with **BIH-BTP** increasing almost 30 fold, suggesting that hydrogen bonding network improves

coplanarity. X-ray diffraction was performed to better understand morphology, however due the low solubility of the polymers no signal was observed. The low electron and hole mobilities can be accounted by the poor film formation and low molecular weight.

Table 5.3: Summary of OTFT measurements

Polymer	150°C		200°C	
	Electron mobility $\text{cm}^{-2}\text{V}^{-1}\text{s}^{-1}$	Hole mobility $\text{cm}^{-2}\text{V}^{-1}\text{s}^{-1}$	Electron mobility $\text{cm}^{-2}\text{V}^{-1}\text{s}^{-1}$	Hole mobility $\text{cm}^{-2}\text{V}^{-1}\text{s}^{-1}$
BI-BTP	2.2×10^{-5}	3.87×10^{-5}	-	-
BIH-BTP	-	-	5.57×10^{-5}	1.10×10^{-4}
BI-DPTQ	5.4×10^{-5}	6.10×10^{-5}	-	-
BIH-DPTQ	-	-	6.57×10^{-5}	7.23×10^{-5}

5.3 Conclusion

Utilizing donor-acceptor strategy, a series of low band gap polymers (**P1-P5**) were synthesized, which show two absorption bands, and the maximum absorption wavelength can be tuned by changing the acceptor units. All of these emission wavelengths are longer than 800 nm, in near-infrared (NIR) region. The presence of heterocyclic and amino groups allow these polymers to undergo reversible electrochemical redox reaction, and as such, they are able to electrochemically attenuate the light at the infrared region in both transmission and reflection mode. These EC materials show high contrast ratio (percent transmittance change between bleached and colored state), high color efficiency, low cost in preparation, good processability, fast switching time and long-time stability. Polymer **P3** can potentially be used in switchable camouflage material.

Two new thiadiazoloquinoxaline-based polymers (**BI-BTP/DPTQ**) bearing a thermal cleavable group were synthesized. The polymers show very low band gap and show a bathochromic shift, reaching near 1000 nm after thermal cleavage. OTFT

measurement show ambipolar performances, however due to low solubility and molecular weight the device performances were not ideal.

5.4 Experimental

5.4.1 Materials

All the chemicals and reagents were used as received from commercial sources without purification. Solvents for chemical synthesis were purified by distillation. Chemical reactions were carried out under an argon atmosphere. Polymers **P1-P5** were previously synthesized [33].

5.4.2 Instruments

Thermogravimetric analysis (TGA) was carried out in nitrogen on a Hi-Res TGA 2950 thermogravimetric analyzer with a heating rate of $10^{\circ}\text{C min}^{-1}$. Absorption and fluorescence spectra were recorded with a Shimadzu UV-3600 spectrophotometer and a PTI fluorescence system or a Lambda 900 Perkin-Elmer spectrophotometer, respectively. FTIR spectra were recorded on a Bio-Rad FTS-135 spectrophotometer. OTFT measurements were externally performed using Agilent B2912A Precision Source/Measure Unit under N_2 .

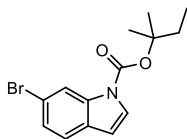
5.4.3 OTFT fabrication

Polymer was evaluated in bottom gate bottom contact OTFT devices. Heavily doped n^{++} -Si wafer was used as substrate with a 300 nm-thick SiO_2 as dielectric layer. 30 nm of Au source and drain pairs were pre-patterned by conventional

photolithography method. The substrates were cleaned by air plasma, followed by acetone and isopropanol in ultrasonic bath. After drying, the substrate was merged in DDTS toluene solution for 20min at room temperature, and then dried by nitrogen. Polymer film was formed by spin-coating a polymer solution (5mg/mL) in chloroform at 3000 RPM for 60 s. Finally, the devices were annealed at 150 and 200 °C for 20min, and measured by Agilent B2912A Precision Source/Measure Unit in N₂. The channel width and length are 30 and 1000 μm, respectively.

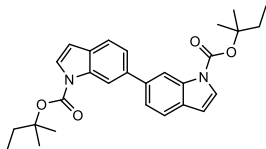
5.4.4 Synthesis

Tert-pentyl 6-bromo-1*H*-indole-1-carboxylate (IV-I)



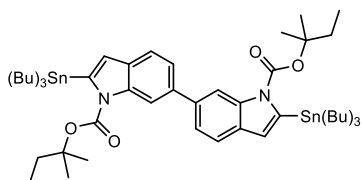
In a round bottom flask flushed with argon, 6-bromoindole (3.25 g, 16.6 mmol), di-*tert*-amyl dicarbonate (4.5g, 18.3 mmol) and 4-dimethylaminopyridine (1 mol %, 0.02 g) was dissolved in 50 mL of dry THF and stirred overnight at room temperature. The solution was quenched with water and extracted with CHCl₃ (3x30 mL). The solution was extracted with 30 mL NaCl (aq) and dried over Na₂SO₄. The solvent was removed under vacuo and purified using column chromatography to afford a color oil (4.52 g, 88%). ¹H NMR (300 MHz, Chloroform-*d*, ppm) δ 8.41 (s, 1H), 7.58 (d, *J* = 3.8 Hz, 1H), 7.47 – 7.33 (m, 2H), 6.55 (dq, *J* = 3.7, 0.8 Hz, 1H), 2.02 (q, *J* = 7.5 Hz, 2H), 1.67 (s, 6H), 1.04 (t, *J* = 7.5 Hz, 3H). ¹³C NMR (75 MHz, Chloroform-*d*, ppm) δ 126.28, 125.87, 121.94, 118.37, 107.05, 86.79, 33.60, 25.58, 8.39.

Di-*tert*-pentyl 1*H*,1'*H*-[6,6'-biindole]-1,1'-dicarboxylate (V-II)



In a dry round bottom flask flushed with argon, **V-I** (1.8 g, 5.8 mmol), Ni(COD)₂ (2 g, 7.27 mmol), COD (1 mL, 8 mmol) and 2,2-bipyridine (1.3 g, 8 mmol) was dissolved in 50 mL of dry toluene. The solution was further flushed with argon for 10 minutes and refluxed for 16 hours. The solution was brought to room temperature and quenched with 50 mL of 1 M HCl and stirred vigorously for half hour. The mixture was then filtered and washed with toluene. The filtrate was extracted with toluene (3x10 mL). The solution was extracted with 50 mL NaCl (aq) and dried over Na₂SO₄. The solvent was removed under vacuum and the crude product was purified by column chromatography using hexane:acetone (9:2 v/v) to give a white viscous oil which solidified over time (2.06 g, 77%). ¹H NMR (300 MHz, CDCl₃, ppm) δ 8.55 (s, 2H), 7.72 – 7.52 (m, 6H), 6.61 (dd, *J* = 3.8, 0.8 Hz, 2H), 2.04 (q, *J* = 7.5 Hz, 4H), 1.68 (s, 12H), 1.05 (t, *J* = 7.5 Hz, 6H). ¹³C NMR (75 MHz, CDCl₃, ppm) δ 138.34, 126.23, 122.50, 120.98, 114.15, 107.08, 86.28, 33.60, 25.68, 8.42. M.P. > 85-87°C. HRMS (ESI)(M+H): Calc. 460.57, Found: 483.4785 (+ Na).

Di-*tert*-pentyl 2,2'-bis(tributylstannyl)-1*H*,1'*H*-[6,6'-biindole]-1,1'-dicarboxylate (V-III)



In a dry round bottom flask, compound **V-II** (0.45 g, 0.98 mmol) was dissolved in 15 mL of dry THF and was brought to -78°C using acetone-dry ice mixture. Lithium diisopropylamide (1.7 M, 1.21 mL) was added dropwise and stirred for 1 hour at that temperature. Tributyltin chloride (0.56 mL, 2.06 mmol) was added dropwise and stirred at -78°C for 30 minutes. The solution was brought to ambient temperature and stirred overnight. The mixture was quenched with water and extracted with CHCl_3 (3x20 mL). The solution was extracted with 30 mL NaCl (aq) and dried over Na_2SO_4 . The solvent was then removed under vacuo and the crude product was used in the next step without purification. ^1H NMR (300 MHz, Chloroform-*d*, ppm) δ 8.32 – 8.26 (m, 2H), 7.66 – 7.56 (m, 4H), 7.50 (dd, $J = 8.1, 1.5$ Hz, 2H), 6.77 (d, $J = 0.8$ Hz, 2H), 2.09 (q, $J = 7.3$ Hz, 5H), 1.74 – 1.66 (m, 18H), 1.62 – 1.50 (m, 16H), 1.43 – 1.29 (m, 18H), 1.15 – 1.01 (m, 24H), 0.91 (t, $J = 7.3$ Hz, 26H). ^{13}C NMR (75 MHz, Chloroform-*d*, ppm) δ 152.04, 144.04, 138.10, 131.19, 122.07, 120.06, 118.23, 114.61, 86.57, 33.20, 29.17, 27.37, 25.76, 13.74, 11.62, 8.48.

General synthesis of Stille cross-coupling polymerization.

In a dry round bottom flask, compound **V-V** (0.55 mmol), **BTP/DPTQ** (0.5 mmol), Pd_2dba_3 (0.038 mmol) and $\text{P}(\text{o-tol})_3$ (0.38 mmol) was dissolved in 7 mL of chlorobenzene. The solution mixture was bubbled with argon for 30 minutes. It was heated to 100°C and stirred for 48 hours. After cooling, the mixture was precipitated in 250 mL of methanol and filtered. Soxhlet extraction were done on the polymers, first with acetone and then with hexane.

Polymer **BI-BTP** Dark green solid (0.30 g, 75%). ^1H NMR (400 MHz, Chloroform-*d*, ppm) δ 9.13 (d, $J = 22.6$ Hz, 6H), 8.96 (d, $J = 16.3$ Hz, 6H), 8.87 – 8.59 (m, 9H), 8.44 (s, 17H), 8.03 – 7.32 (m, 79H), 6.67 (d, $J = 5.2$ Hz, 4H), 2.08 (d, $J = 7.3$ Hz, 8H), 1.58 (s, 18H), 1.39 – 0.79 (m, 82H), 0.48 (s, 16H). ^{13}C NMR (101 MHz, Chloroform-*d*, ppm) δ 150.15, 131.69, 129.94, 128.63, 127.76, 123.03, 122.59, 121.13, 114.91, 114.28, 107.15, 33.38, 25.75, 25.71, 24.57, 8.48, 7.88.

Polymer **BI-DPTQ** Dark green solid (0.25 g, 79%). ^1H NMR (300 MHz, Chloroform-*d*, ppm) δ 8.71 (d, $J = 58.2$ Hz, 2H), 7.95 – 7.30 (m, 22H), 6.62 (d, $J = 14.0$ Hz, 3H), 1.58 (s, 5H), 1.41 – 0.96 (m, 13H), 0.95 – 0.83 (m, 3H), 0.44 (s, 3H). ^{13}C NMR (75 MHz, Chloroform-*d*, ppm) δ 138.29, 130.23, 130.11, 129.98, 129.66, 128.83, 128.68, 128.51, 128.27, 33.29, 31.59, 25.70, 25.12, 24.56, 22.66, 8.46, 7.85.

References

- [1] G. Sonmez, *Chem. Commun.*, **2005**, 42, 5251.
- [2] G. Sonmez, H. Meng, F. Wudl, *Chem. Mater.*, **2004**, 16, 574.
- [3] S. A. Sapp, G. A. Sotzing, J. R. Reynolds, *Chem. Mater.*, **1998**, 10, 2101.
- [4] B. C. Thompson, P. Schottland, K. Zong, J. R. Reynolds, *Chem. Mater.*, **2000**, 12, 1563.
- [5] G. Sonmez, F. Wudl, *J. Mater. Chem.*, **2005**, 15, 20.
- [6] P.-H. Aubert, A. A. Argun, A. Cirpan, D. B. Tanner, J. R. Reynolds, *Chem. Mater.*, **2004**, 16, 2386.

- [7] G. Sonmez, C. K. Shen, Y. Rubin, F. Wudl, *Angew. Chem. Int. Ed. Engl.*, **2004**, *43*, 1498.
- [8] G. Sonmez, H. B. Sonmez, C. K. F. Shen, F. Wudl, *Adv. Mater.*, **2004**, *16*, 1905.
- [9] I. Schwendeman, R. Hickman, G. Sonmez, P. Schottland, K. Zong, D. M. Welsh, J. R. Reynolds, *Chem. Mater.*, **2002**, *14*, 3118.
- [10] A. L. Dyer, C. R. G. Grenier, J. R. Reynolds, *Adv. Funct. Mater.*, **2007**, *17*, 1480.
- [11] J. Zheng, W. Q. Qiao, X. H. Wan, J. P. Gao, Z. Y. Wang, *Chem. Mater.*, **2008**, *20*, 6163.
- [12] H. J. Yen, G. S. Liou, *Chem. Mater.*, **2009**, *21*, 4062.
- [13] H. J. Yen, H. Y. Lin, G. S. Liou, *Chem. Mater.*, **2011**, *23*, 1874.
- [14] L. T. Huang, H. J. Yen, J. H. Wu, G. S. Liou, *Org. Electron.*, **2012**, *13*, 840.
- [15] Y. W. Chuang, H. J. Yen, J. H. Wu, G. S. Liou, *ACS Appl. Mater. Interfaces*, **2014**, *6*, 3594.
- [16] B. B. Cui, C. J. Yao, J. N. Yao, Y. W. Zhong, *Chem. Sci.*, **2014**, *5*, 932.
- [17] Y. Liu, D. Chao, H. Yao, *Org. Electron.*, **2014**, *15*, 1422.
- [18] F. Garnier, Field-effect transistors based on conjugated materials, *Electronic Materials: The Oligomer Approach*, Wiley-VCH: New York, **1998**, 559.
- [19] M. G. Harrison, H. R. Friend, Optical applications. *Electronic Materials: The Oligomer Approach*, Wiley-VCH: New York, **1998**, 515.
- [20] V. Martina, K. Ionescu, L. Pigani, F. Terzi, A. Ulrici, C. Zanardi, R. Seeber, *Anal. Bioanal. Chem.*, **2007**, *387*, 2101.
- [21] S. Kirchmeyer, K. Reuter, *J. Mater. Chem.*, **2005**, *15*, 2077.

- [22] H. W. Heuer, R. Wehrmann, S. Kirchmeyer, *Adv. Funct. Mater.*, **2002**, *12*, 89.
- [23] D. R. Rosseinsky, R. J. Mortimer, *Adv. Mater.*, **2001**, *13*, 783.
- [24] E. E. Havinga, W. ten Hoeve, H. Wynberg, *Syn. Metals*, **1993**, *55*, 299.
- [25] U. Salzner, *Syn. Metals*, **2001**, *119*, 215.
- [26] G. Qian, Z. Y. Wang, *Can. J. Chem.*, **2010**, *88*, 192.
- [27] G. Qian, Z. Y. Wang, *Chem.–Asian J.*, **2010**, *5*, 1006.
- [28] G. Qian, B. Dai, M. Luo, D. Yu, J. Zhan, Z. Zhang, D. Ma, Z. Y. Wang, *Chem. Mater.*, **2008**, *20*, 6208.
- [29] G. Qian, Z. Zhong, M. Luo, D. Yu, Z. Zhang, D. Ma, Z. Y. Wang, *J. Phys. Chem. C*, **2009**, *113*, 1589.
- [30] M. Karikomi, C. Kitamura, S. Tanaka, Y. Yamashita, *J. Am. Chem. Soc.*, **1995**, *117*, 6791.
- [31] C. L. Pai, C. L. Liu, W. C. Chen, S. A. Jenekhe, *Polymer*, **2006**, *47*, 699.
- [32] T. L. D. Tam, T. Salim, H. Li, F. Zhou, S. G. Mhaisalkar, H. Su, Y. M. Lam, A. C. Grimsdale, *J. Mater. Chem.*, **2012**, *22*, 18528.
- [33] G. Qian, H. Abu, Z. Y. Wang, *J. Mater. Chem.*, **2011**, *21*, 7678.
- [34] D. Baran, A. Balan, B.-M. Esteban, H. Neugebauer, N. S. Sariciftci, L. Toppare, *Chem. Phys.*, **2010**, *211*, 2602.
- [35] D. Baran, G. Oketem, S. Celebi, L. Toppare, *Macromol. Chem. Phys.*, **2011**, *212*, 799.
- [36] C. Peyron, R. Benhida, C. Bories, P. M. Loiseau, *Bioorganic Chemistry*, **2005**, *33*, 439.
- [37] Y. Yamashita, K. Ono, M. Tomura, S. Tanaka, *Tetrahedron*, **1997**, *53*, 10169.

- [38] Y. Li, Y. Cao, J. Gao, D. Wang, G. Yu, A. J. Heeger, *Synth. Met.*, **1999**, *99*, 243.
- [39] J. Pommerehne, H. Vestweber, W. Guss, R. F. Mahrt, H. Bässler, M. Porsch, J. Daub, *Adv. Mater.*, **1995**, *7*, 551.
- [40] S. Hellstrom, F. Zhang, O. Inganäs, M. R. Andersson, *Dalton Trans.*, **2009**, 10032.
- [41] T. T. Steckler, P. Henriksson, S. Mollinger, A. Lundin, A. Salleo, M. R. Andersson, *J. Am. Chem. Soc.*, **2014**, *136*, 1190.
- [42] S.-H. Hsiao, G.-S. Liou, Y.-C. Kung, H.-J. Yen, *Macromolecules*, **2008**, *41*, 2800.
- [43] B. D. Reeves, C. R. G. Grenier, A. A. Argun, A. Cirpan, T. D. McCarley, J. R. Reynolds, *Macromolecules*, **2004**, *37*, 7559.
- [44] J. D. Zhang, H. A. Yu, X. G. Wu and Z. Y. Wang, *Opt. Mater.*, **2004**, *27*, 265.

6.1 Conclusion and Outlook

Solution-processed organic optoelectronics are a promising development for addressing technological drawbacks of inorganic materials. They demonstrate several advantages such as low-cost, light-weight, flexible and large-area devices. This thesis consists of four sections and variety of π -conjugated polymers have been explored for application in optoelectronics. In the first section, several **BDPP**-based polymers were synthesized bearing thermally cleavable moiety (Fig. 6.1). They exhibit large spectral response from 300-800 nm and suitable for processing multilayer films. Implementing BOC group show reasonable solubility prior to cleavage, however, optimal film formation was not achieved. Improvement of the solubility and attaining high molecular weight polymers can be accomplished by incorporating long alkyl chloroformate or larger dicarbonate esters, which can be thermally cleaved off.

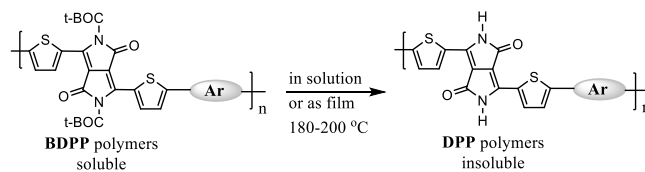


Figure 6.1: BDPP-based polymers

In the second section, design and formation of multilayer devices for photodetector application using the BDPP polymers and new DAP polymers was demonstrated (Fig. 6.2). The DAP polymers exhibit very low band gap and large spectral response ranging from 300 nm to 1300 nm. Several devices were formulated with different combination of BDPP and DAP polymers, with **DPP-DTPa** and **DAPb-DTPa** showing the best result in the NIR. The device display detectivity above 10^{11} Jones from 500 to 1100 nm, EQE of 25% from 750 to 900 nm and responsivity of 177 mA/W at 900 nm, which is one of the highest reported in the NIR region.

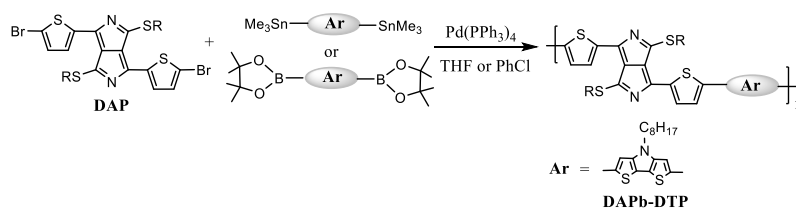


Figure 6.2: DAP polymers

In the third section, a series of co-polymers with N-alkylated indole-isoindigo with different ratio of carbazole were successfully synthesized. Using Pd catalyst, the polymers were chemically cross-linked and thus rendering them insoluble. Preliminary devices incorporating the co-polymers as HTL show very high dark current, likely due to residual Pd. A non metallic oxidizing agent would be more ideal to form the cross-linking such as ammonium persulfate or hypervalent iodine.

In the last section, electrochromic study of modified benzobisthiadiazole polymers were explored. The polymers undergo reversible oxidation and electrochemically attenuate light at the infrared region in both transmission and reflection mode. Polymer **P3** was extensively studied and can potentially be used for switchable camouflage material. Furthermore, two new thiadiazoloquinoline-based polymers were synthesized bearing cleavable moiety. After thermal cleavage, intramolecular hydrogen bonding dominates showing a bathochromic shift reaching near 1400 nm. OFET measurements showed ambipolar characteristics, however carrier mobilities are far inferior to common FET devices. This is likely due to low solubility of the polymers and low molecular weight. Similar approach of incorporating alkyl chloroformate can improve solubility.

6.2 Contribution to Knowledge

The primary aim of this research is to investigate and gain insight into relationship between structure, band gap and properties of conjugated polymers. The knowledge gained can be applied into optoelectronic applications. While this research provides a number of important insights, especially in regard to electrochromic switchable material (J. Mater. Chem., 2011, 21, 7678), it devotes significant effort on optimizing NIR photodetectors. In particular, research on developing on a complete solution processable multilayer photodetector. This development is conceptually intriguing because it bridges well known methods into feasible improvement of construction of tandem devices. Our results contribute to an understanding of band gap and structure to provide advantageous material responsive in NIR region.

APPENDIX A

^1H and ^{13}C NMR spectra of compounds and polymers.

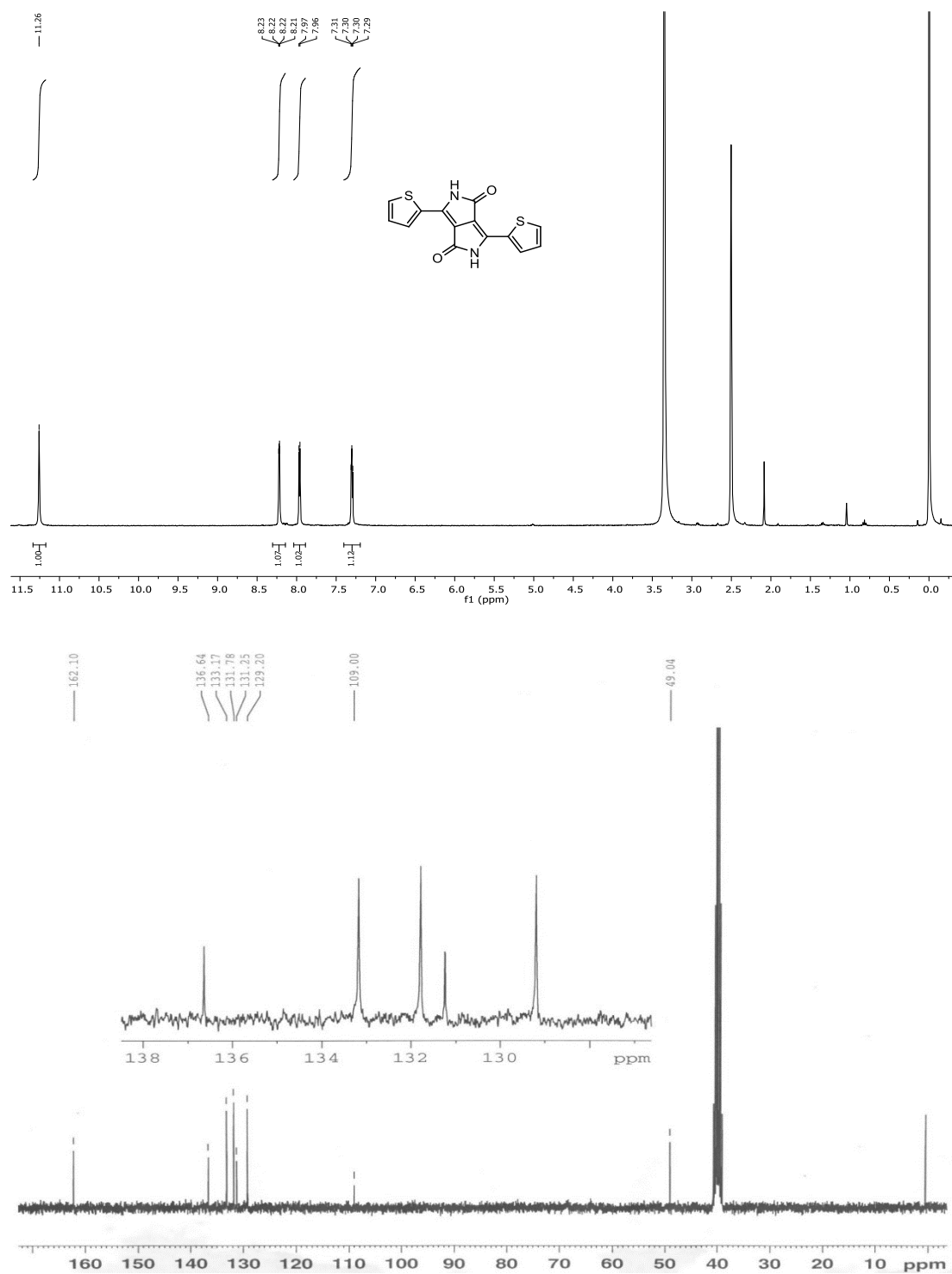


Figure A.1. ^1H NMR (400 MHz, DMSO) and ^{13}C NMR (75 MHz, DMSO) spectrum of 3,6-di(thiophen-2-yl)-2,5-dihydropyrrolo[3,4-c]pyrrole-1,4-dione (DPP).

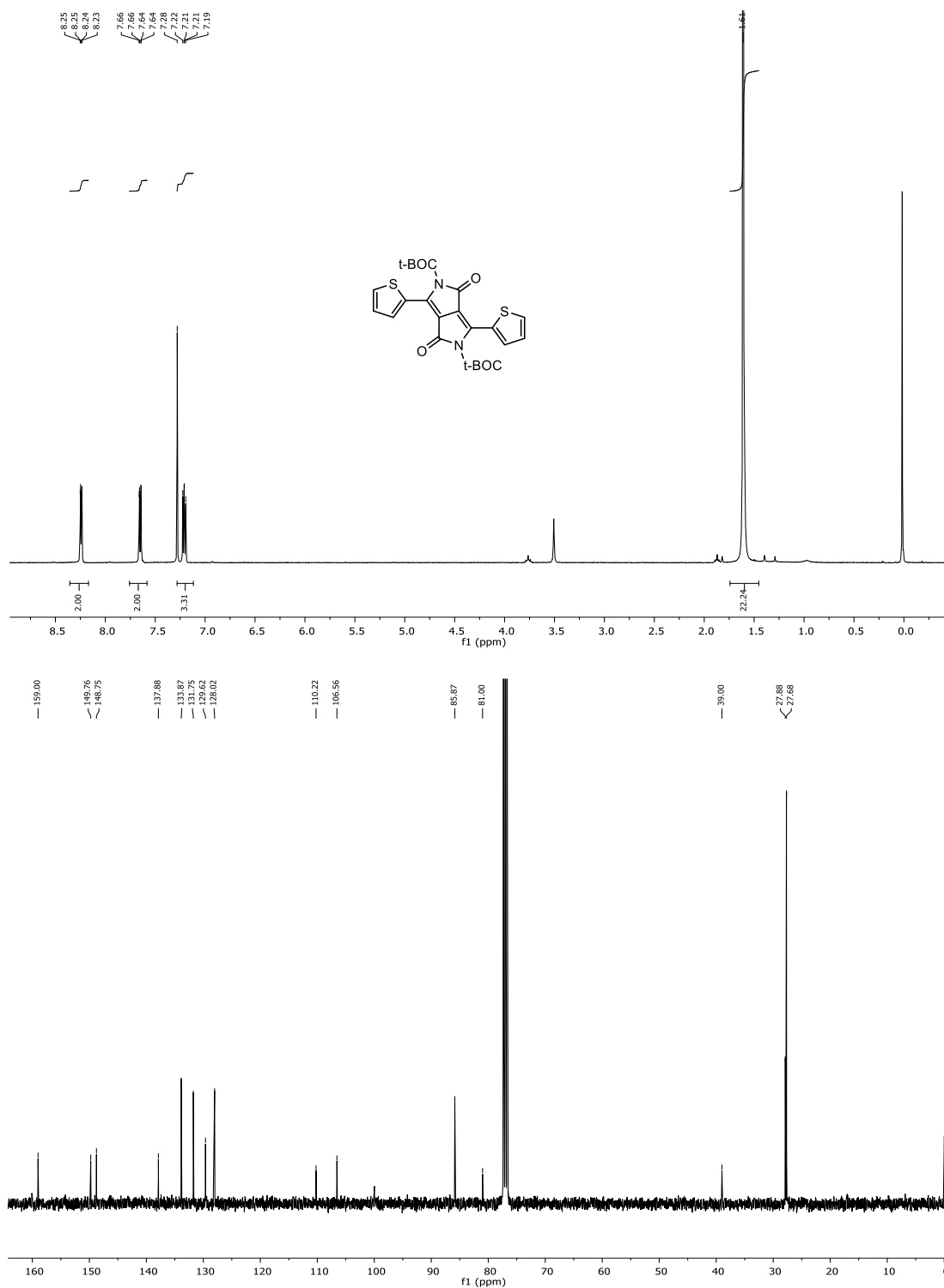


Figure A.2. ¹H NMR (400 MHz, CDCl₃) and ¹³C NMR (100 MHz, CDCl₃) spectrum of di-tert-butyl 1,4-dioxo-3,6-di(thiophen-2-yl)pyrrolo[3,4-c]pyrrole-2,5(1H,4H)-dicarboxylate.

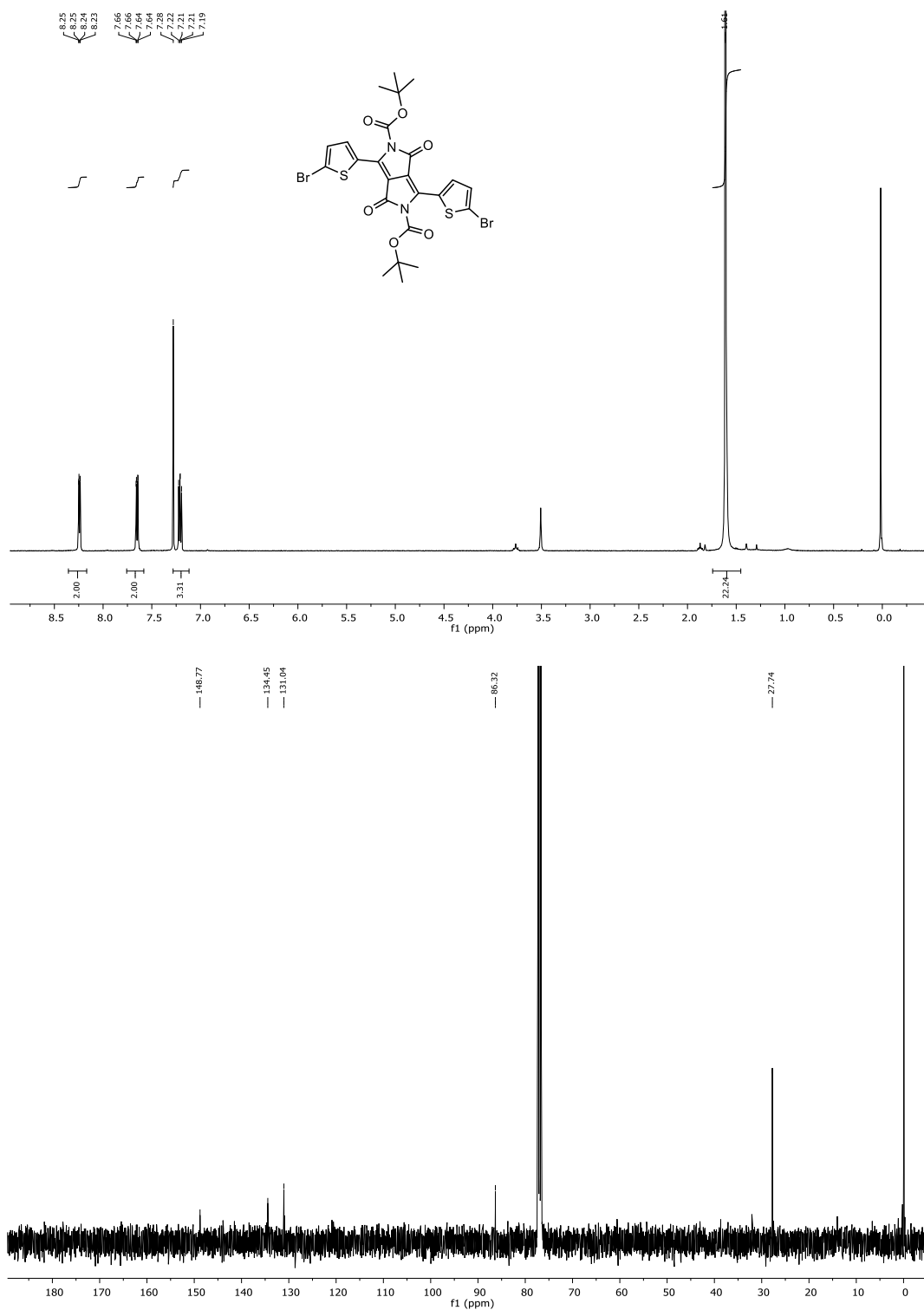


Figure A.3. ^1H NMR (400 MHz, CDCl_3) and ^{13}C NMR (100 MHz, CDCl_3) spectrum of di-*tert*-butyl 3,6-bis(5-bromothiophen-2-yl)-1,4-dioxopyrrolo[3,4-*c*]pyrrole-2,5(1*H*,4*H*)-dicarboxylate.

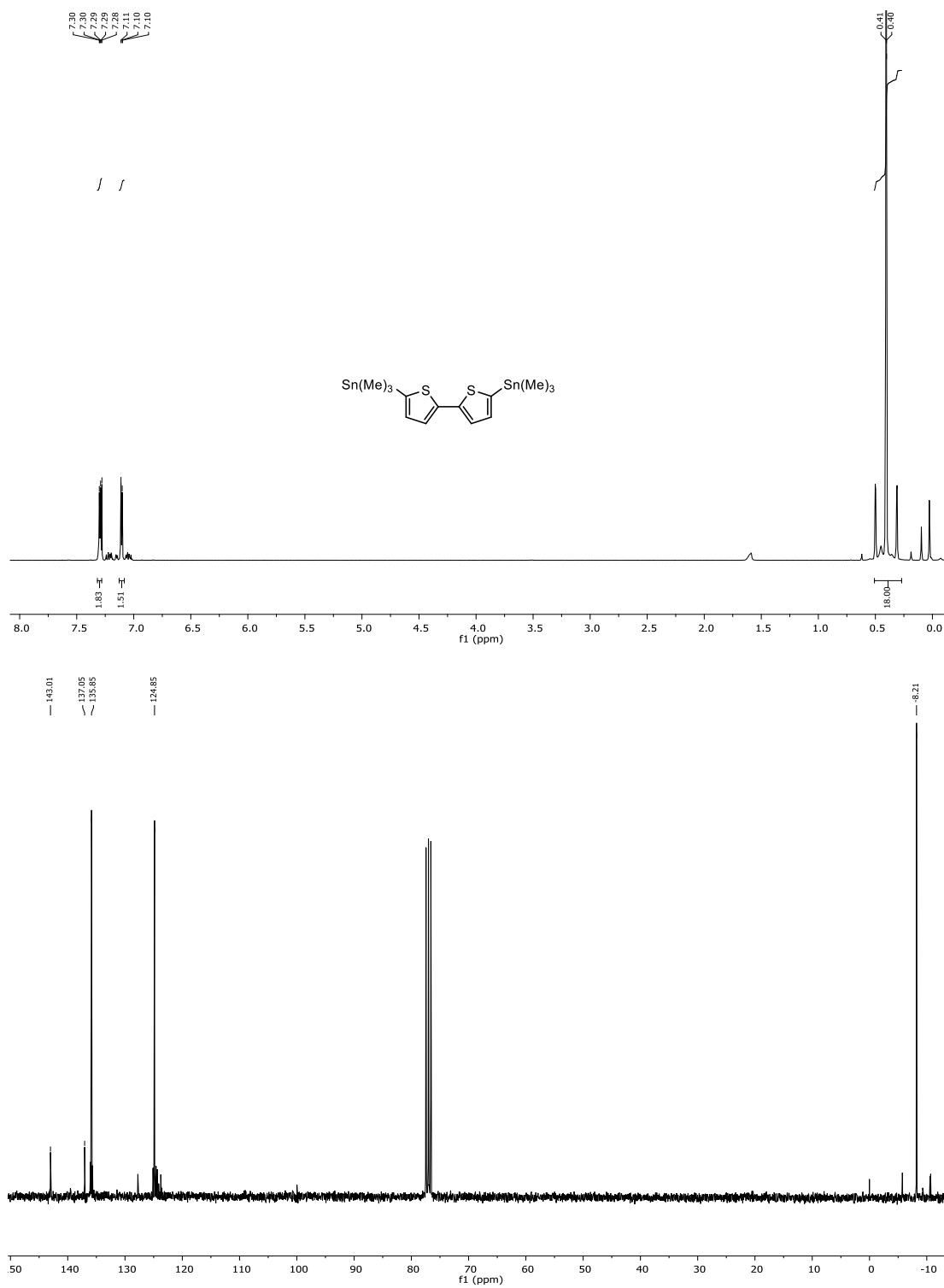


Figure A.4. ¹H NMR (400 MHz, CDCl₃) and ¹³C NMR (75 MHz, CDCl₃) spectrum of 5,5'-bis(trimethylstannyl)-2,2'-bithiophene (**BT**).

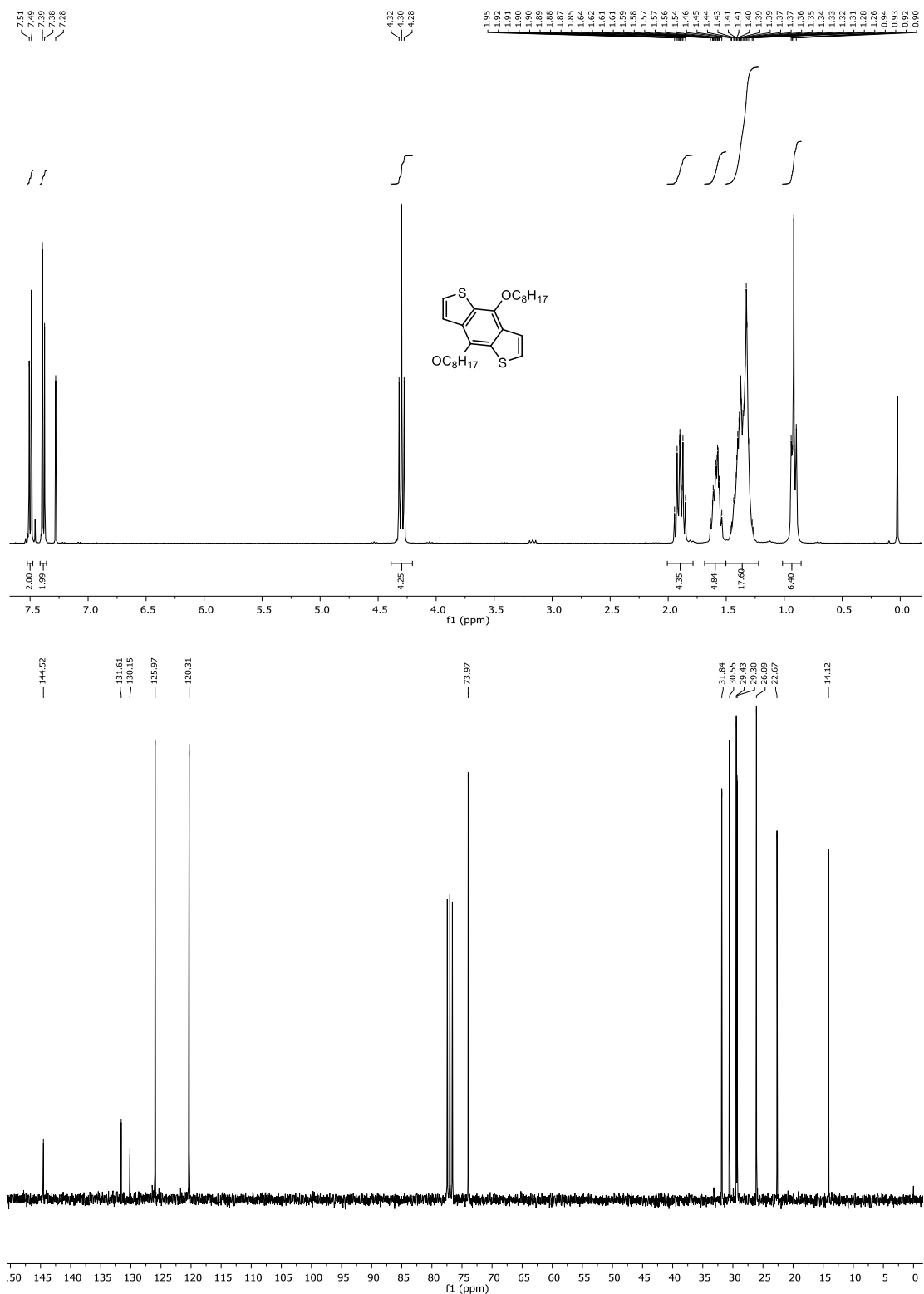


Figure A.5. ¹H NMR (300 MHz, CDCl₃) and ¹³C NMR (75 MHz, CDCl₃) spectrum of 4,8-bis(octyloxy)benzo[1,2-*b*:4,5-*b'*]dithiophene.

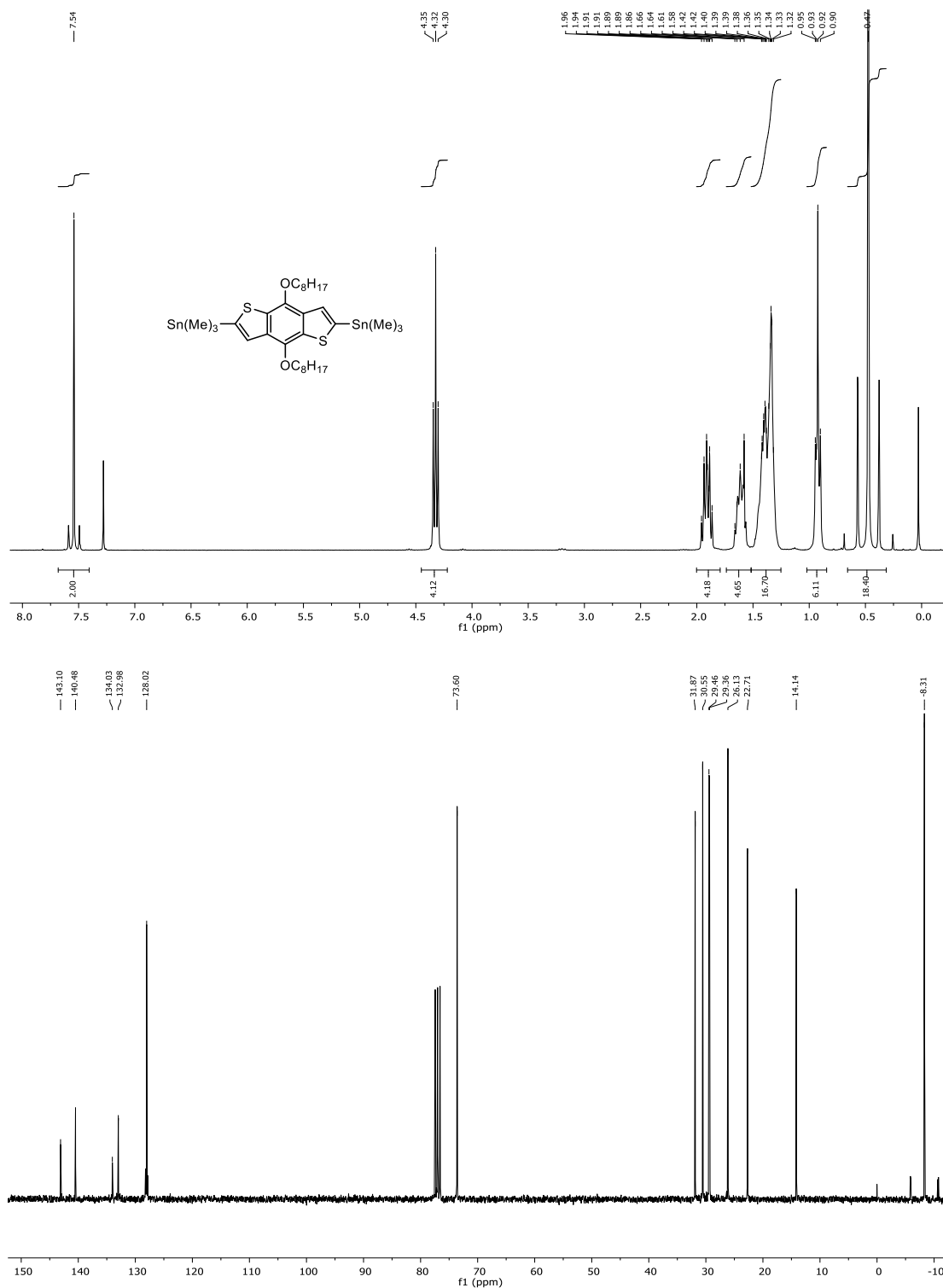


Figure A.6. ^1H NMR (300 MHz, CDCl_3) and ^{13}C NMR (75 MHz, CDCl_3) spectrum of (4,8-bis(octyloxy)benzo[1,2-*b*:4,5-*b'*]dithiophene-2,6-diyl)bis(trimethylstannane) (TBT).

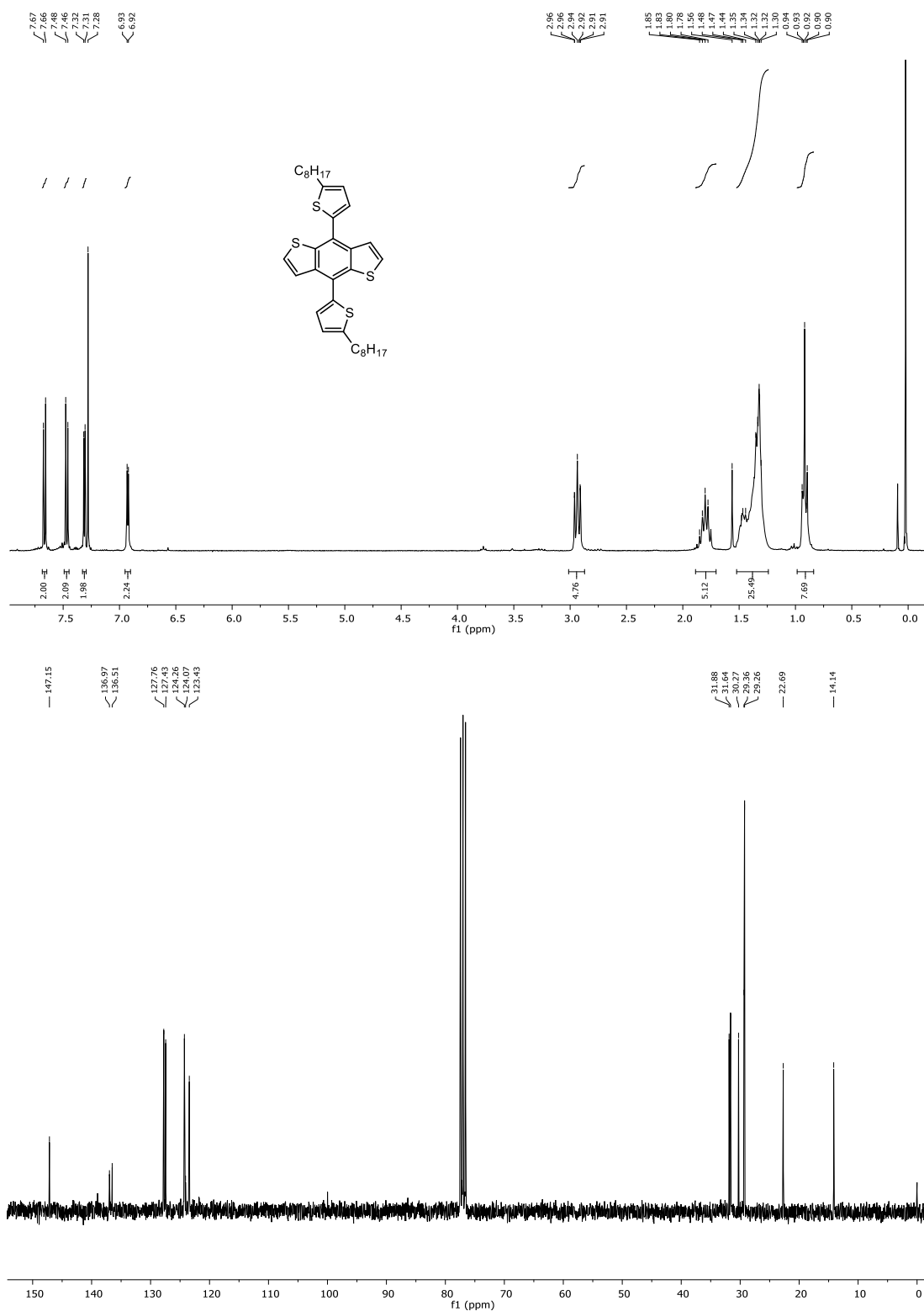


Figure A.7. ^1H NMR (300 MHz, CDCl_3) and ^{13}C NMR (75 MHz, CDCl_3) spectrum of 4,8-bis(5-octylthiophen-2-yl)benzo[1,2-*b*:4,5-*b'*]dithiophene.

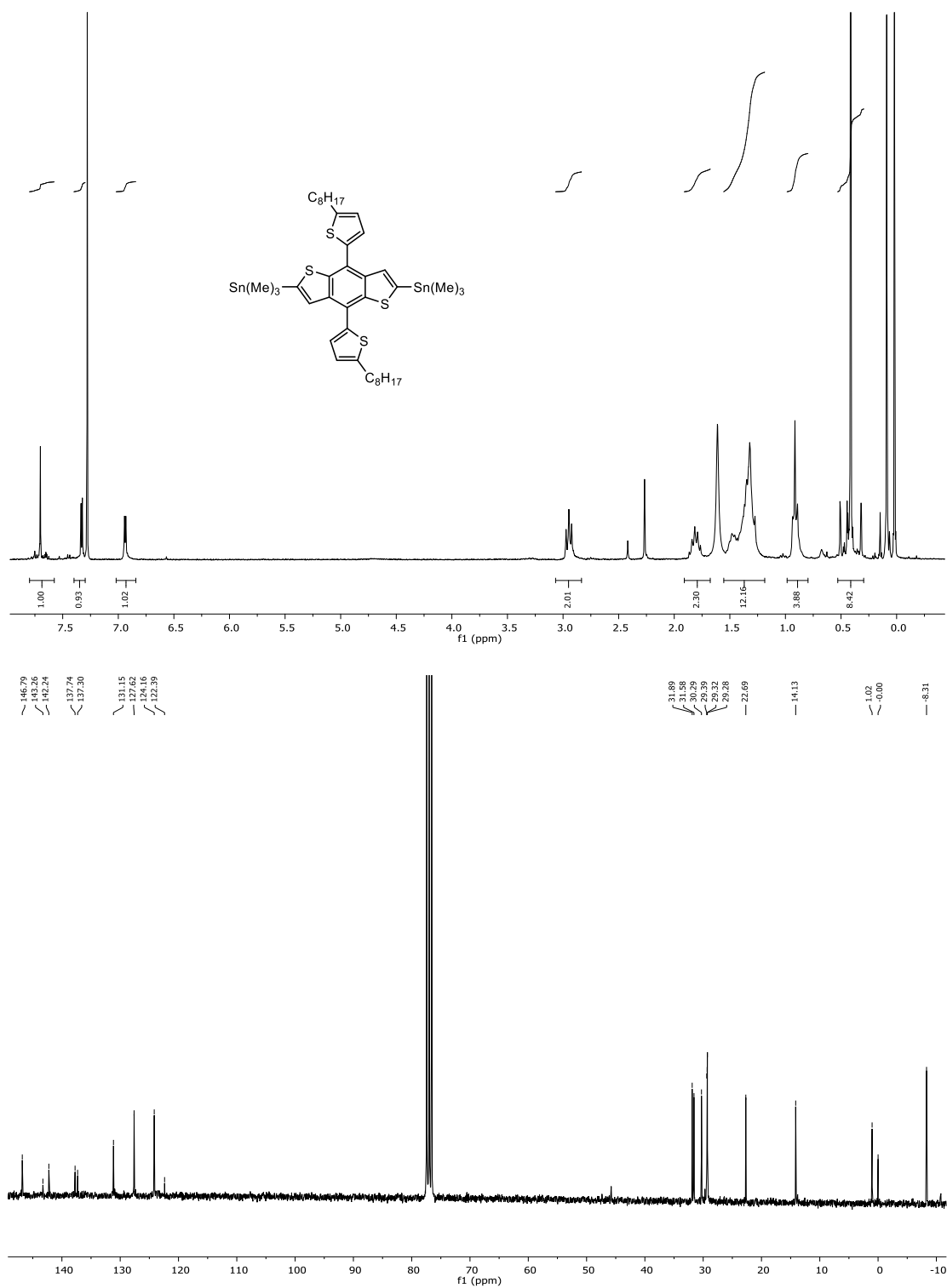


Figure A.8. ¹H NMR (300 MHz, CDCl₃) and ¹³C NMR (75 MHz, CDCl₃) spectrum of (4,8-bis(5-octylthiophen-2-yl)benzo[1,2-*b*:4,5-*b'*]dithiophene-2,6-diyl)bis(trimethylstannane) (TBTT).

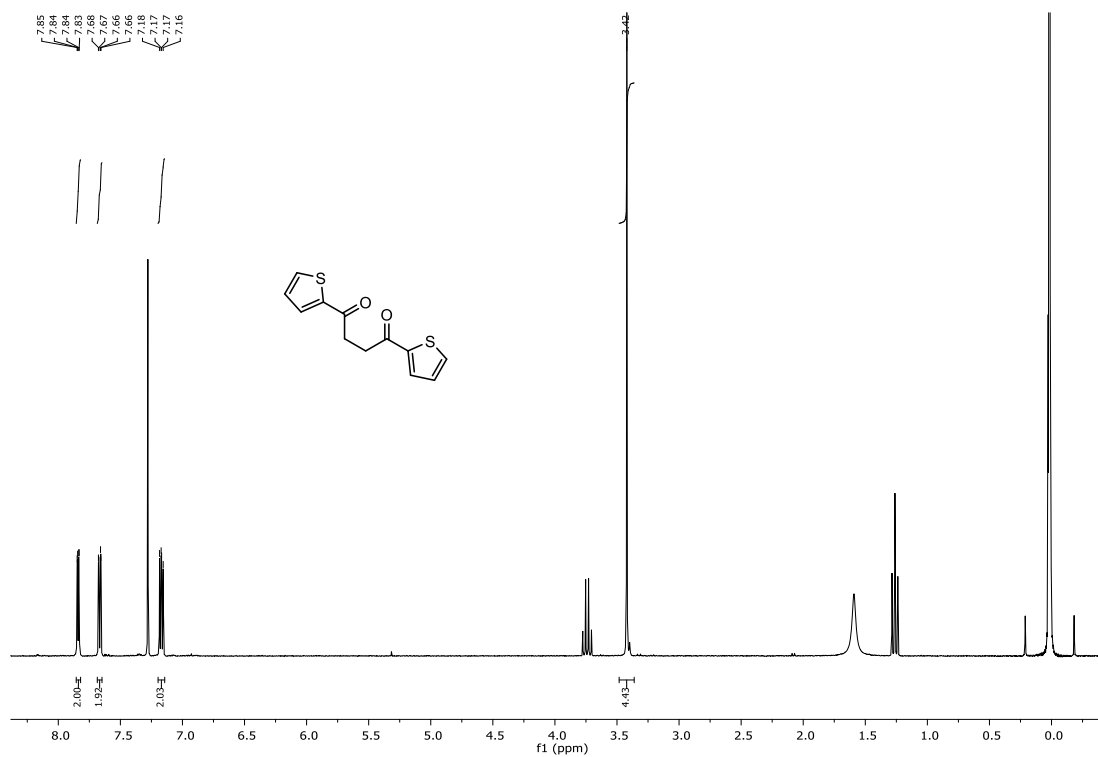
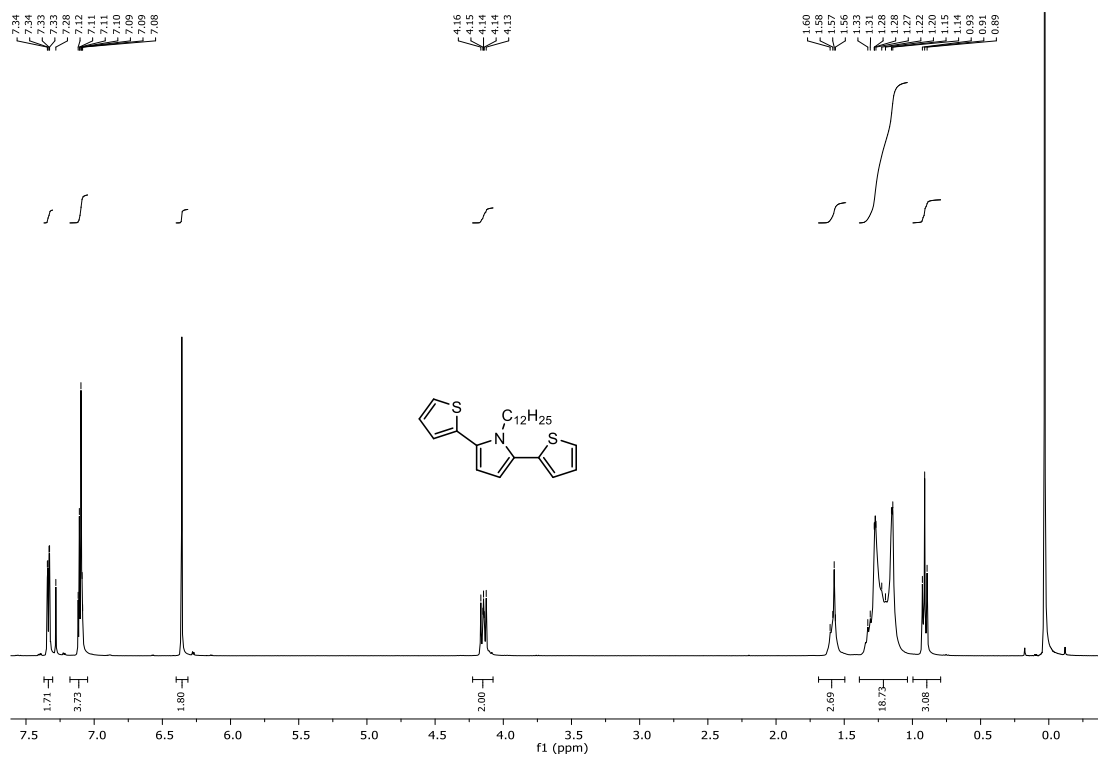


Figure A.9. ¹H NMR (400 MHz, CDCl₃) spectrum of 1,4-di(thiophen-2-yl)butane-1,4-dione.



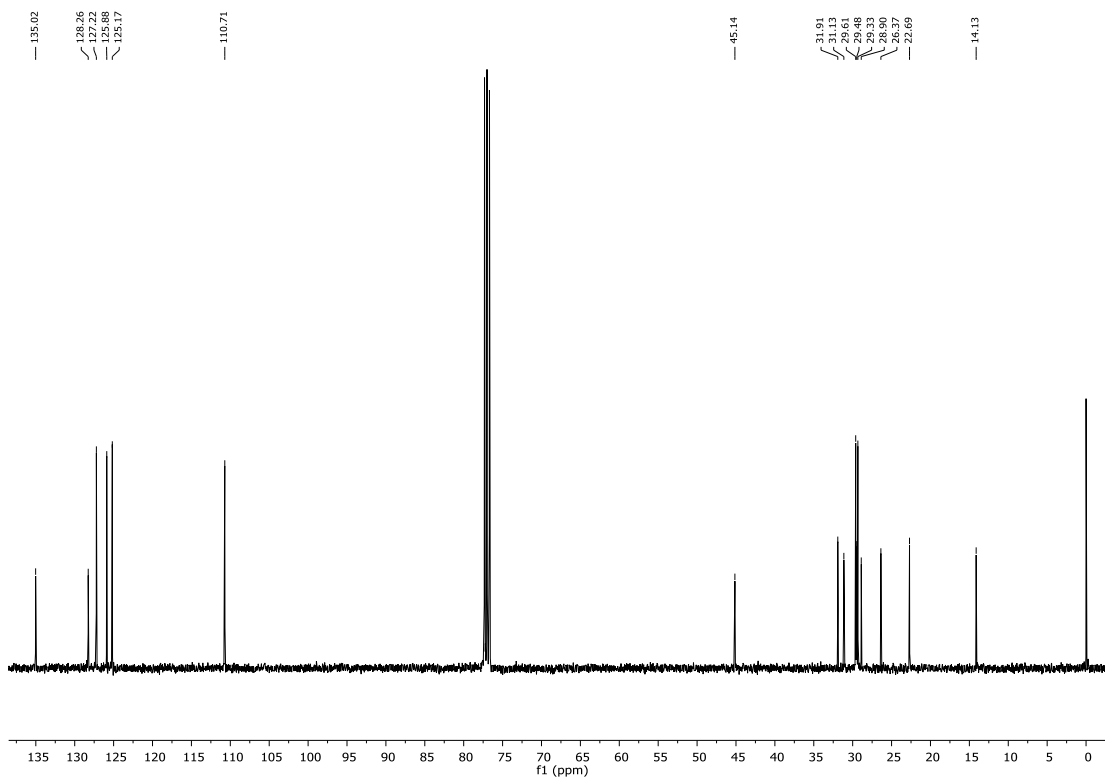
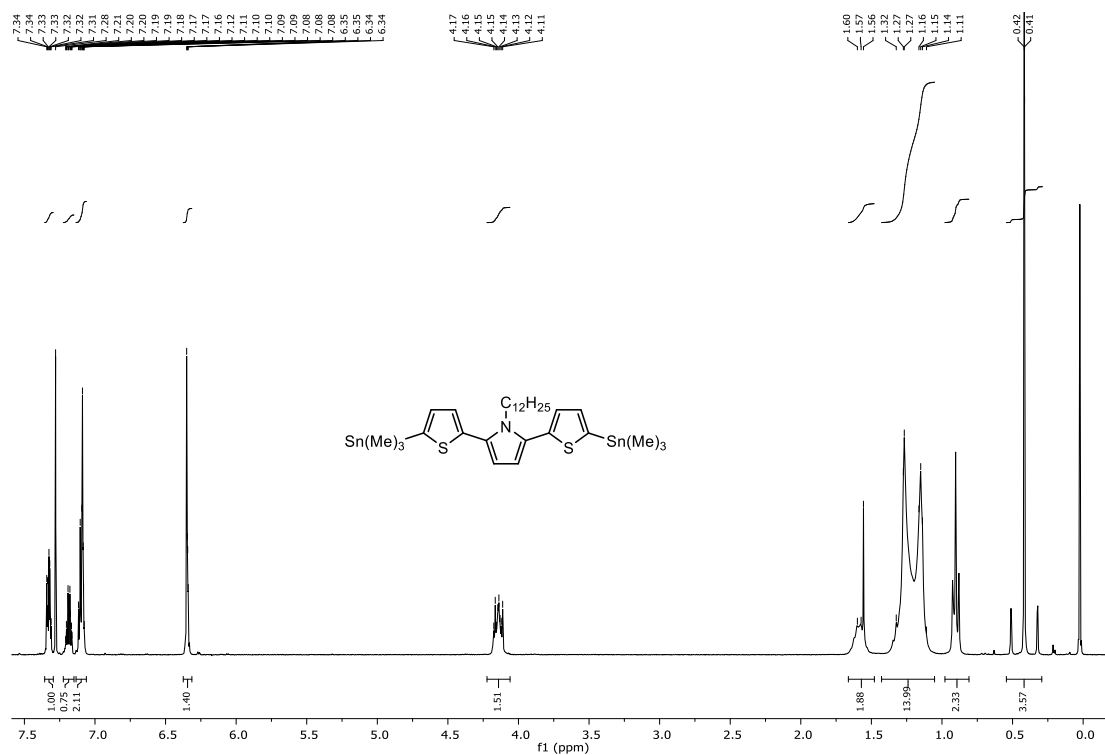


Figure A.10. ^1H NMR (400 MHz, CDCl_3) and ^{13}C NMR (100 MHz, CDCl_3) spectrum of 1-dodecyl-2,5-di(thiophen-2-yl)-1H-pyrrole.



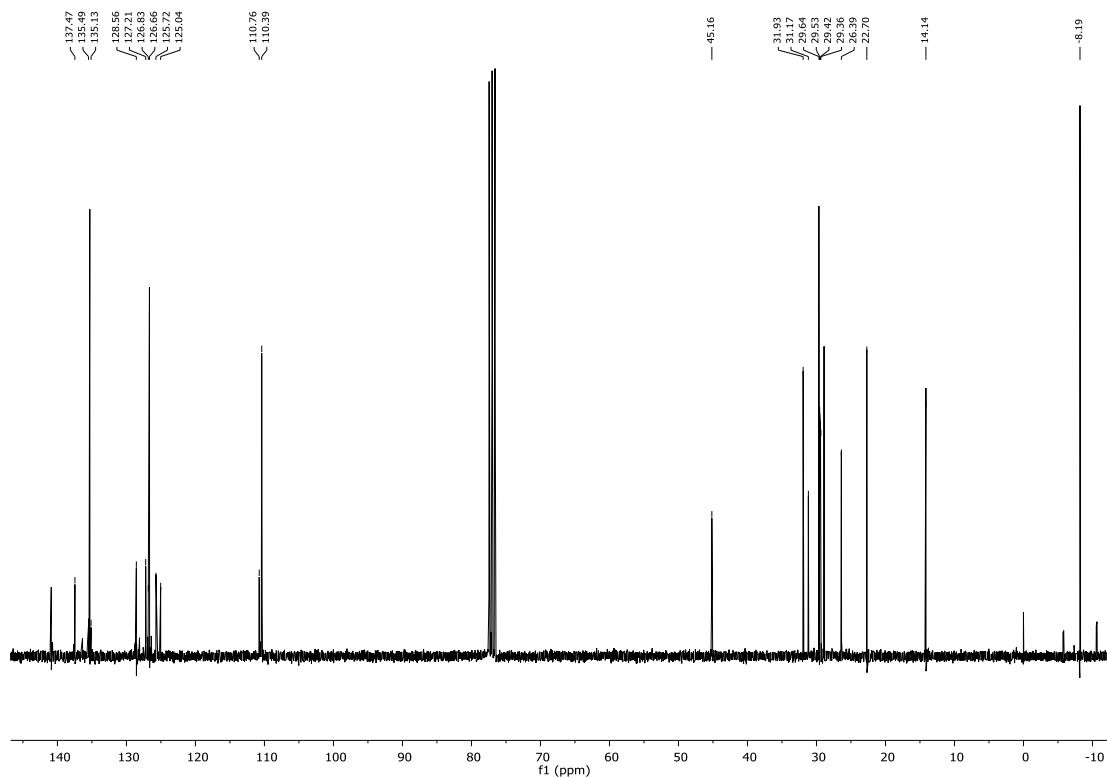
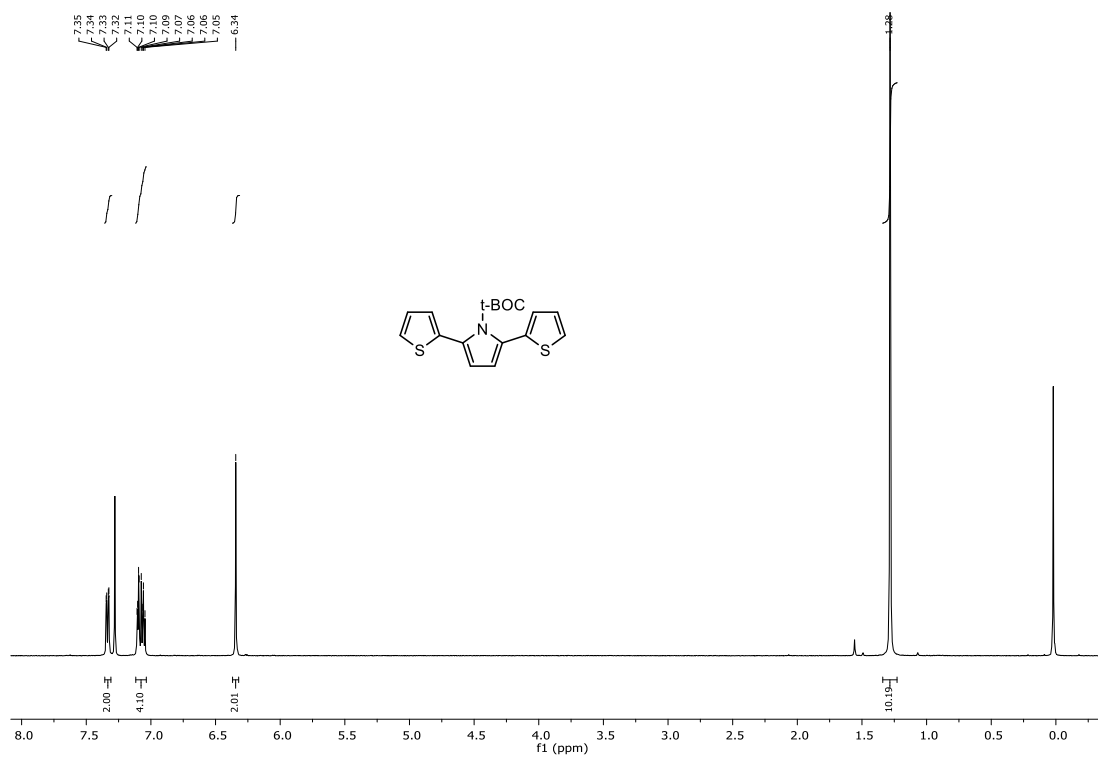


Figure A.11. ^1H NMR (400 MHz, CDCl_3) and ^{13}C NMR (75 MHz, CDCl_3) spectrum of 1-dodecyl-2,5-bis(5-(trimethylstannyl)thiophen-2-yl)-1H-pyrrole (TPTa).



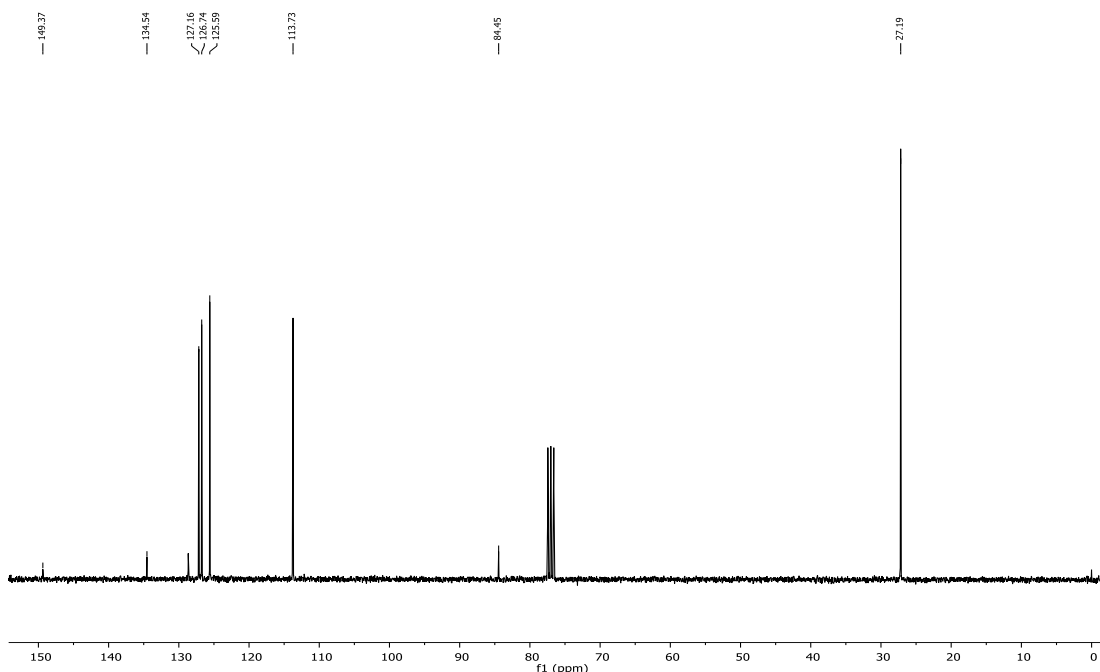


Figure A.12. ^1H NMR (400 MHz, CDCl_3) and ^{13}C NMR (75 MHz, CDCl_3) spectrum of *tert*-butyl 2,5-di(thiophen-2-yl)-1*H*-pyrrole-1-carboxylate.

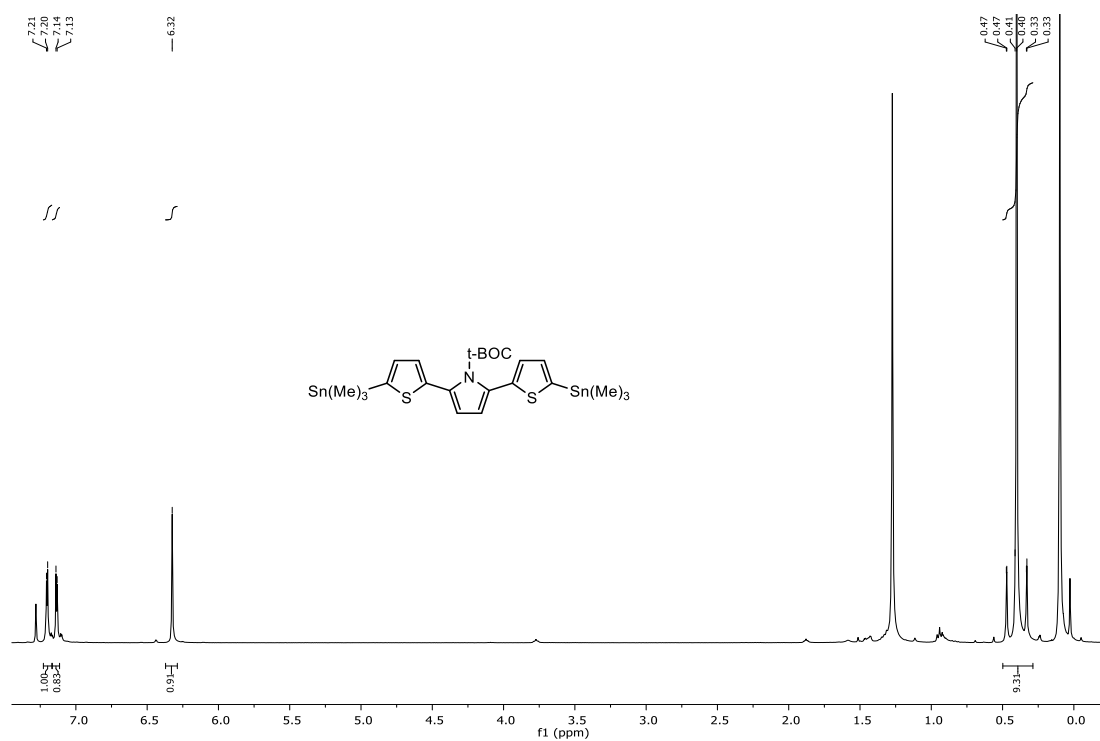


Figure A.13. ^1H NMR (400 MHz, CDCl_3) spectrum of *tert*-butyl 2,5-bis(5-(trimethylstannyl)thiophen-2-yl)-1*H*-pyrrole-1-carboxylate (**TPTb**)

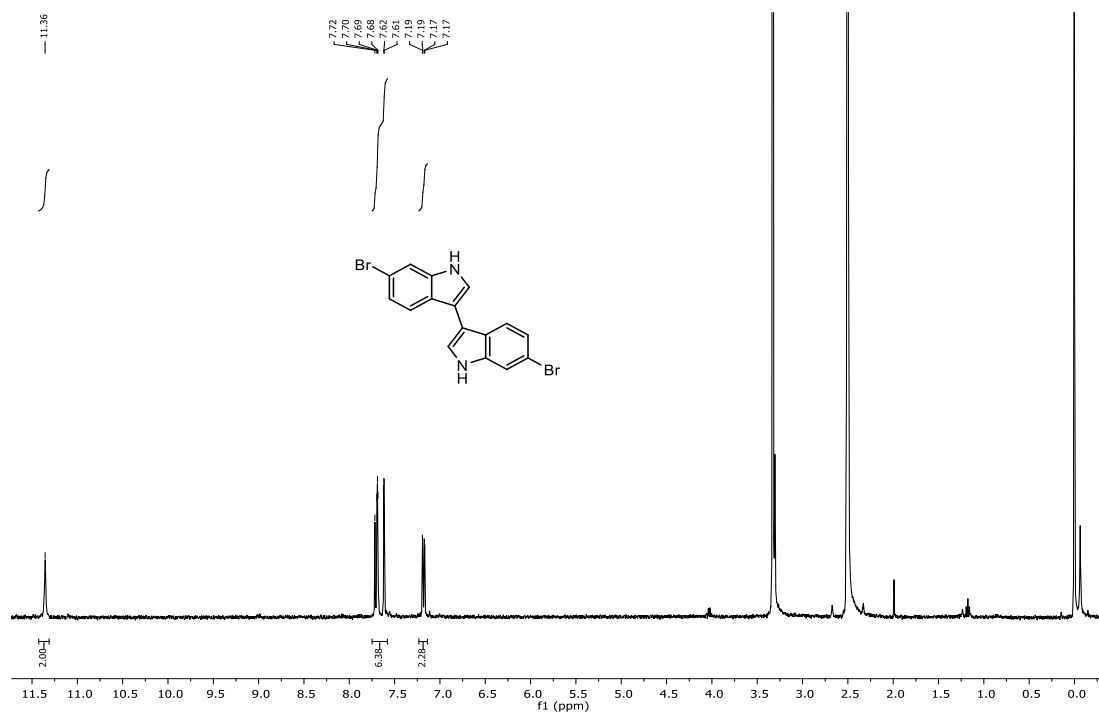


Figure A.14. ^1H NMR (400 MHz, DMSO-d_6) spectrum of 6,6'-dibromo-1*H*,1'*H*-3,3'-biindole

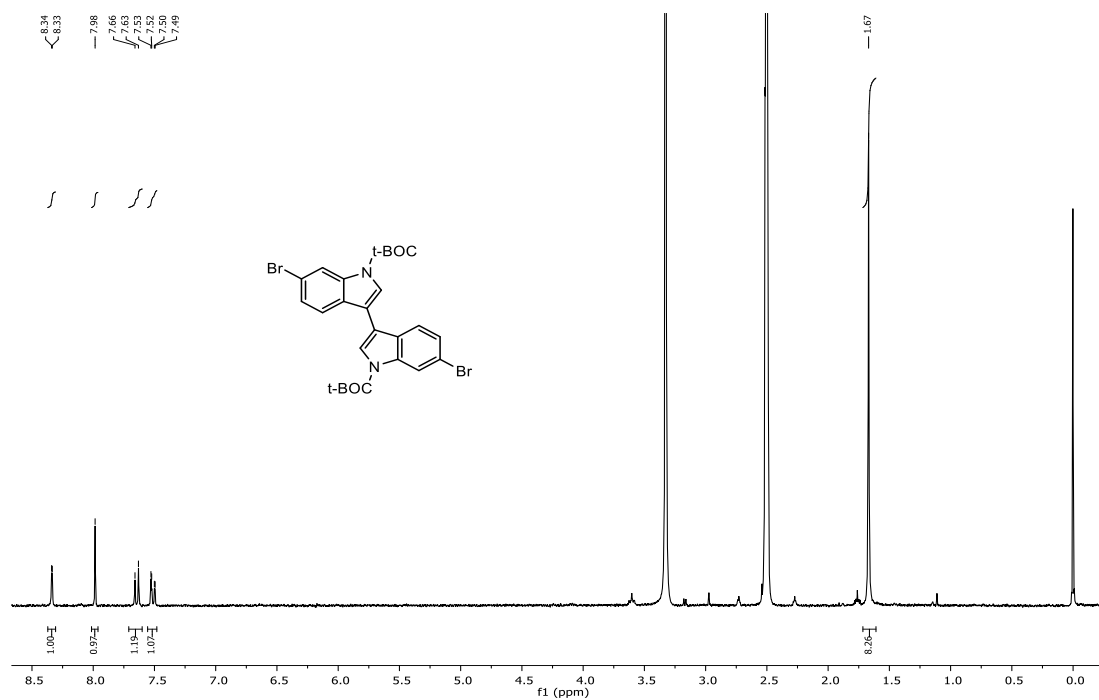


Figure A.15. ^1H NMR (300 MHz, DMSO-d_6) spectrum of di-*tert*-butyl 6,6'-dibromo-1*H*,1'*H*-[3,3'-biindole]-1,1'-dicarboxylate

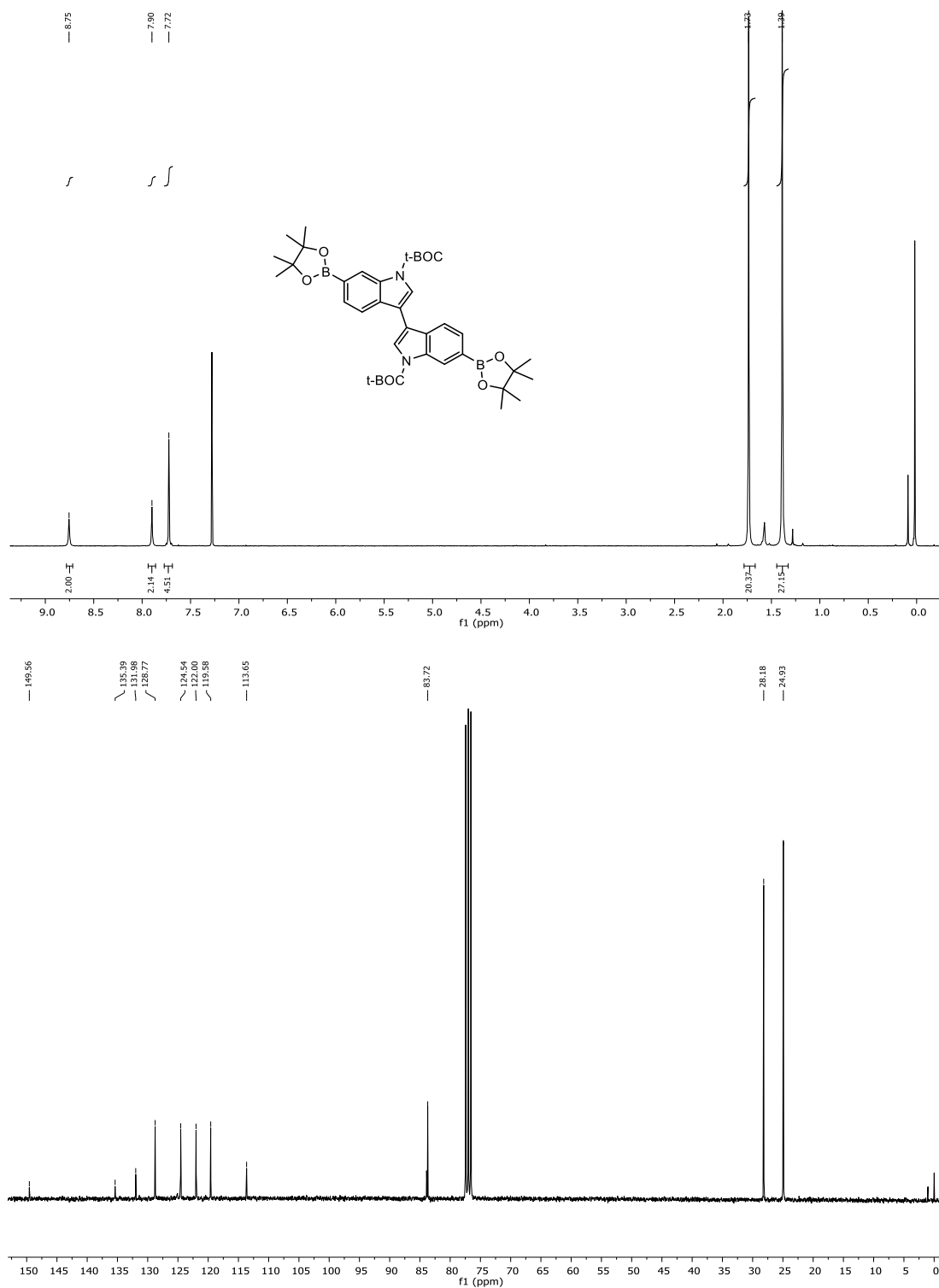


Figure A.15. ^1H NMR (300 MHz, CDCl_3) and ^{13}C NMR (75 MHz, CDCl_3) spectrum of di-*tert*-butyl 6,6'-bis(4,4,5,5-tetramethyl-1,3,2-dioxaborolan-2-yl)-1*H*,1'*H*-[3,3'-biindole]-1,1'-dicarboxylate.

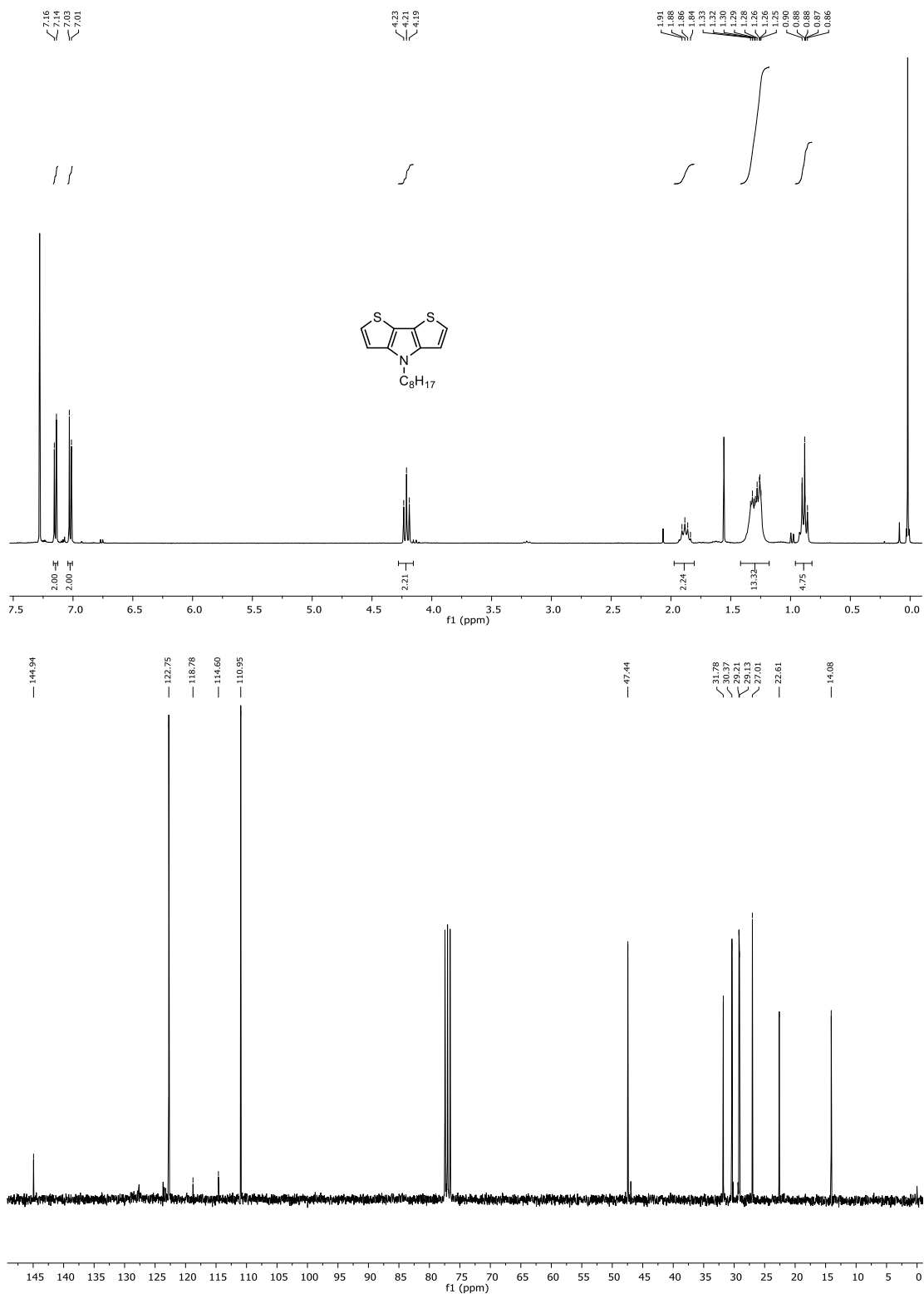


Figure A.16. ¹H NMR (300 MHz, CDCl₃) and ¹³C NMR (75 MHz, CDCl₃) spectrum of 4-octyl-4H-dithieno[3,2-*b*:2',3'-*d*]pyrrole.

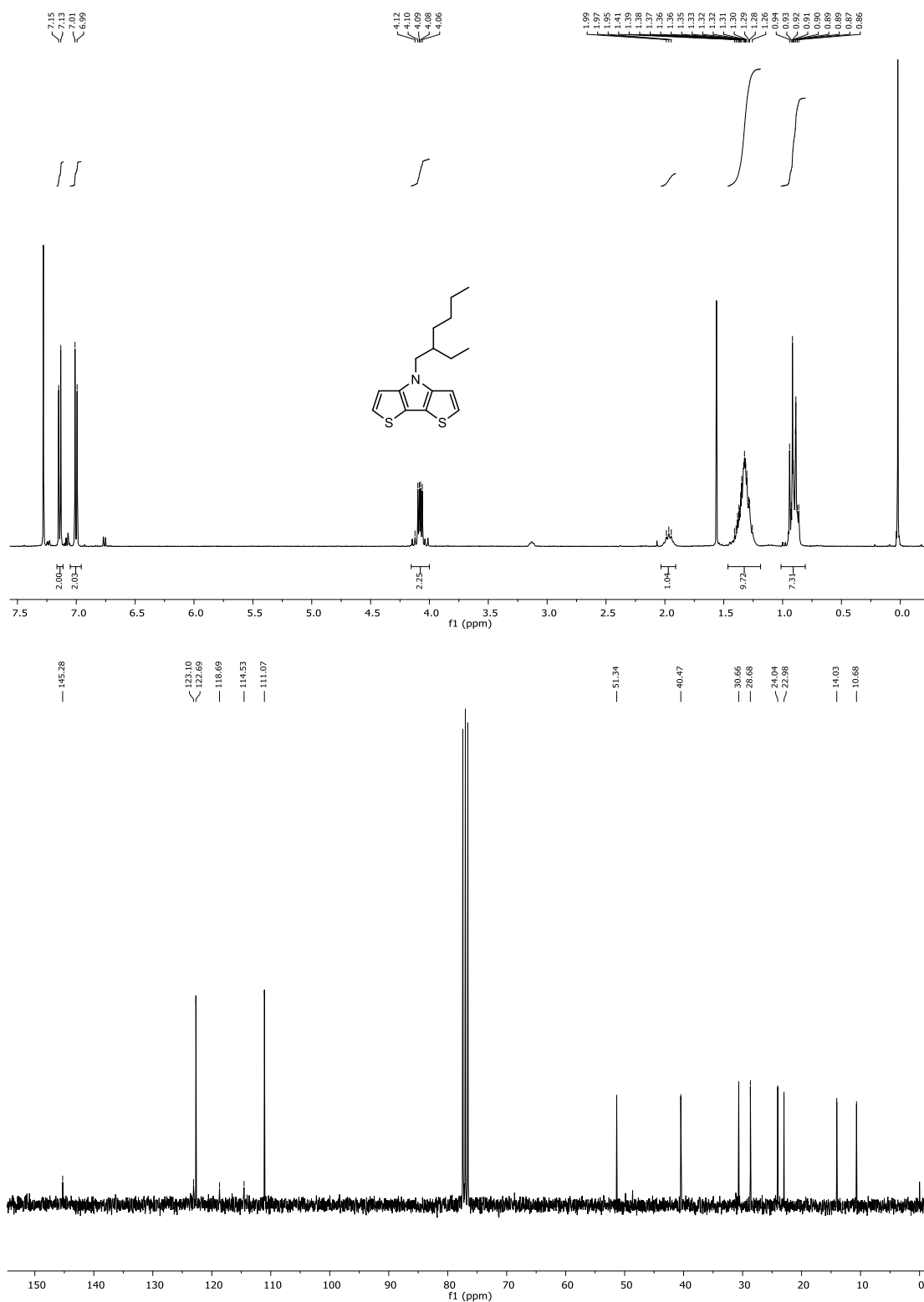


Figure A.16. ¹H NMR (300 MHz, CDCl₃) and ¹³C NMR (75 MHz, CDCl₃) spectrum of 4-(2-ethylhexyl)-4H-dithieno[3,2-*b*:2',3'-*d*]pyrrole.

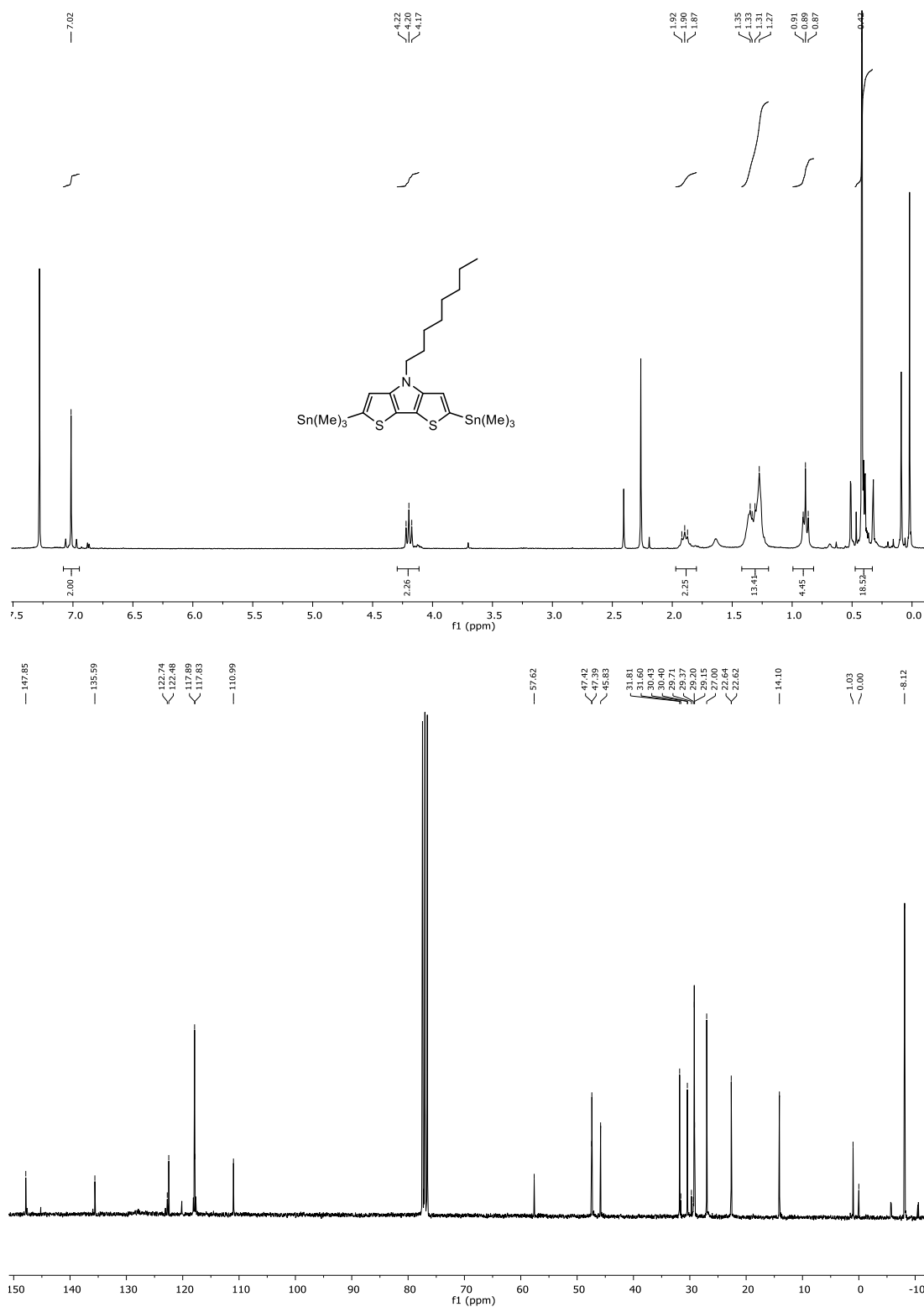


Figure A.17. ¹H NMR (300 MHz, CDCl₃) and ¹³C NMR (75 MHz, CDCl₃) spectrum of 4-octyl-2,6-bis(trimethylstannyl)-4H-dithieno[3,2-b:2',3'-d]pyrrole (DTPa).

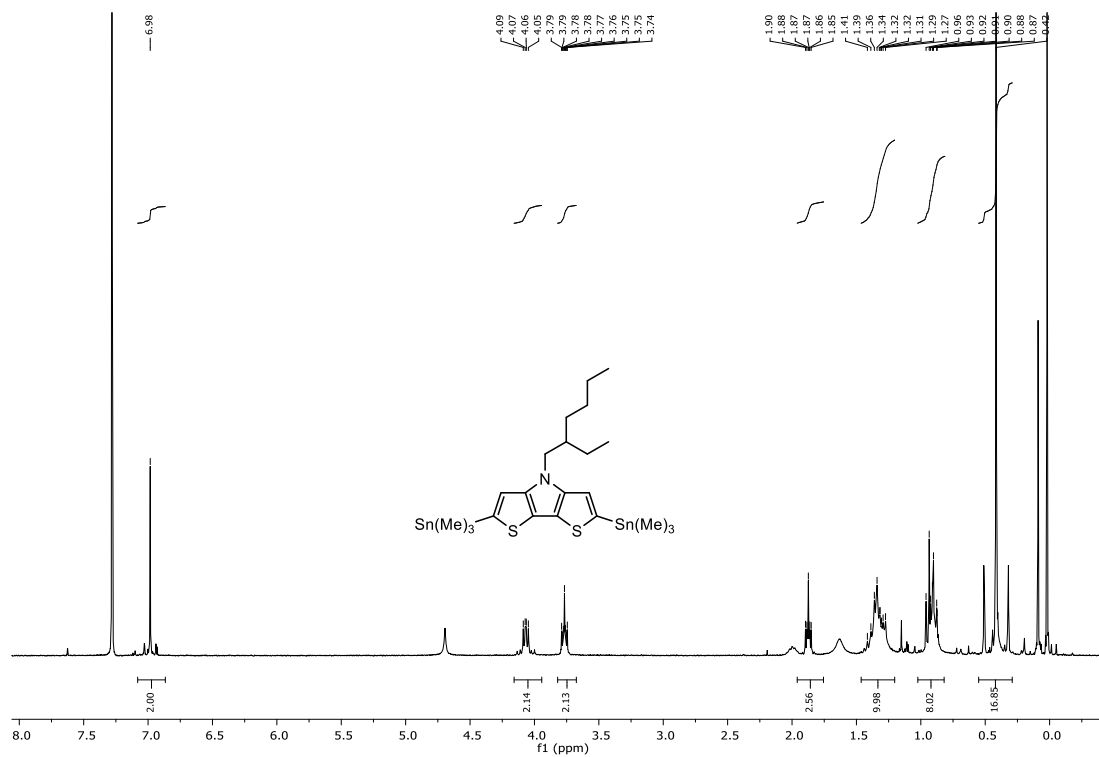


Figure A.18. ¹H NMR (300 MHz, CDCl₃) and ¹³C NMR (75 MHz, CDCl₃) spectrum of 4-(2-ethylhexyl)-2,6-bis(trimethylstannyl)-4*H*-dithieno[3,2-*b*:2',3'-*d*]pyrrole.

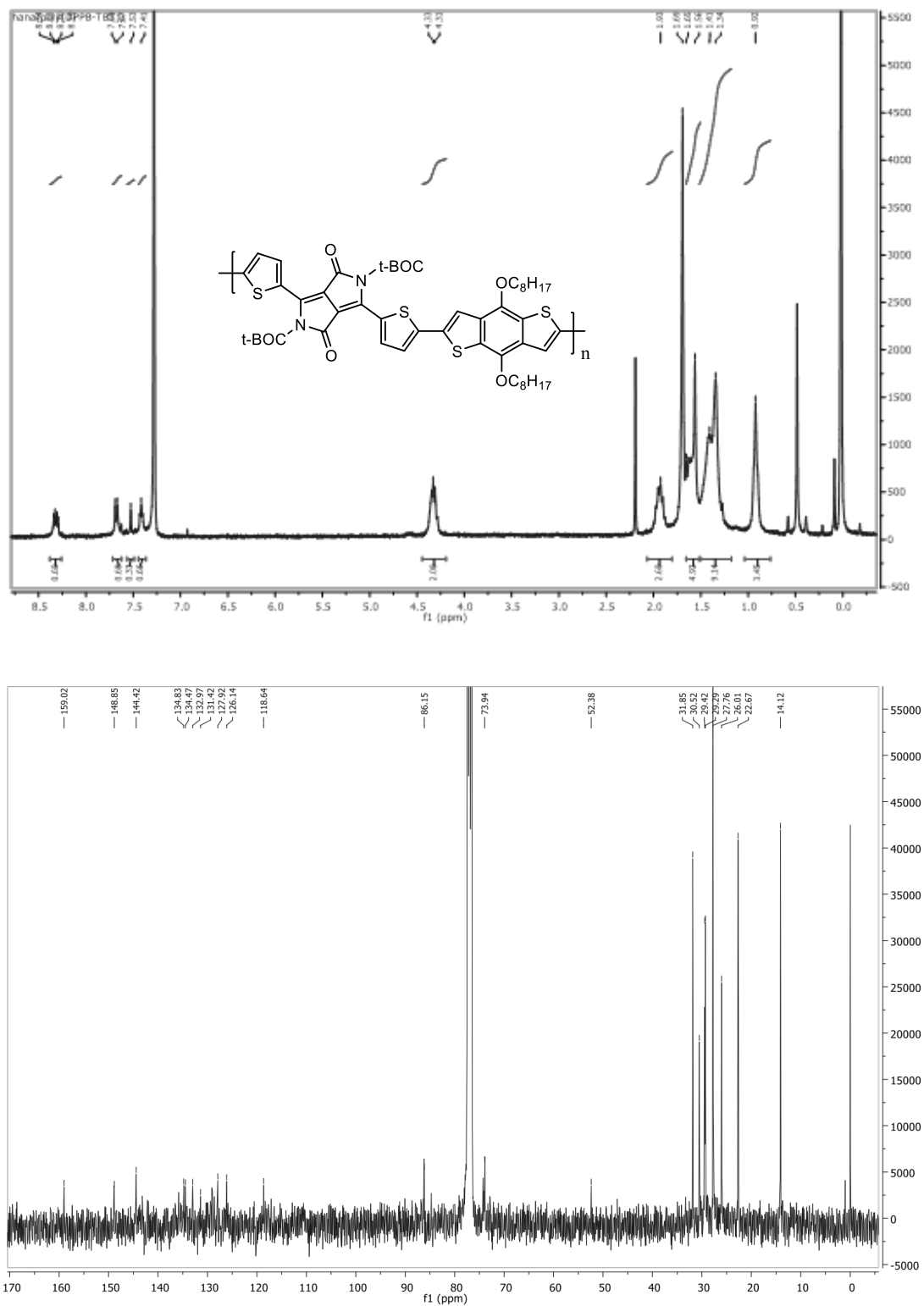
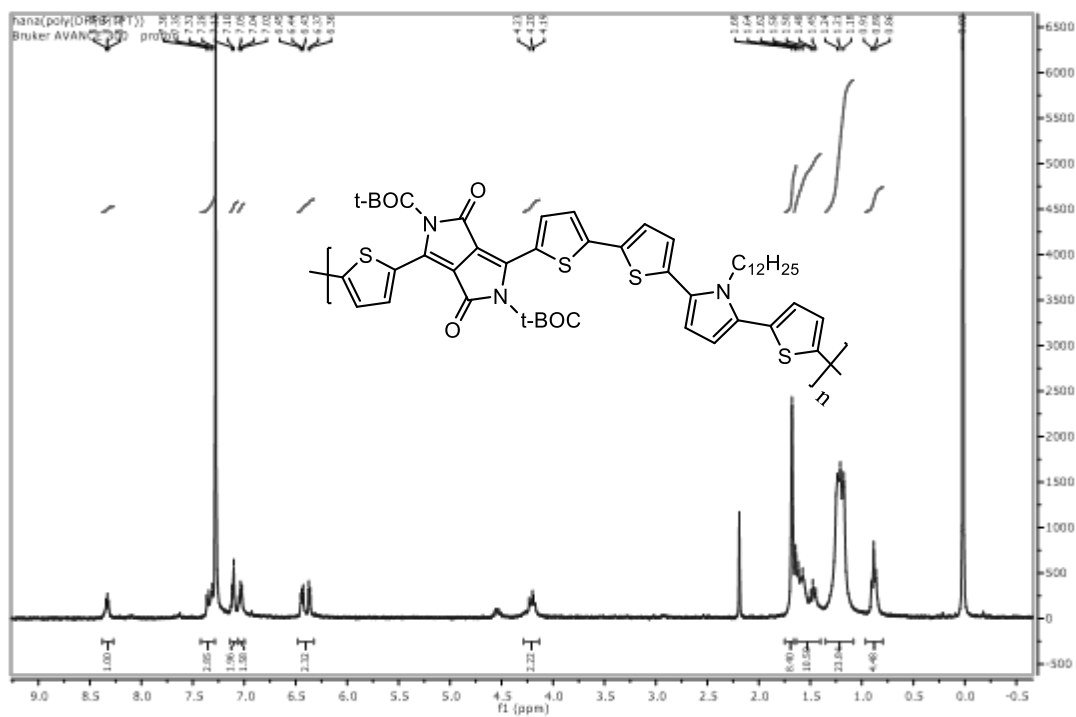
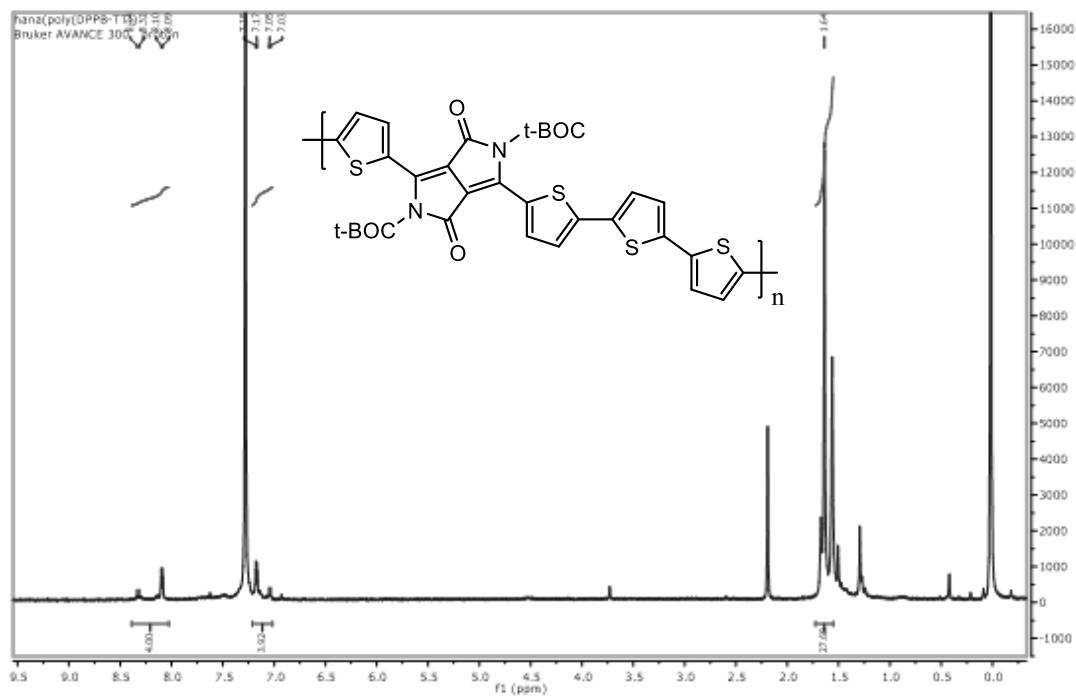


Figure A.19. The ^1H NMR (300 MHz, CDCl_3) and ^{13}C (100 MHz, CDCl_3) spectra of polymer **BDPP-TBT**.



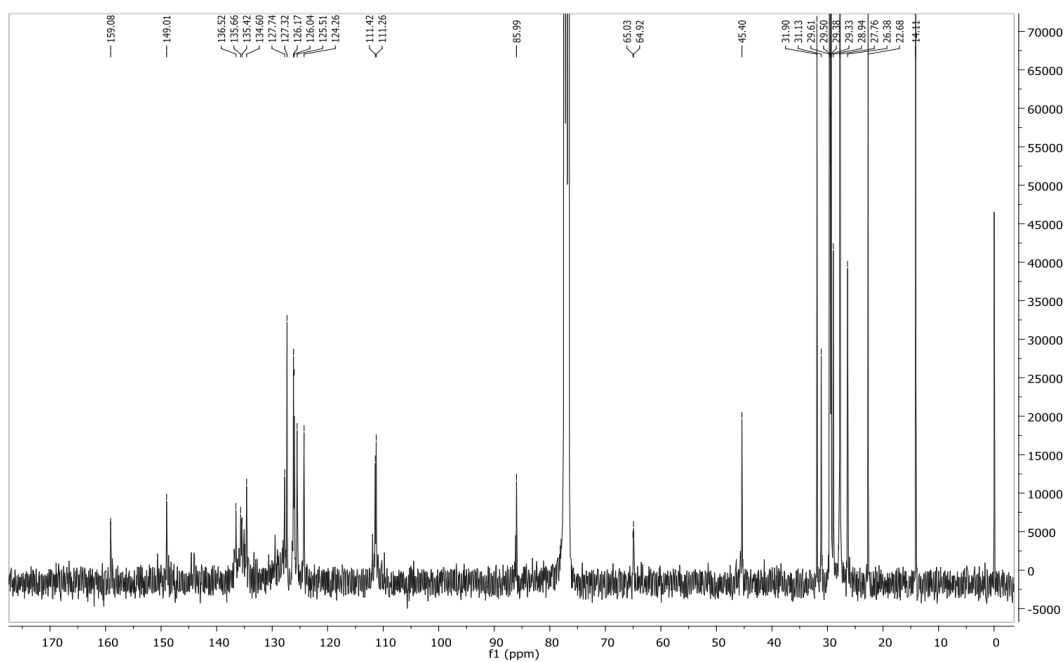


Figure A.21. The ^1H NMR (300 MHz, CDCl_3) and ^{13}C (100 MHz, CDCl_3) spectra of polymer **BDPP-TPTa**.

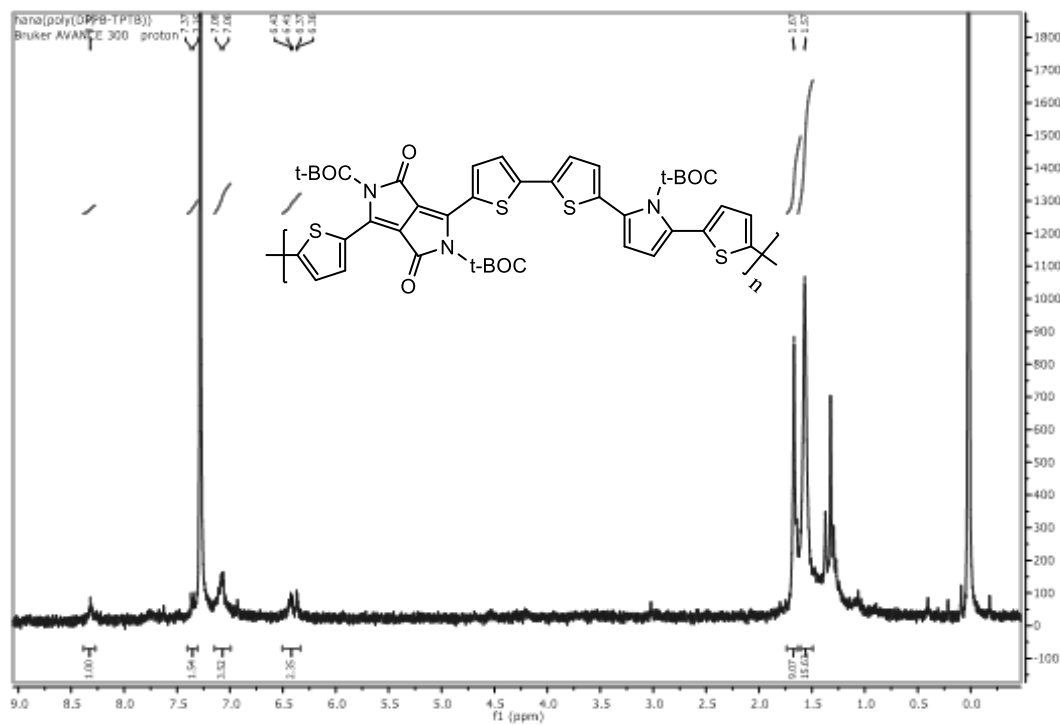


Figure A.22. The ^1H NMR spectrum (300 MHz, CDCl_3) of **BDPP-TPTB**.

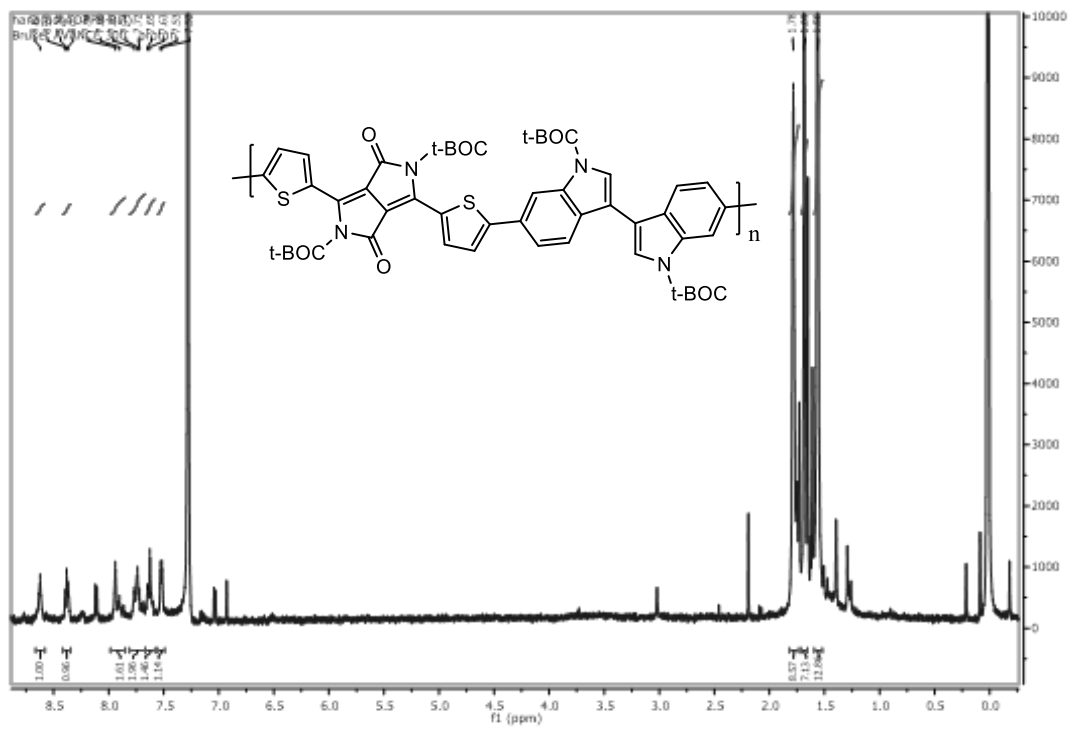
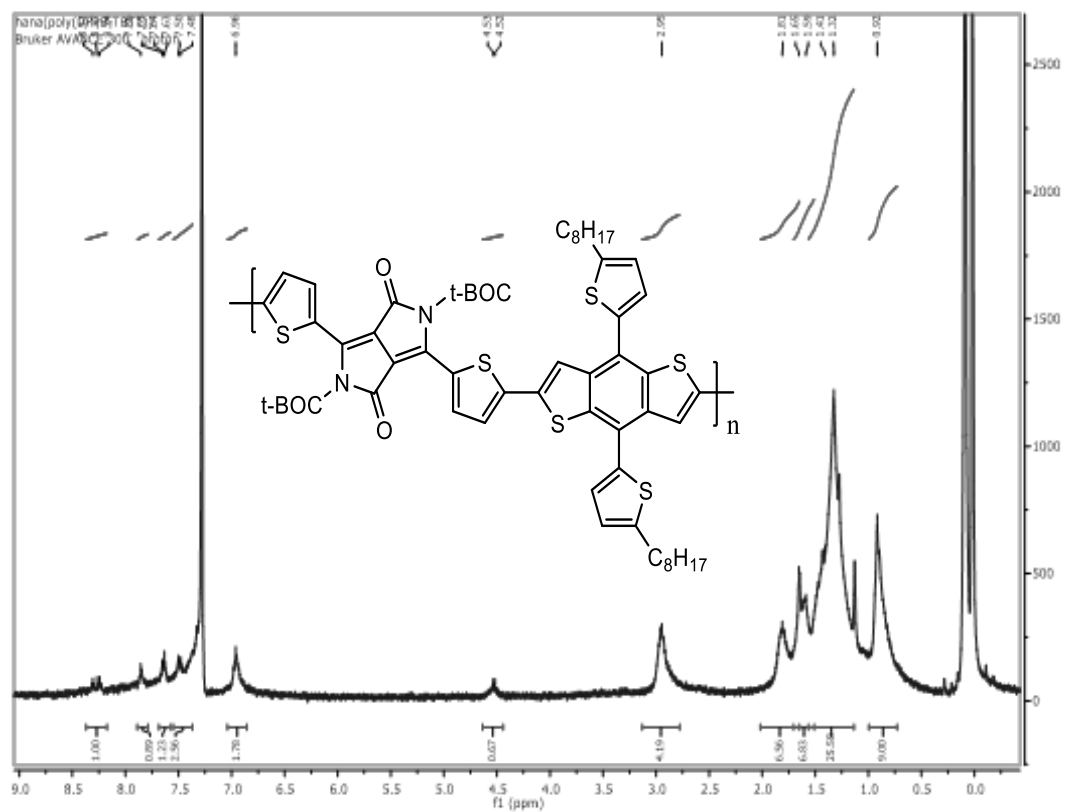


Figure A.23. The ^1H NMR spectrum (300 MHz, CDCl_3) of polymer **BDPP-BI**.



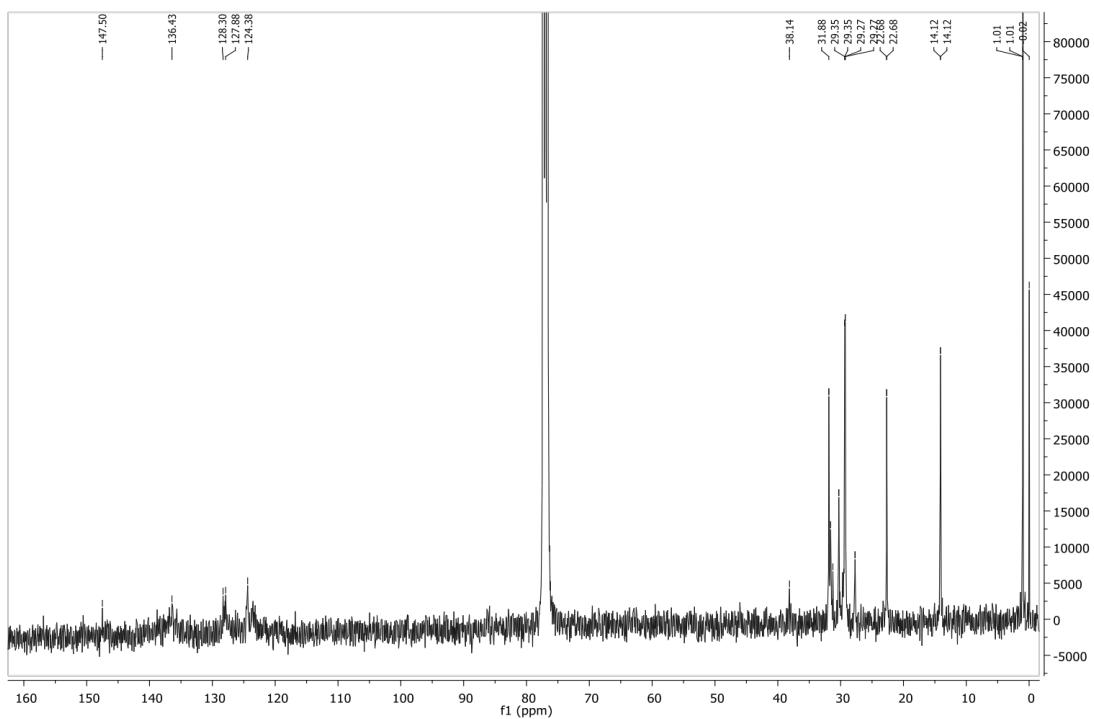


Figure A.24. The ^1H NMR (300 MHz, CDCl_3) and ^{13}C (100 MHz, CDCl_3) spectra of **BDPP-TBTT**.

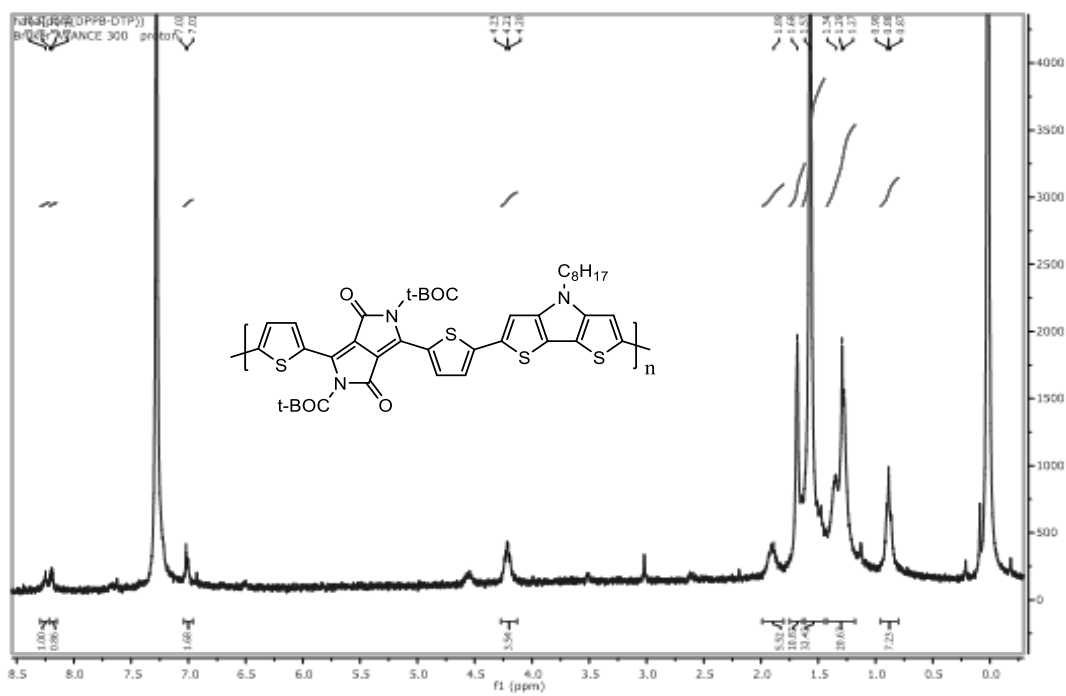


Figure A.25. The ^1H NMR spectrum (300 MHz, CDCl_3) of **BDPP-DTP**.

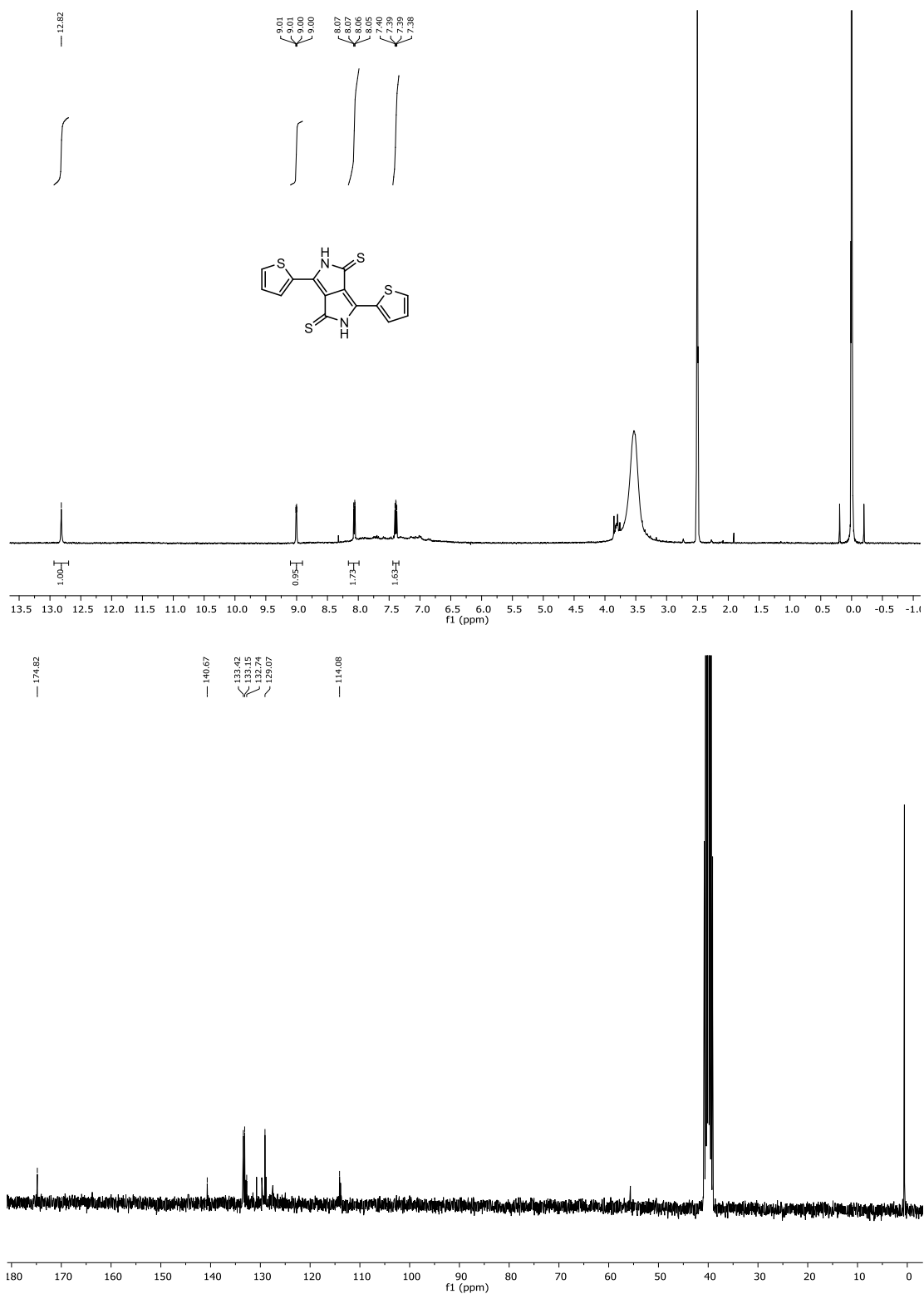


Figure A.26. ^1H NMR (400 MHz, CDCl_3) and ^{13}C NMR (75 MHz, CDCl_3) spectra of DTPP.

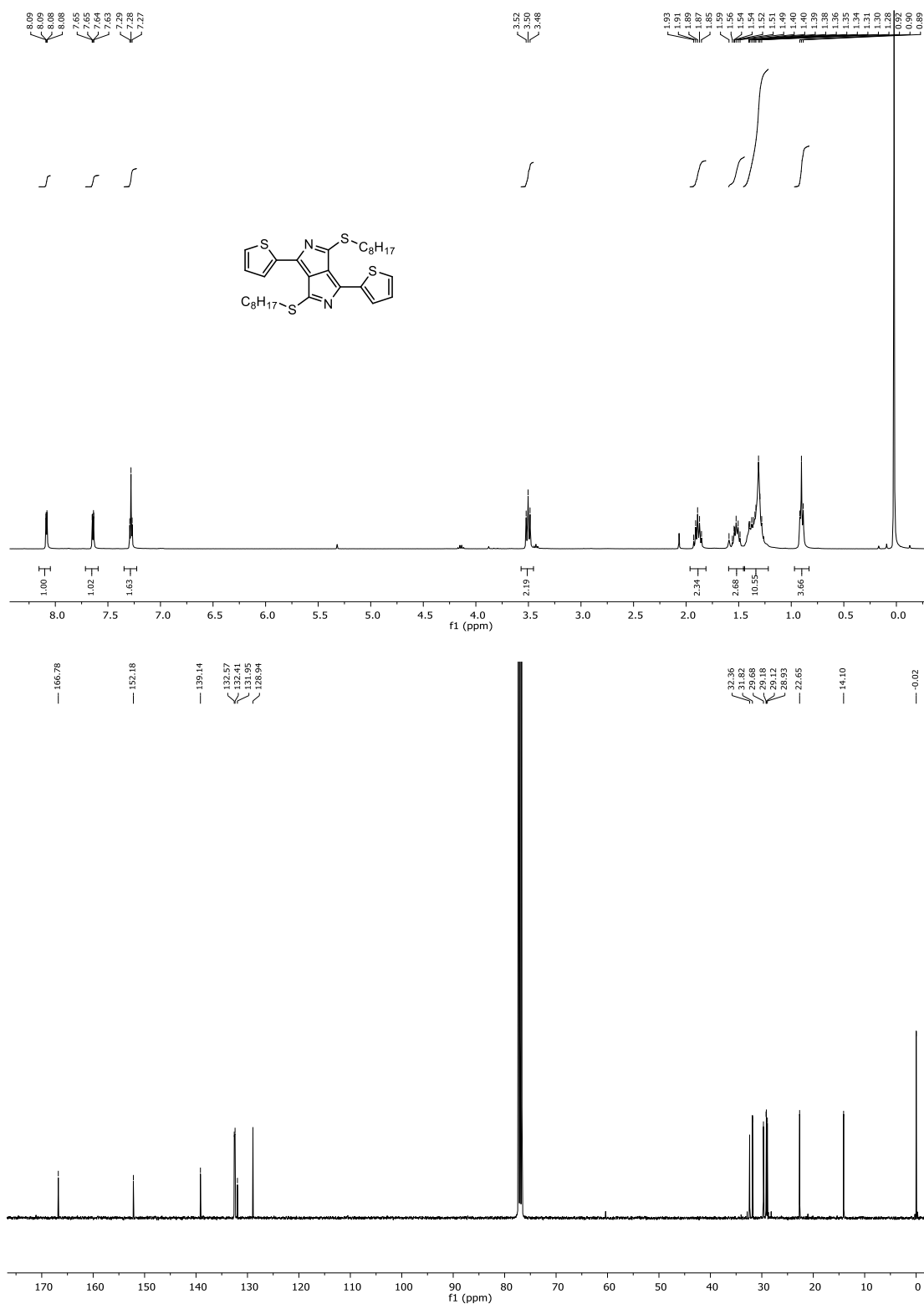


Figure A.27. ¹H NMR (400 MHz, CDCl₃) and ¹³C NMR (75 MHz, CDCl₃) spectra of 1,4-bis(octylthio)-3,6-di(thiophen-2-yl)pyrrolo[3,4-*c*]pyrrole.

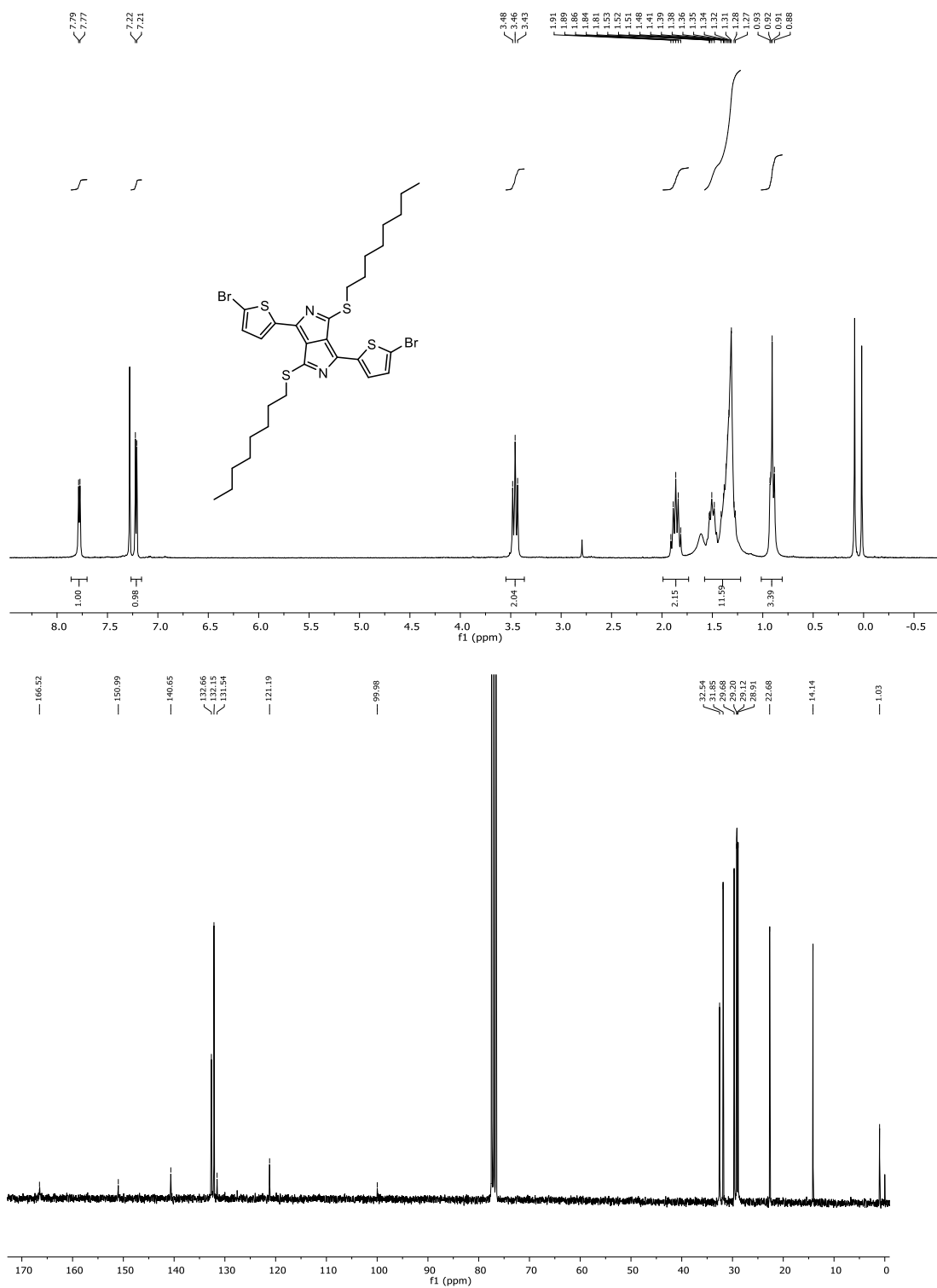


Figure A.28. ^1H NMR (400 MHz, CDCl_3) and ^{13}C NMR (75 MHz, CDCl_3) spectra of 1,4-bis(5-bromothiophen-2-yl)-3,6-bis(octylthio)pyrrolo[3,4-c]pyrrole.

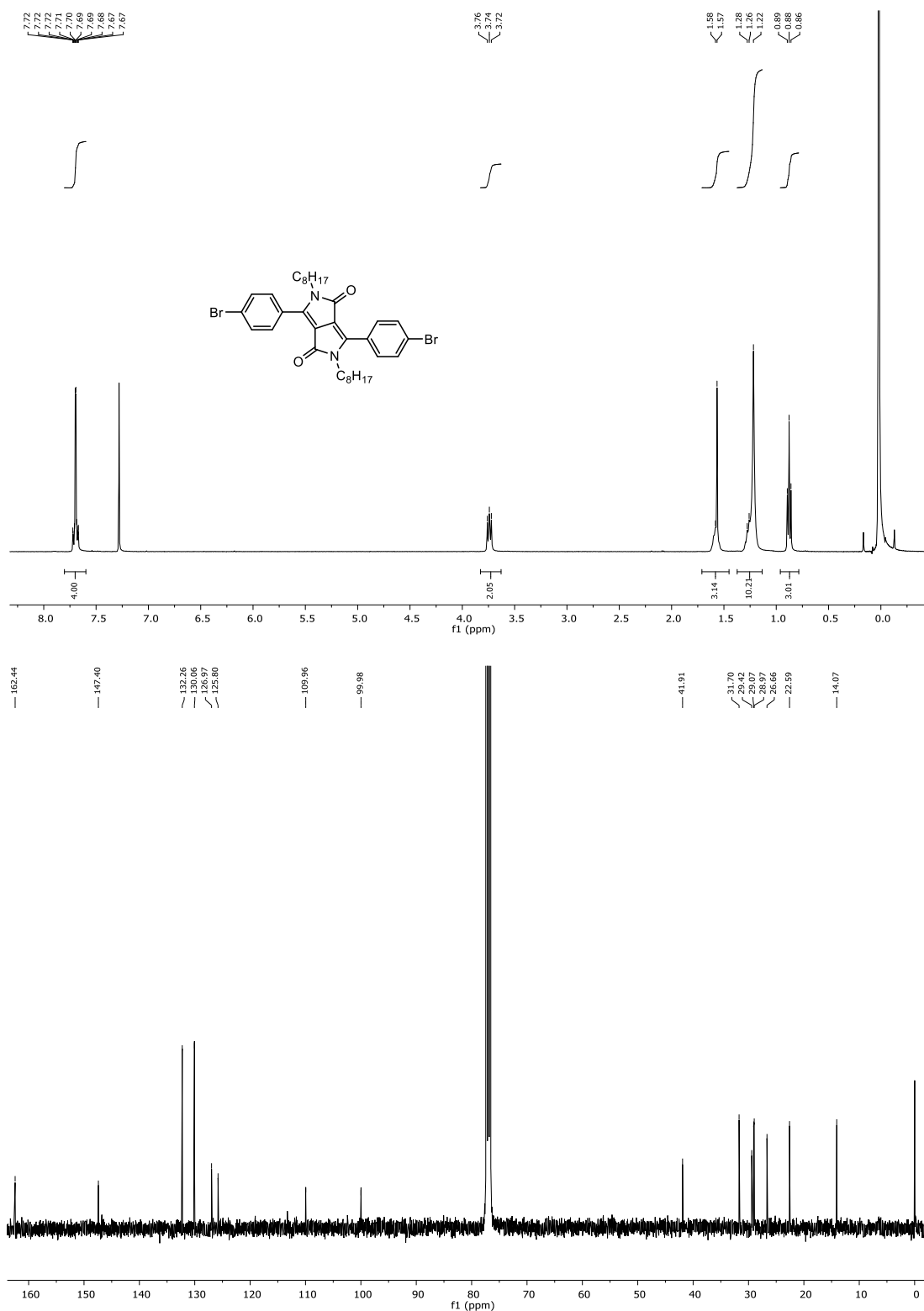


Figure A.29. ¹H NMR (400 MHz, CDCl₃) and ¹³C NMR (75 MHz, CDCl₃) spectra of 3,6-bis(4-bromophenyl)-2,5-dioctyl-2,5-dihydropyrrolo[3,4-*c*]pyrrole-1,4-dione.

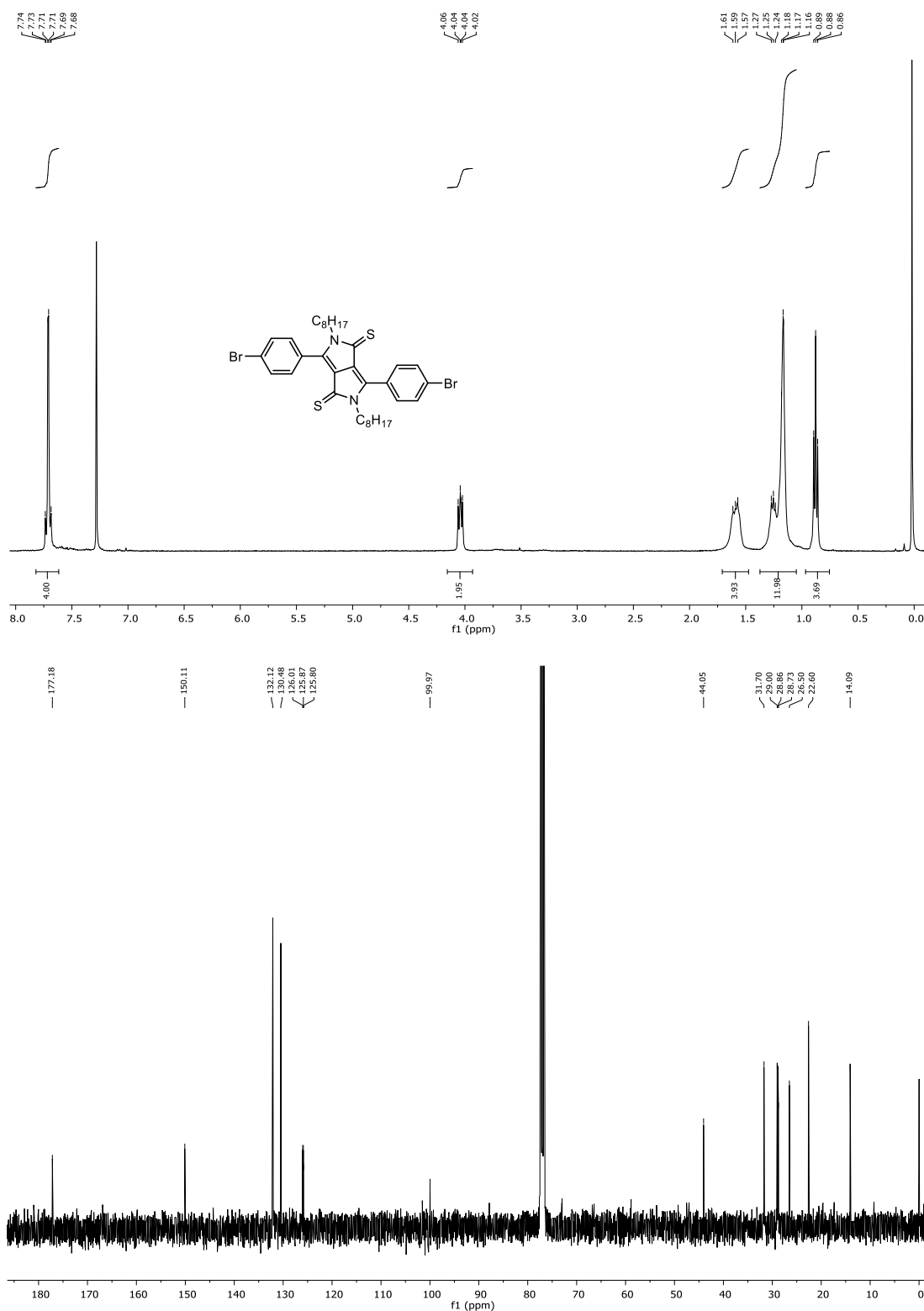


Figure A.30. ^1H NMR (400 MHz, CDCl_3) and ^{13}C NMR (75 MHz, CDCl_3) spectra of 3,6-bis(4-bromophenyl)-2,5-dioctyl-2,5-dihydropyrrolo[3,4-c]pyrrole-1,4-dithione.

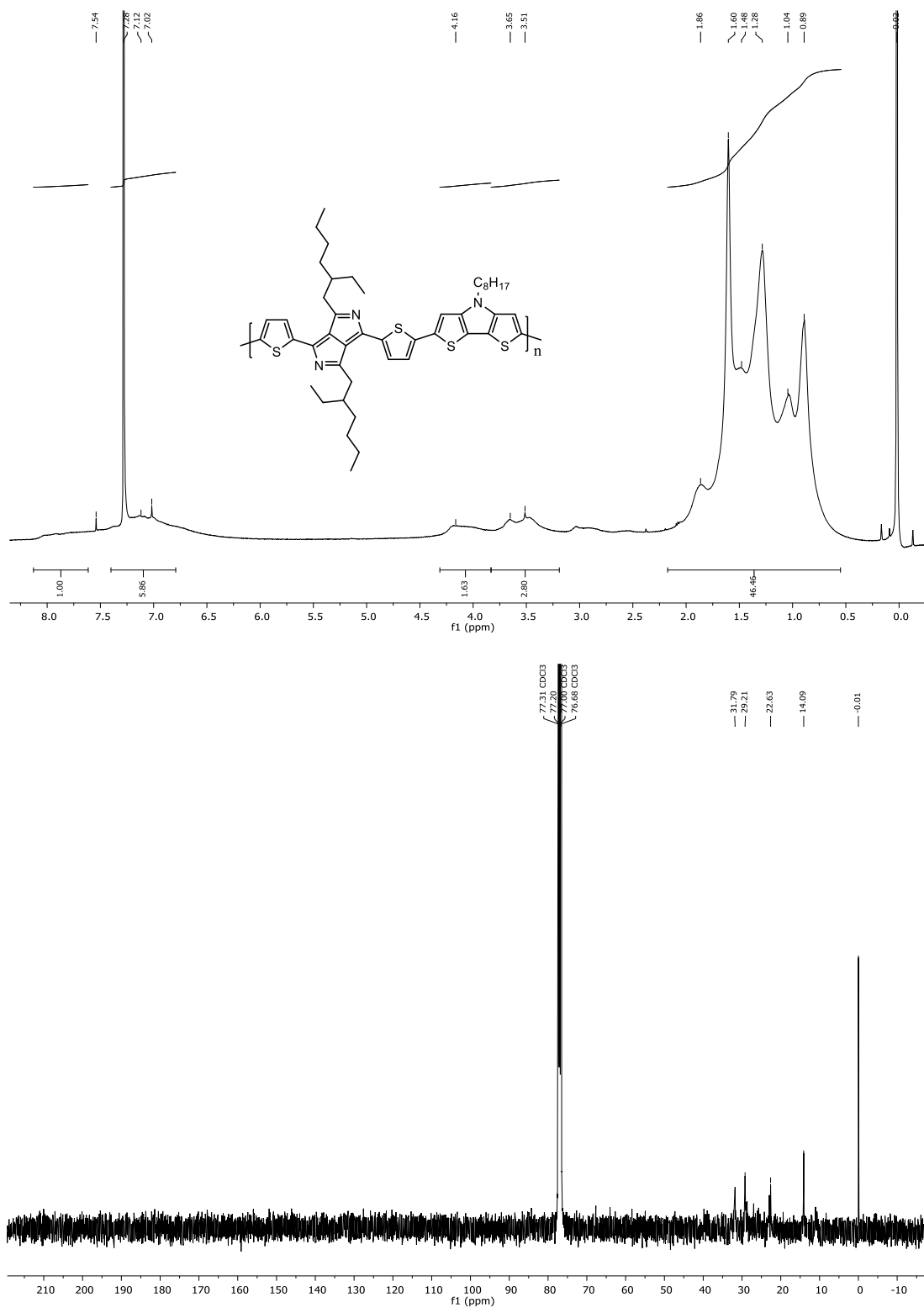


Figure A.31. ^1H NMR (400 MHz, CDCl_3) and ^{13}C NMR (75 MHz, CDCl_3) spectra of polymer DAPb-DTPa.

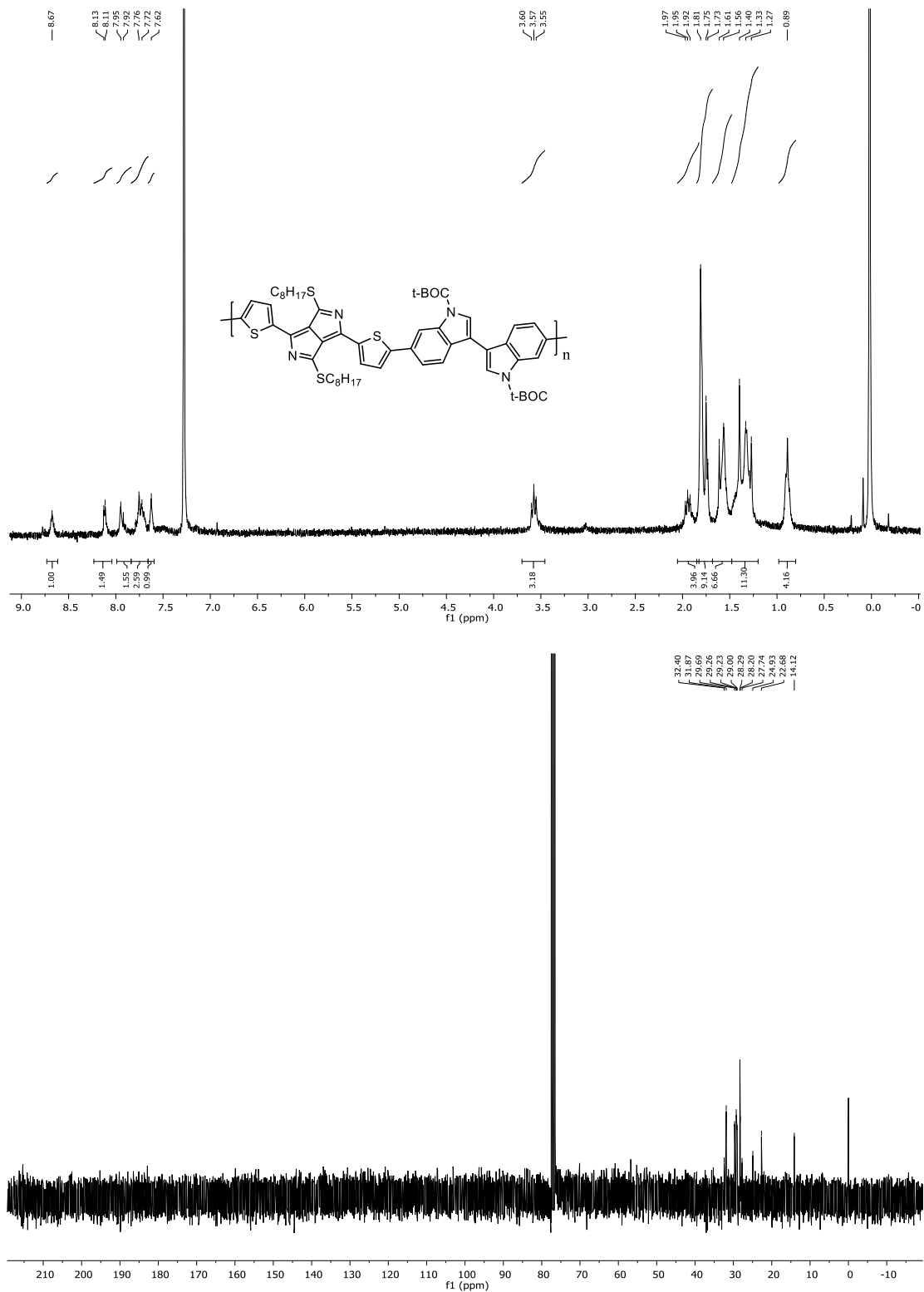


Figure A.33. ^1H NMR (400 MHz, CDCl_3) and ^{13}C NMR (75 MHz, CDCl_3) spectra of polymer DAPa-BI.

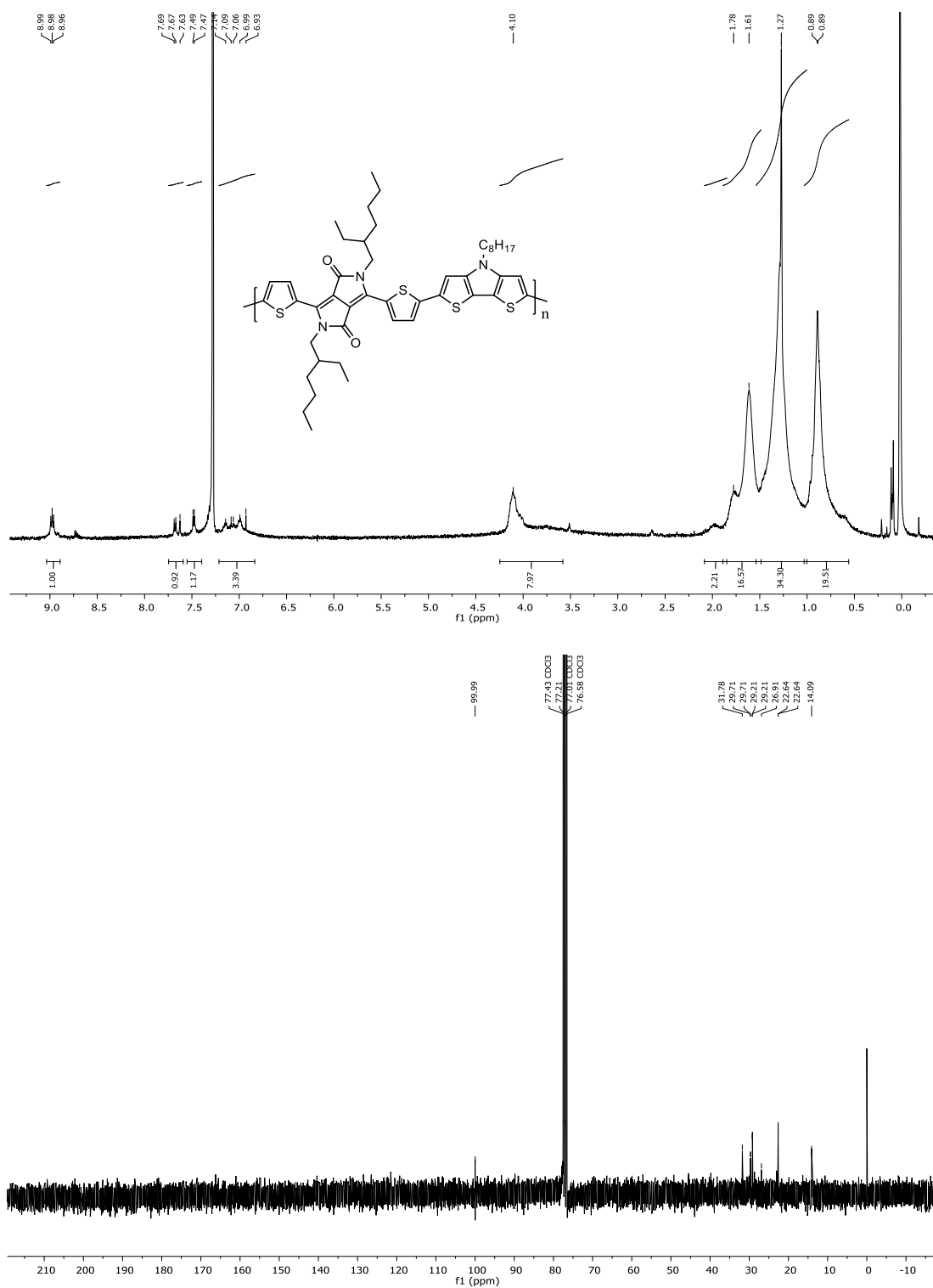


Figure A.34. ^1H NMR (400 MHz, CDCl_3) and ^{13}C NMR (75 MHz, CDCl_3) spectra of polymer DPP-DTPa.

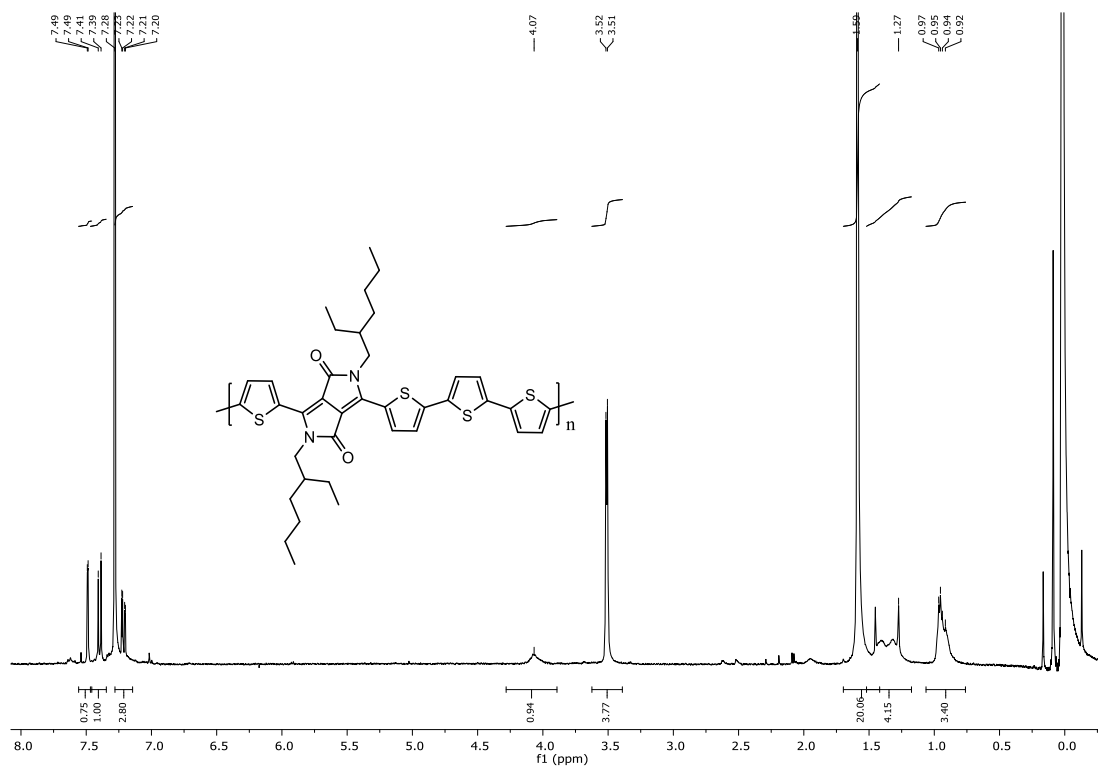


Figure A.35. ^1H NMR (400 MHz, CDCl_3) spectrum of polymer DPP-BT.

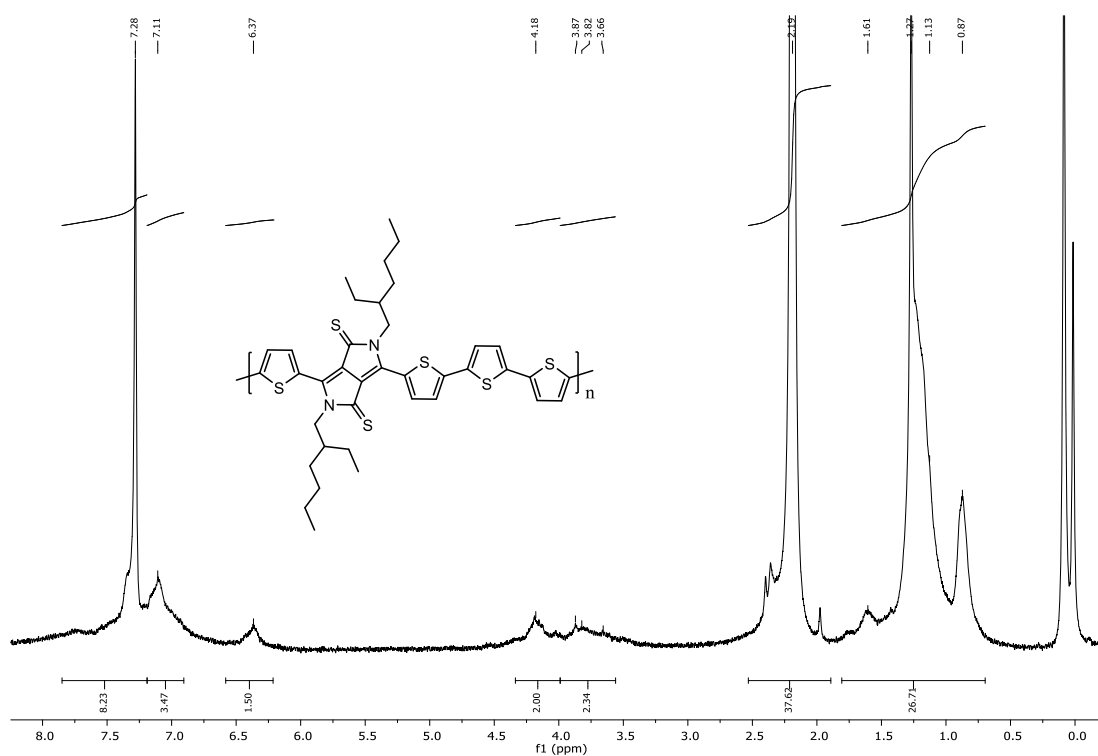


Figure A.36. ^1H NMR (400 MHz, CDCl_3) spectrum of polymer DTPP-BT.

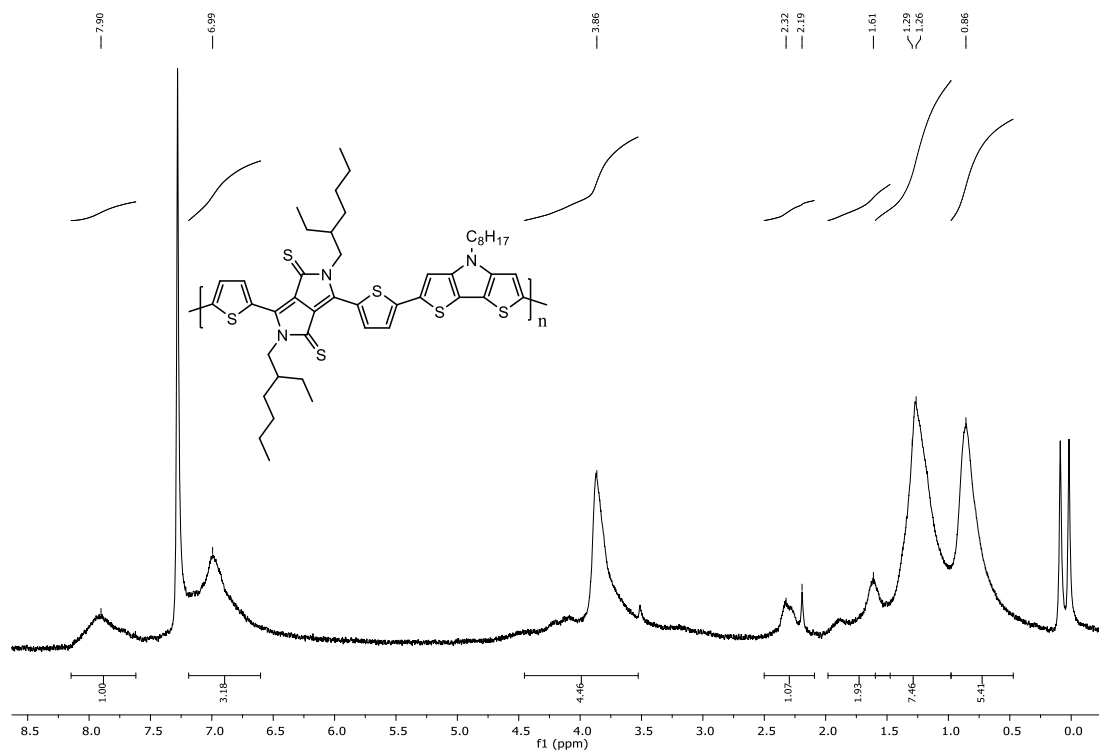
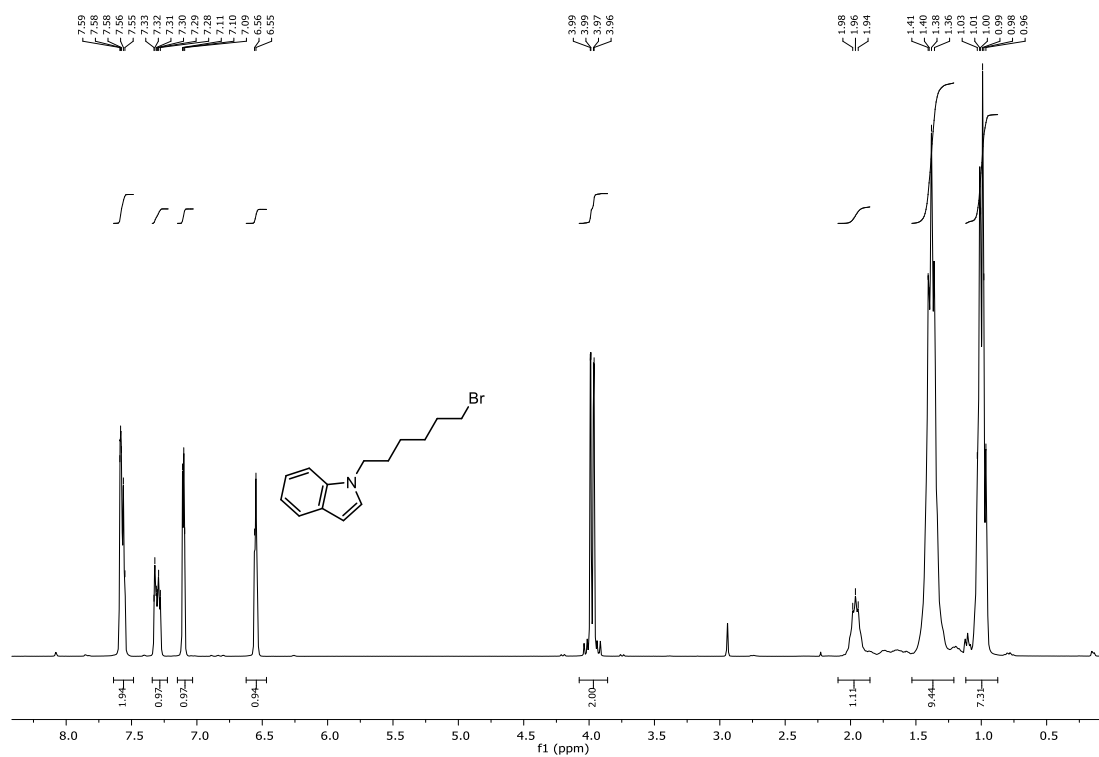


Figure A.37. ^1H NMR (400 MHz, CDCl_3) spectrum of polymer **DTPP-DTPa**.



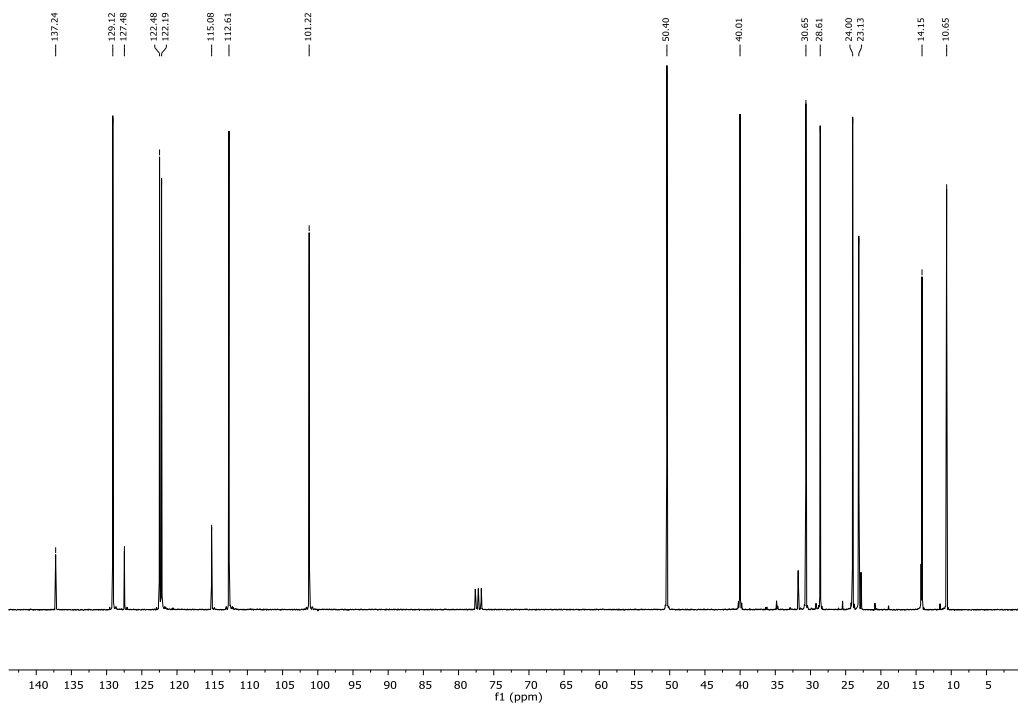


Figure A.38. ^1H NMR (300 MHz, CDCl_3) and ^{13}C NMR (75 MHz, CDCl_3) spectra of 1-(6-bromohexyl)-1*H*-indole (**IV-1**).

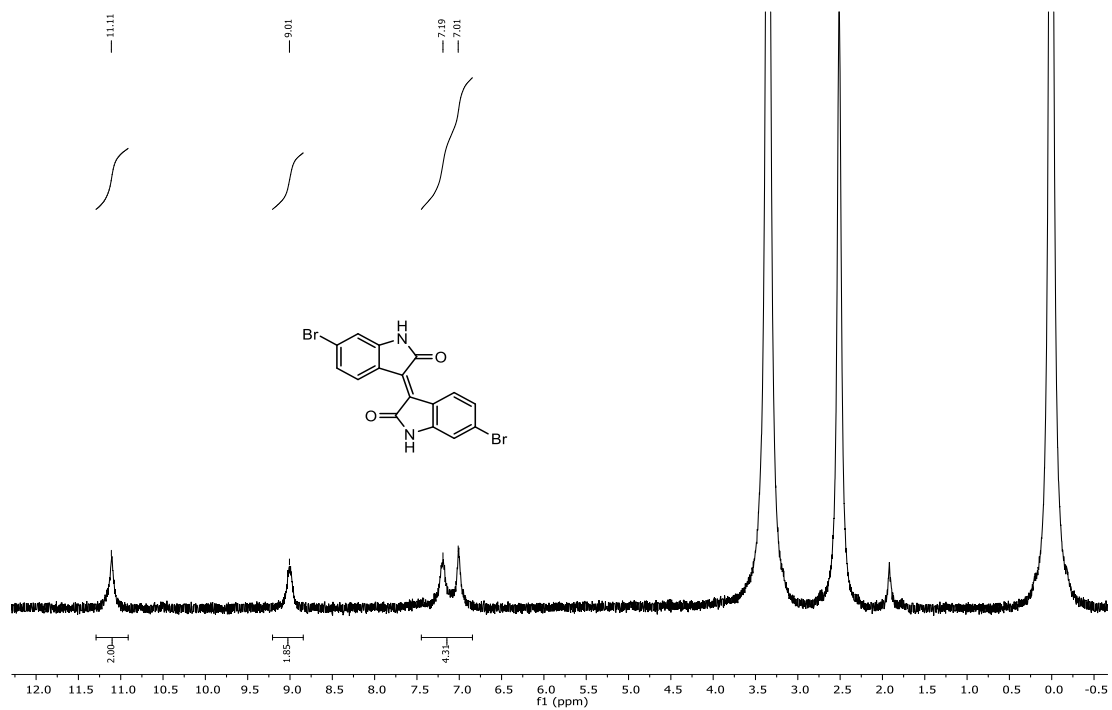


Figure A.38. ^1H NMR (300 MHz, CDCl_3) spectrum of (*E*)-6,6'-dibromo-[3,3'-biindolylidene]-2,2'-dione (**IV-2**).

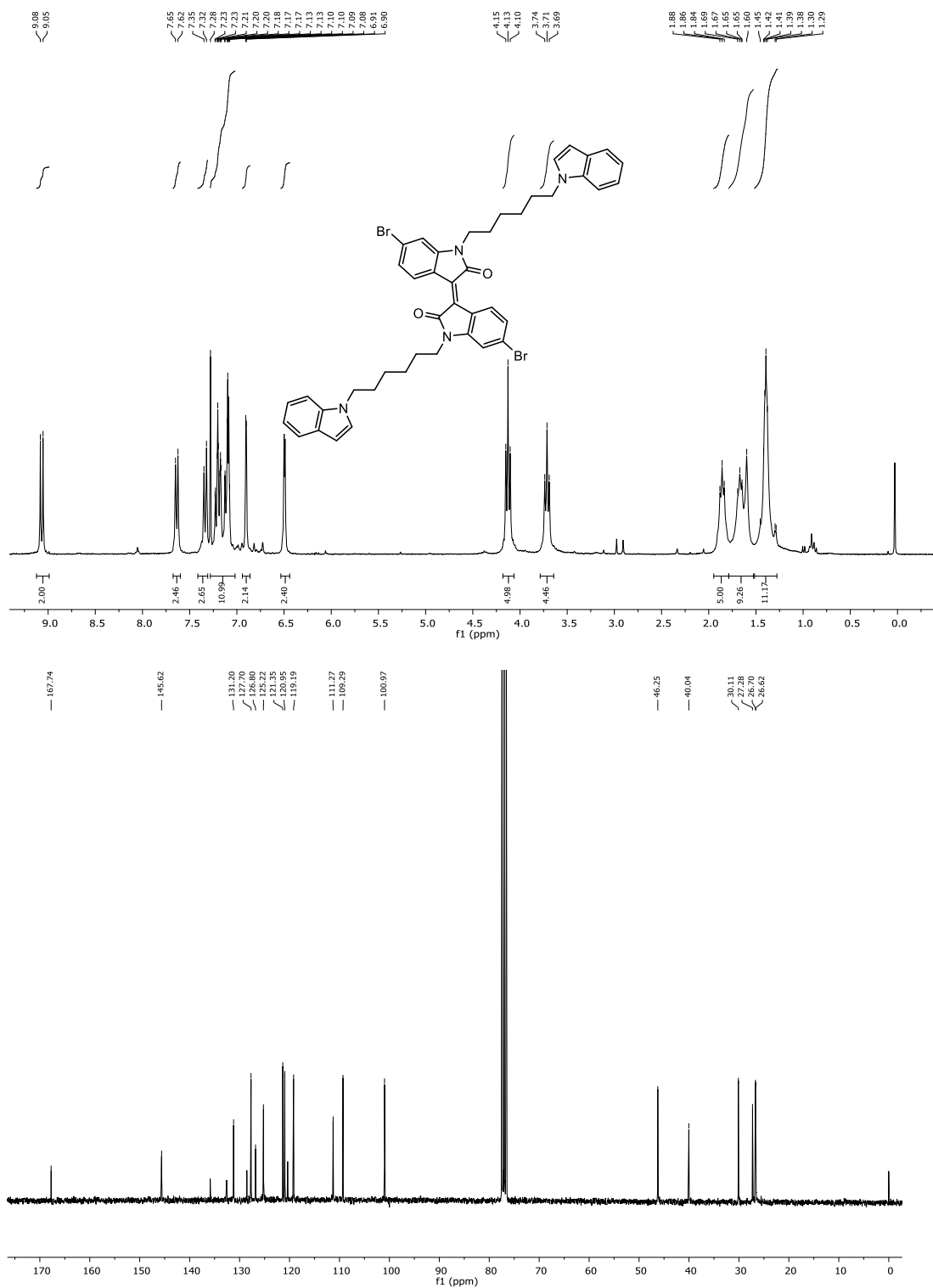


Figure A.39. ¹H NMR (300 MHz, CDCl₃) and ¹³C NMR (75 MHz, CDCl₃) spectra of (E)-1-(6-(1'-(6-(1H-indol-1-yl)hexyl)-6,6'-dibromo-2,2'-dioxo-[3,3'-biindolinylidene]-1-yl)hexyl)-1H-indol-1-ium (**II**).

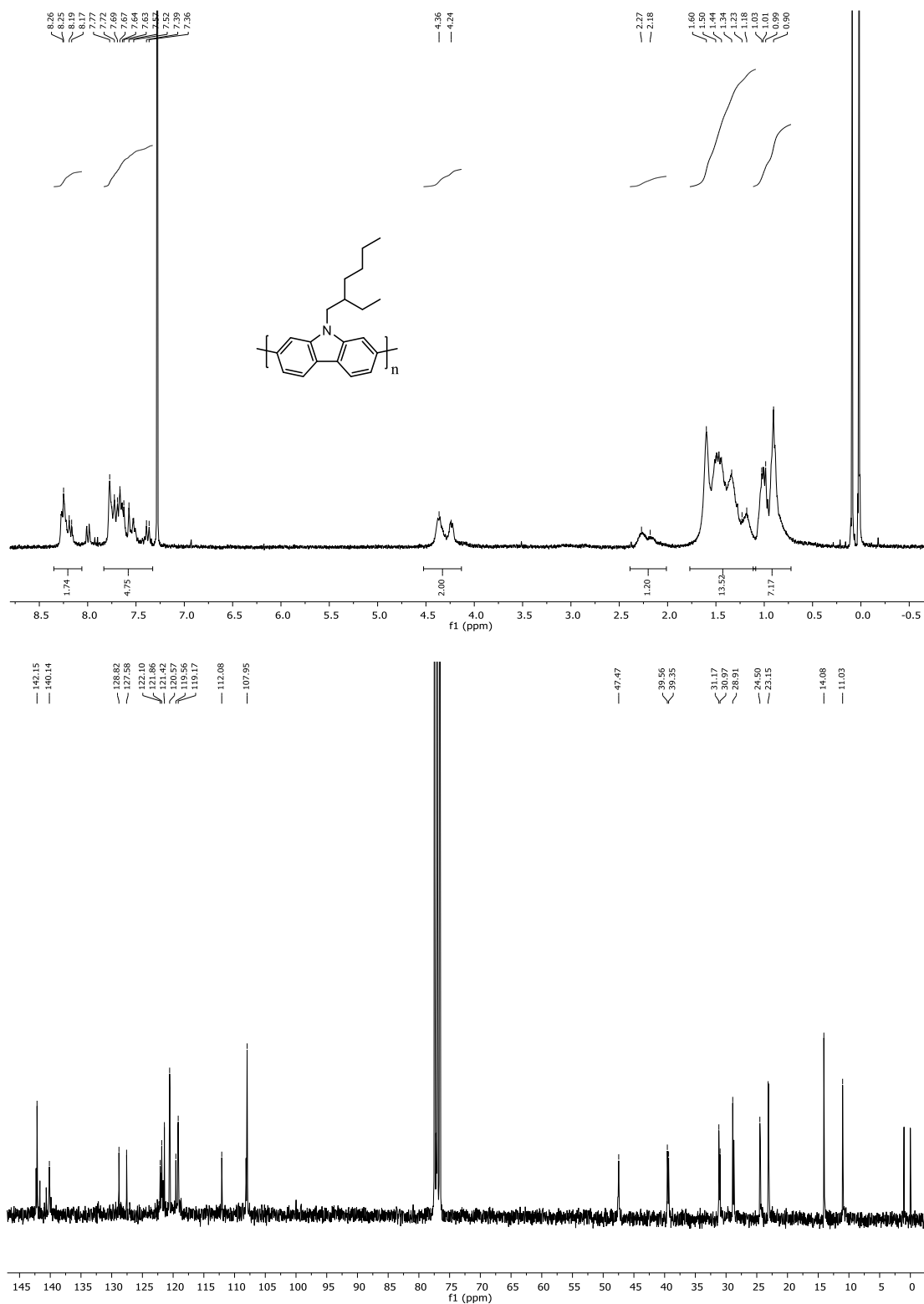


Figure A.41. ^1H NMR (300 MHz, CDCl_3) and ^{13}C NMR (75 MHz, CDCl_3) spectra of polymer PCbz.

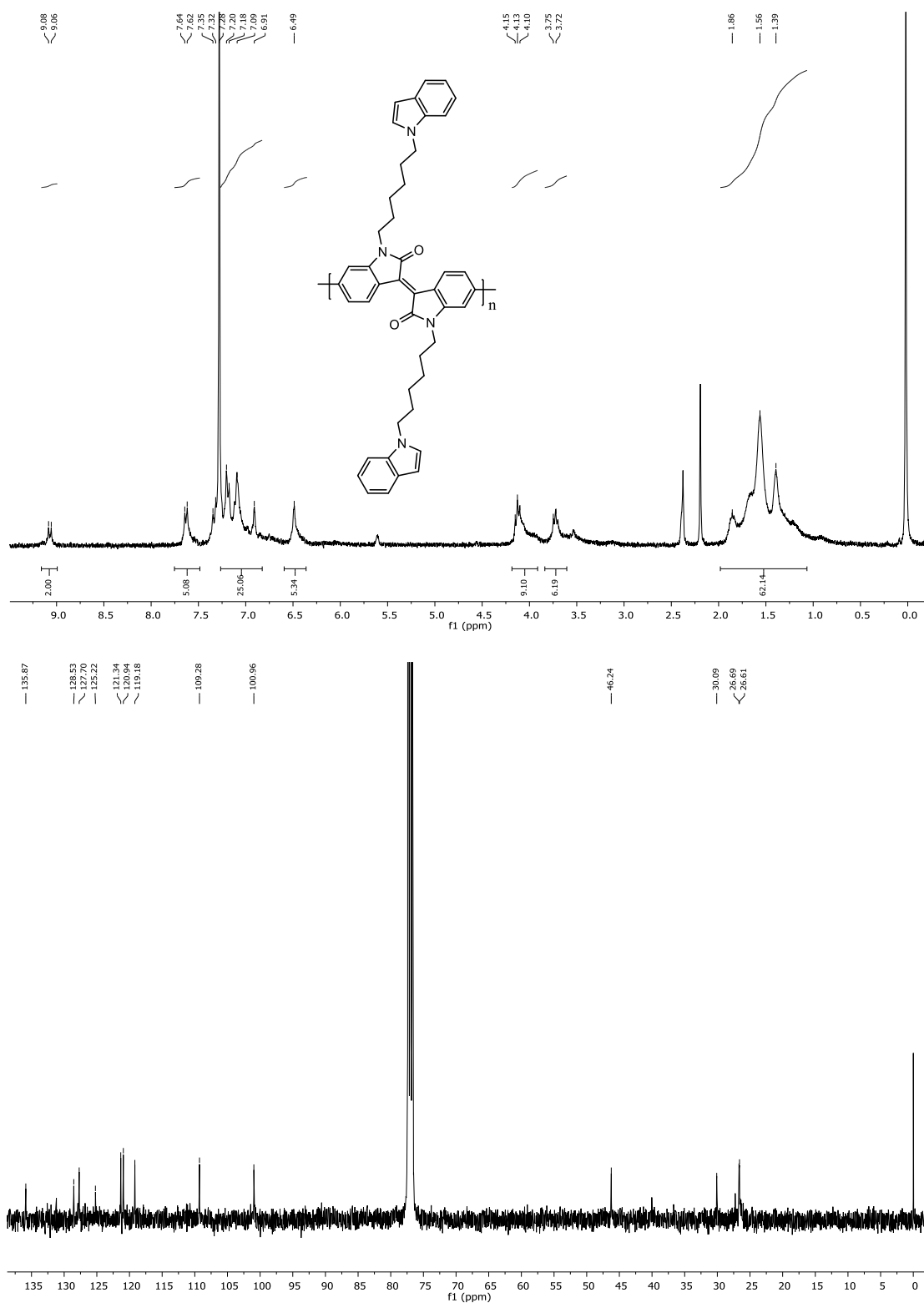


Figure A.42. ^1H NMR (300 MHz, CDCl_3) and ^{13}C NMR (101 MHz, CDCl_3) spectra of polymer **PiI**.

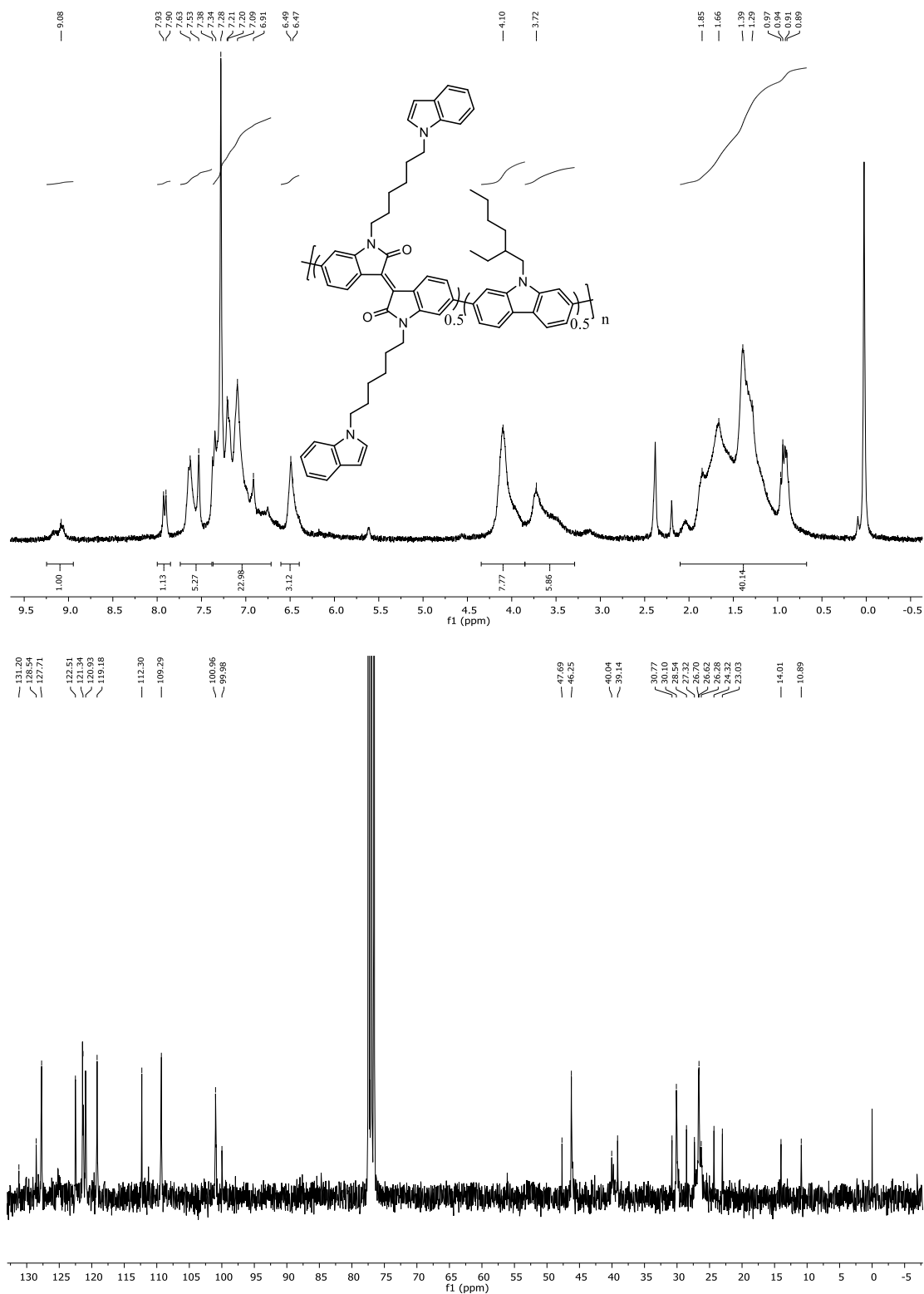


Figure A.43. ^1H NMR (300 MHz, CDCl_3) and ^{13}C NMR (75 MHz, CDCl_3) spectra of polymer **ii-Cbz-1**.

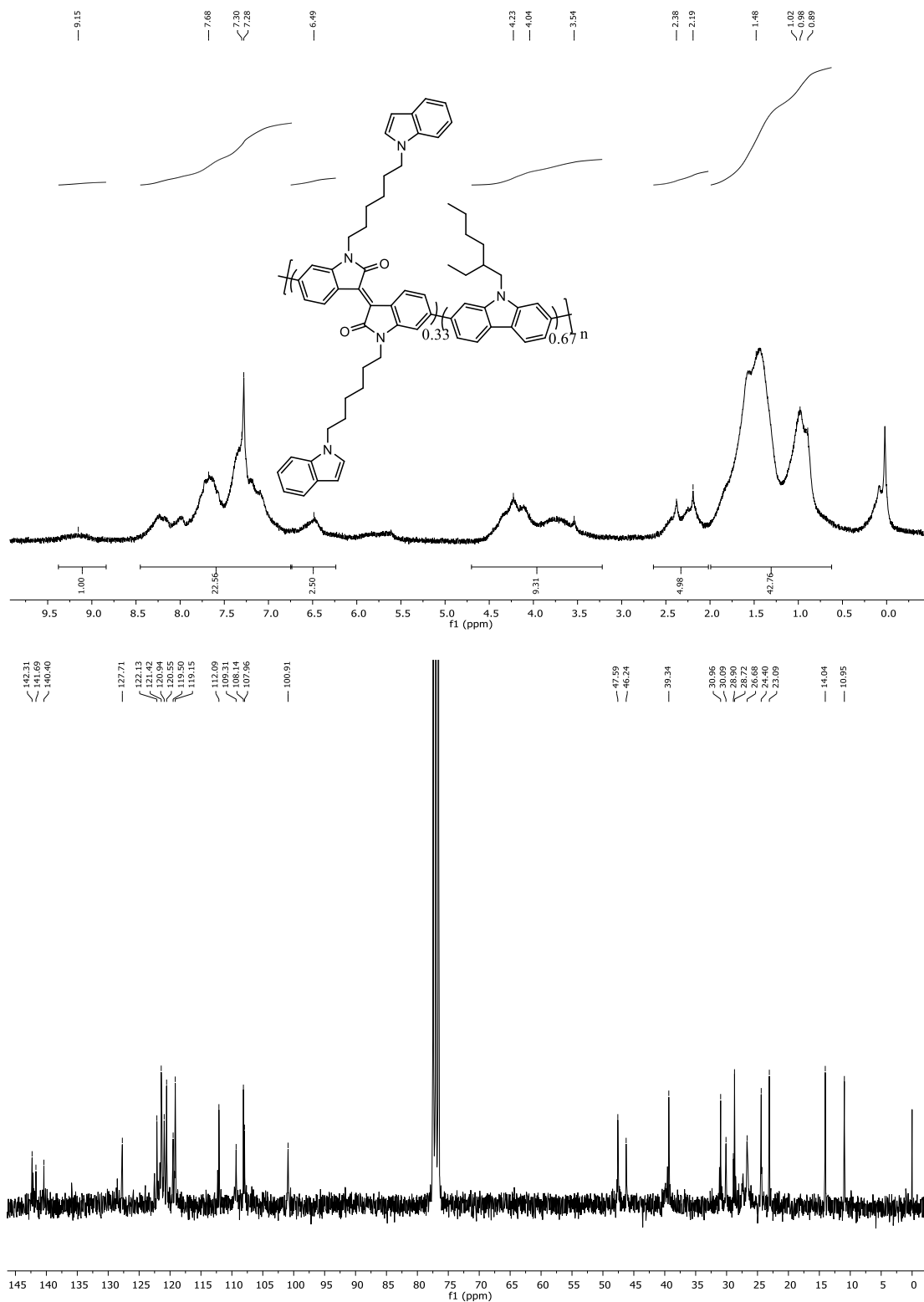


Figure A.44. ^1H NMR (300 MHz, CDCl_3) and ^{13}C NMR (75 MHz, CDCl_3) spectra of polymer **il-Cbz-2**.

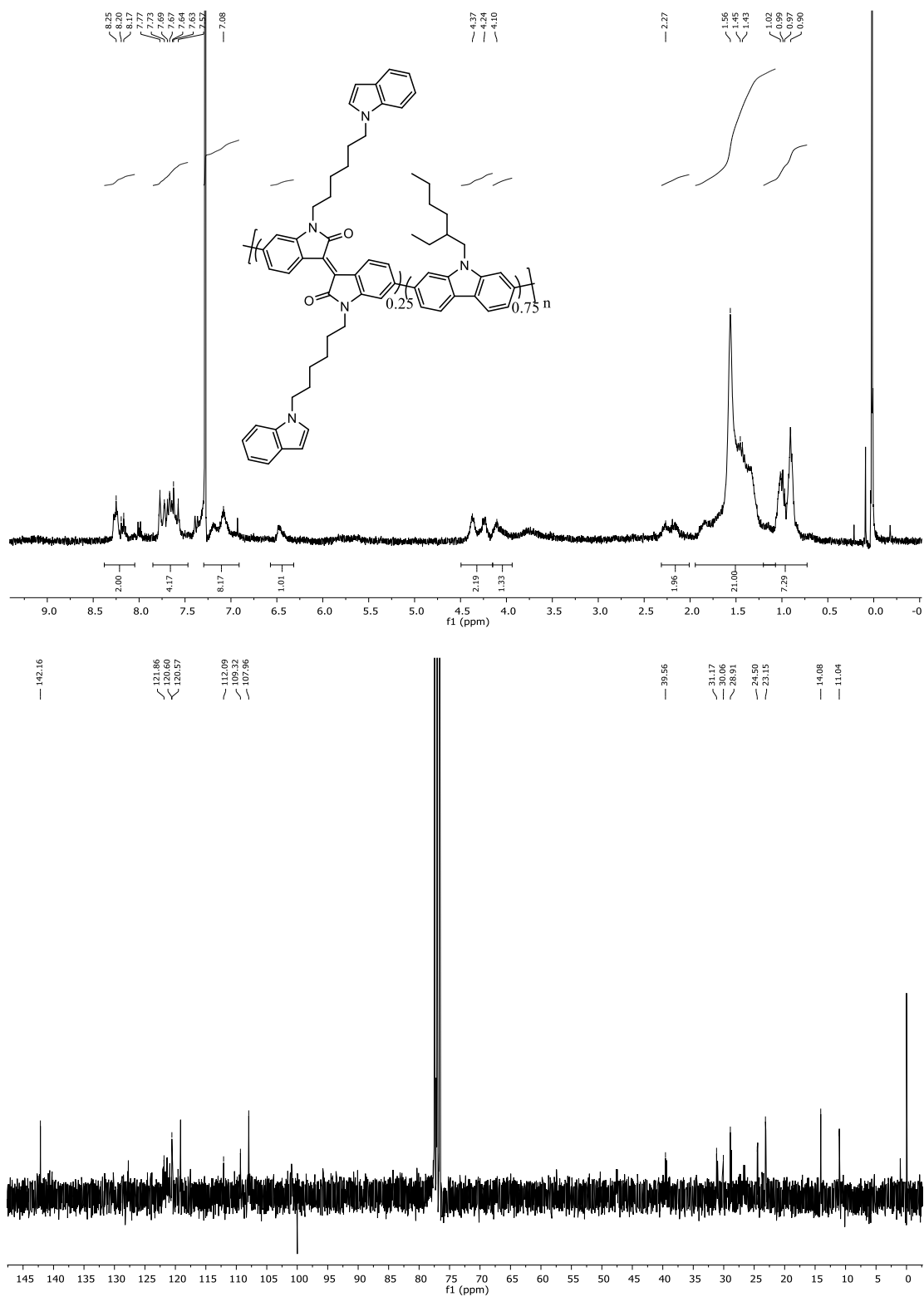


Figure A.45. ^1H NMR (300 MHz, CDCl_3) and ^{13}C NMR (75 MHz, CDCl_3) spectra of polymer **il-Cbz-3**.

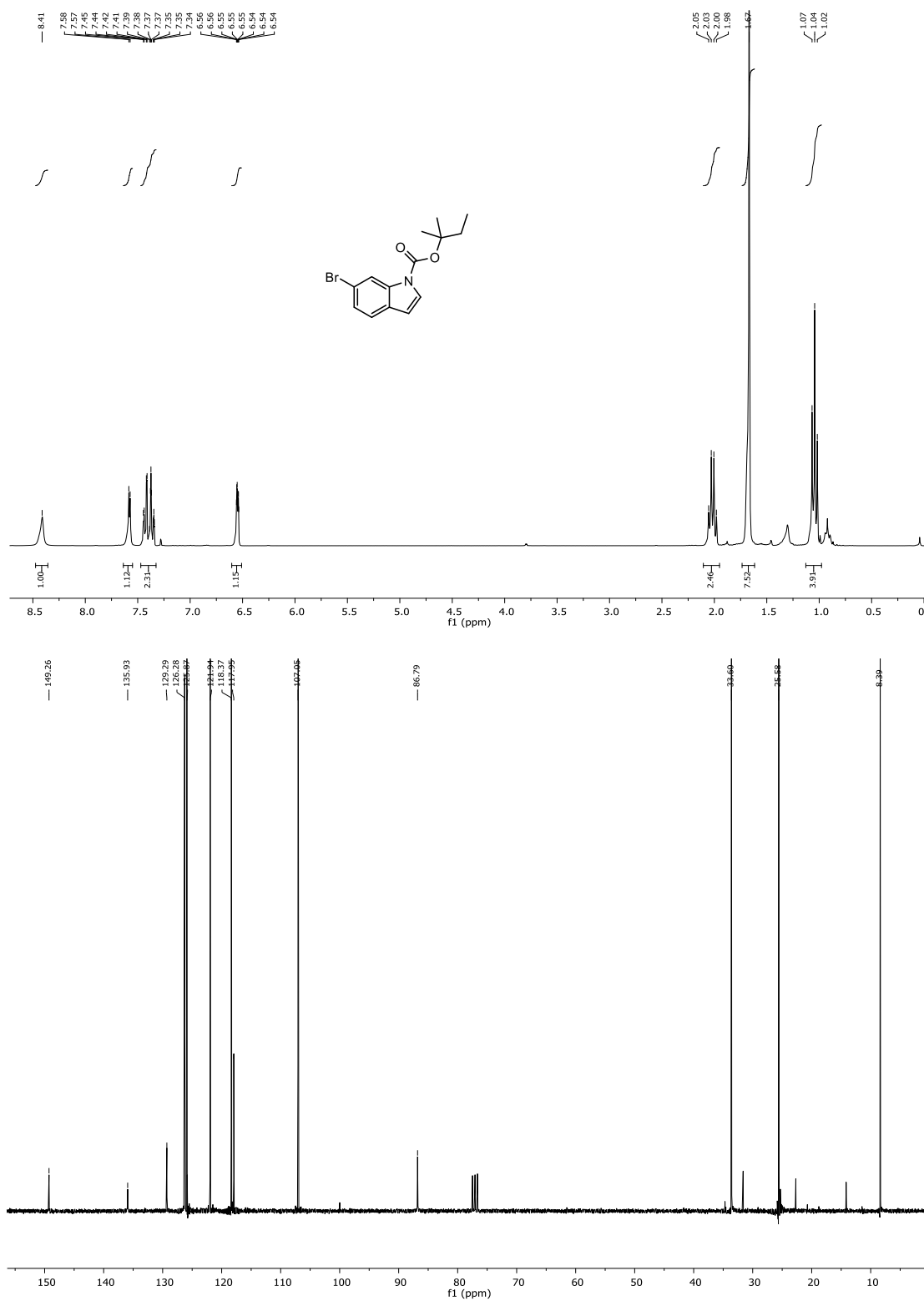


Figure A.46. ^1H NMR (300 MHz, CDCl_3) and ^{13}C NMR (75 MHz, CDCl_3) spectra of *tert*-pentyl 6-bromo-1*H*-indole-1-carboxylate (V-I).

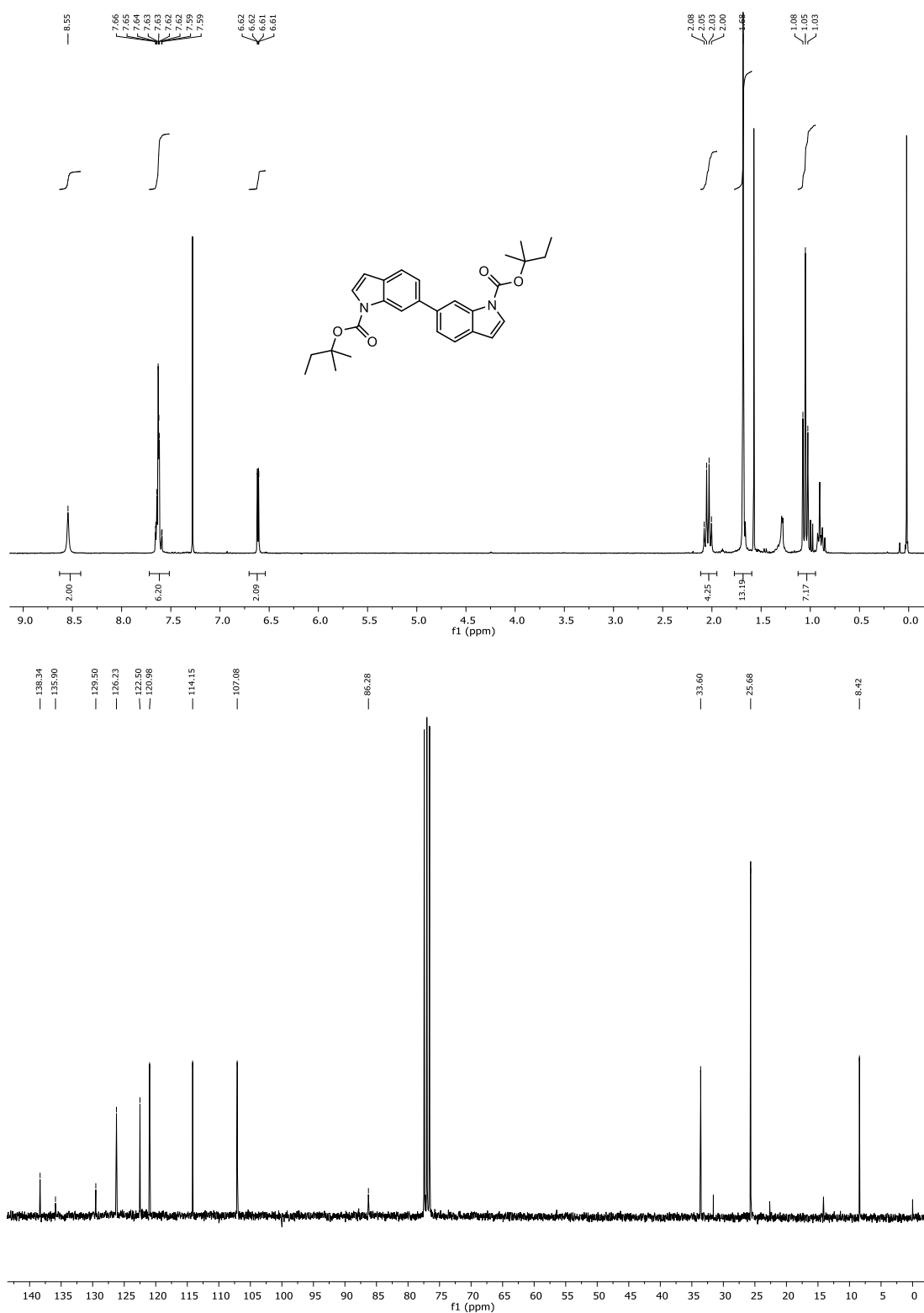


Figure A.47. ¹H NMR (300 MHz, CDCl₃) and ¹³C NMR (75 MHz, CDCl₃) spectra of di-*tert*-pentyl 1*H*,1'*H*-[6,6'-biindole]-1,1'-dicarboxylate (**V-II**).

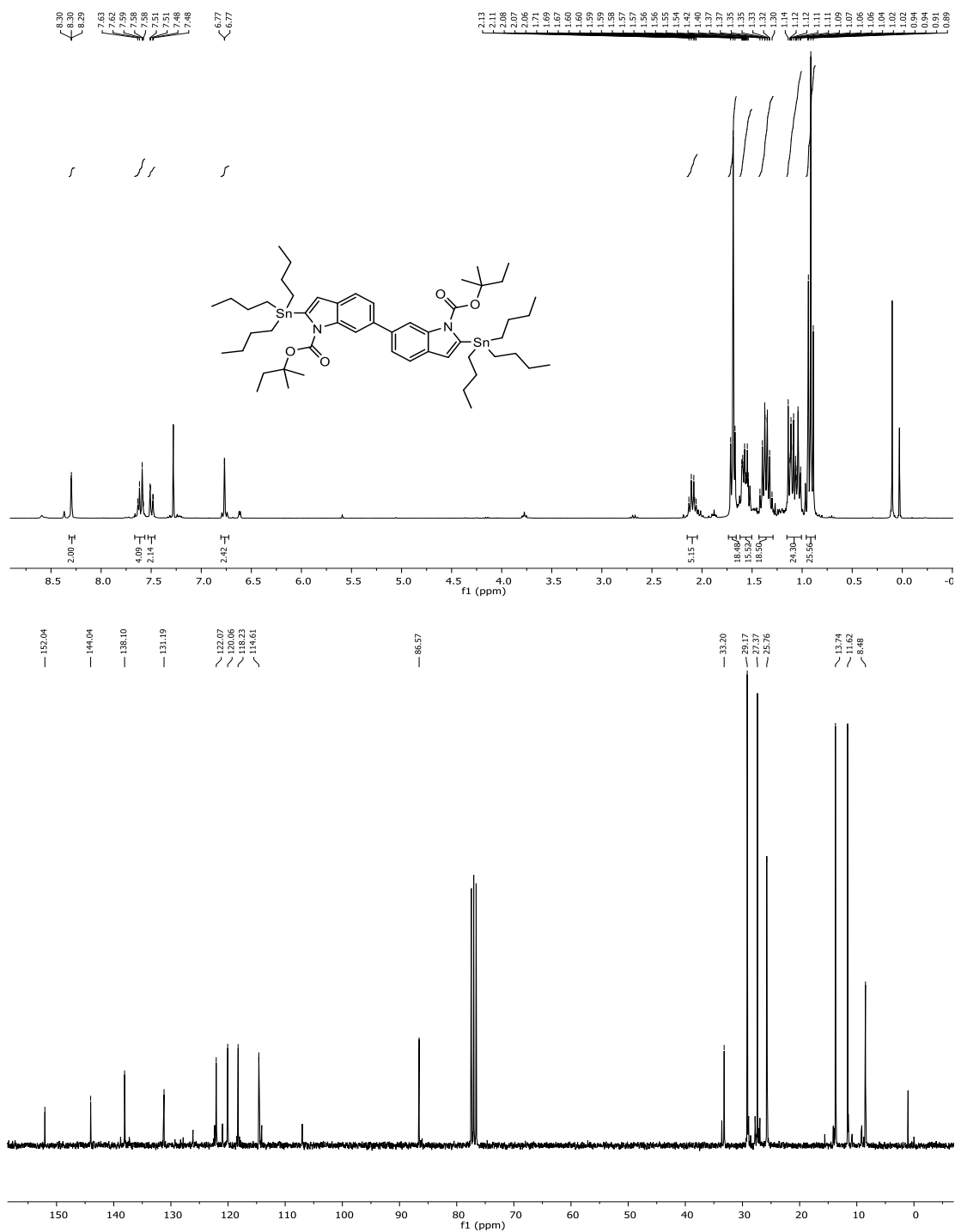


Figure A.48. ¹H NMR (300 MHz, CDCl₃) and ¹³C NMR (75 MHz, CDCl₃) spectra of di-*tert*-pentyl 2,2'-bis(tributylstannyl)-1*H*,1'*H*-[6,6'-biindole]-1,1'-dicarboxylate (**V-III**).

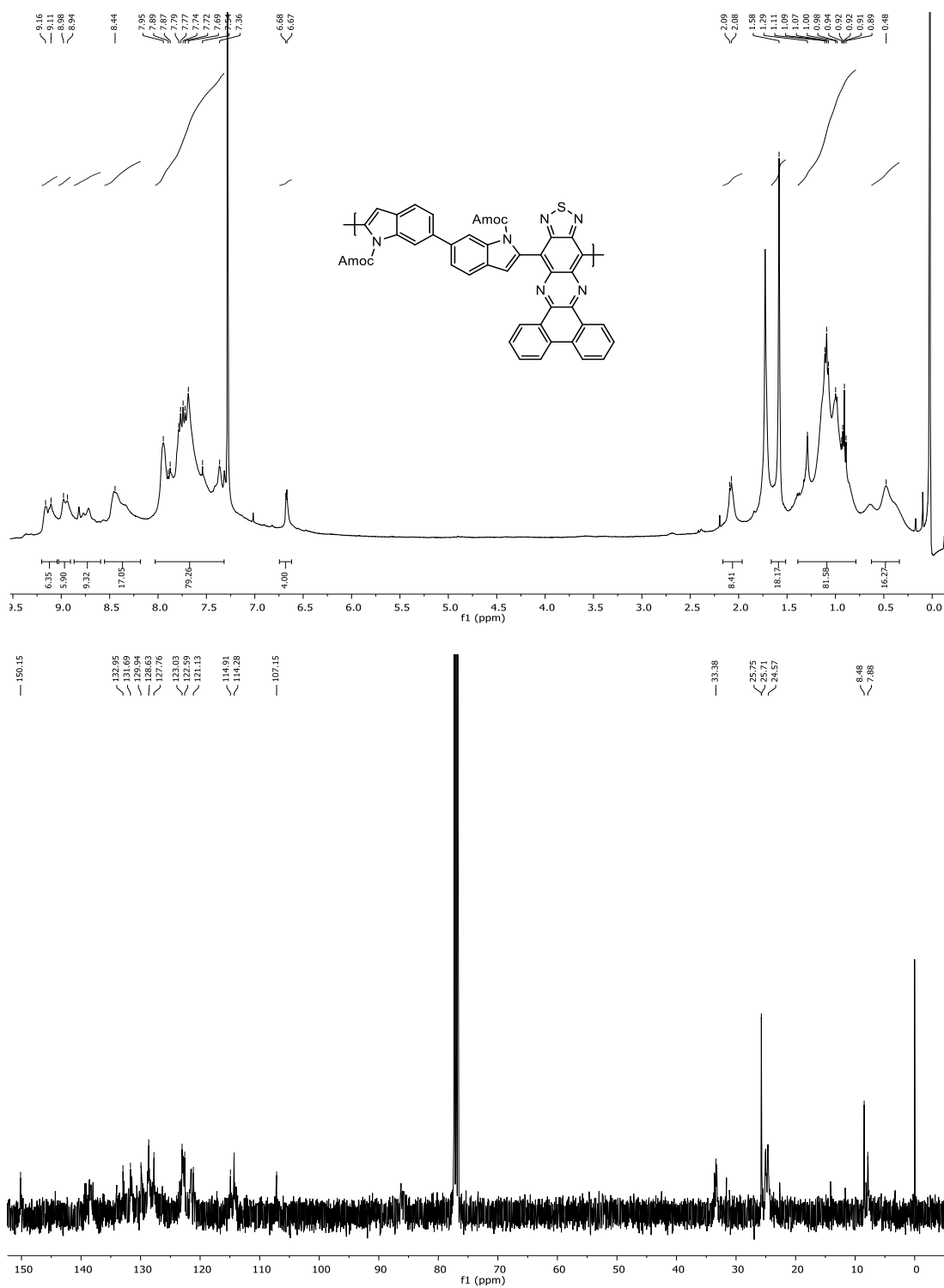


Figure A.49. ^1H NMR (400 MHz, CDCl_3) and ^{13}C NMR (101 MHz, CDCl_3) spectra of polymer BI-BTP.

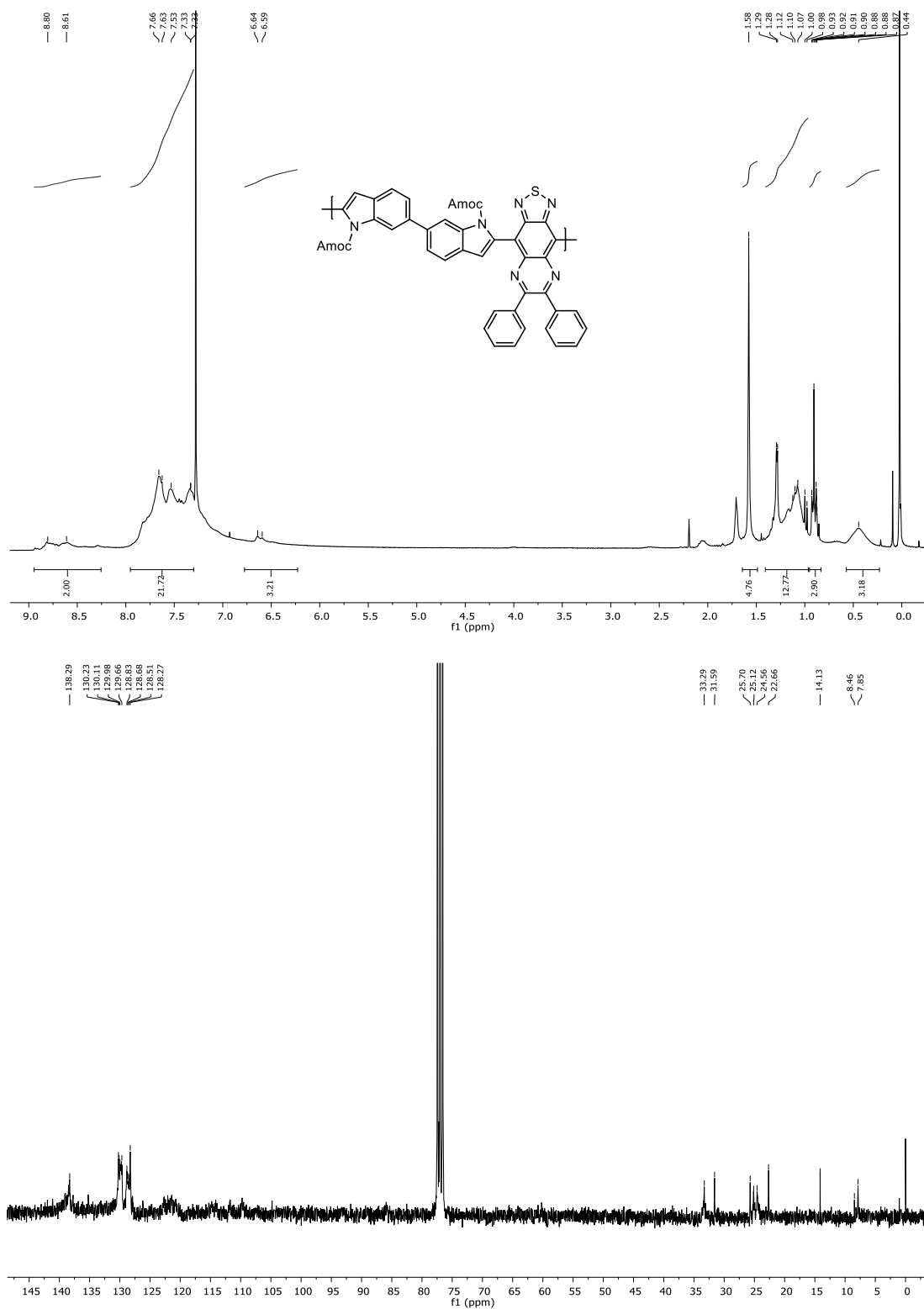


Figure A.50. ^1H NMR (300 MHz, CDCl_3) and ^{13}C NMR (75 MHz, CDCl_3) spectra of polymer BI-DPTQ.

APPENDIX B

IR, Mass spectra and GPC data

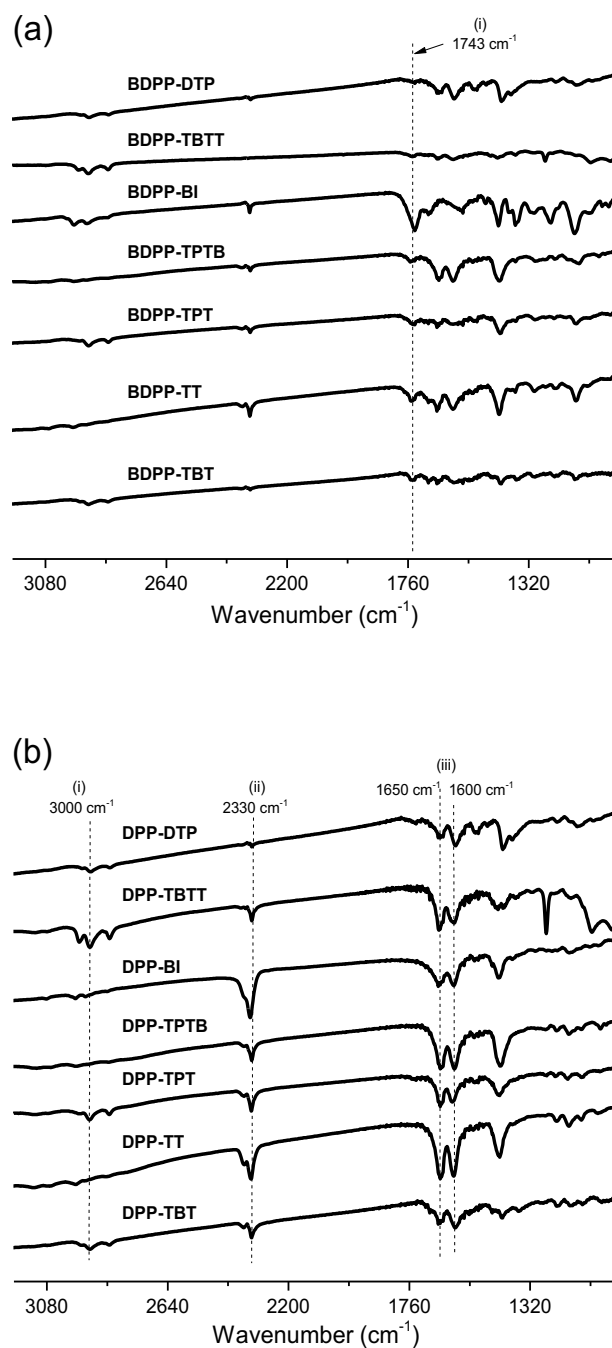


Figure B1. IR spectra of polymers in KBr pellet (a) at room temperature (i) t-BOC ester at 1743 cm⁻¹, (b) after heating at 180 °C (i) increase broadness at 3000 cm⁻¹ for N-H peak (ii) CO₂ trapped in KBr decomposition of t-BOC (iii) increase sharpness of DPP ketone peak.

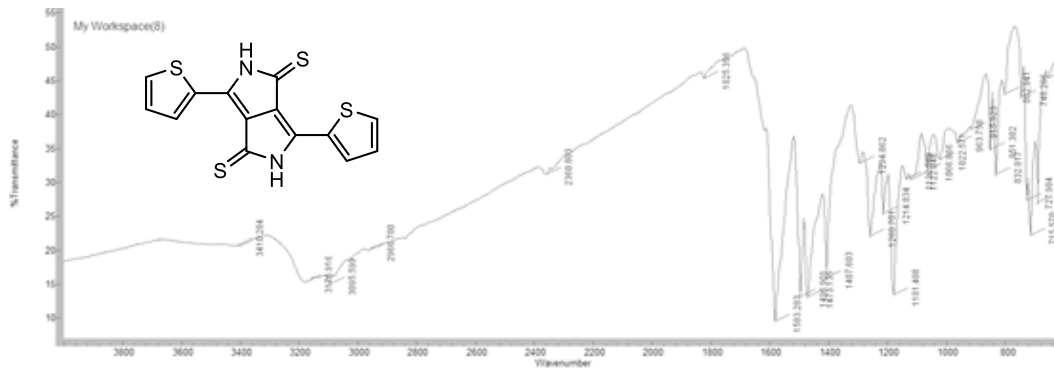


Figure B.2. IR spectrum of DTPP in KBr pellet

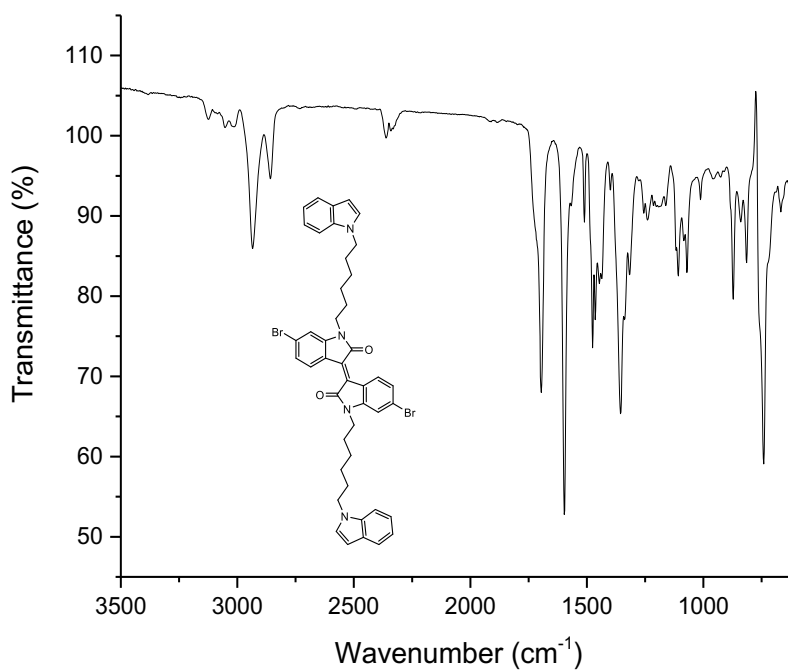


Figure B.3. IR spectrum of (*E*)-1,1'-Bis(6-(1*H*-indol-1-yl)hexyl)-6,6'-dibromo-[3,3'-biindolinylidene]-2,2'-dione (**ii**) on NaCl.

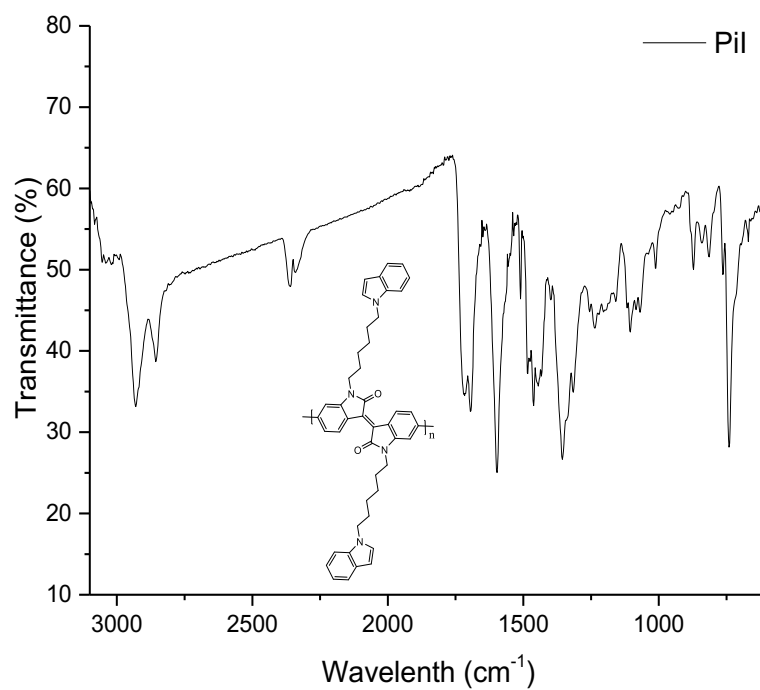


Figure B.4. IR spectrum of polymer **PiI** on NaCl.

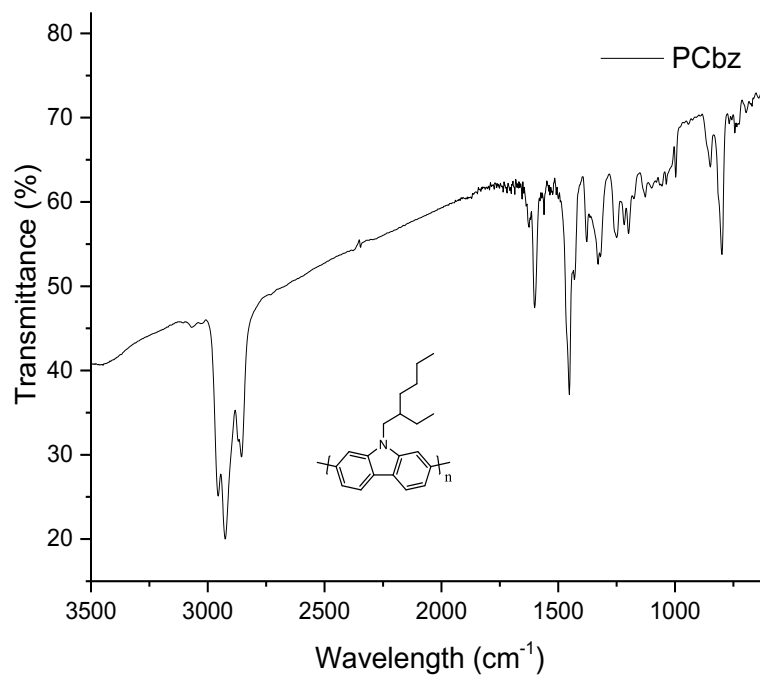


Figure B.5. IR spectrum of polymer **PiI** on NaCl.

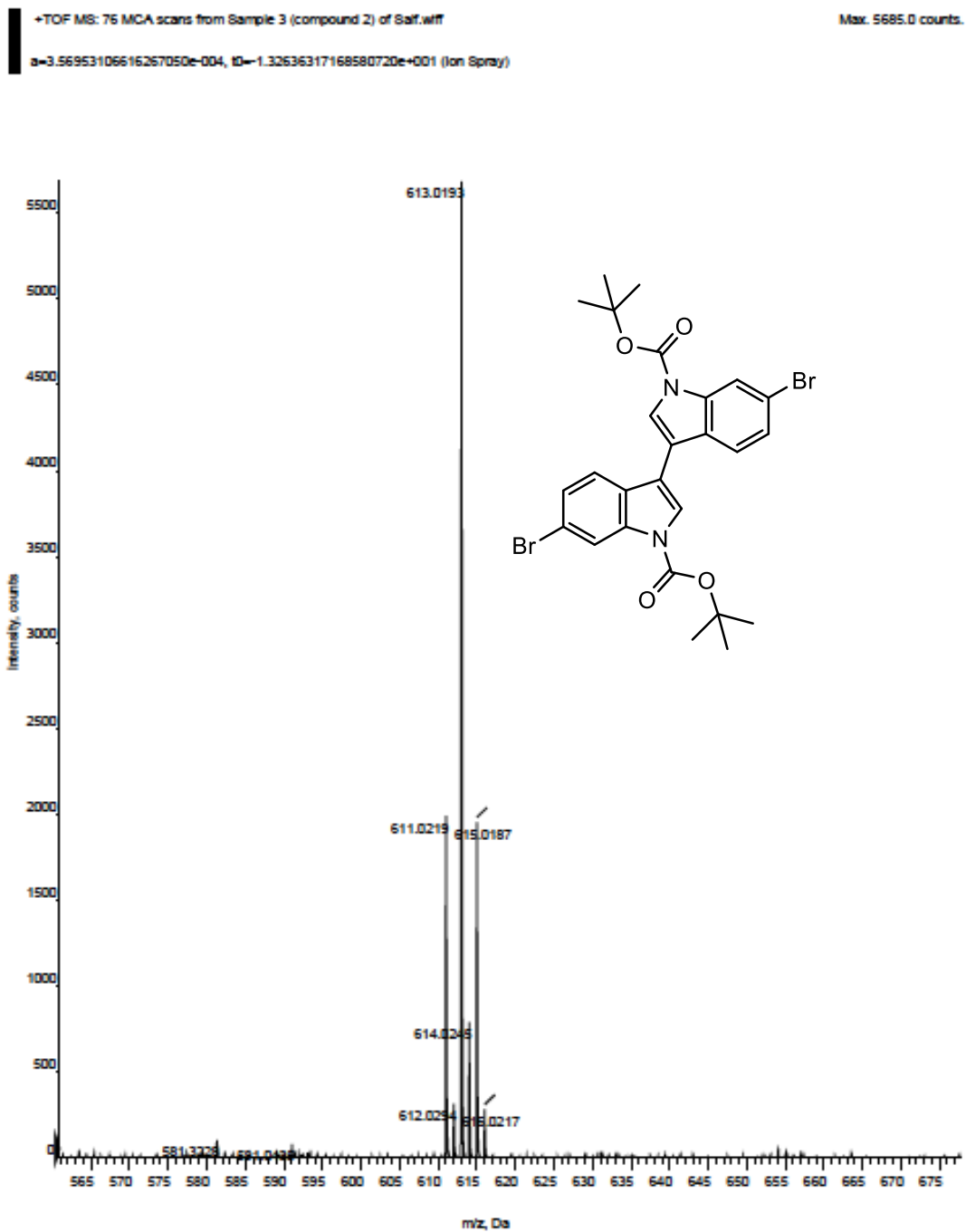


Figure B.6. High resolution mass spectrum of di-*tert*-butyl 6,6'-dibromo-1*H*,1'*H*-[3,3'-biindole]-1,1'-dicarboxylate (**II-9**)

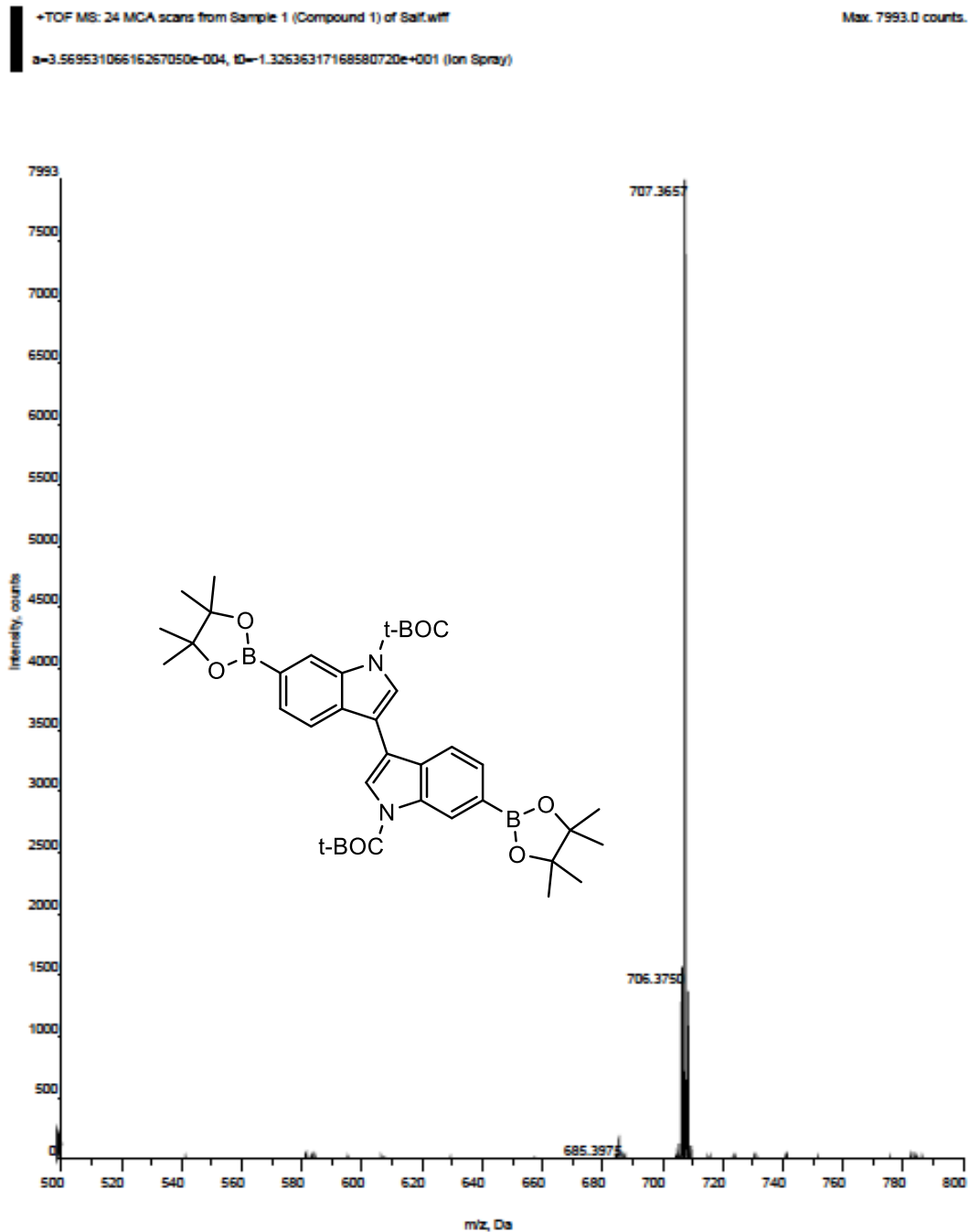


Figure B.7. High resolution mass spectrum of di-*tert*-butyl 6,6'-bis(4,4,5,5-tetramethyl-1,3,2-dioxaborolan-2-yl)-1*H*,1'*H*-[3,3'-biindole]-1,1'-dicarboxylate (**BI**)

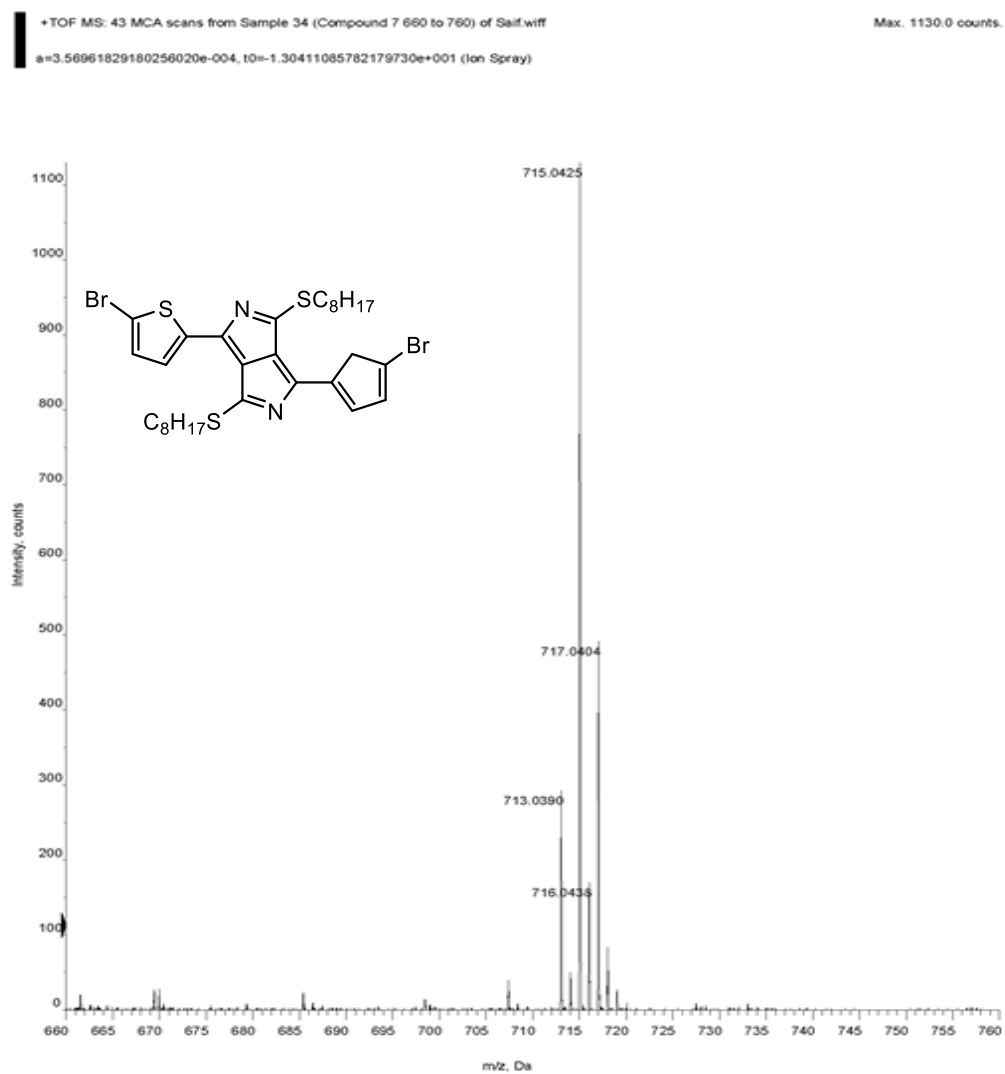


Figure B.8. High resolution mass spectrum of 1,4-bis(5-bromothiophen-2-yl)-3,6-bis(octylthio)pyrrolo[3,4-c]pyrrole (**DAPa**).

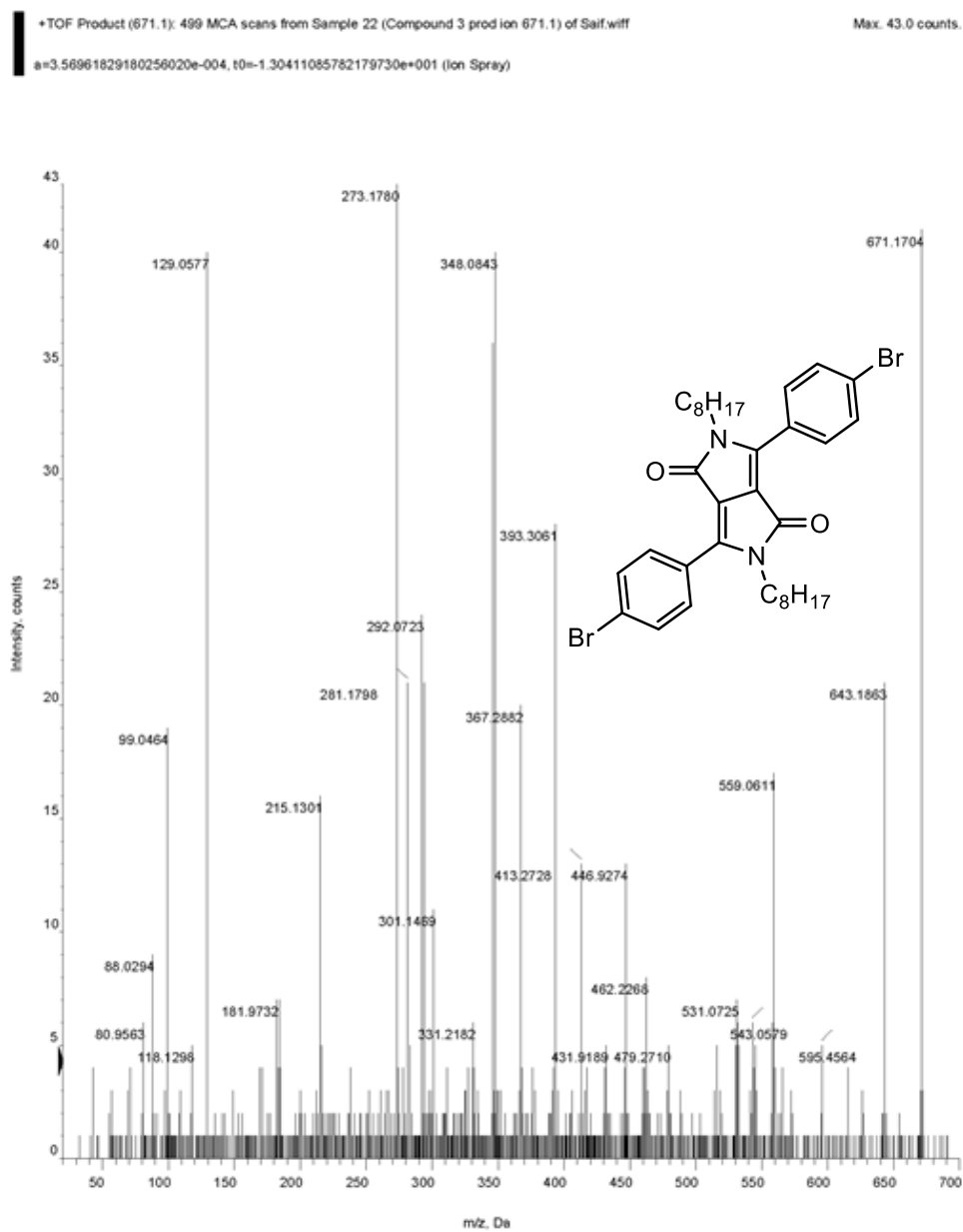


Figure B.9. High resolution mass spectrum of 3,6-bis(4-bromophenyl)-2,5-dioctyl-2,5-dihydropyrrolo[3,4-c]pyrrole-1,4-dione (PDPP).

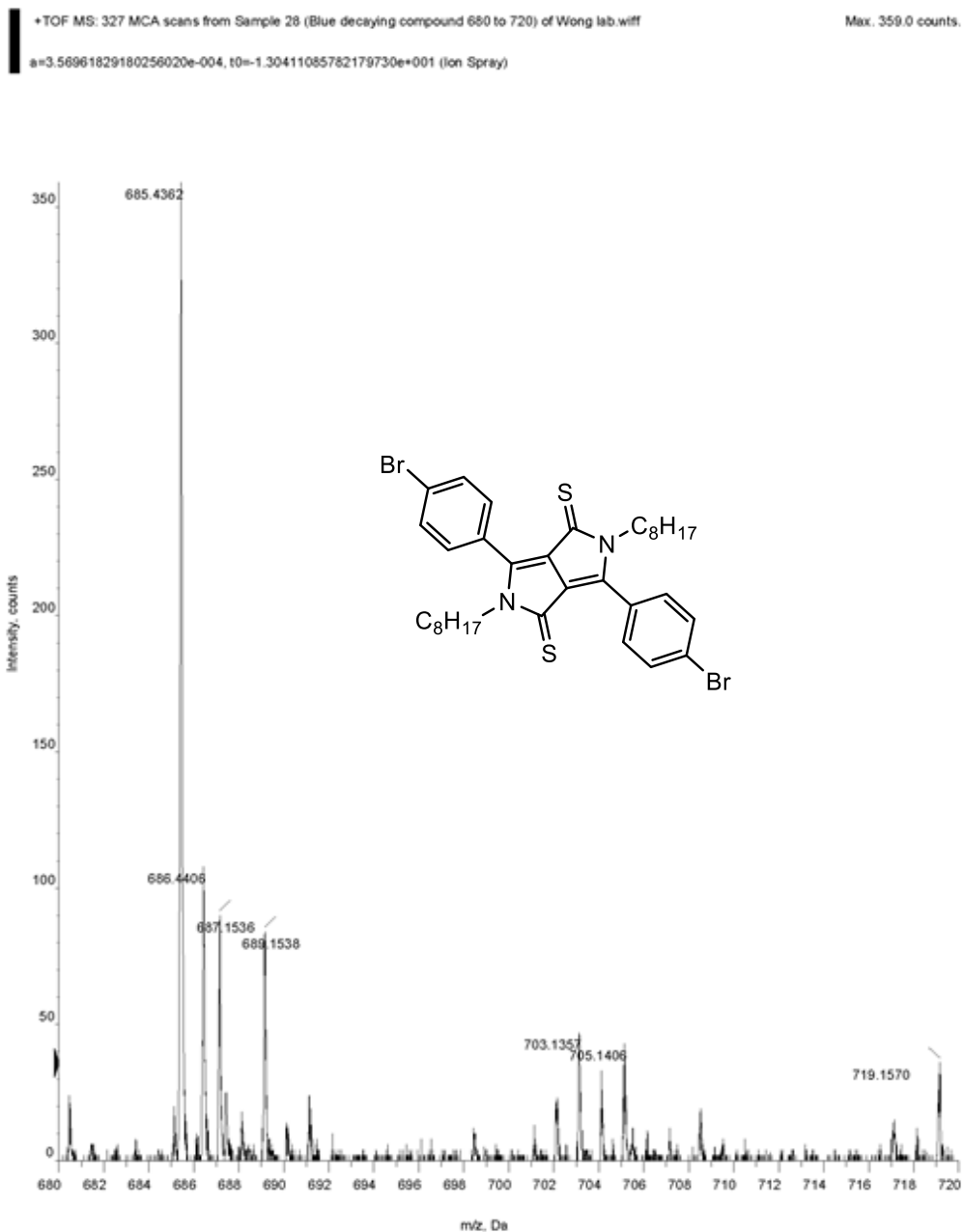


Figure B.10. High resolution mass spectrum of 3,6-bis(4-bromophenyl)-2,5-dioctyl-2,5-dihydropyrrolo[3,4-c]pyrrole-1,4-dithione (**PDTPP**).

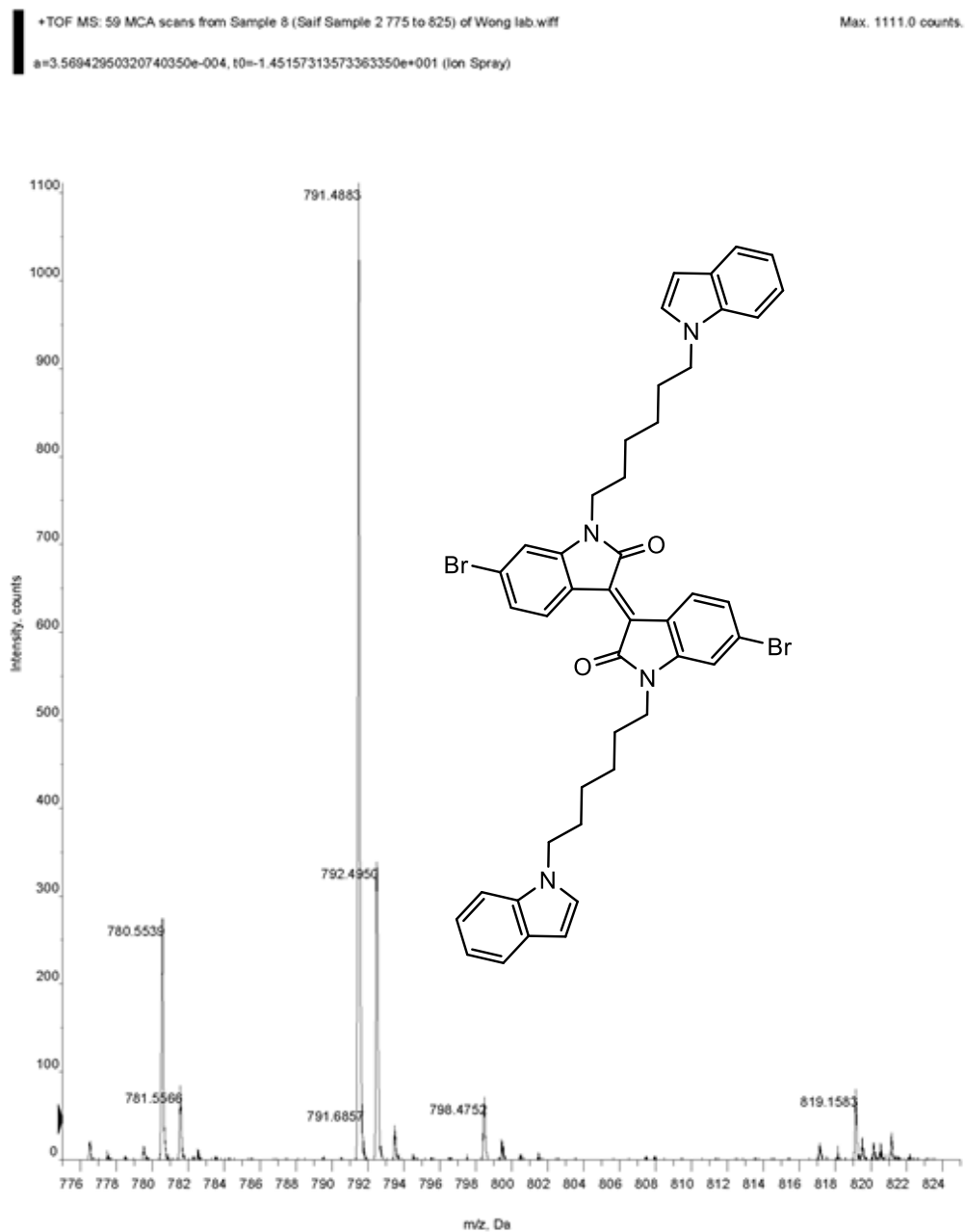


Figure B.11. High resolution mass spectrum of (E)-1-(6-(1'-(6-(1H-indol-1-yl)hexyl)-6,6'-dibromo-2,2'-dioxo-[3,3'-biindolylidene]-1-yl)hexyl)-1H-indol-1-ium (**ii**)

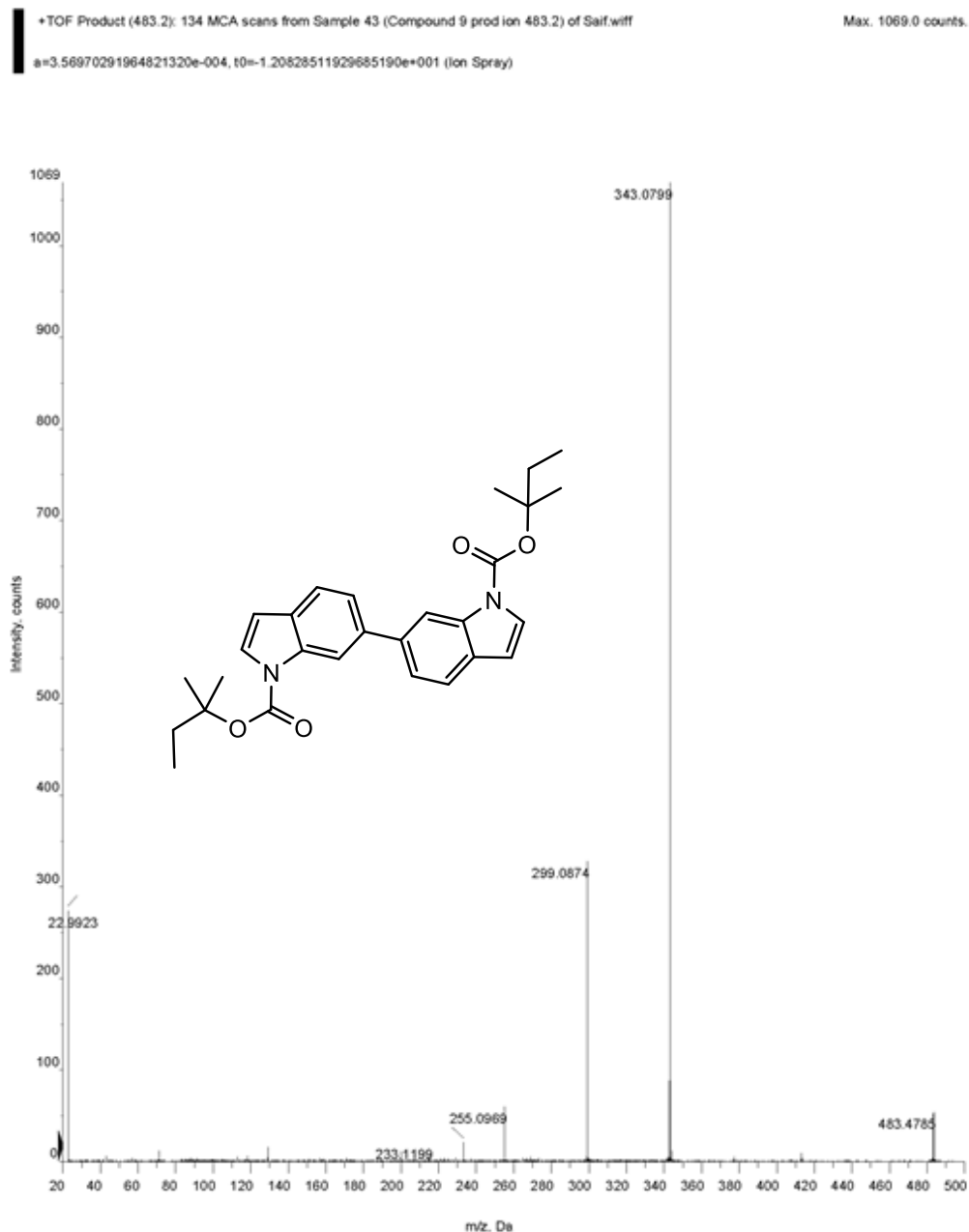


Figure B.12. High resolution mass spectrum of di-*tert*-pentyl 1H,1'H-[6,6'-biindole]-1,1'-dicarboxylate (**V-II**).



GPC 缺省单个报告 报告

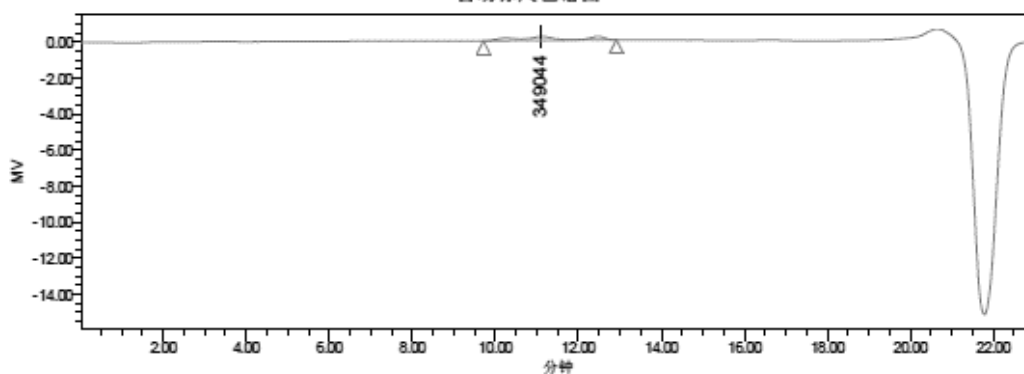
用户名称: Breeze 用户 (Breeze)

项目名称: GPC_Default

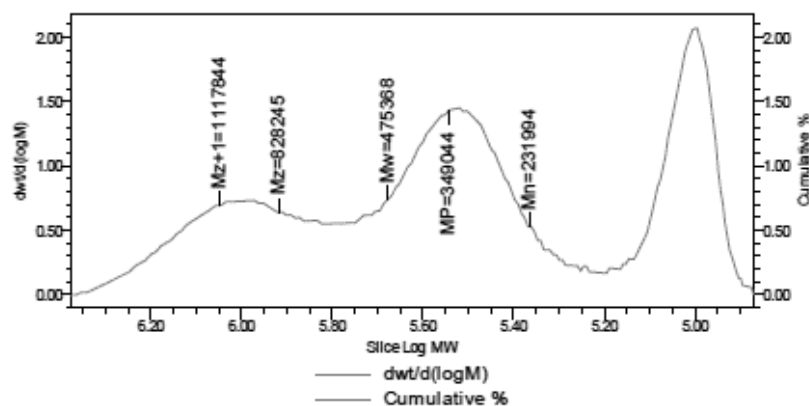
样品信息

样品名称:	p3	采集者:	Breeze
样品类型:	宽分布未知样	采集时间:	2014/10/27 15:17:50 CST
瓶号:	31	采集方法组:	20141009
进样次数:	1	处理日期:	2014/10/29 9:46:33 CST
进样体积:	20.00 ul	处理方法:	1029
运行时间:	23.0 Minutes	通道名称:	410
样品组名称:		处理通道注释:	410

自动标尺色谱图



SampleName p3; Vial 31; Injection 1; Channel 410 ; Date Acquired 2014/10/27 15:17:50 CST



GPC 结果

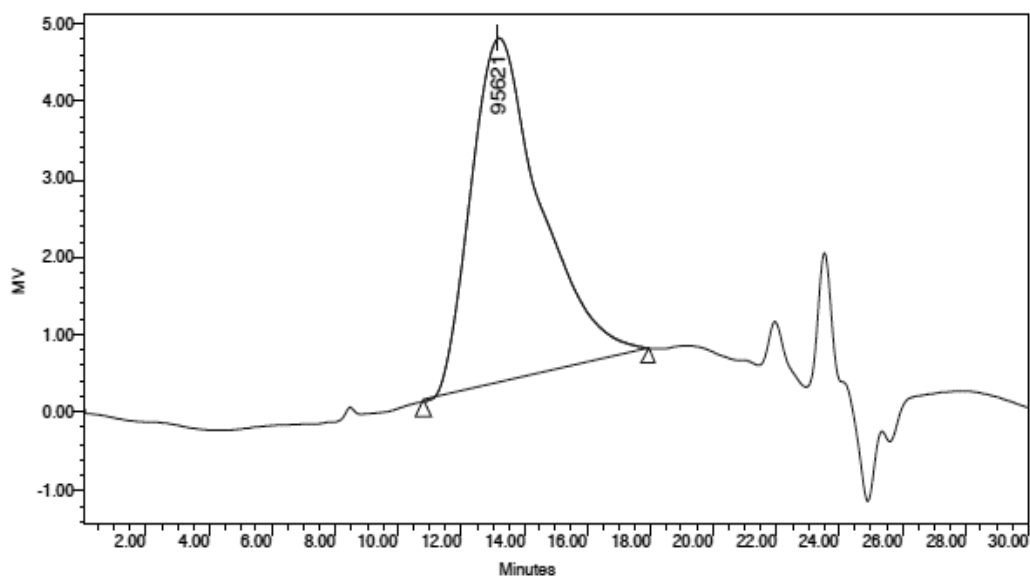
分布名称	Mn	Mw	MP	Mz	Mz+1	Mv	多分散性	MW 标记 1	MW 标记 2
1	231994	475368	349044	828245	1117844		2.049051		

Figure B.13. GPC of polymer BDPP-BT.

Project Name: Defaults
Reported by User: System

SAMPLE INFORMATION			
Sample Name	qj-3	Acquired By :	System
Sample Type	Broad Unknown	Date Acquired :	2014-5-5 22:08:00
Vial:	7	Acq. Method:	GPC20130613
Injection #:	1	Date Processed :	2014-5-12 18:01:08
Injection Volume:	10.00 ul	Channel Name:	410
Run Time	30.00 Minutes	Channel Desc.:	RI Detector
Column Type		Sample Set Name	w

Broad Unknown Relative Chromatogram



Broad Unknown Relative Peak Table

Distribution Name	Mn (Daltons)	Mw (Daltons)	MP (Daltons)	Mz (Daltons)	Mz+1 (Daltons)	Polydispersity	Mz/Mw	Mz+1/Mw
1	49869	103617	95621	186278	286555	2.077763	1.797755	2.765531

Figure B.14. GPC of polymer BDPP-TBT



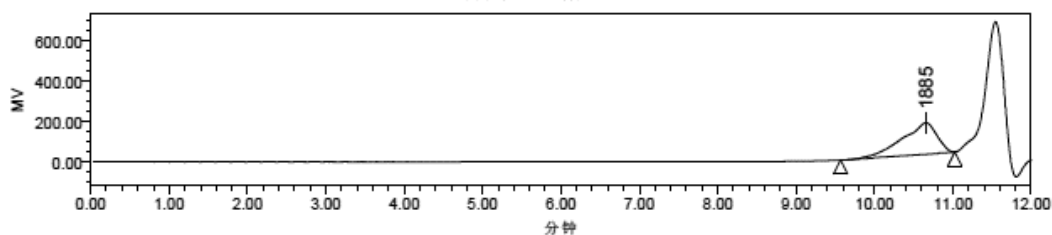
用户名称: System

项目名称: yjw 2011

样品信息

样品名称:	qj-2	采集者:	System
样品类型:	宽分布未知样	采集时间:	2014-8-28 18:07:40
瓶号:	24	采集方法组:	20110724 w 410
进样次数:	1	处理日期:	2014-8-28 18:23:53
进样体积:	50.00 ul	处理方法:	20120726
运行时间:	12.0 Minutes	通道名称:	410
样品组名称:	140828	处理通道注释:	

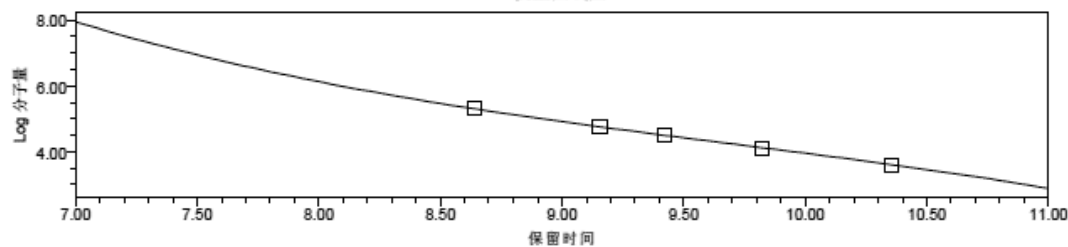
自动标尺色谱图



GPC 结果

	Mn (道尔顿)	Mw (道尔顿)	MP	多分散性	总面积	保留时间 (分钟)
1	2267	3077	1885	1.357012	4802558	10.659

GPC 校正曲线图



GPC 校正表

	分子量 (道尔顿)	保留时间 (分钟)	计算 重量 (道尔顿)	% 残留
1	197000	8.641	196595	0.206
2	55100	9.156	55945	-1.511
3	31400	9.424	30730	2.179
4	12800	9.823	12929	-0.999
5	3950	10.355	3943	0.165

$$\text{方程 } \text{Log 分子量} = 6.81e+001 - 1.79e+001 T^*1 + 1.74e+000 T^*2 - 5.99e-002 T^*3$$

R 0.999954

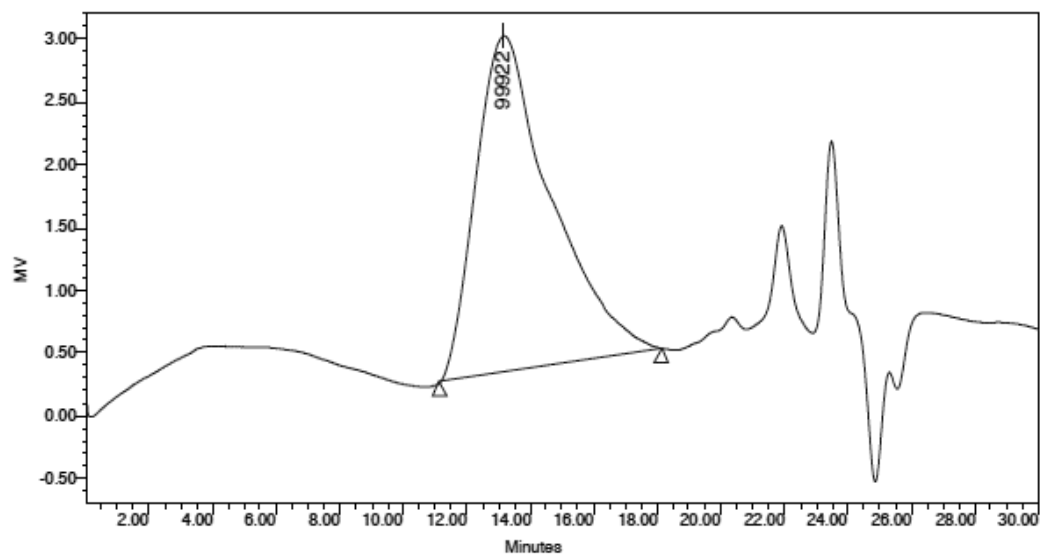
Figure B.15. GPC of polymer BDPP-TPTa.

Project Name: Defaults
Reported by User: System



SAMPLE INFORMATION			
Sample Name	qj-4	Acquired By :	System
Sample Type	Broad Unknown	Date Acquired :	2014-5-5 22:42:03
Vial:	8	Acq. Method:	GPC 20130613
Injection #:	1	Date Processed :	2014-5-12 18:01:12
Injection Volume:	10.00 ul	Channel Name:	410
Run Time	30.00 Minutes	Channel Desc.:	RI Detector
Column Type		Sample Set Name	w

Broad Unknown Relative Chromatogram



Broad Unknown Relative Peak Table

Distribution Name	Mn (Daltons)	Mw (Daltons)	MP (Daltons)	Mz (Daltons)	Mz+1 (Daltons)	Polydispersity	Mz/Mw	Mz+1/Mw
1	44560	100028	99922	185263	282468	2.244814	1.852112	2.823884

Figure B.16. GPC of polymer BDPP-TPTB



用户名称: System

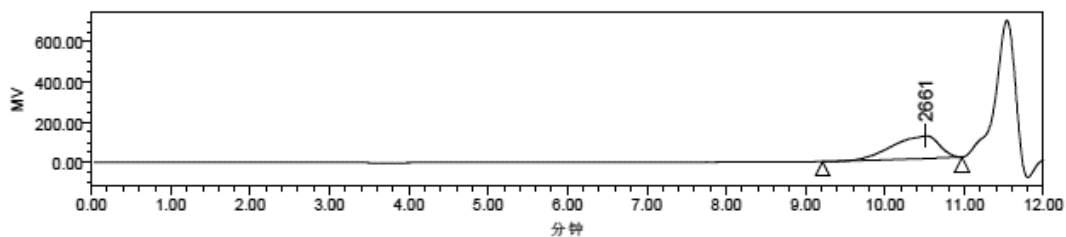
项目名称: yjw 2011

GPC 报告

样品信息

样品名称:	qj-7	采集者:	System
样品类型:	宽分布未知样	采集时间:	2014-8-28 18:43:47
瓶号:	26	采集方法组:	20110724 w 410
进样次数:	1	处理日期:	2014-8-28 19:01:51
进样体积:	50.00 ul	处理方法:	20120726
运行时间:	12.0 Minutes	通道名称:	410
样品组名称:	140828	处理通道注释:	

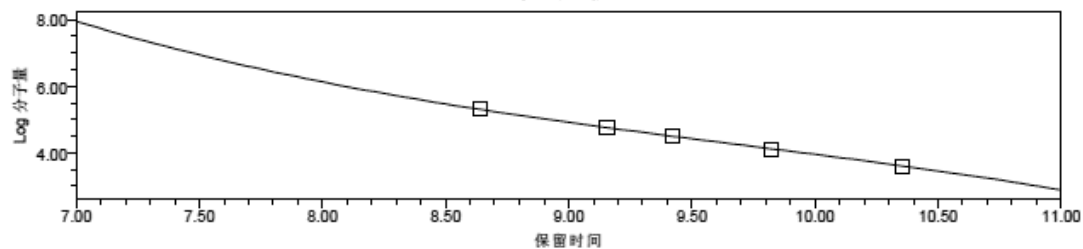
自动标尺色谱图



GPC 结果

	Mn (道尔顿)	Mw (道尔顿)	MP	多分散性	总面积	保留时间 (分钟)
1	3348	4838	2661	1.444969	4612866	10.520

GPC 校正曲线图



GPC 校正表

	分子量 (道尔顿)	保留 时间 (分钟)	计算 重量 (道尔顿)	% 残留
1	197000	8.641	196595	0.208
2	55100	9.156	55945	-1.511
3	31400	9.424	30730	2.179
4	12800	9.823	12929	-0.999
5	3950	10.355	3943	0.165

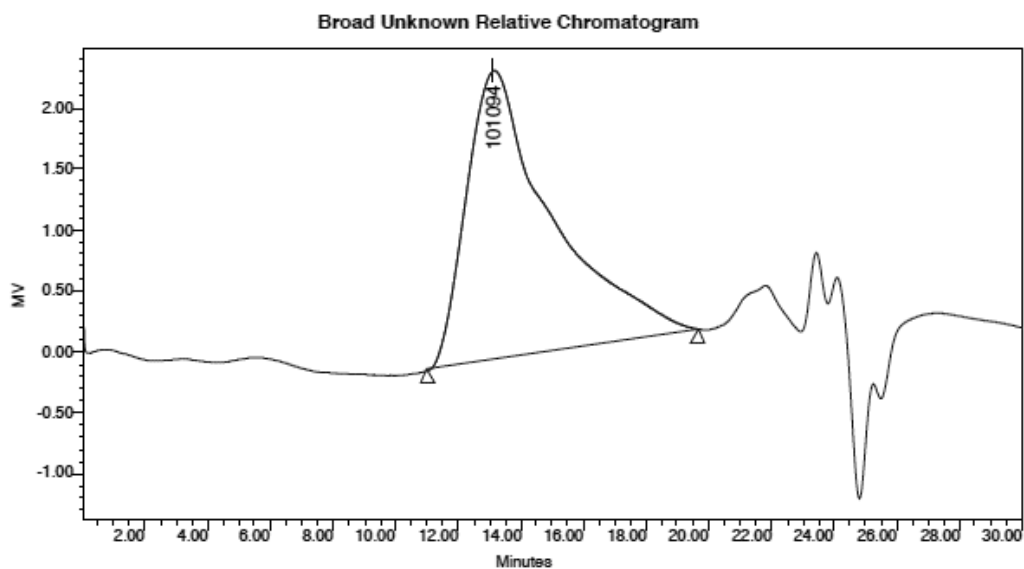
$$\text{方程 Log 分子量} = 6.81e+001 - 1.79e+001 T^1 + 1.74e+000 T^2 - 5.99e-002 T^3$$

R 0.999954

Figure B.17. GPC of polymer BDPP-TBTT

Project Name: Defaults
Reported by User: System

SAMPLE INFORMATION			
Sample Name	qj-5	Acquired By :	System
Sample Type	Broad Unknown	Date Acquired :	2014-5-5 23:21:02
Vial	9	Acq. Method:	GPC20130613
Injection #:	1	Date Processed :	2014-5-12 18:01:19
Injection Volume:	10.00 ul	Channel Name:	410
Run Time	30.00 Minutes	Channel Desc.:	RI Detector
Column Type		Sample Set Name:	w



Broad Unknown Relative Peak Table

Distribution Name	Mn (Daltons)	Mw (Daltons)	MP (Daltons)	Mz (Daltons)	Mz+1 (Daltons)	Polydispersity	Mz/Mw	Mz+1/Mw
1	26333	90497	101094	188112	292957	3.436705	2.078651	3.237194

Figure B.18. GPC of polymer **BDPP-BI**.



GPC 缺省单个报告 报告

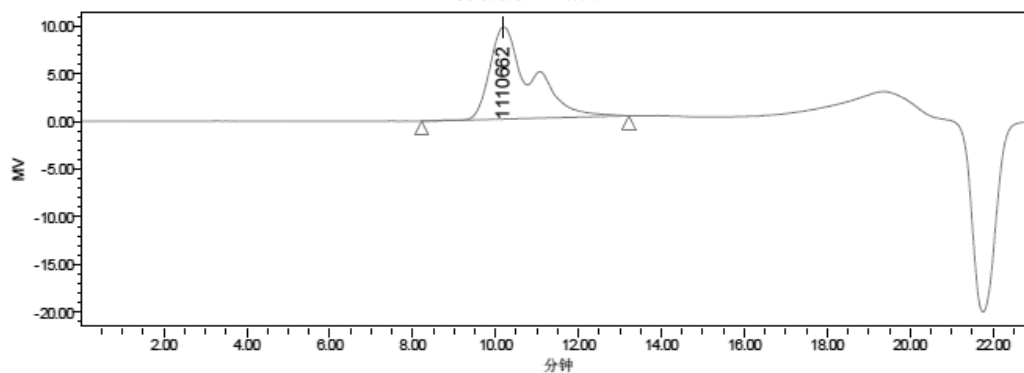
用户名称: Breeze 用户 (Breeze)

项目名称: GPC_Default

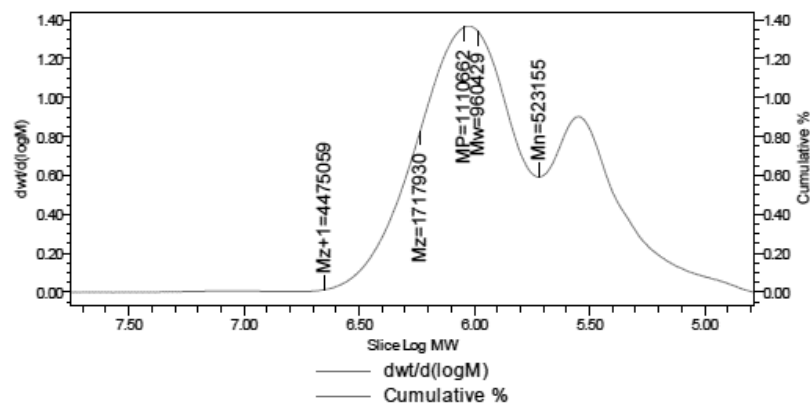
样品信息

样品名称:	p12	采集者:	Breeze
样品类型:	宽分布未知样	采集时间:	2014/10/27 16:02:26 CST
瓶号:	32	采集方法组:	20141009
进样次数:	1	处理日期:	2014/10/29 9:44:50 CST
进样体积:	20.00 ul	处理方法:	1029
运行时间:	23.0 Minutes	通道名称:	410
样品组名称:		处理通道注释:	410

自动标尺色谱图



— SampleName p12; Vial 32; Injection 1; Channel 410 ; Date Acquired 2014/10/27 16:02:26 CST



GPC 结果

分布名称	Mn	Mw	MP	Mz	Mz+1	Mv	多分散性	MW 标记 1	MW 标记 2
1	523155	960429	1110662	1717930	4475059		1.835840		

Figure B.19. GPC of polymer DAPb-DTP.



GPC 缺省单个报告 报告

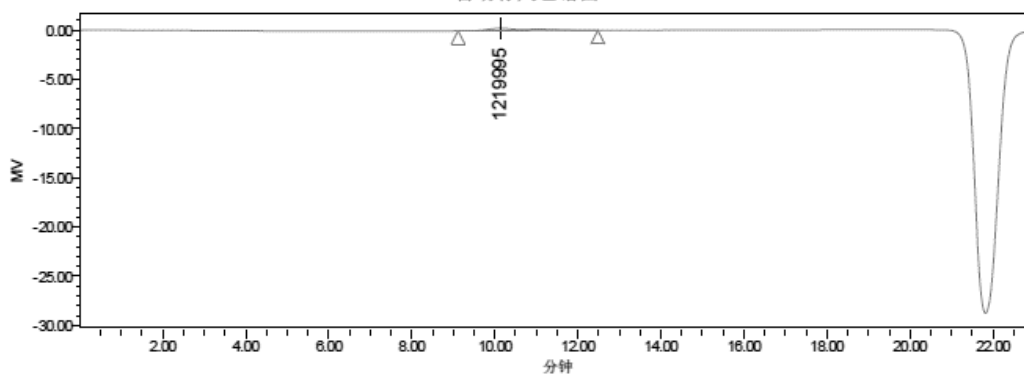
用户名称: Breeze 用户 (Breeze)

项目名称: GPC_Default

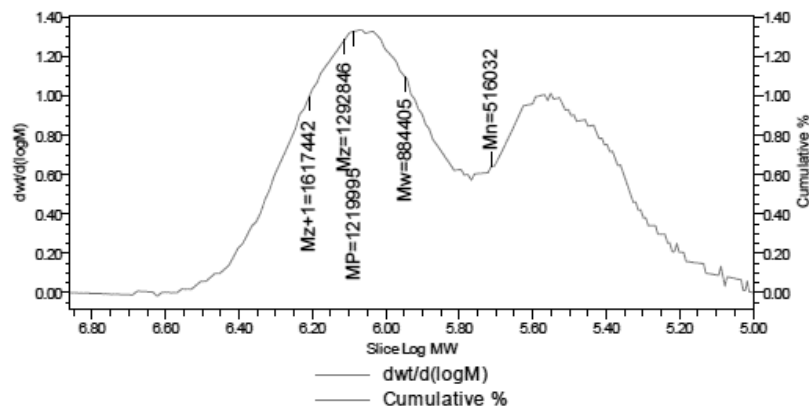
样品信息

样品名称:	p13	采集者:	Breeze
样品类型:	宽分布未知样	采集时间:	2014/10/27 16:39:45 CST
瓶号:	33	采集方法组:	20141009
进样次数:	1	处理日期:	2014/10/29 9:42:28 CST
进样体积:	20.00 ul	处理方法:	1029
运行时间:	23.0 Minutes	通道名称:	410
样品组名称:		处理通道注释:	410

自动标尺色谱图



— SampleName p13; Vial 33; Injection 1; Channel 410 ; Date Acquired 2014/10/27 16:39:45 CST



GPC 结果

分布名称	Mn	Mw	MP	Mz	Mz+1	Mv	多分散性	MW 标记 1	MW 标记 2
1	516032	884405	1219995	1292846	1617442		1.713857		

Figure B.20. GPC of polymer DAPa-TBTT.



GPC 缺省单个报告 报告

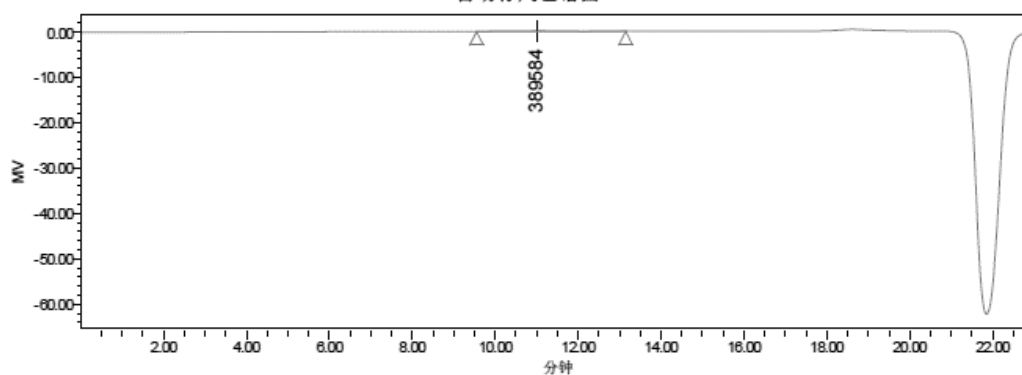
用户名称: Breeze 用户 (Breeze)

项目名称: GPC_Default

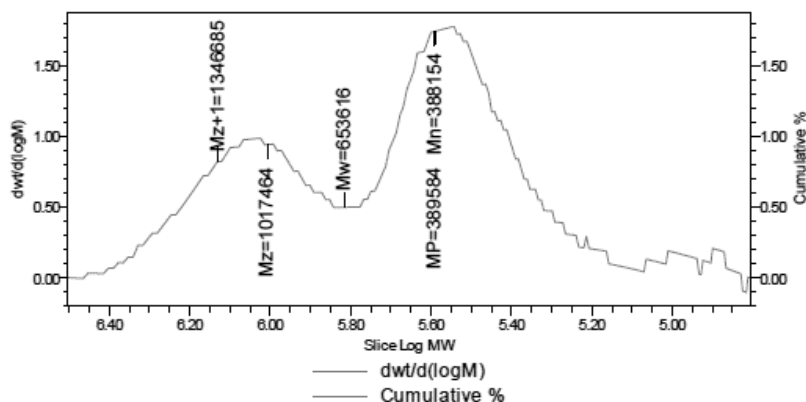
样品信息

样品名称:	p14	采集者:	Breeze
样品类型:	宽分布未知样	采集时间:	2014/10/28 9:59:29 CST
瓶号:	34	采集方法组:	20141009
进样次数:	1	处理日期:	2014/10/29 9:27:59 CST
进样体积:	20.00 ul	处理方法:	1029
运行时间:	23.0 Minutes	通道名称:	410
样品组名称:		处理通道注释:	410

自动标尺色谱图



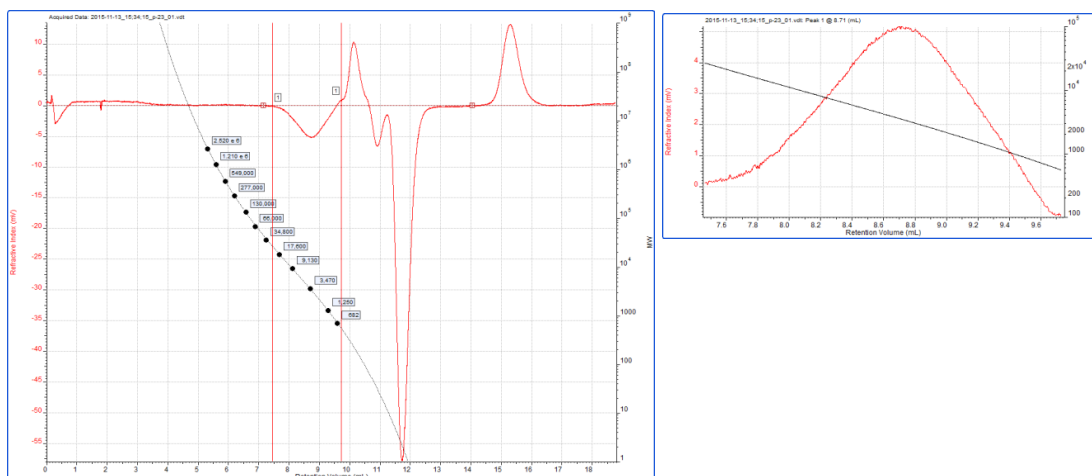
SampleName p14; Vial 34; Injection 1; Channel 410 ; Date Acquired 2014/10/28 9:59:29 CST



GPC 结果

分布名称	Mn	Mw	MP	Mz	Mz+1	Mv	多分散性	MW标记 1	MW标记 2
1	388154	653616	389584	1017464	1346685		1.683910		

Figure B.21. GPC of polymer DAPa-BI.



Data File: 2015-11-13_15:34:15_p-23_01.vdt Method:
PS_Calibration_01302015-0005.vcm

Peak RV - (ml) 8.705
Mn - (Daltons) 3,328
Mw - (Daltons) 4,773
Mz - (Daltons) 7,232
Mp - (Daltons) 3,480
Mw / Mn 1.434
Percent Above Mw: 0 100.000
Percent Below Mw: 0 0.000
Mw 10.0% Low 1,480
Mw 10.0% High 12,876
Wt Fr (Peak) 1.000
RI Area - (mVml) 5.23
UV Area - (mVml) 0.00

Annotation

Method File Unsaved Method (PS_Calibration_01302015-0005.vcm)

Limits File

Date Acquired Nov 13, 2015 - 15:34:15

Solvent TCB w 500ppm BHT

Acquisition Operator admin : Administrator

Calculation Operator admin : Administrator

Column Set Jordi Mixed Bed

System System 1

Flow Rate - (ml/min) 0.750

Inj Volume - (ul) 200.0

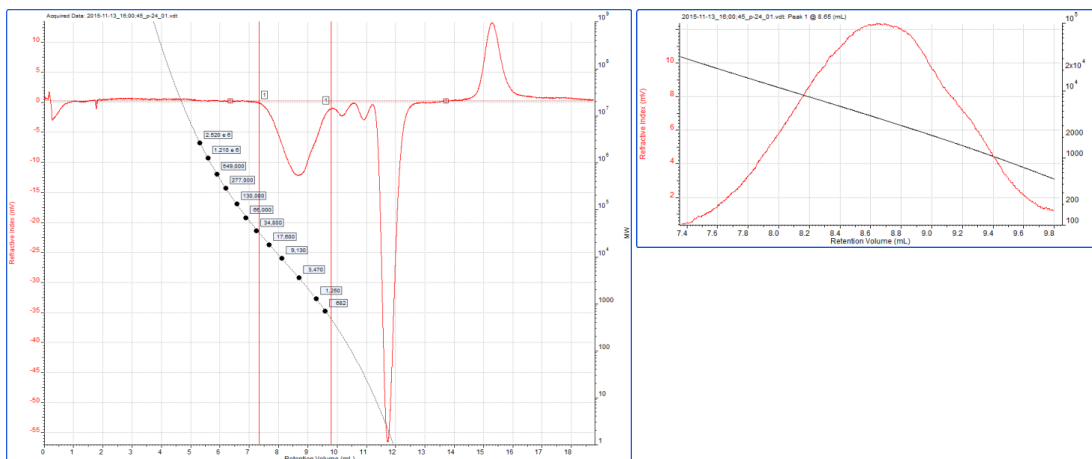
Volume Increment - (ml) 0.00250

Detector Temp. - (deg C) 140.0

Column Temp. - (deg C) 140.0

OmniSEC Build Number 406

Figure B.22. GPC of polymer **BI-BTP**.



Data File: 2015-11-13_16:00:45_p-24_01.vdt Method: PS_Calibration_01302015-0005.vcm

Peak RV - (ml) 8.648
 Mn - (Daltons) 2,752
 Mw - (Daltons) 5,221
 Mz - (Daltons) 8,998
 Mp - (Daltons) 3,818
 Mw / Mn 1.897
 Percent Above Mw: 0 100.000
 Percent Below Mw: 0 0.000
 Mw 10.0% Low 937
 Mw 10.0% High 15,635
 Wt Fr (Peak) 1.000
 RI Area - (mVml) 15.81
 UV Area - (mVml) 0.00
 Annotation
 Method File Unsaved Method (PS_Calibration_01302015-0005.vcm)
 Limits File
 Date Acquired Nov 13, 2015 - 16:00:45
 Solvent TCB w 500ppm BHT
 Acquisition Operator admin : Administrator
 Calculation Operator admin : Administrator
 Column Set Jordi Mixed Bed
 System System 1
 Flow Rate - (ml/min) 0.750
 Inj Volume - (ul) 200.0
 Volume Increment - (ml) 0.00250
 Detector Temp. - (deg C) 140.0
 Column Temp. - (deg C) 140.0
 OmniSEC Build Number 406

Figure B.23. GPC of polymer **BI-DPTQ**.

APPENDIX C

Thermal and electrochemical data

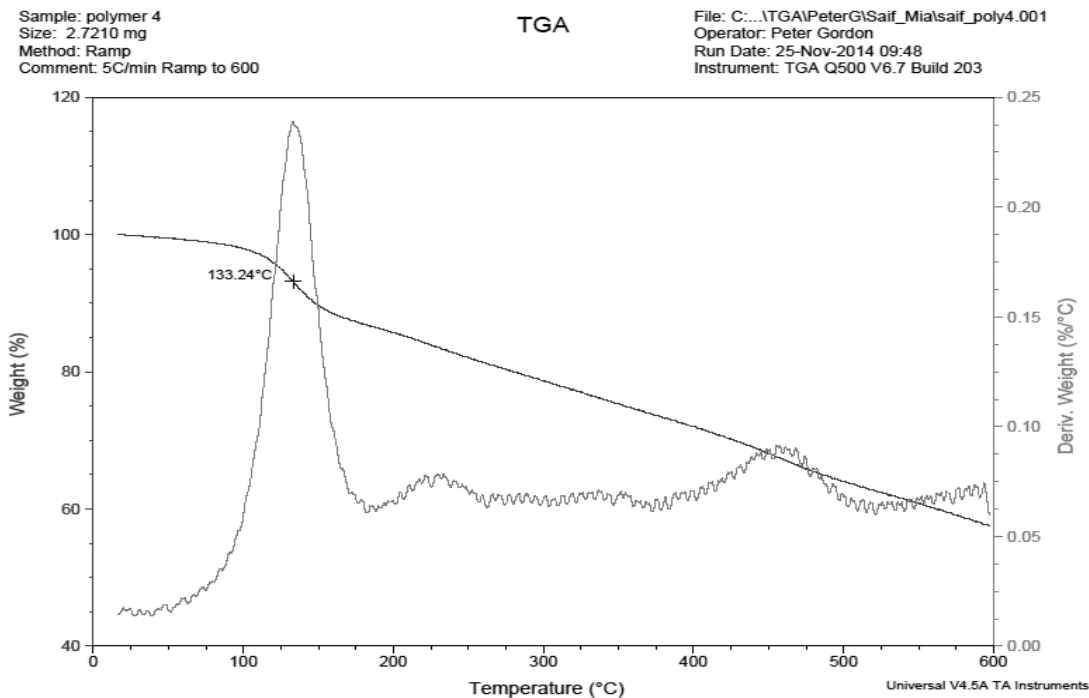


Figure C.1. TGA of polymer **BDPP-TPTB**.

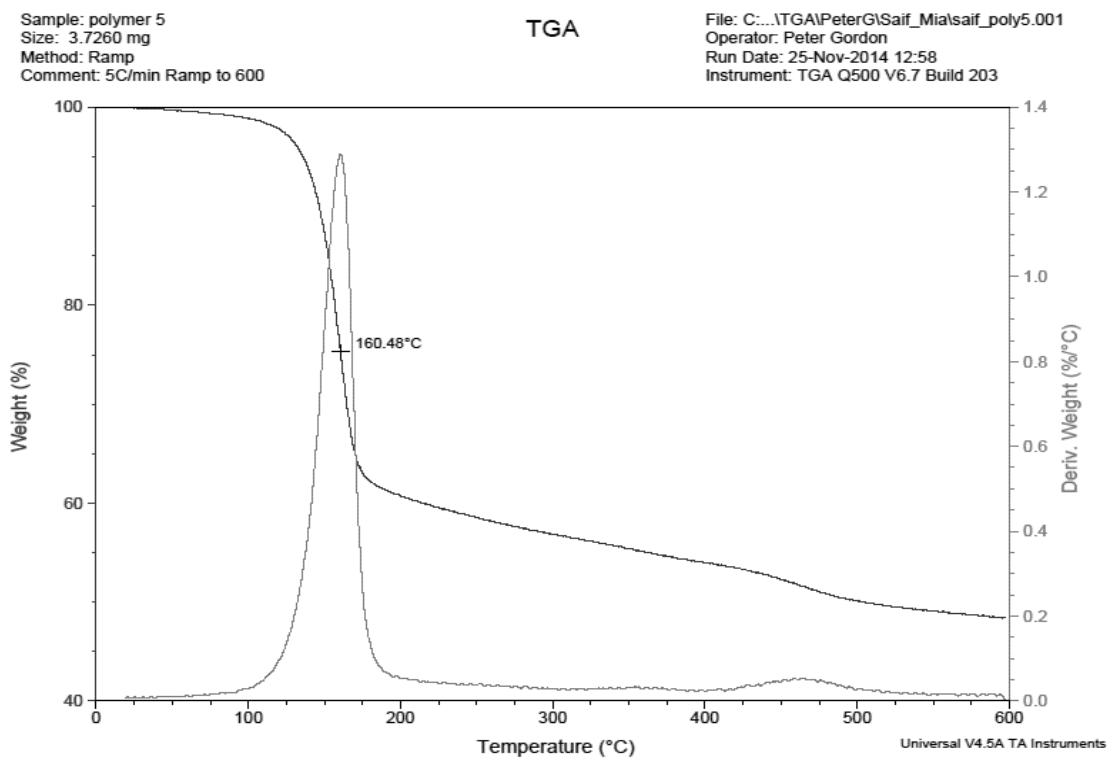


Figure C.2. TGA of polymer **BDPP-BI**.

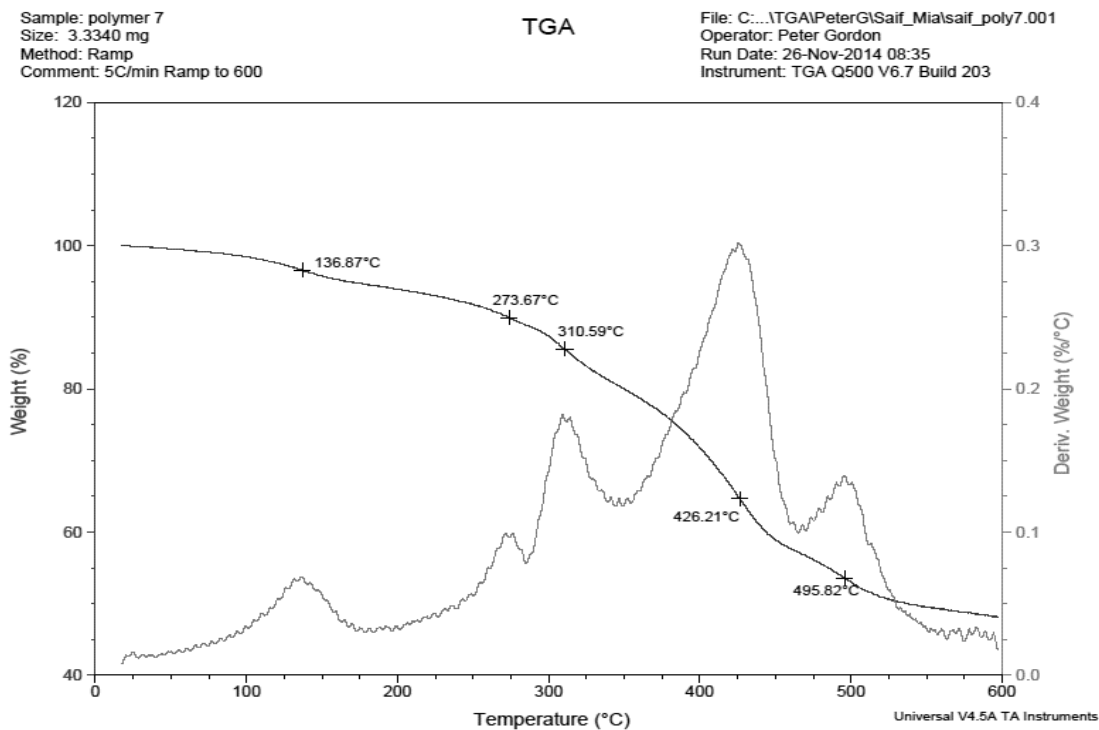


Figure C.3. TGA of polymer **BDPP-TBTT**.

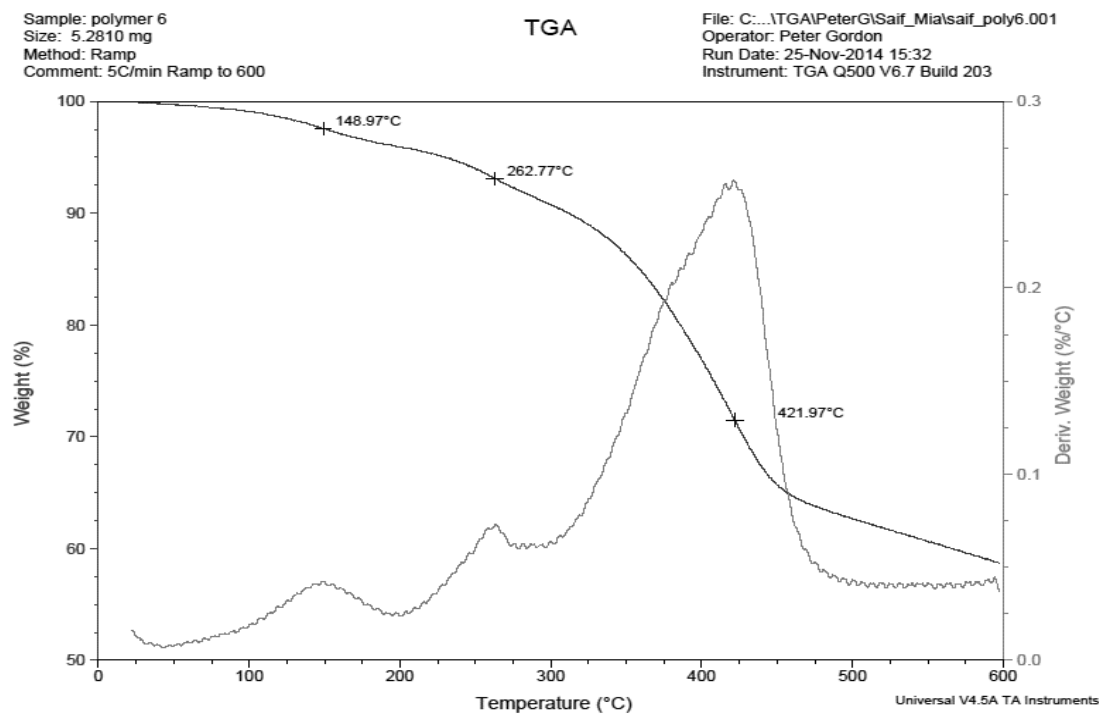
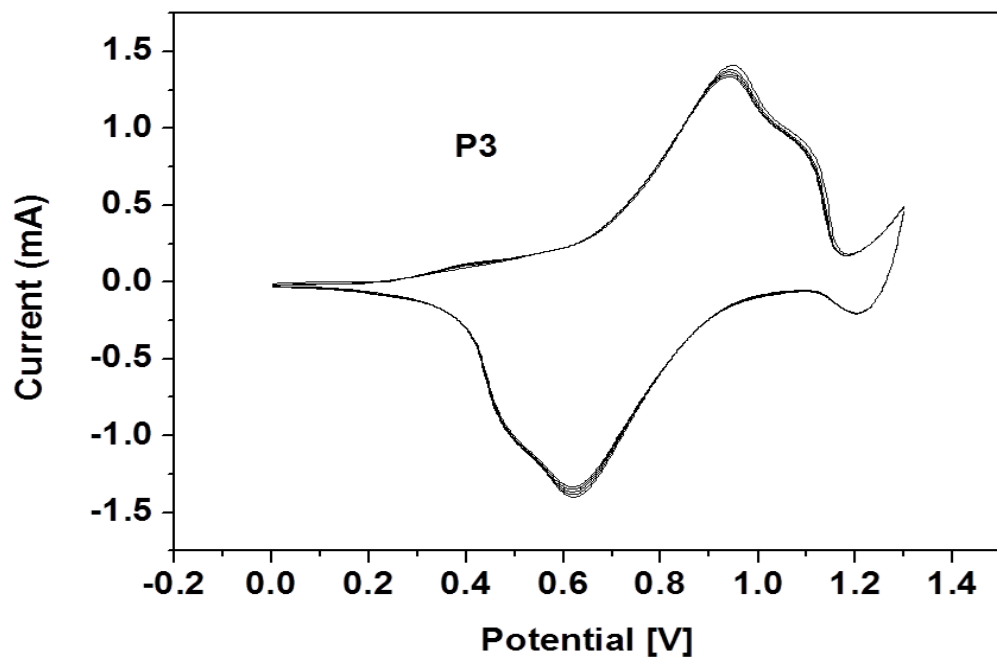
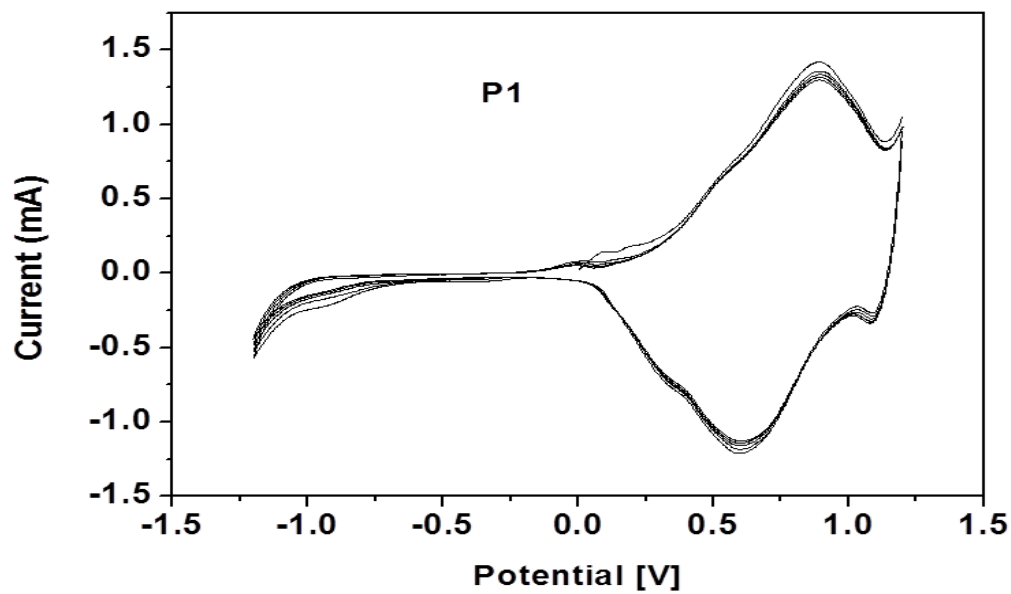


Figure C.4. TGA of polymer **BDPP-DTPa**.



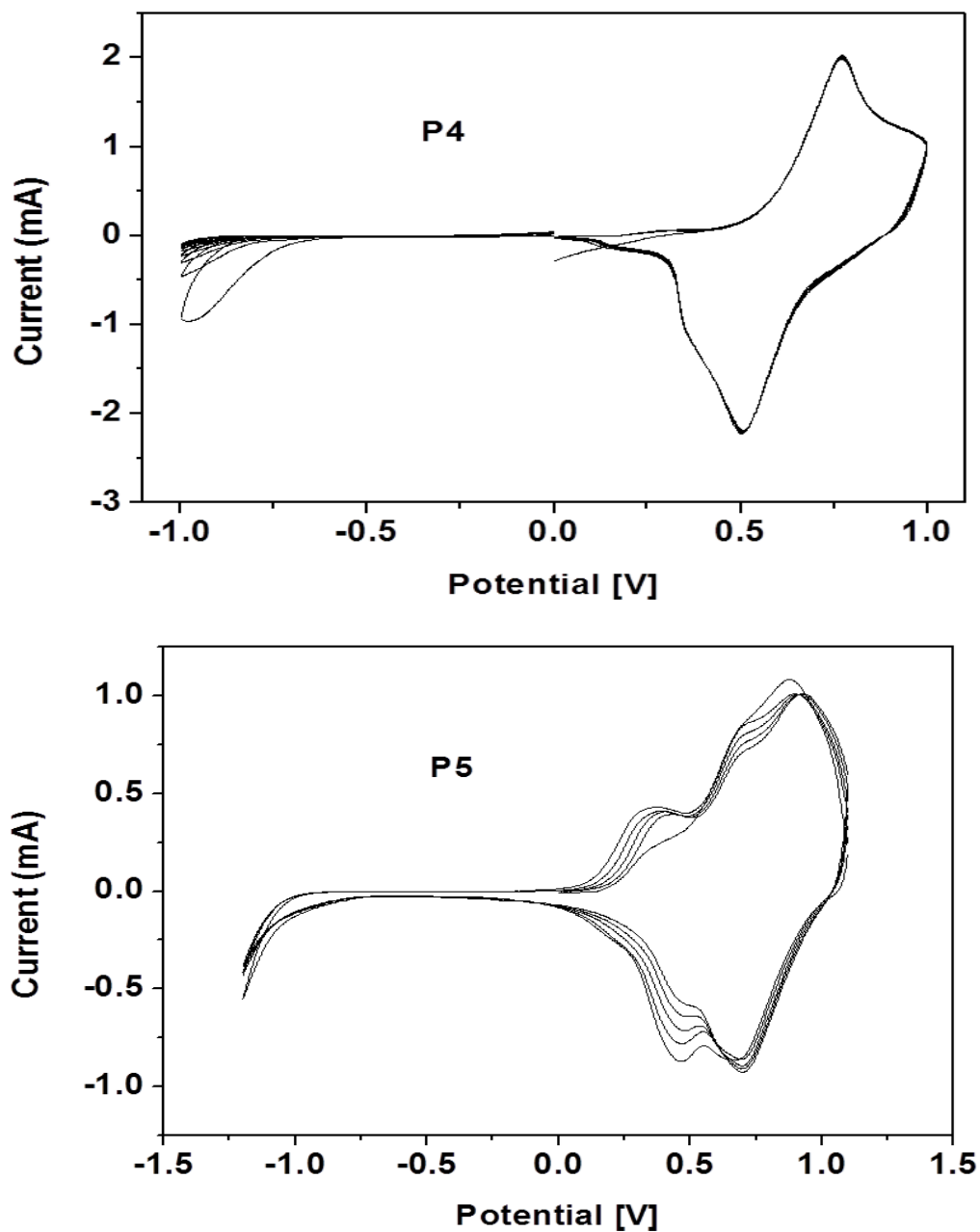


Figure C.5: Cyclic voltammetric diagrams of polymers **P1**, **P3-P5** films on an ITO-coated glass substrate in CH_3CN solutions containing 0.1 M Et_4NClO_4 .

APPENDIX D

Film Properties

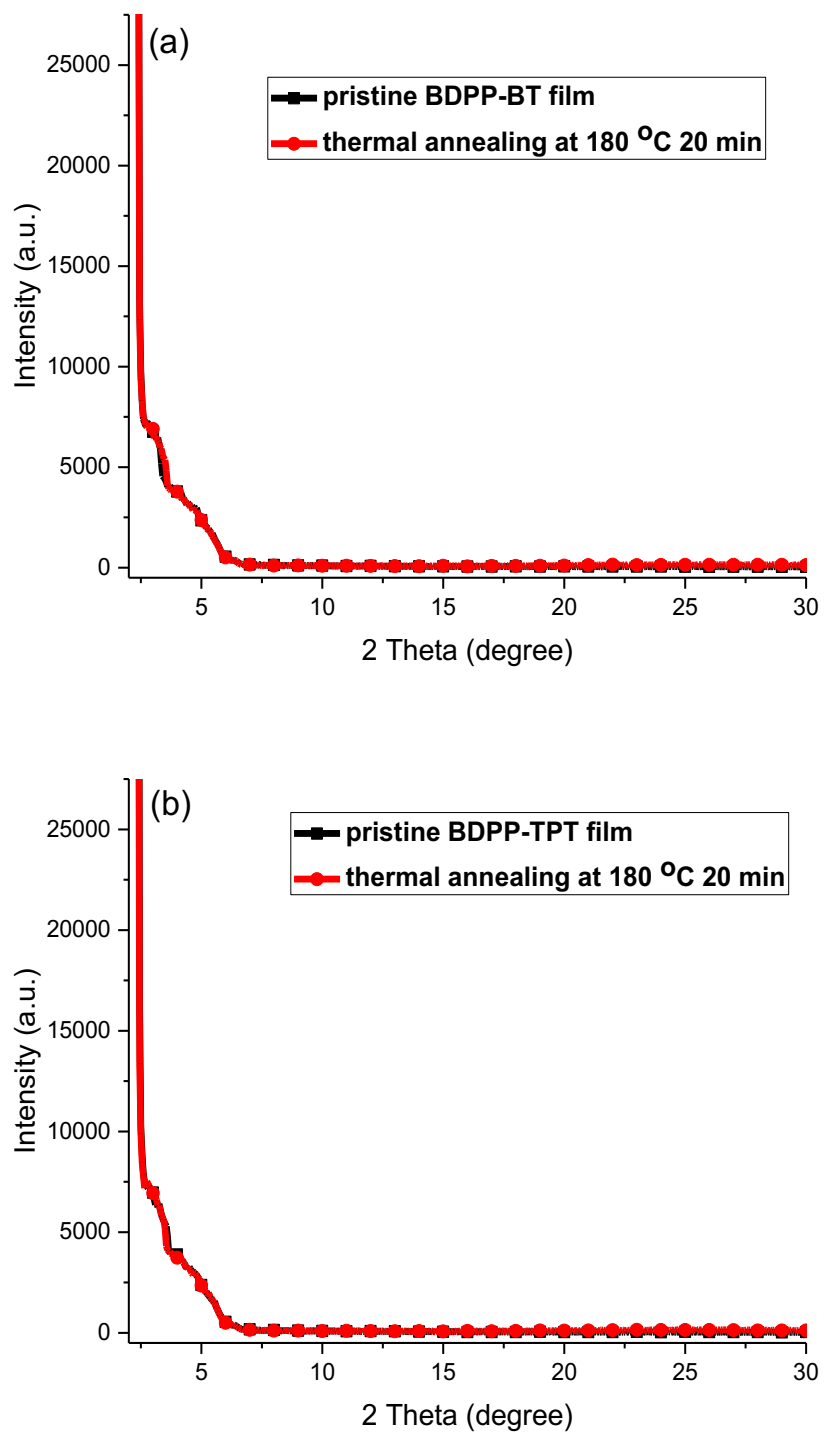


Figure D.1: XRD of (a) **BDPP-BT** (b) **BDPP-TPT** on glass before and after thermal cleavage.

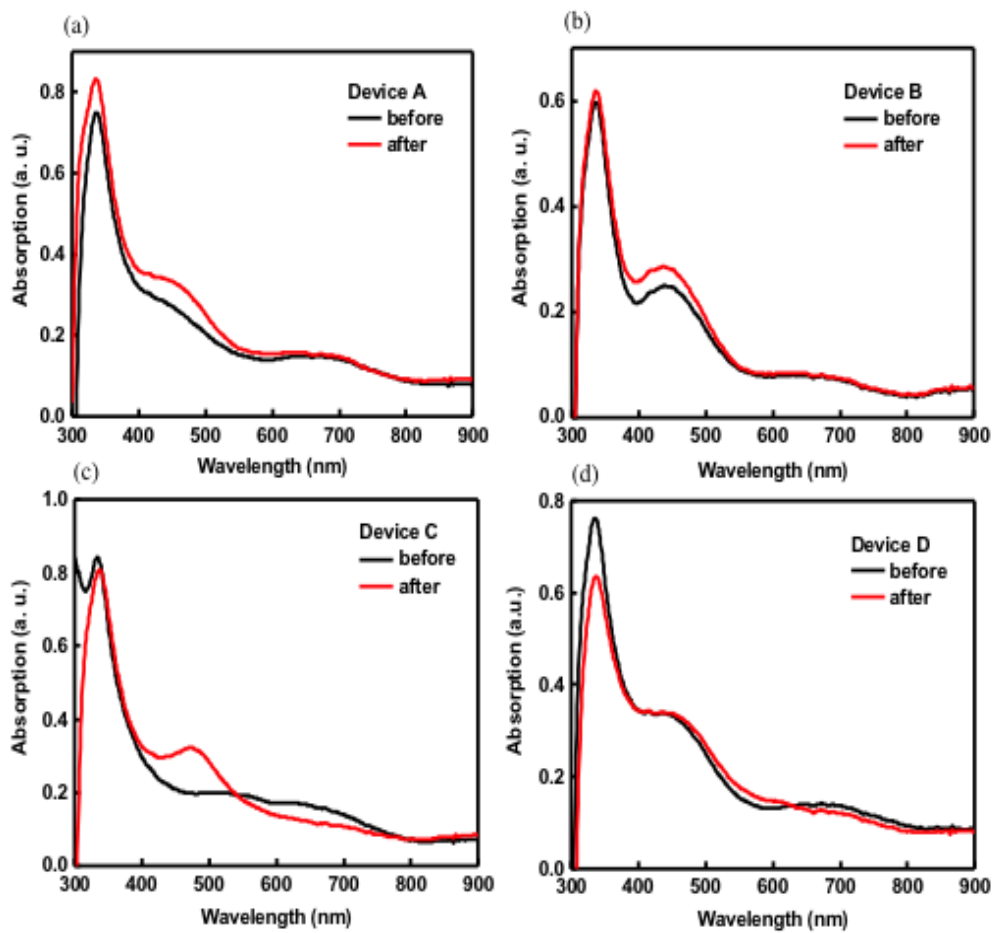


Figure D.2. Absorption changes after thermal annealing (a) Device A (**BDPP-TBT**) ((b) Device B (**BDPP-BT**) (c) Device C (**BDPP-TPT**) (d) Device D (**P3HT:BDPP-TBT**).

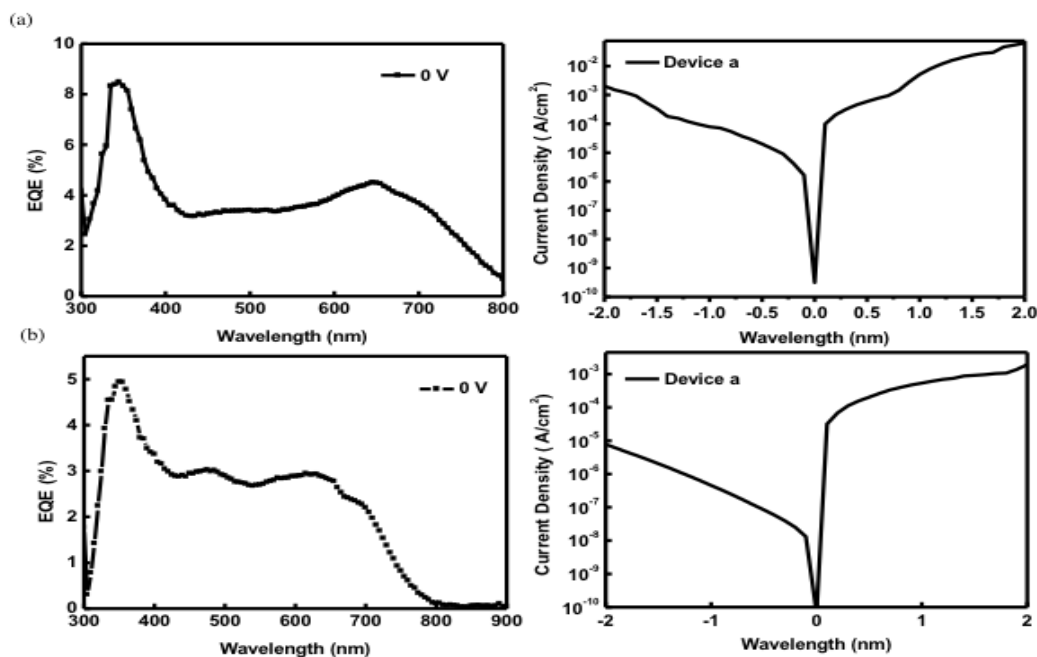


Figure D.3. EQE and Dark current measurement for Device A (**BDPP-TBT**) (a) before thermal annealing (b) after thermal annealing at 180°C.

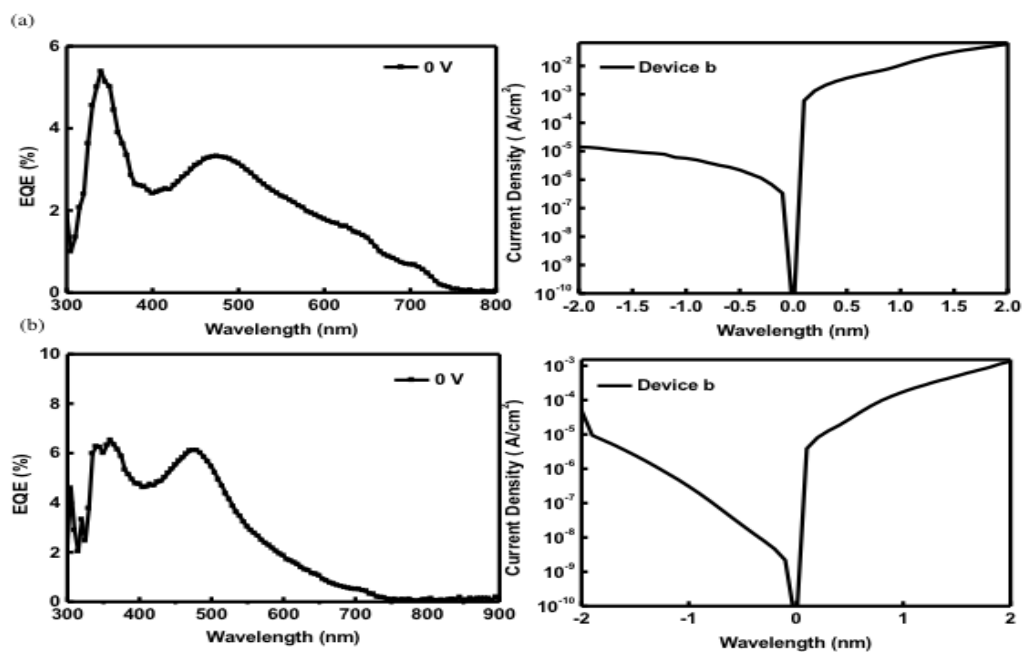


Figure D.4: EQE and Dark current measurement for Device B (**BDPP-BT**) (a) before thermal annealing (b) after thermal annealing at 180°C.

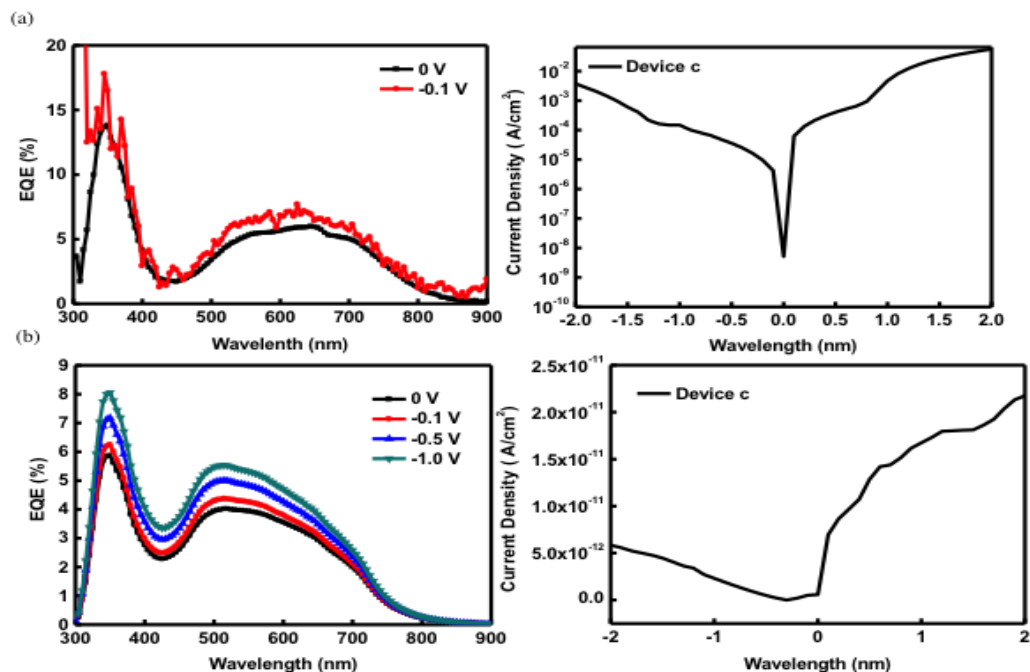


Figure D.5: EQE and Dark current measurement for Device C (**BDPP-TPT**) (a) before thermal annealing (b) after thermal annealing at 180⁰C

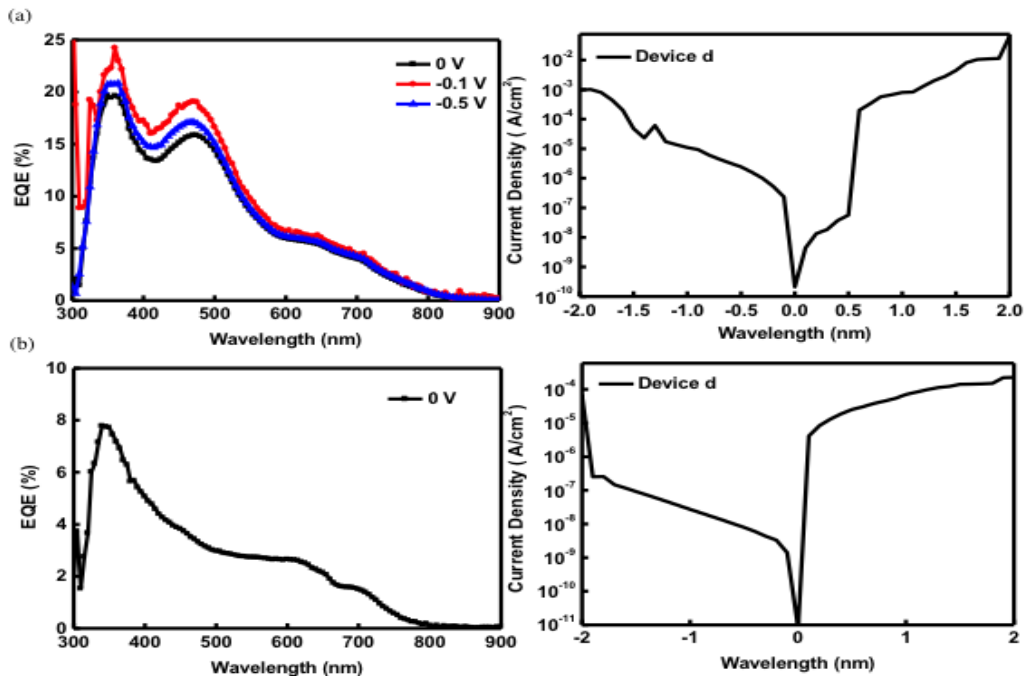


Figure D.6: EQE and Dark current measurement for Device D (**P3HT:BDPP-TBT**) (a) before thermal annealing (b) after thermal annealing at 180⁰C.

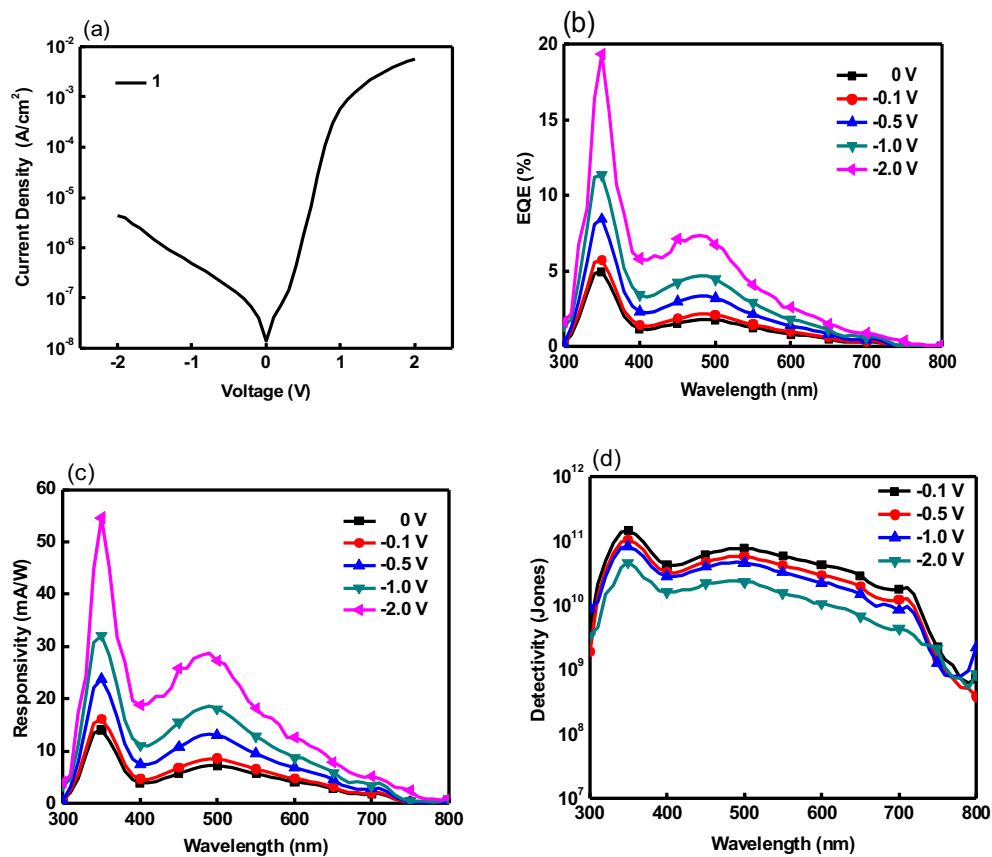
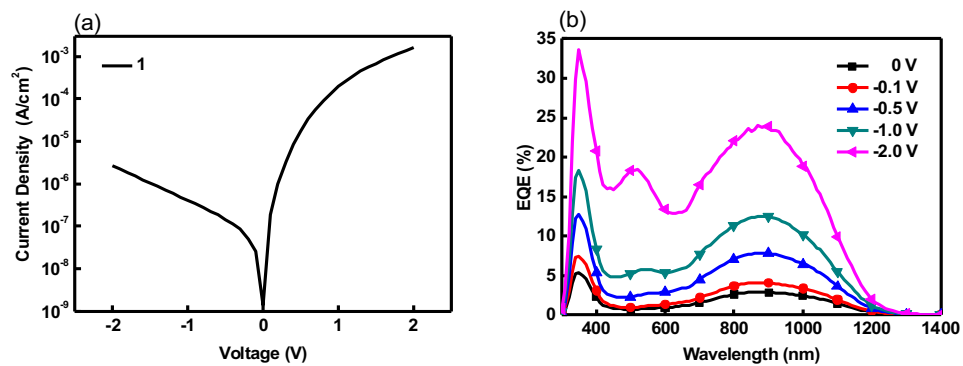


Figure D.7: Photodetector properties of **DPP-DTPa** (a) current-density voltage (J-V) characteristics (b) EQE (c) responsivity (d) detectivity at different bias.



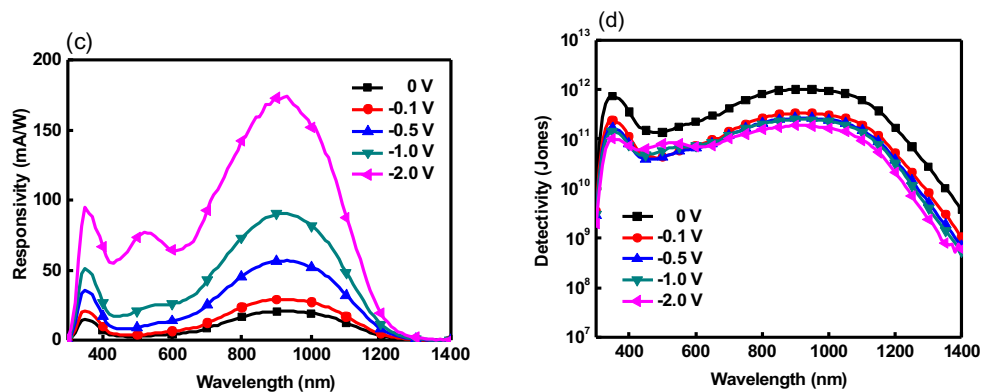


Figure D.8: Photodetector properties of **DAPb-DTP** (a) current-density voltage (J-V) characteristics (b) EQE (c) responsivity (d) detectivity at different bias.

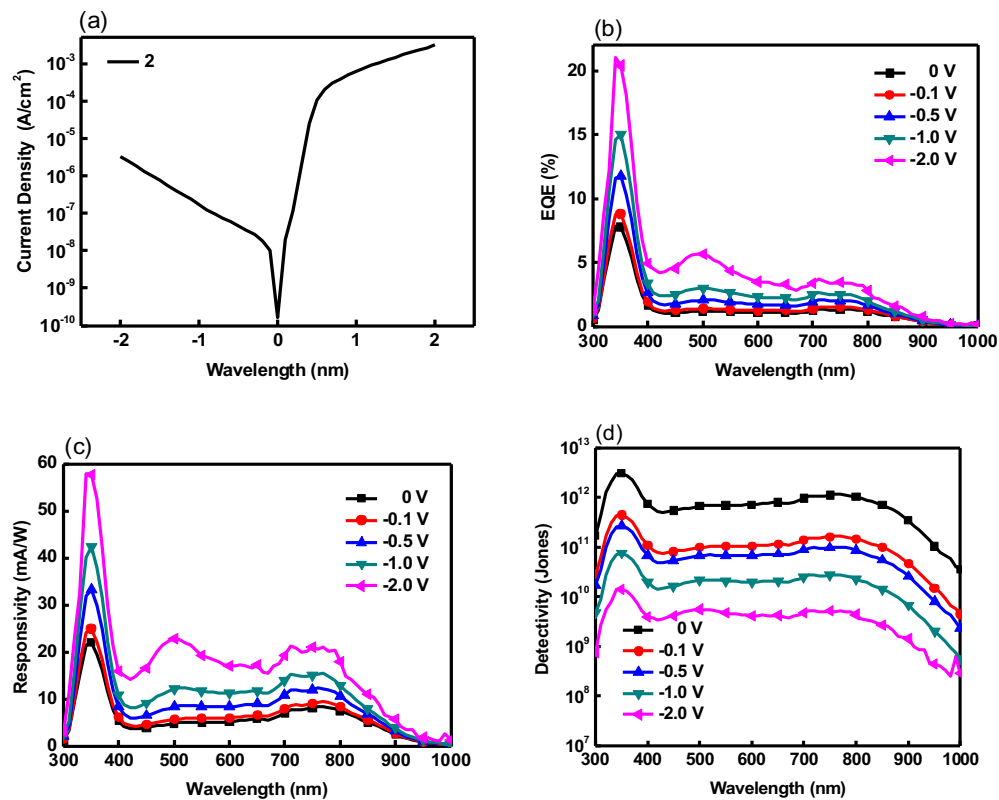


Figure D.9: Photodetector properties of **DAPa-TBTT** (a) current-density voltage (J-V) characteristics (b) EQE (c) responsivity (d) detectivity at different bias.

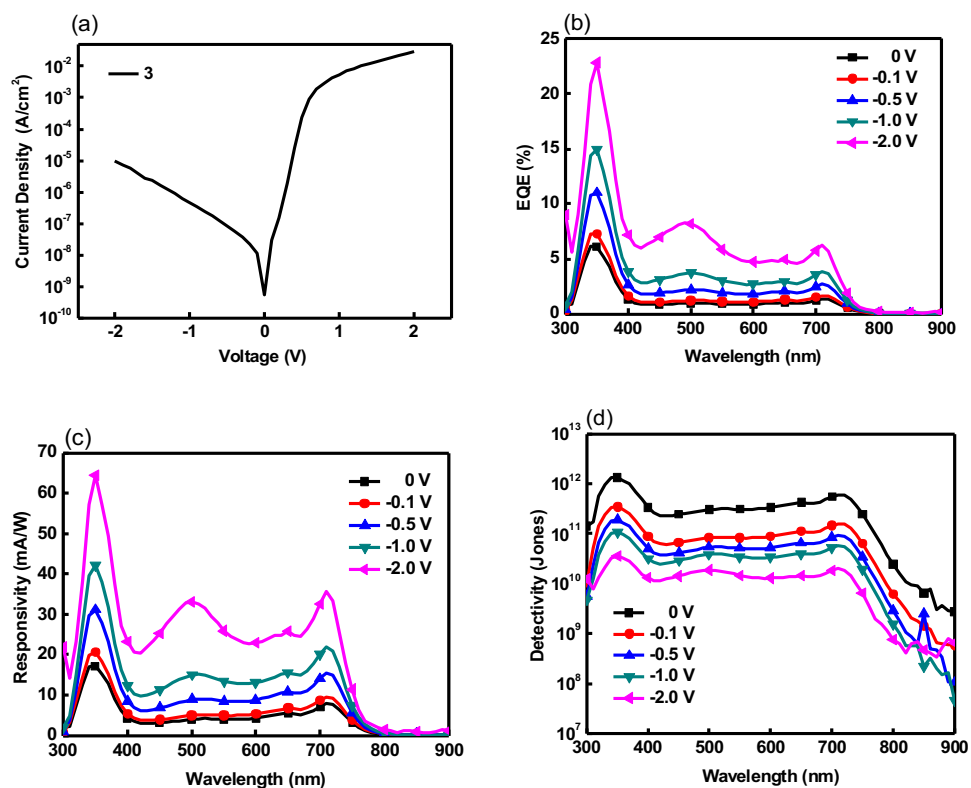
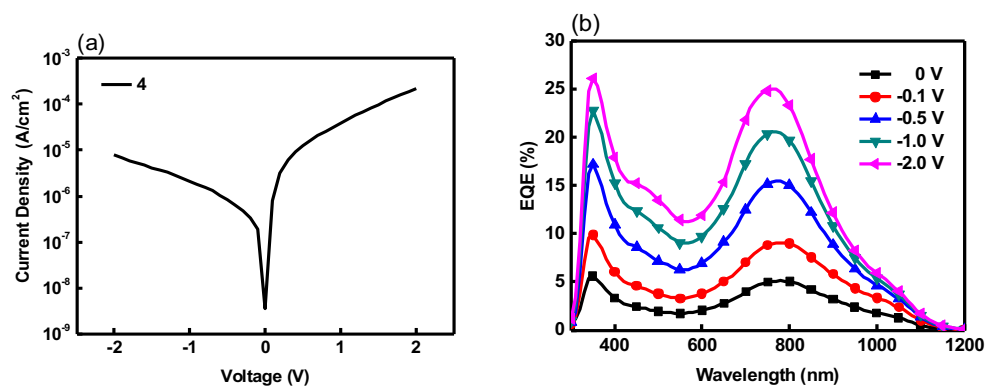


Figure D.10: Photodetector properties of **DAPa-BI** (a) current-density voltage (J-V) characteristics (b) EQE (c) responsivity (d) detectivity at different bias.



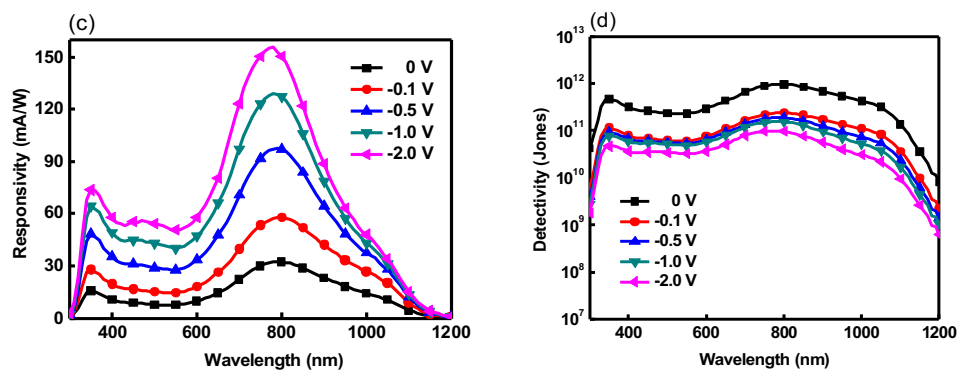


Figure D.11: Photodetector properties of **DAPb-TPT** (a) current-density voltage (J-V) characteristics (b) EQE (c) responsivity (d) detectivity at different bias.

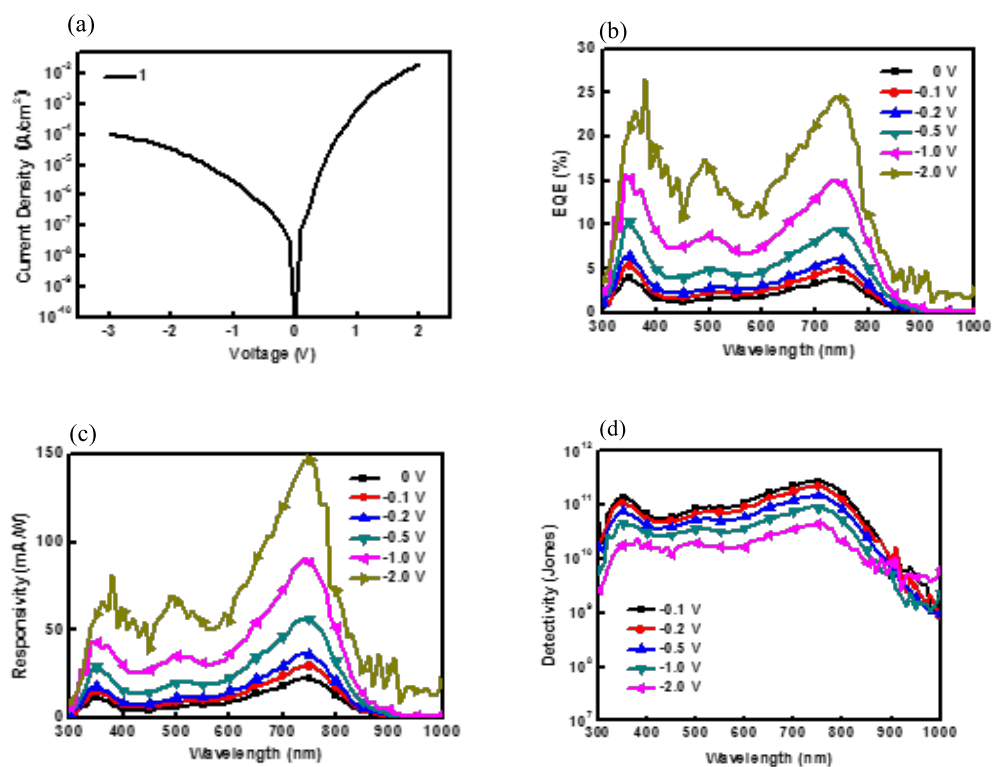


Figure D.12: Photodetector properties of multilayer **DPP-BT:DAPb-TPT** (a) current-density voltage (J-V) characteristics (b) EQE (c) responsivity (d) detectivity at different bias.

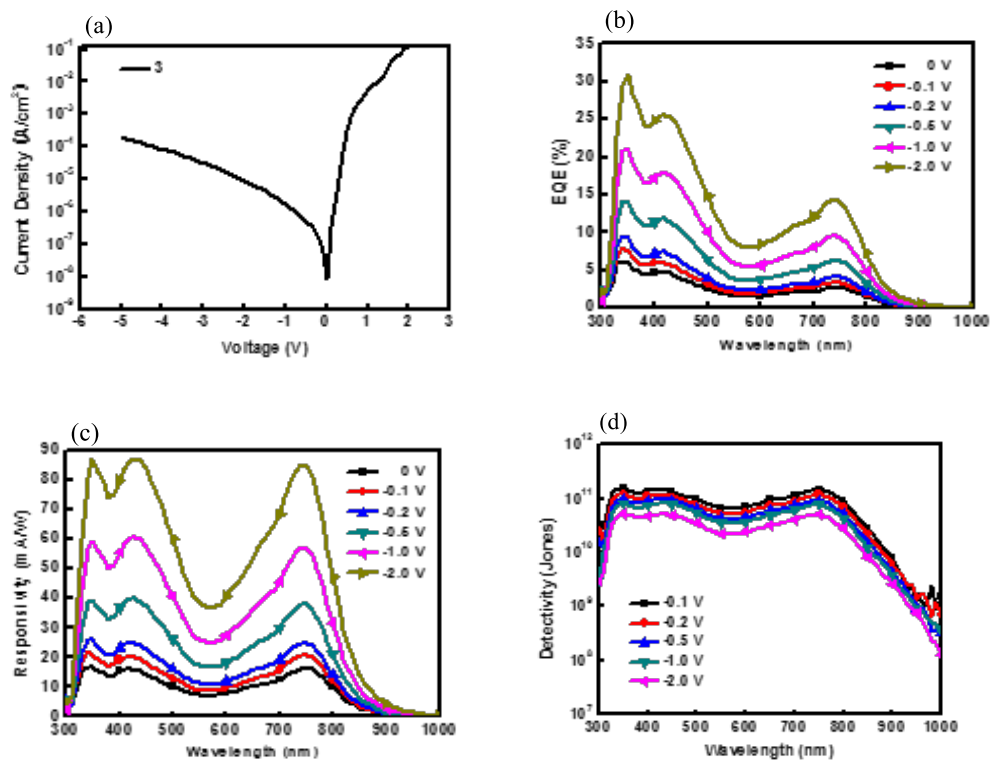
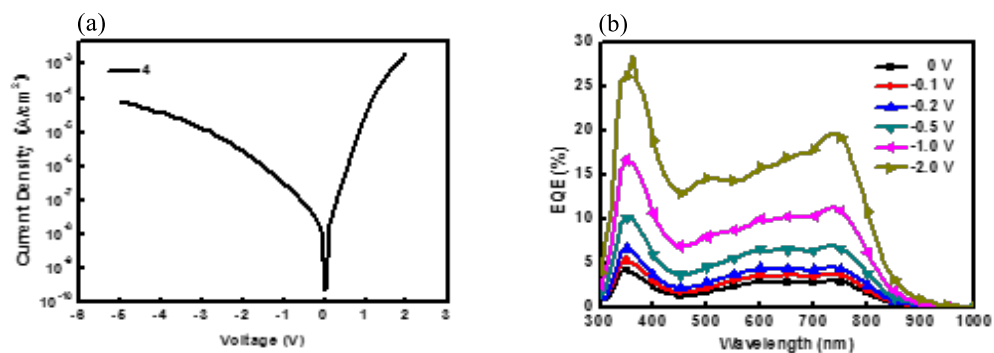


Figure D.13: Photodetector properties of multilayer **DPP-TPTB:DAPb-TPT** (a) current-density voltage (J-V) characteristics (b) EQE (c) responsivity (d) detectivity at different bias.



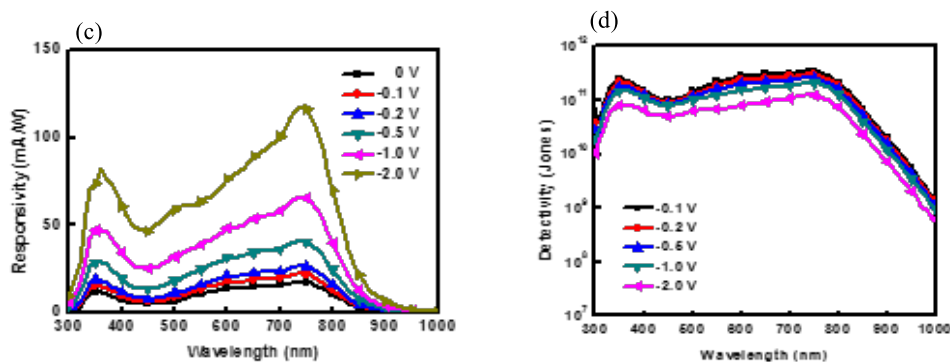


Figure D.14: Photodetector properties of multilayer **DPP-BI:DAPb-TPT** (a) current-density voltage (J-V) characteristics (b) EQE (c) responsivity (d) detectivity at different bias.

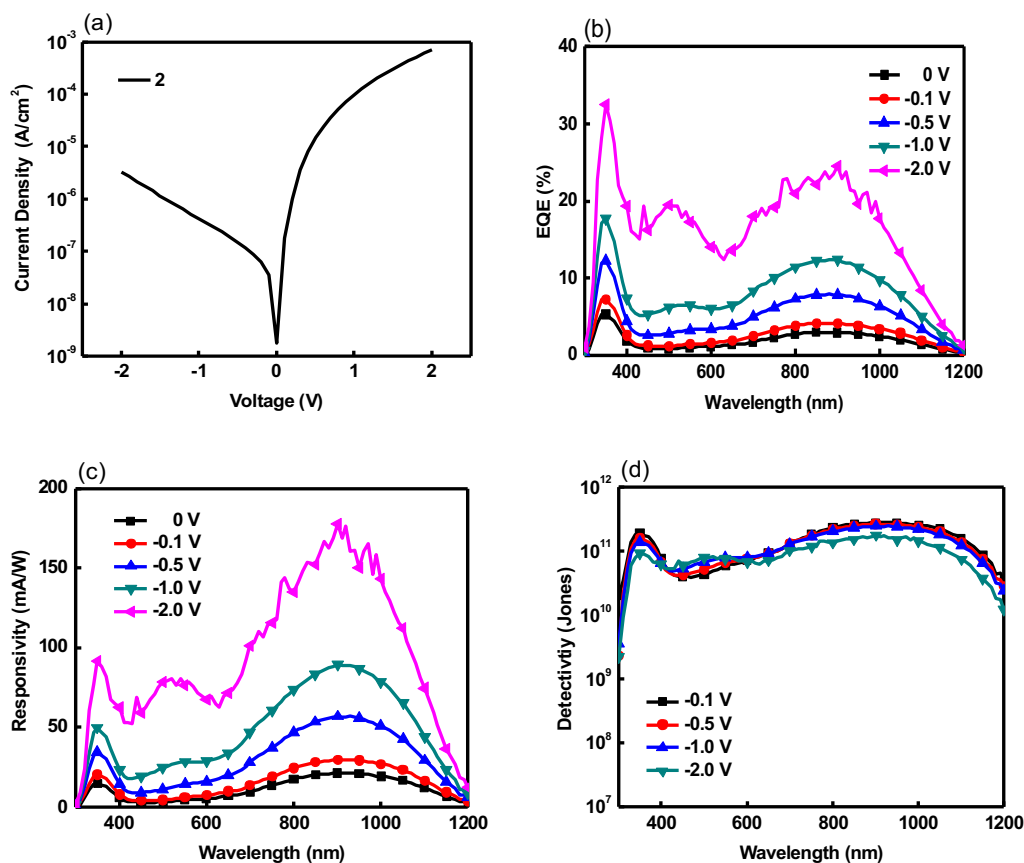


Figure D.15: Photodetector properties of multilayer **DPP-DTPa:DAPb-DTPa** (a) current-density voltage (J-V) characteristics (b) EQE (c) responsivity (d) detectivity at different bias.

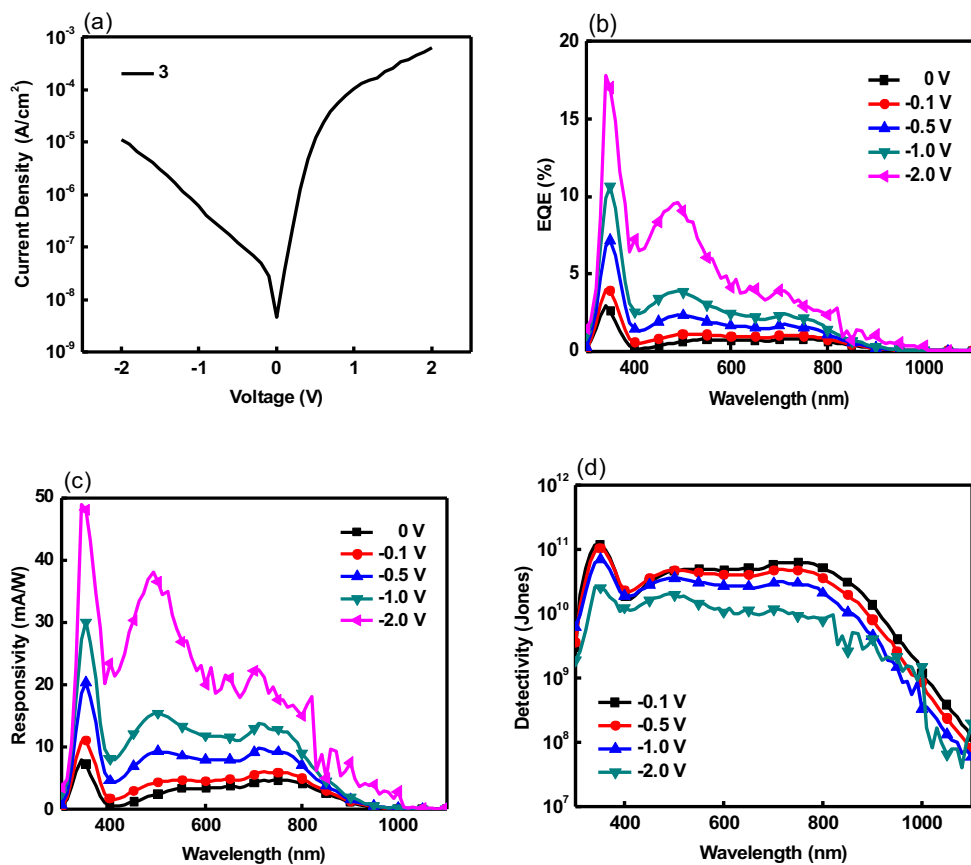
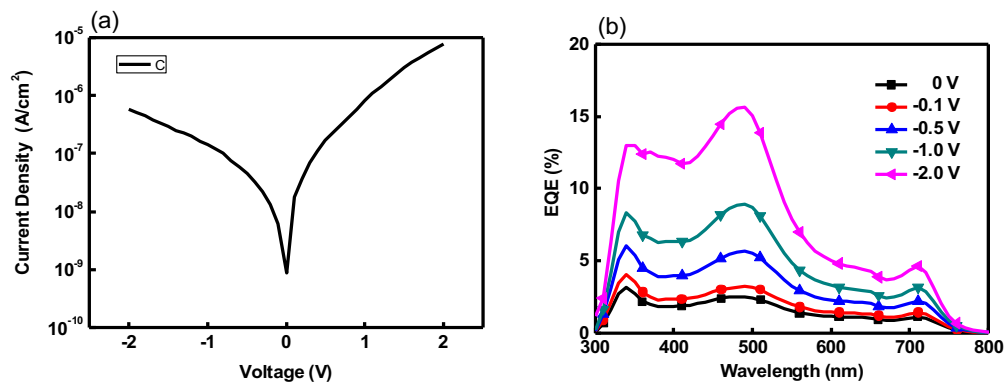


Figure D.16: Photodetector properties of multilayer **DPP-DTPa:DAPa-TBTT** (a) current-density voltage (J-V) characteristics (b) EQE (c) responsivity (d) detectivity at different bias.



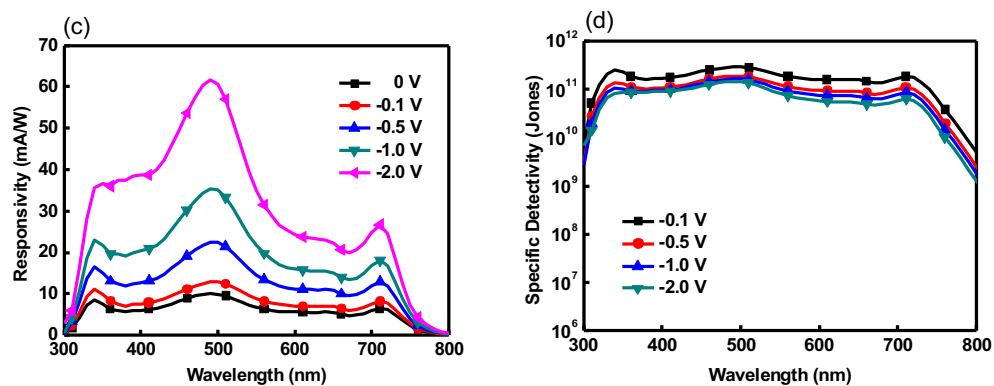


Figure D.17: Photodetector properties of multilayer **DPP-BI:DAPa-BI** (a) current-density voltage (J-V) characteristics (b) EQE (c) responsivity (d) detectivity at different bias.

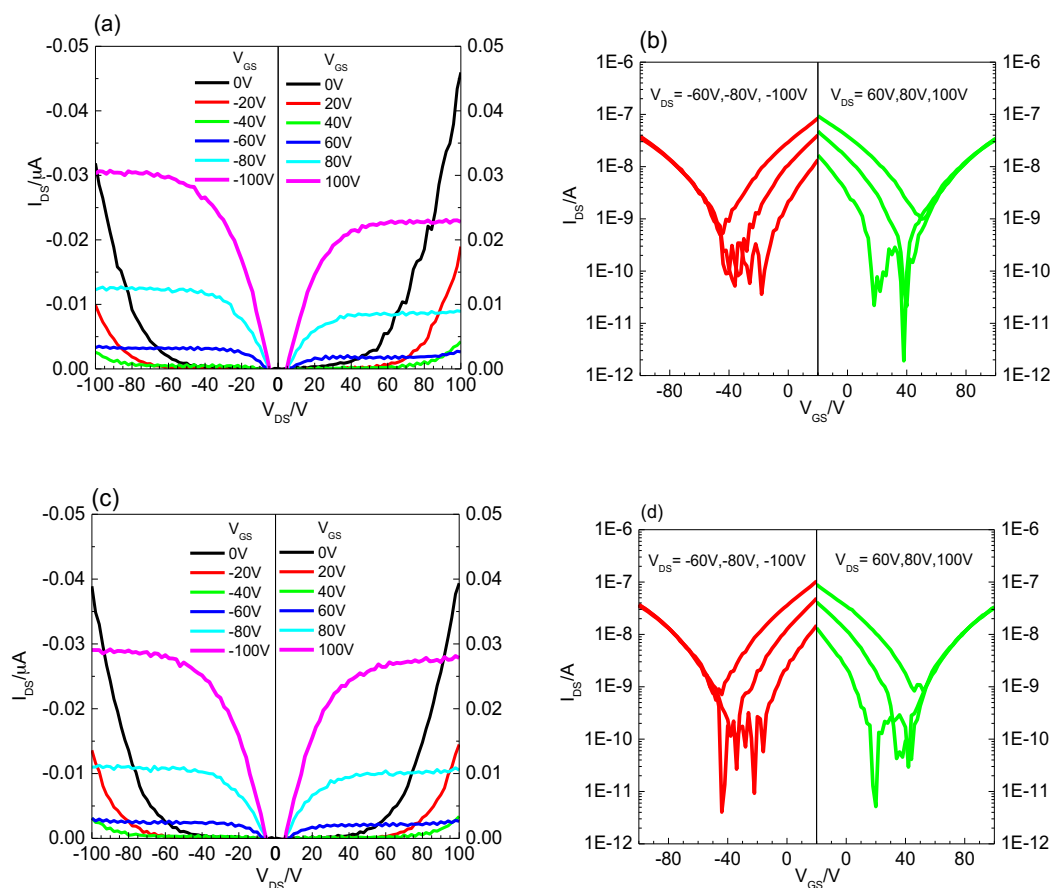


Figure D.18: OTFT measurement of polymers **BI/H -DPTQ** (a) output curve (b) transfer curve at 150 °C (c) output curve (d) transfer curve at 200 °C for 20 min.

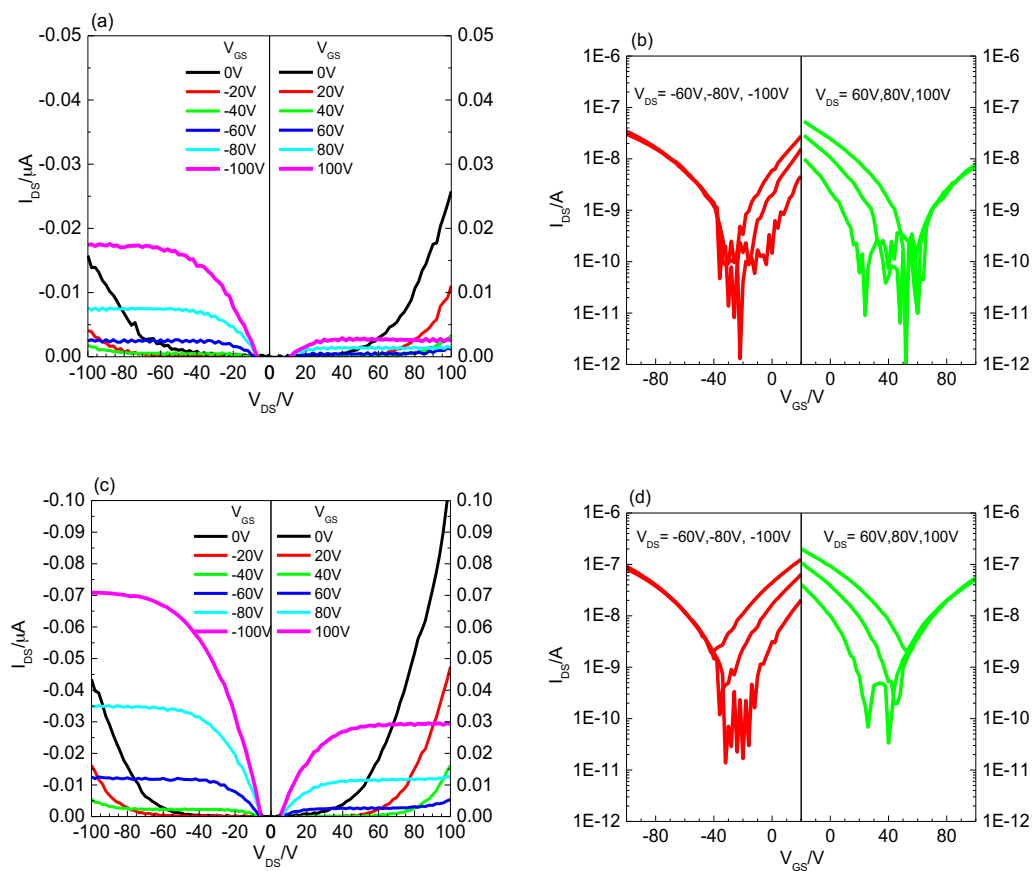


Figure D.19: OTFT measurement of polymers **BI/H -BTP** (a) output curve (b) transfer curve at 150 °C (c) output curve (d) transfer curve at 200 °C for 20 min.